

**PROBABILISTIC MODELING OF MICROGRINDING WHEEL  
TOPOGRAPHY**

A Dissertation  
Presented to  
The Academic Faculty

by

Jacob A. Kunz

In Partial Fulfillment  
of the Requirements for the Degree  
Doctor of Philosophy in the  
G.W. Woodruff School of Mechanical Engineering

Georgia Institute of Technology  
August 2013

Copyright © 2013 by Jacob A. Kunz

**PROBABILISTIC MODELING OF MICROGRINDING WHEEL  
TOPOGRAPHY**

Approved by:

Dr. J. Rhett Mayor, Advisor  
G. W. Woodruff School of Mechanical  
Engineering  
*Georgia Institute of Technology*

Dr. Steven Y. Liang  
G. W. Woodruff School of Mechanical  
Engineering  
*Georgia Institute of Technology*

Dr. O. Burak Ozdoganlar  
Department of Mechanical Engineering  
*Carnegie Mellon University*

Dr. Shreyes N. Melkote  
G. W. Woodruff School of Mechanical  
Engineering  
*Georgia Institute of Technology*

Dr. Jianjun Shi  
H. Milton Stewart School of Industrial  
and Systems Engineering  
*Georgia Institute of Technology*

Date Approved: July 1, 2013

*In Dedication to my beautiful, intelligent bride, Katie*

## **ACKNOWLEDGEMENTS**

I would like to first thank my advisor, Dr. Mayor, for his years of mentoring and guidance. I would also like to thank the thesis reading committee for their valuable time and insight into improving this work. The completion of this body of work would also not be possible without the technical and social support of my graduate school peers: Andrew, Alex, Angela, and Howard. In addition, I am forever grateful to the Woodruff School for supporting me in the quest for my degree. Specifically, I would like to thank the Precision Machining Research Center and the Manufacturing Research Center at Georgia Tech for the continuous resource support.

# TABLE OF CONTENTS

<b>ACKNOWLEDGEMENTS</b> .....	<b>iv</b>
<b>LIST OF TABLES</b> .....	<b>viii</b>
<b>LIST OF FIGURES</b> .....	<b>ix</b>
<b>SUMMARY</b> .....	<b>xviii</b>
<b>CHAPTER 1 – INTRODUCTION</b> .....	<b>1</b>
1.1 Motivation.....	1
1.2 Limitations in Microgrinding and the Ability to Machine High Aspect Ratio Micro-Features .....	5
1.3 Need for Advanced Stochastic Model of Microgrinding Wheel Topography...	9
1.4 Research Objectives .....	14
1.5 Thesis Organization .....	15
<b>CHAPTER 2 – ANALYTIC MODELING OF STATIC WHEEL TOPOGRAPHY</b> .....	<b>17</b>
2.1 Introduction.....	17
2.2 Review of Salient Literature .....	17
2.3 Wheel Model.....	23
2.4 Analytic Abrasive Model .....	24
2.5 Analytic Calculation of the Number of Grits in the Wheel .....	26
2.6 Numerical Simulation of the Number of Grits in the Wheel .....	30
2.7 Analytical Calculation of Grit Location in the Wheel .....	33
2.8 Analytical Calculation of Static Grit Density in the Wheel.....	39
2.8.1 Probability of a Grit Intersecting in the Angular and Axial Domains ..	40
2.8.2 Probability of a Grit Intersecting in the Radial Domain .....	41
2.8.3 Combined Probability of a Single Grit Intersecting the Surface .....	49
2.8.4 Static Grit Density using the Probability of a Particular Grit Intersecting the Surface.....	49
2.9 Analytic Static Grit Density Model Results.....	52
2.10 Discussion .....	54
2.11 Summary .....	56
<b>CHAPTER 3 – NUMERICAL VALIDATION OF ANALYTIC MODEL</b> .....	<b>58</b>
3.1 Introduction.....	58
3.2 Review of Salient Literature .....	58
3.3 Numerical Simulation of Static Wheel Topography without Considering Grit Overlap.....	59
3.4 Placing the Grits in the Wheel Considering Grit Overlap.....	65
3.4.1 Algorithm of Grit Relocation to Minimize Grit Overlap.....	66
3.4.2 Effect of Grit Overlap Reduction on Grit Position Probabilities .....	70
3.4.3 Effect of Grit Overlap Reduction on Static Grit Density.....	71

3.5	Comparison between the Analytic Model and Numerical Simulation.....	73
3.6	Statistical Distribution of Static Grit Density .....	77
3.7	Discussion .....	80
3.8	Summary .....	83
<b>CHAPTER 4 – STATIC MEASUREMENT OF MICROGRINDING WHEELS..</b>		<b>84</b>
4.1	Introduction .....	84
4.2	Review of Salient Literature .....	85
4.3	Machine Vision Inspection and Measurement of Microgrinding Wheels .....	90
4.3.1	Imaging of the Wheel Surface .....	90
4.3.2	Machine Vision Analysis of Fully Imaged Wheels .....	93
4.3.3	Measurement of Wheel Specifications .....	96
4.4	Comparison of Machine Vision Algorithm to Manual Inspection .....	98
4.5	Measurement of Microgrinding Wheel Specification Accuracy .....	99
4.6	Static Grit Density Model Accuracy .....	105
4.7	Static Grit Density Variance Scale Effect.....	109
4.8	Static Grit Positions .....	110
4.9	Static Grit Spacings.....	111
4.10	Discussion .....	115
4.11	Summary .....	117
<b>CHAPTER 5 – STATIC WHEEL TOPOGRAPHY SCALE EFFECTS .....</b>		<b>119</b>
5.1	Introduction .....	119
5.2	Review of Salient Literature .....	120
5.3	Investigation of Scale Effect Associated with Stochastic Distributions using Analytic Topography Model.....	121
5.4	Effect of Manufacturing Variance at the Microscale.....	125
5.5	Static Grit Density Measurement at the Microscale .....	129
5.5.1	Static Grit Density Sample Measurement to Estimate Static Grit Density of a Single Wheel.....	130
5.5.2	Sample Size to Estimate Static Grit Density of a Single Wheel.....	132
5.5.3	Static Grit Density Sample Measurement to Estimate Static Grit Densities across a Set of Wheels from the Same Manufacturer .....	136
5.6	Summary .....	139
<b>CHAPTER 6 –DYNAMIC TOPOGRAPHY IN STRAIGHT TRAVERSE GRINDING .....</b>		<b>140</b>
6.1	Introduction.....	140
6.2	Review of Salient Literature .....	141
6.3	Analytic Model of Dynamic Wheel Topography.....	146
6.3.1	Probability of the Penetration Depth Difference between Two Grits.....	147
6.3.2	Probability of the Arc Length between Two Grits.....	149
6.3.3	Probability of a Grit Not Being Overshadowed.....	150
6.3.4	Dynamic Grit Density using the Probability of a Positive Chip Thickness .....	152
6.4	Analytic Dynamic Grit Density Model Results .....	154
6.5	Numerical Simulation of Straight Traverse Grinding.....	157

6.5.1	Simulation Algorithm .....	157
6.5.2	Dynamic Grit Density Distribution Statistics .....	158
6.5.3	Dynamic Grit Density Probability Distribution .....	160
6.5.4	Cutting Force Simulation .....	161
6.6	Experimental Measurement of Microgrinding Forces .....	167
6.6.1	Setup for Straight Traverse Razorblade Grinding .....	167
6.6.2	Characteristics of the System Free-Response .....	168
6.6.3	Characteristics of the System Forced-Response .....	169
6.6.4	Measured Dynamic Cutting Forces .....	174
6.7	Discussion .....	180
6.8	Summary .....	181
<b>CHAPTER 7 – DYNAMIC TOPOGRAPHY IN INFEEED GRINDING.....</b>		<b>182</b>
7.1	Introduction .....	182
7.2	Review of Salient Literature .....	183
7.3	Analytic Model of Dynamic Wheel Topography.....	186
7.3.1	Analysis of the Cutting Action of Individual Grits.....	186
7.3.2	Probabilistic Model of the Dynamic Grit Density .....	187
7.3.3	Probability of the Dynamic Grit Density .....	187
7.3.4	Probability of Grit <i>i</i> being Active .....	190
7.3.5	Probability of Grit <i>i</i> not being Overshadowed by Grit <i>j</i> .....	191
7.4	Numerical Simulation of Dynamic Wheel Topography .....	194
7.5	Comparison between Analytic Model and Numerical Simulation .....	194
7.5.1	Probability of the Engagement of a Single Grit Caused by the Shadowing of another Grit.....	195
7.5.2	Probability of a Single Grit being Active .....	195
7.5.3	Dynamic Grit Density .....	196
7.6	Measurement of Dynamic Microgrinding Wheel Topography using In-Feed Grinding .....	198
7.6.1	Setup .....	198
7.6.2	Details of Experimentation .....	200
7.6.3	Results.....	206
7.7	Discussion .....	211
7.8	Summary .....	213
<b>CHAPTER 8 – CONCLUSIONS .....</b>		<b>216</b>
8.1	Summary and Conclusions.....	216
8.2	Contributions.....	219
8.3	Recommendations and Future Work.....	221
<b>APPENDIX A – SOLUTION TO ANALYTIC STATIC MODEL .....</b>		<b>224</b>
<b>APPENDIX B – RESULTS FOR MEASURED INFEEED GRINDING FORCES</b>		<b>232</b>
<b>REFERENCES .....</b>		<b>239</b>

## LIST OF TABLES

Table 2.1 – Stochastic Models for Static Grind Wheel Topography Characteristics .....	22
Table 2.2 – Grit size distribution data for sample grits.....	25
Table 2.3 – Data for simulation of number of grits in a #220 and #1200 wheel .....	31
Table 2.4 – Number of grits distribution data for simulations.....	33
Table 3.1 – Simulation results for the static grit density at the wheel Surface.....	72
Table 3.2 - Comparison of analytical and simulated wheel topography models .....	82
Table 4.1 – Methods for characterizing conventional grind wheel topographies.....	85
Table 4.2 - Results from machine vision and manual inspection of #220 grit, 50 concentration diamond microgrinding wheels.....	99
Table 4.3 – Experimental plan of inspected wheels .....	100
Table 4.4 – Experimentally measured specifications of microgrinding wheels .....	101
Table 4.5 – Measured specification interactions and distribution parameters.....	104
Table 4.6 – Static Grit Density Model Residuals and Experimentally Measured Circumferential Static Grit Spacing Distribution Parameters.....	107
Table 4.7 – Grit spacing distribution results.....	115
Table 5.1 – Microgrinding as defined by distinct process characteristics[18] .....	120
Table 5.2 – Parameters for scaling study of static grit density .....	121
Table 7.1 – Stochastic models for dynamic grind wheel characteristics .....	184
Table 7.2 – Wheel set A chosen for measurement of dynamic topography distributions .....	201
Table 7.3 – Outline of experimental test plan with measured dynamic grit density. Test execution order was randomized. ....	202
Table 7.4 – Comparison between measured dynamic grit density distribution parameters for wheel 3.1 with predicted parameters from analytic model using 10% grit retainment depth.....	207

## LIST OF FIGURES

Figure 1.1 – Industrial micro-components utilize ceramics for various material properties such as (a) micro-neural probes in the medical industry [3], (b) micro-channeling in fuel cells [4], and (c) micro-valving in micro-fluidics [5] ...	1
Figure 1.2 – 10 $\mu\text{m}$ diameter, 2-flute WC micro-endmill next to a human hair[6] .....	2
Figure 1.3 – Tungsten carbide mold insert microgrinding [11].....	4
Figure 1.4 - SEM image of 1mm OD, electroplated, #220 diamond microgrinding wheel	5
Figure 1.5 – HAR microgrinding (a) process schematic and (b) vibrational lumped parameter model.....	6
Figure 1.6 – Geometric inaccuracy effect due to static deflection on HAR workpieces [17].....	7
Figure 1.7 – Difficulties in machining HAR micro-features are currently addressed using complicated fixturing techniques to support the workpiece [19].....	7
Figure 1.8 – End-views of a (a) 4-flute endmill, (b) conventional grinding wheel, and ..	11
Figure 1.9 – Measured probability distribution of static cutting edge spacing along the perimeter of a conventional grind wheel [29].....	12
Figure 1.10 – Measured probability distributions of the dynamic cutting edge spacing and undeformed chip thickness of a conventional grind wheel [30] .....	12
Figure 1.11 – Simulated probability distribution of static cutting edge spacing on a conventional superabrasive grind wheel <sup>[29]</sup> .....	13
Figure 1.12 – Simulated average number of grits per unit area on the surface of a static conventional superabrasive grind wheel <sup>[30]</sup> .....	14
Figure 2.1 – (a) PDF for individual grit diameters and (b) histogram of the number of grits in a 1mm OD, 10mm width, single-layered #220 grind wheel.....	20
Figure 2.2 – (a) Model of single-layered, spherical grit microgrinding wheel with a low concentration number, (b) diced microgrinding wheel with clean edge, and (c) end view of the diced wheel .....	24
Figure 2.3 – PDF for the grit diameters in (a) #220 and (b) #1200 wheels .....	26
Figure 2.4 – Individual grit volume probability density distribution for #220 grits.....	28

Figure 2.5 – Summary of method for analytical calculation of number of grits in a grinding wheel .....	30
Figure 2.6 – Numerical simulation algorithm to verify number of grits in wheel model.	31
Figure 2.7 – Normal probability plot of the simulated number of grits required to fill a #1200 wheel .....	32
Figure 2.8 - Simulation PDF of the number of grits required to fill a #220 wheel.....	32
Figure 2.9 – Boundary condition for grit retainment on wheel surface.....	34
Figure 2.10 - Grit position coordinate systems.....	34
Figure 2.11 – Grind wheel Cartesian coordinate system boundaries.....	35
Figure 2.12 – Simulation of 50,000 grits yielded the CDF for the (a) radial and (b) angular grit positions along with the PDF for the (c) radial and (d) position .....	39
Figure 2.13 – Sampling of possible locations of grit $i$ with known diameter $D_i$ .....	42
Figure 2.14 – Bar representation of the intersection of grit $i$ with a cylindrical surface ..	42
Figure 2.15 – Bar representation of the intersection of grit $i$ with a cylindrical surface in a single-layered wheel .....	44
Figure 2.16 – Method for analytical calculation of a the probability of a grit intersecting a surface with radius $R_c$ .....	48
Figure 2.17 - Summary of method for analytical calculation of a microgrinding wheel static grit density.....	52
Figure 2.18 – Static grit density distribution parameters from analytic model for (a) #220 and (b) #1200 microgrinding wheels .....	53
Figure 2.19 - Boundary range of 95% of the possible static grit densities of in (a) #220 and (b) #1200 microgrinding wheels .....	54
Figure 2.20 – Abrasive shapes investigated by Kramer and Wagenheim <sup>[49]</sup> .....	55
Figure 2.21 – Impact of modeled abrasive shapes <sup>[49]</sup> .....	56
Figure 3.1 – Numerical simulation algorithm to model grits within a grind wheel.....	60
Figure 3.2 – Plots of simulated wheel surfaces for #220 wheel with grit overlap.....	62
Figure 3.3 - Static grit density distribution on the wheel surface simulated with grit overlap for (a) #220 and (b) #1200 wheels.....	63

Figure 3.4 - Static grit density as a function of the distance from the wheel core simulated with grit overlap in (a) #220 and (b) #1220 grit wheels .....	64
Figure 3.5 - Static grit density normal distribution parameters as a function of distance from the wheel core simulated with grit overlap in (a) #220 and (b) #1200 grit wheels.....	65
Figure 3.6 – Calculation for the separation between particles $i$ and $j$ .....	66
Figure 3.7 – Visualization of the repositioning of an overlapping particle .....	67
Figure 3.8 – Grit relocation algorithm to minimize grit overlap within a grind wheel ....	69
Figure 3.9 - Plots of simulated wheel surfaces for #220 wheel with no grit overlap without verifying BC .....	70
Figure 3.10 – Simulation of 50,000 #220 grits with reduced overlap produced the CDF of the (a) radial and (b) angular grit positions along with the PDF of the (c) radial and (d) angular positions.....	71
Figure 3.11 - Static grit density normal distribution parameters as a function of radial distance from the core simulated with grit overlap reduced to 5% in (a) #220 and (b) #1200 grit wheels .....	73
Figure 3.12 - Static grit density expectation for #220 wheel from analytic and simulation models.....	74
Figure 3.13 - Static grit density expectation deviation from analytic model for #220 wheel .....	75
Figure 3.14 - Static grit density std. dev. for #220 wheel from analytic and simulation models.....	76
Figure 3.15 - Static grit density std. dev. deviation from analytic model for #220 wheel	76
Figure 3.16 – Static grit density mean from analytic and simulation models for a #1200, 1mm OD multi-layered grinding wheel.....	77
Figure 3.17 – Static grit density std. dev. from analytic and simulation models for a #1200, 1mm OD multi-layered grinding wheel.....	77
Figure 3.18 - Skewness and kurtosis for the distribution of static grit density at various radii in #220 wheels .....	79
Figure 3.19 – Skewness and kurtosis for the distribution of static grit density at various radii in #1200 wheels .....	79

Figure 3.20 – Normal probability plot for static grit density at the bond surface of a #1200 wheel .....	80
Figure 4.1 - 1mm OD microgrinding wheel profilometry with (a) a conventional 2 $\mu$ m diamond probed, (b) conventional rotary profilometer and (c) conventional linear profilometer .....	87
Figure 4.2 – Rotary profilometry profiles for a #220, 1mm wheel using trace paths at 3 different axial positions (a), (b), and (c) on the wheel.....	88
Figure 4.3 – Surface of #220, 1mm wheel measured using white light interferometer....	89
Figure 4.4 – Potential setup for an <i>in-situ</i> microgrinding wheel topography measurement tool [61].....	90
Figure 4.5 – Setup for test Approach for <i>in-situ</i> machine vision measurement of microgrinding wheel topography.....	91
Figure 4.6 - Image of a 1mm OD, #220 grit diamond microgrinding wheel in a microscope at 10x magnification .....	91
Figure 4.7 - Illustration of space distortion in projected image due to grind wheel curvature .....	92
Figure 4.8 - Stitched surface image of 0.5mm OD, #200 grit diamond grinding wheel composed from 61 individual images .....	93
Figure 4.9 - Raw grayscale image of #220 grit diamond wheel used for machine vision analysis.....	94
Figure 4.10 - Machine vision algorithm for locating individual grits.....	95
Figure 4.11 - Effects of machine vision algorithm steps on select region of a #220 microgrinding wheel .....	95
Figure 4.12 – Inspection measurement of #200, 508 $\mu$ m wheel.....	96
Figure 4.13 - Inspection measurement of #200, 508 $\mu$ m wheel stitched surface image....	97
Figure 4.14 - Bond thickness measurements showing no definite variation across different wheel diameters .....	102
Figure 4.15 - Bond thickness measurements showed no definite variation across different wheel widths .....	103
Figure 4.16 - Bond thickness measurements showed no definite variation across different grit sizes .....	103

Figure 4.17 - Normal probability plots for the measured wheel (a) concentration number, (b) bond thickness, (c) shank diameter error, and (d) wheel width error across all wheels .....	105
Figure 4.18 - Histogram of static grit density residual error between experimental measurement and (a) numerical simulation model and (b) probabilistic model.....	106
Figure 4.19 – Potential scale effect of higher static grit density relative standard deviation in microgrinding wheels due to the few number of grits in the wheel ...	109
Figure 4.20 – Occurrence frequency of angular grit position in wheel set 3 .....	110
Figure 4.21 - Occurrence frequency of axial grit position in wheel set 3.....	111
Figure 4.22 – Measurement strips used to verify that static grit density is independent of the strip direction .....	112
Figure 4.23 – Histogram of the circumferential grit spacings in wheel 6.2.....	112
Figure 4.24 – Frequency PDF of measured circumferential grit spacings in wheel 6.2 with fitted distribution comparison between the currently used Rayleigh distribution and proposed (a) lognormal distribution and (b) loglogistic distribution .....	113
Figure 5.1 – Microgrinding as defined by the size of the grinding wheel[18] .....	120
Figure 5.2 –Variation of static grit density in #220 single-layered grind wheels as a function of the outer bond diameter formed as the (a) expectations and standard deviation and (b) as the relative standard deviation .....	122
Figure 5.3 –Variation of static grit density in #220 single-layered grind wheels as a function of the wheel width formed as the (a) expectations and standard deviation and (b) as the relative standard deviation.....	123
Figure 5.4 - Variation of static grit density in single-layered grind wheels as a function of the outer bond diameter and grit size .....	124
Figure 5.5- Variation of static grit density in single-layered grind wheels as a function of the outer bond diameter divided by the mean grit diameter .....	124
Figure 5.6- Variation of static grit density in single-layered grind wheels as a function of the outer bond diameter divided by the mean grit diameter .....	125
Figure 5.7 – Effect of concentration number relative standard deviation on static grit density variance .....	129

Figure 5.8 – Total sample population and number of samples needed to estimate the total number of surface grits on single-layered grind wheels .....	135
Figure 5.9 – Sampling ratio required on varying OD single-layered grind wheels to estimate the total number of surface grits and static grit density to within 5% with 95% confidence .....	135
Figure 5.10 – Sampling ratio required to estimate the total number of surface grits and static grit density to within 5% with 95% confidence .....	136
Figure 5.11 – Effect of the number of grits in a wheel on the number of wheel measurements needed to estimate static grit density to within 5%.....	138
Figure 5.12 – Effect of manufacturing variance on the number of wheel measurements needed to estimate static grit density to within 5%.....	138
Figure 6.1 – Grinding process geometry and parameters <sup>[2]</sup> .....	141
Figure 6.2 – Single cutting chip geometry in a topographically uniform wheel <sup>[2]</sup> .....	142
Figure 6.3 – Maximum undeformed chip thickness of grits in a wheel with varying grit protrusion height and linear spacing <sup>[2]</sup> .....	143
Figure 6.4 – Grit penetration depth as defined from the radial depth of cut and position of the outermost grit .....	148
Figure 6.5 – Summary of analytical calculation of number of grits in a grinding wheel	155
Figure 6.6 –Analytically calculated $C_d$ (a) expectation and (b) variance for a #220, 1mm OD wheel operating at 10 krpm (feedrate in mm/sec).....	156
Figure 6.7 – Analytically calculated $C_d$ (a) expectation and (b) variance for a #220, 1mm OD wheel operating at a 40 mm/sec feedrate .....	156
Figure 6.8 – Algorithm to simulating the grind action of a single wheel .....	158
Figure 6.9 – Comparison of the dynamic grit density mean and Std. Dev. as predicted by the analytic model and (a) numerical simulation with overlapping grits and (b) numerical simulation with grit relocation .....	159
Figure 6.10 - #220 wheel dynamic grit density distribution at wheel surface without grit overlap.....	160
Figure 6.11 – Simulated cutting force by individual grits in a #220 wheel with a 150 $\mu$ m grind width, 40 $\mu$ m radial depth of cut, 40mm/s feedrate, and 10krpm spindle speed.....	162
Figure 6.12 – Total simulated cutting force as the sum of the force of each active grit.	162

Figure 6.13 – FFT of the total grinding force .....	163
Figure 6.14 – Simulated cutting force of individual grits in a #220 wheel with a 75 $\mu\text{m}$ grind width, 40 $\mu\text{m}$ radial depth of cut, 40mm/s feedrate, and 10krpm spindle speed.....	163
Figure 6.15 – Total simulated cutting force as the sum of the force of each active grit. 164	
Figure 6.16 – FFT of the total grinding force .....	164
Figure 6.17 – Mean FFT magnitude for 1,000 simulations of the grinding process .....	165
Figure 6.18 – Standard deviation of FFT magnitude for 1,000 simulations of the grinding process.....	165
Figure 6.19 – Simulation of a cutting force of a 5-flute cutting tool with tool-tip runout at 10 krpm .....	166
Figure 6.20 – FFT of the 5-flute tool simulated cutting force .....	167
Figure 6.21 – Setup for straight traverse microgrinding on a razorblade .....	168
Figure 6.22 – Impact response of the workpiece-fixture system measured with hammer load cell, 2 accelerometers, and dynamometer .....	169
Figure 6.23 – FFT of dynamometer signal of engraving tool rubbing at 30 krpm .....	170
Figure 6.24 - FFT of accelerometer signal of engraving tool rubbing at 30 krpm .....	170
Figure 6.25 – Dominant response peak frequency versus spindle drive frequency.....	171
Figure 6.26 – Dominant peak magnitude versus response frequency .....	171
Figure 6.27 - Dominant peak magnitude divided by spindle speed squared versus response frequency.....	172
Figure 6.28 - Dynamometer peak magnitudes divided by spindle speed squared versus driving spindle frequency .....	173
Figure 6.29 – Harmonic peak magnitudes relative to fundamental peak as a function of driving spindle frequency .....	174
Figure 6.30 – FFT of dynamometer output before grinding contact .....	174
Figure 6.31 – FFT of grinding force at 4krpm (66Hz) from dynamometer.....	175
Figure 6.32 – FFT of grinding force at 5krpm (83 Hz) from dynamometer.....	176
Figure 6.33 - FFT of grinding force at 7krpm (117 Hz) from dynamometer .....	176

Figure 6.34 – FFT of grinding workpiece acceleration at 7krpm from 20kHz accelerometer .....	176
Figure 6.35 – Time-frequency plot of force during microgrinding with a #220 grit wheel as it is accelerated from 1-2 krpm.....	177
Figure 6.36 – Time-frequency plot of acceleration during microgrinding with a #220 grit wheel as it is accelerated from 1-2 krpm .....	178
Figure 6.37 – Time-frequency plot of force during microgrinding with a #220 grit wheel as it is accelerated from 1-2 krpm with mean power removed by frequency .....	179
Figure 6.38 – Time-frequency plot of acceleration during microgrinding with a #220 grit wheel as it is accelerated from 1-2 krpm with mean power removed by frequency.....	179
Figure 7.1 – Schematic of in-feed grinding approach: straight infeed grinding with a small grind zone angle .....	184
Figure 7.2 - Kinematically active grits overshadowing multiple inactive grits.....	186
Figure 7.3 - Probability density of grit radial protrusion height above the bond surface in the simulations of a #400, 1mm single-layered wheel.....	193
Figure 7.4 - Probability density of the engagement of a single grit caused by the possible overshadowing by another individual grit $f_{Hijhij}$ shows a Gaussian distribution, $\Omega = 30\text{krpm}$ , $v_f = 30\text{m/s}$ .....	195
Figure 7.5 -Analytic calculations of the probability of a grit being active matching well with numerical simulation results .....	196
Figure 7.6 - Statistical nature of expectation and mean of the dynamic grit density are seen to be well modeled by the analytic solution .....	197
Figure 7.7 - Results from the numerical simulation technique that eliminates overlapping grits shows that the approximations made by the analytic model allow it to accurately predict the more realistic dynamic grit density characteristics. ....	197
Figure 7.8 – Experimental setup for measuring microgrinding forces using the in-feed technique .....	198
Figure 7.9 – Micrographs of WC workpiece micro-pin features with a $150\mu\text{m}$ engagement width in the circumferential direction (a) and a $50\mu\text{m}$ engagement width in the axial direction (b) of the grind wheel .....	199

Figure 7.10 – Impact response of in-feed experimental measurement system to force ping on workpiece without grind wheel interaction with 30 kHz lowpass filtering.....	200
Figure 7.11 – Characteristic experimental force data, from test 26, showing discernible force pulses and entry-zone of initial wheel contact.....	203
Figure 7.12 - Detailed examination of the lowpass-filtered cutting force signal for test 23 after process stabilization.....	205
Figure 7.13 – Detailed examination of the lowpass-filtered cutting force signal for test 26 after process stabilization.....	206
Figure 7.14 – Actual grit retainment depth determined to be 48% at the maximum $R^2$ value between the analytic model and measured dynamic grit density parameters .....	208
Figure 7.15 – Comparison of the dynamic grit density distribution parameters between the measured values for grind wheels 3.4, 3.7, 3.12, and 3.15 and that predicted by the analytic model using 48% retainment .....	209
Figure 7.16 – Distribution of dynamic distance between active grits along wheel periphery for grinding Wheel Set A, $\tan \alpha = 0.02$ .....	210
Figure 7.17 – Distribution of measured peak individual grit cutting force for grinding Wheel Set A, $\tan \alpha = 0.02$ .....	211
Figure 8.1 – Potential algorithm for adaptive model-based control of microgrinding using the developed probabilistic models.....	222

## SUMMARY

This work addresses the advanced probabilistic modeling of the stochastic nature of microgrinding in the machining of high-aspect ratio, ceramic micro-features. The heightened sensitivity of such high-fidelity workpieces to excessive grit cutting force drives a need for improved stochastic modeling. Statistical propagation is used to generate a comprehensive analytic probabilistic model for static wheel topography. Numerical simulation and measurement of microgrinding wheels show the model accurately predicts the stochastic nature of the topography when exact wheel specifications are known. Investigation into the statistical scale affects associated microgrinding wheels shows that the decreasing number of abrasives in the wheel increases the relative statistical variability in the wheel topography although variability in the wheel concentration number dominates the source of variance. An *in situ* microgrinding wheel measurement technique is developed to aid in the calibration of the process model to improve on the inaccuracy caused by wheel specification error. A probabilistic model is generated for straight traverse and infeed microgrinding dynamic wheel topography. Infeed microgrinding was shown to provide a method of measuring individual grit cutting forces with constant undeformed chip thickness within the grind zone. Measurements of the dynamic wheel topography in infeed microgrinding verified the accuracy of the probabilistic model.

# CHAPTER 1 – INTRODUCTION

## 1.1 MOTIVATION

Many advanced industries having growing needs for micro-scaled components. These components allow product manufacturers to reduce system size, increase function density, and interact between the nano and macro-worlds. Micro-components constructed of ceramics are increasing in popularity due to the unique material properties they provide. These properties include high hardness, high strength, increased chemical compatibility, and high corrosion resistance. Various industries value different properties depending on the application. For example, the medical industry has a large need for micro-devices with materials that have high bio-compatibility. Ceramics, such as zirconia, provide this with increased material stiffness over currently used plastics and stainless steel. The fuel cell industry also has need for ceramic components that provide high corrosion and chemical compatibility. The micro-fluidics industry utilizes the high hardness of ceramics to reduce frictional wear in micro-valves. The high thermal stability of ceramics is highly sought in many industries such as in micro-thermal systems. Example products from these industries are shown in Figure 1.1.

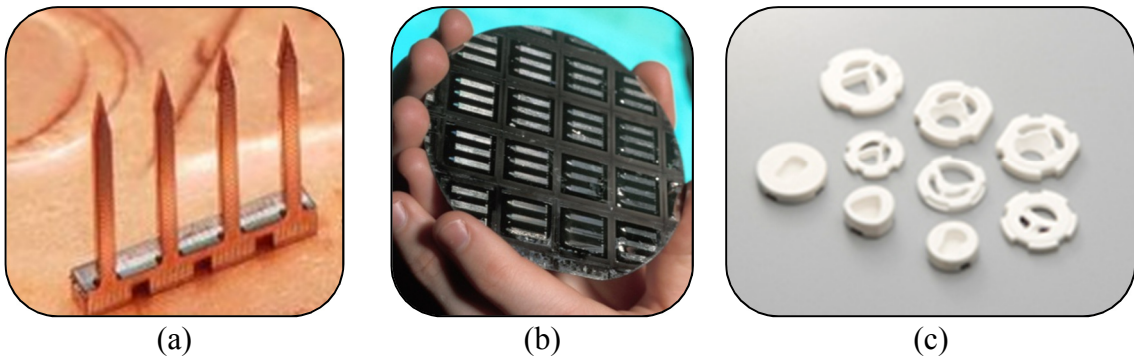


**Figure 1.1 – Industrial micro-components utilize ceramics for various material properties such as (a) micro-neural probes in the medical industry [3], (b) micro-channeling in fuel cells [4], and (c) micro-valving in micro-fluidics [5]**

The micro-tooling industry also utilizes ceramics because of the benefits of high stiffness, surface hardness, and hot-hardness. Tungsten carbide milling cutters, such as the one seen in Figure 1.2, provide one of the cheapest and most productive methods of manufacturing components at the micro-scale.

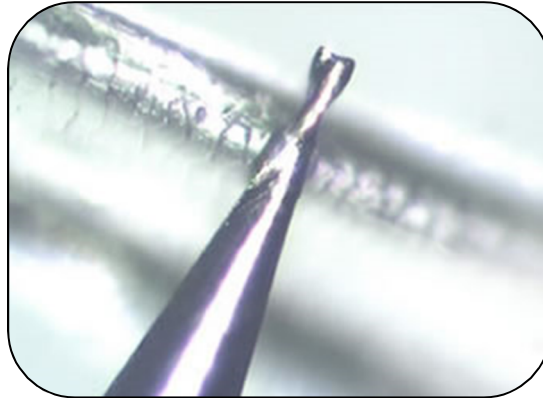


**Figure 1.2 – 10 µm diameter, 2-flute WC micro-endmill next to a human hair[6]**

The manufacturing of these complex micro-features in ceramics has traditionally used either machining, defined as discrete material removal from a bulk workpiece blank, or near-net shape molding. Grinding is a widely used method of machining ceramic components as it provides high material removal rates for increased productivity, high dimensional accuracy, and ultra-fine surface finishes. In addition, it provides a method of creating complex 3-D structures from ceramics that are not achievable with other manufacturing methods such as lithography. However, the use of conventional grinding for the manufacturing of micro-components is limited due to constraints imposed by the large tool size. The challenge of tool-size has not been addressed. Consequently, alternative processes have been developed to shape these micro-scale ceramic features including micro-laser machining, micro-electric discharge machining and micromilling

processes. Micromolding processes have been successfully developed to replicate the shape into ceramic work pieces, using metal molds, or tools, that have been shaped with the above micro-scale machining processes.

These new manufacturing technologies are effective in creating 3-D ceramic micro-components but each has limitations. Laser micro-machining offers benefits of having no contact force and high precision. However, the process utilizes vaporization of the removed ceramic material which can lead to thermal cracking and the re-deposition of waste material. Therefore, high quality surfaces are difficult to laser machine at the micro-scale without having to limit material removal rates [7].

Micro-molding is utilized for the high-productivity generation of bulky ceramic micro-components such as the micro-valves seen in Figure 1.1. However, issues of shrinkage deformation over the large temperature range of the process limits feature shapes and sizes without resorting to post-process shaping of the features [8]. In addition, the need to consolidate porosity in the part requires complex techniques such as hot isostatic pressing.

Micromilling offers benefits of high material removal rate and 3-dimensional flexibility. Strict micromilling of brittle ceramics requires precise modeling and control to operate in the realm of ductile-mode machining. Tooling for this operation utilizes polycrystalline diamond coatings to improve tool hardness and facilitate the ductile cutting regime. Advanced methods in this process include ultrasonic vibration to increase material removal rates and workpiece thermal softening through laser pre-heating [9, 10]. However, vibration-assisted milling produces micro-cracking which leads to low quality

surface finishes while laser-assisted micro-machining suffers from the limitations of laser spot sizes on micro-features.

Recently, the use of miniature microgrinding wheels has become popular as a method to machine brittle micro-components. High spindle speeds on the order of 200 krpm are utilized to maintain high material removal rates with low undeformed chip thicknesses. This results in the ability to create 3-D surfaces in ceramics with mirror finishes. One example is the grinding of micro-lens molds in tungsten carbide by Chen et al. as seen in Figure 1.3 [11]. Superabrasive microgrinding tools have simple structures consisting of cylindrical cores which have abrasives either electroplated or sintered onto its surface. Figure 1.4 shows an SEM image of a 1mm microgrinding wheel, or grinding pin, with the abrasive abrasives electroplated to the core. The simplistic wheel structures and limited volume of abrasive utilized in microgrinding wheels make the process highly cost effective. In addition, microgrinding wheels can be used effectively in standard micro-milling machine tools to easily jig-grind complex structures without the need for separate equipment.

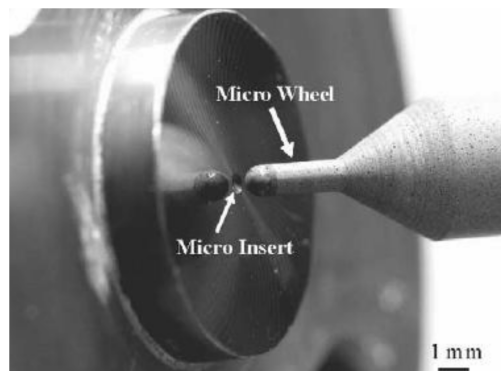


**Figure 1.3 – Tungsten carbide mold insert microgrinding [11]**

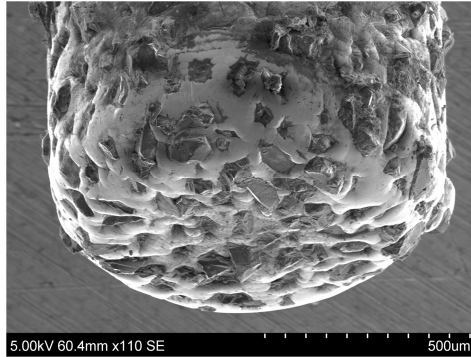


**Figure 1.4 - SEM image of 1mm OD, electroplated, #220 diamond microgrinding wheel**

## **1.2 LIMITATIONS IN MICROGRINDING AND THE ABILITY TO MACHINE HIGH ASPECT RATIO MICRO-FEATURES**

The process strengths of microgrinding include superior surface finishes and residual surface compressive stresses that can resist crack formation and improve surface hardness. These part characteristics are highly beneficial in ceramic components such as process molds [12], micro-optics [13] and various forms of micro-machining tooling [14, 15]. Machining tooling in this category includes micro-drills, micro-endmills, and micro-EDM forms [15-17]. The processing of these brittle materials requires operation in the realm of ductile-mode machining in which high compressive force allows for discrete material removal without brittle fracture of the workpiece. Microgrinding is characterized by cutting edges with large cutting-edge-radius to depth-of-cut ratios which is the defining characteristic of the ductile-mode machining regime [18].

The most difficult micro-part components to machine through mechanical material removal are high-aspect ratio (HAR) part features characterized by small cross-sections and extended lengths. Parts with these HAR micro-features include miniature biomedical probes, micro-heat exchanger, micro-sensors, and micro-machining tools. HAR features

present unique challenges for mechanical material removal due to increased workpiece receptance and increased dynamic vibrations.

A schematic of a system creating a HAR feature is shown in Figure 1.5a. Typical microgrinding wheels have 1/8” steel shanks and 0.5~5 mm wheel cores. They operate on high-speed micro-machining spindles in overhung machine tool structures. This system is characterized by significant compliance due to decreased bearing stiffness in high-speed spindles, decreased tool stiffness in HAR grinding wheels, and decreased structural stiffness in small, overhung machine tools. Additionally, a HAR workpiece further decreases the stiffness of such a system. Figure 1.5b depicts the lumped parameter dynamic model of that system. The dynamics of the individual structures are linked in series. The grinding action dynamics are a local interaction of the grind wheel and workpiece. The interaction dynamics are a function of the local wheel bond stiffness, grit stiffness, local damping caused by coolant and the effects of grind swarf in the grind zone.

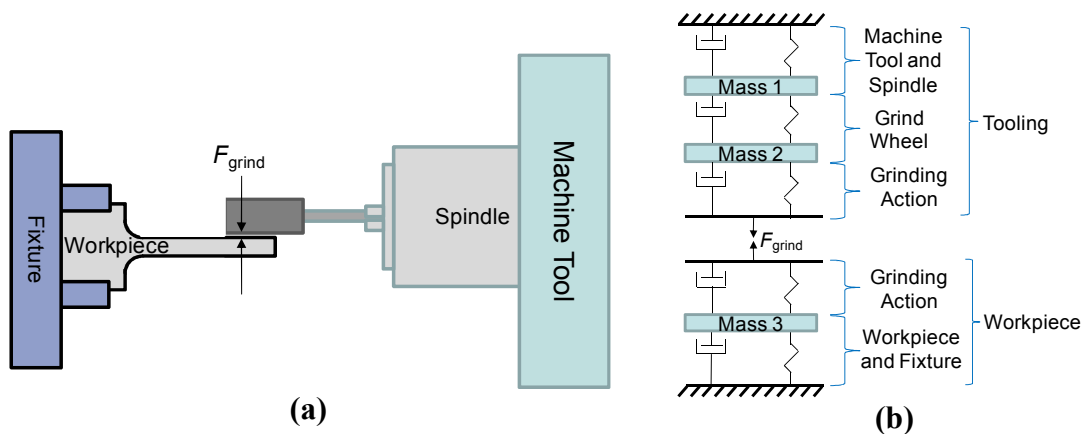


**Figure 1.5 – HAR microgrinding (a) process schematic and (b) vibrational lumped parameter model**

The compliance in such a system leads to static deflection being an issue in grinding accuracy. A consequence of this static deflection is decreased depth of cut leading to inaccurate final part geometries as shown in Figure 1.6 where a micrograph of a high-aspect ratio pin shows a larger final diameter at the end of the part. Current technologies address the difficulties in workpiece flexibility and vibration in HAR workpiece fixtures through complicated and time-consuming fixturing such as that used by micro-tooling manufacturers as seen in Figure 1.7. Fixturing methods such increase process cost and limit feature arrangements on the part due to accessibility issues.

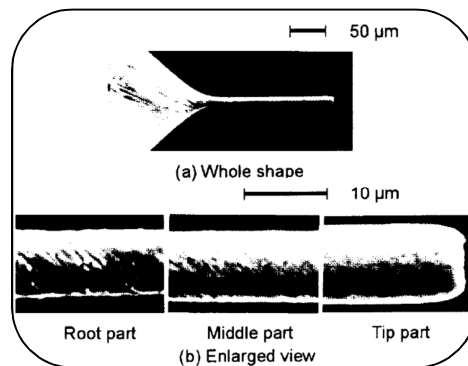


**Figure 1.6 – Geometric inaccuracy effect due to static deflection on HAR workpieces [17]**



**Figure 1.7 – Difficulties in machining HAR micro-features are currently addressed using complicated fixturing techniques to support the workpiece [19]**

An alternative method of addressing compliance issues in HAR microgrinding is advanced process modeling and control. Simple compensation techniques, various novel

grinding methods, and complex workpiece fixturing can compensate for static deflection. However, this requires accurate modeling of the system driving force  $F_{\text{grind}}$ . In addition, static compensation requires that the grinding operation proceed in a region outside of dynamic chatter and in a regime of limited dynamic excitation. This requires more advanced process modeling and control techniques.

Many advanced intelligent control techniques have been used to address issues grinding dynamics and its compensation. The 1994 key note paper of CIRP, presented by Rowe, compiled a comprehensive survey of the state of the art in the application of intelligent control in conventional grinding [20]. However, these techniques have not been extended to microgrinding and require lengthy learning and system identification procedures to tune. Control techniques that utilize advanced process modeling provide the benefit of simplistic control algorithms and limited up-front tuning. In 2006, Brinksmeier presented a CIRP keynote paper which provides a thorough survey of the state-of-the-art in conventional grinding process modeling and simulation while a similar endeavor in 2010, led by the same group of authors, investigated modeling in the domain of ultra-precision grinding which includes microgrinding [21, 22].

The predominance of research to date focuses on mechanistic modeling of conventional grinding. The number of microgrinding studies is limited and those that are available focus on the mechanics of chip formation as it pertains to microgrinding. However, a review of grinding literature by Inasaki shows that proper characterization of grinding wheel topography is crucial to the improved accuracy of a grinding model [23]. Studies have shown that the superabrasive wheels used in microgrinding have tougher grits and do not wear as much over time as conventional wheels so initial topography

modeling is usually sufficient for good grinding model accuracy [2, 24]. The following section introduces challenges unique to microgrinding and expands on the shortcomings of existing modeling of wheel topography.

### **1.3 NEED FOR ADVANCED STOCHASTIC MODEL OF MICROGRINDING WHEEL TOPOGRAPHY**

The definition of microgrinding differs among various authors. The earliest definitions specified the process utilize micron or sub-micron sized abrasives [25, 26]. However, Brinksmeier points out that this definition overlaps with many others including ultra-precision grinding, ductile-regime grinding, ductile-regime finish machining, semi-ductile machining, semi-ductile mode machining, ductile-regime removal and ELID grinding[22]. Many authors consider microgrinding the utilization of micron-sized abrasives on meso-scaled wheels less than 3mm in diameter which represent miniature versions of conventional wheels [27]. Park set forth a definition of microgrinding as being characterized by wheels that have small wheel-to-abrasive diameter ratios [18]. This definition continues to hold to the terminology used in current research [28]. This study will take microgrinding to specify wheels with a meso-scaled outer diameter 1.5 mm or less with abrasives between  $1\mu\text{m}$  and  $100\mu\text{m}$  in size.

The current microgrinding modeling knowledge accurately captures the mechanics of material removal by individual abrasive grits. Current models can also characterize the global grinding wheel attributes that capture the *average* number of abrasives that participate in the grinding action along with the *averaged* pertinent material removal characteristics such as individual cutting edge radii and undeformed chip thickness.

However, unique attributes of microgrinding wheels requires improvements to these models. Specifically, there is a need for models that are less reliant on single-value estimators, typically averages.

Grinding wheels are characterized by a surface topography that consists of abrasive grits of various shapes and sizes that are randomly located on the surface of the wheel. Figure 1.8 shows the end-view of a milling cutter which has distinct, well-established cutting edges while a schematic of a conventional grind wheel shows abrasive grits distributed on the wheel surface in a stochastic manner. In comparison, a microgrinding wheel has a defining difference in the relative grit size.

Modeling of the grinding process is fundamentally based on the description of the surface topography of the wheel. In milling, the cutter surface topography has distinct, well defined cutting edges which in turn yield single, repetitive cutting forces. Conventional grinding wheels have grits that number on the hundreds of thousands. The surface topography descriptions used for the force modeling of such wheels are sufficient in capturing the average grinding force. In addition, the very large surface grinding speeds result in very high frequency, broadband individual grit force signals that have limited effects on workpieces. Microgrinding wheels, however, have a limited number of abrasives. Such a small abrasive population size could lead to large variability in the wheel surface topography. In addition, individual grit force signals can have more distinct cutting frequencies as only a limited number of abrasives contribute to the grinding action. A statistical description of microgrinding wheel surface topography is needed to build a probabilistic model of the complete grinding process.

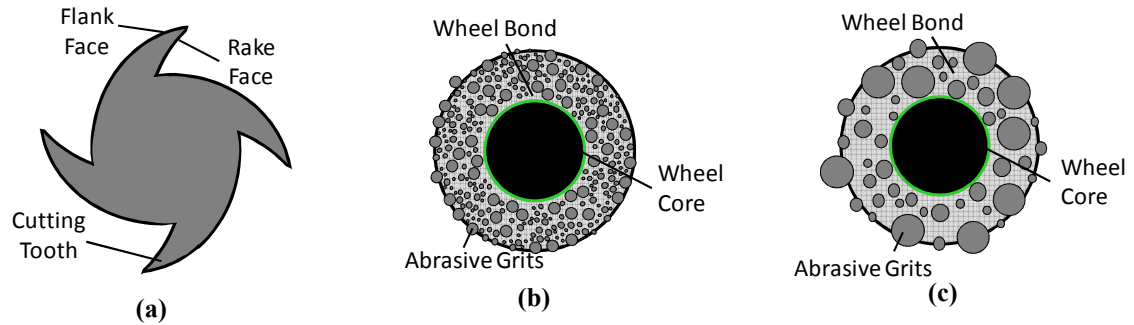


**Figure 1.8 – End-views of a (a) 4-flute endmill, (b) conventional grinding wheel, and (c) microgrinding wheel**

The stochastic nature of the grit attributes and locations makes it impractical to measure and model fully the exact surface profile of every wheel before its use. Instead, gross statistical descriptions of the topography allows for modeling to capture the probabilities of different attributes. Early works investigated this by measuring the stochastic nature of conventional grind wheels. One of the first studies was conducted by Hasegawa in 1974 where profilometry was used to measure the probability distribution of the spacings between grits along the circumference of a static conventional grind wheel [29]. The measured spacings, seen in Figure 1.9, showed that a definite distribution profile exists for the wheel. Another early study, conducted by König in 1975, used grinding force pulses to populate distributions for the spacings between grits and their undeformed chip thickness on a conventional wheel during dynamic grinding [30]. The measured probability distributions are seen in Figure 1.10 using the upper histogram for the dynamic grit spacing and the right-side histogram for the dynamic undeformed chip thickness. Examination of the distributions shows again that discernible profiles exist for the stochastic attributes. Once measured, these dynamic cutting attributes of a particular wheel can be used to model the grinding action stochastically as a convolution of the probability of individual grit forces with the probability of the time spacings between the

individual forces. However, these probability distributions were generated by thorough wheel measurement.

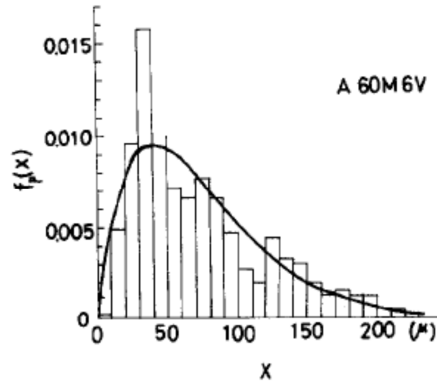


**Figure 1.9 – Measured probability distribution of static cutting edge spacing along the perimeter of a conventional grind wheel [29]**

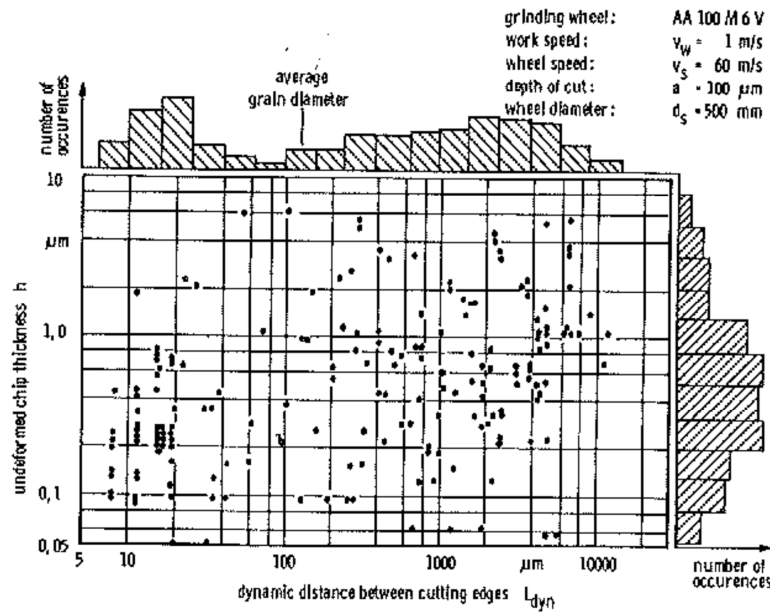


**Figure 1.10 – Measured probability distributions of the dynamic cutting edge spacing and undeformed chip thickness of a conventional grind wheel [30]**

Stochastic descriptions such as these are not thoroughly investigated for superabrasive microgrinding wheels. A numerical simulation study by Koshy in the

1990s aimed at generating such probability profiles through stochastic generation of grit sizes and locations on virtual superabrasive grind wheels. The simulated distributions of static grit spacing, shown in Figure 1.11, showed similar probability profiles as measured in other studies. They also showed that variations in either the grit size or concentration number, which is a ratio of total volume of abrasive to total wheel volume, within the simulated wheel have a definite impact on the shape of the profile. The numerical simulation was also used to calculate the average number of grits per unit area, or static grit density, on the surface of the wheel. The impact of grit size and concentration number on the static grit density was also investigated with the results shown in Figure 1.12. A key conclusion of this result is that for wheels with the same geometry and concentration number, larger grits caused the average static grit density to decrease but there was an increase in the variance of the static grit density across individual simulation iterations. A key question exists on how this increased variance would impact microgrinding wheels where the grits are very large in comparison to the wheel diameter.

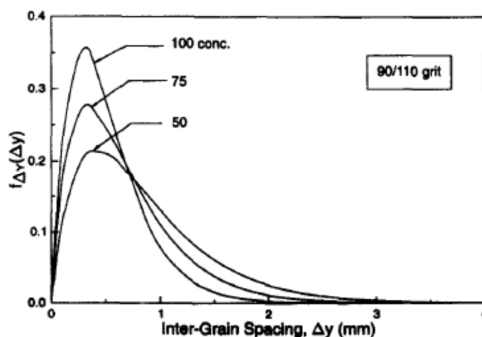


**Figure 1.11 – Simulated probability distribution of static cutting edge spacing on a conventional superabrasive grind wheel <sup>[29]</sup>**

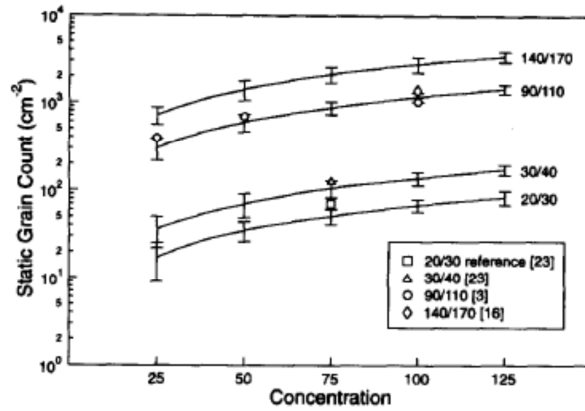


**Figure 1.12 – Simulated average number of grits per unit area on the surface of a static conventional superabrasive grind wheel [30]**

## 1.4 RESEARCH OBJECTIVES

This work aims to develop a probabilistic model for the wheel topography of superabrasive microgrinding wheels for the purpose of improving understanding and process control capabilities. The model generated will seek to maintain an analytic model form by utilizing base stochastic descriptions of the wheel composition and propagating the analytic representation of the statistics into final stochastic descriptions without resorting to costly simulation or intermediate measurement techniques.

It is hypothesized that the large relative size of the grits in microgrinding wheels causes increased variance in the wheel topography characteristics. This can lead to large variability in the performance of identical microgrinding wheels under identical process conditions. Advanced stochastic modeling of microgrinding wheel topography is needed to understand the impact of this variability on the process mechanics. In particular, the variability in the attributes of cutting edge spacing and undeformed chip thickness are the most important when grinding HAR micro-features. The model needs to capture the nature of the variability on the static wheel surface and then extend into the dynamic

microgrinding wheel topography in order to fully describe the variability associated with the process forces. Such a model can be used in advanced process control of microgrinding in order to increase material removal rate while maintaining workpiece surface integrity and geometric accuracy in manufacturing of challenging component features such as high-aspect ratio ceramic micro-features.

The high-sensitivity of the ceramic microgrinding process to undeformed chip thickness and cutting speed requires accurate modeling and prediction of microgrinding wheel surface topography. Inherent stochastic variability in microgrinding wheels limits the ability to accurately predict the important cutting characteristics. Some metrology needs to be conducted on each wheel in order to narrow the distribution of possible grinding force attributes. A metrology method for quickly and easily characterizing the static wheel topography of microgrinding wheels needs to be developed to limit the predicted force variability by eliminating uncertainties in microgrinding wheel specifications and combating variability associated with the few number of abrasives in each microgrinding wheel.

## **1.5 THESIS ORGANIZATION**

The structure of this thesis is outlined as follows. CHAPTER 2 details the development of the probabilistic model for the static wheel topography while CHAPTER 3 details the verification and limitations of the analytics. CHAPTER 4 details the development of a fast *in situ* metrology tool to measure static wheel topography of microgrinding wheels which is then used to experimentally verify the analytic static model and investigate the effect of the uncertainties associated with the manufacturing of

microgrinding wheels. CHAPTER 5 investigates scaling effects associated with the topography of microgrinding wheels. CHAPTER 6 details the development of a probabilistic model of dynamic microgrinding wheel topography for traverse grinding, following the analytic statistical technique pursued in the static wheel topography model. CHAPTER 7 details the development of a dynamic model of a unique microgrinding technique that facilitates easy measurement of dynamic topography in microgrinding wheels which is used then used for experimental validation. The conclusions, contributions, and recommendations for future work are presented in CHAPTER 8. Each chapter includes a detailed review of the relevant salient literature.

## **CHAPTER 2 – ANALYTIC MODELING OF STATIC WHEEL**

### **TOPOGRAPHY**

#### **2.1 INTRODUCTION**

This chapter details with the development of a probabilistic model for the static wheel topography of superabrasive grinding wheels using analytical stochastic propagation techniques. High-fidelity control of HAR microgrinding requires accurate prediction of the probability distributions of individual grit cutting forces and frequencies due to the high sensitivity to excessive cutting force and dynamic excitation. The prediction of these distributions requires an accurate stochastic model of the static wheel topography. This model needs to provide the stochastic description without relying on time-consuming methods such as exhaustive numerical simulation, such as Monte Carlo techniques, and complete wheel measurement. Rather, the model should be based on simple assumptions about the statistical distribution of abrasive sizes and locations in a general 3-D space based on the nature of wheel manufacturing. Statistical propagation can then be used to convert these distributions into a final stochastic description of pertinent static wheel topography characteristics via appropriate distributions. The development of the model is statistically rigorous in order maintain analytic formulation for the purpose of fast computation while limiting the number of assumptions and simplifications that are required.

#### **2.2 REVIEW OF SALIENT LITERATURE**

Several simplistic analytic models of conventional grinding wheels have been developed using basic assumptions about the nature of the grits in wheel. Most

superabrasive grinding wheel models assume that the grits can be represented as spheres with radii  $r$  and undetermined orientation, following a generally accepted methodology established in the literature [18, 31, 32]. The implications of the spherical grit assumption, having been reviewed in literature at length, on the wheel model presented in this work discussed in the discussion section of this chapter. This is based on information provided by abrasives interest groups such as the Federation of European Producers of Abrasives and the Unified Abrasives Manufacturers' Association. It has been shown that for a grinding wheel with a given standard superabrasive grit size classification, the probability of encountering a given grit diameter can be modeled by a Gaussian distribution [31-33]. The Gaussian model fits the incidence of grit diameters between the two sift-hole diameters that bound the sorting process for the particular grit set. Equation 2.1 and Equation 2.2 are used to determine the upper and lower bounds of the grit diameters respectively. Here,  $S_u$  and  $S_l$  are the upper and lower sift numbers respectively that determine the upper and lower grit diameters  ${}_u d_g$  and  ${}_l d_g$  respectively. Notice that the terms upper and lower refer to the grit dimensional diameter such that larger physical grits are the upper bound. Therefore, the upper sieve number is smaller than the lower sieve number.

$${}_u d_g = \frac{0.6}{S_u} \cdot 25.4 \text{ [mm]} \quad \text{Equation 2.1}$$

$${}_l d_g = \frac{0.6}{S_l} \cdot 25.4 \text{ [mm]} \quad \text{Equation 2.2}$$

The grits in the wheel have diameters that fit between these two sizes. Equation 2.3 determines the mean diameter for the Gaussian distribution while Equation 2.4 determines the standard deviation for the distribution.

$$\mu_D = \frac{u d_g + l d_g}{2} \quad \text{Equation 2.3}$$

$$\sigma_D = \frac{u d_g - l d_g}{6} \quad \text{Equation 2.4}$$

A representation of the resulting Gaussian distribution is shown in Figure 2.1a for a #220 superabrasive microgrinding wheel where the mean grit diameter is 71.6  $\mu\text{m}$  and the standard deviation is 4.34  $\mu\text{m}$ .

Grinding wheels are also characterized by their concentration number,  $C$ , which describes the ratio of net abrasive volume in a particular wheel to the total wheel volume. Koshy *et al* used this to numerically simulate a grind wheel by adding abrasives with diameters that fit the Gaussian PDF to a virtual wheel until the volumetric ratio meets the concentration number specification [31]. This method was reproduced to simulate 1,000 microgrinding wheels with #220 grits with Figure 2.1b showing the distribution of the number of grits needed to fill the wheels in the simulation. Notice the distinct but unknown distribution of how many grits are in a single wheel. There are subtle manufacturing variations, however, which limit the ability to predict the topography of superabrasive grinding wheels accurately using only the manufacturer's specifications. For example, grit concentration numbers vary in the way that they are computed between companies [2].

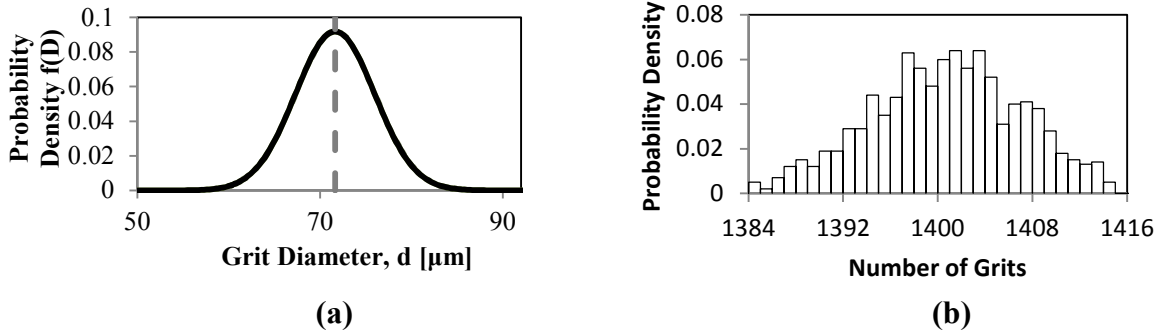


**Figure 2.1 – (a) PDF for individual grit diameters and (b) histogram of the number of grits in a 1mm OD, 10mm width, single-layered #220 grind wheel**

Stochastic descriptions of conventional static wheel topography has been measured and modeled in many ways in the past few decades. A summary of the results of these modeling efforts are summarized in Table 2.1. Most of these grit spacing and location distributions have been measured using either profilometry or simulation techniques which are time consuming and have limited extension to other wheels. The analytical models generated using statistics provide a faster, more thorough model for obtaining the characteristic distributions but they fail to result in distributions that are consistent in shape to those that have been measured on actual wheels.

The static cutting edge density  $C_s$  is the standard representation of the number of cutting edges per unit area that are observed on the surface of a stationary grind wheel. Pandit modeled conventional wheels using a single surface grit density  $G_s$  with a superimposed cutting edge density  $C_s$  which accounts for multiple cutting edges per grit [34]. However, superabrasive grits usually have only one cutting edge per grit so  $G_s$  and  $C_s$  are assumed identical [2]. These representations of cutting edge spacing occur at a set radial position on the wheel of which the default is at the average bond surface. It is known that the mean of  $C_s$  scales with the radial depth according to a power law [2].

Two investigations have specifically characterized conventional diamond grit wheels which are needed for the grinding of hard brittle ceramics such as tungsten carbide [35, 36]. A mathematical model is presented by Koshy *et al* to “estimate the planar grit density, the percentage area due to the abrasives on the wheel surface, and the abrasive protrusion height distribution of a freshly dressed resin/metal bonded diamond grinding wheel” [31]. The model by Koshy is unique to diamond wheels due to the methods of the wheel manufacturing process which result in minimal grit and bond porosity.

**Table 2.1 – Stochastic Models for Static Grind Wheel Topography Characteristics**

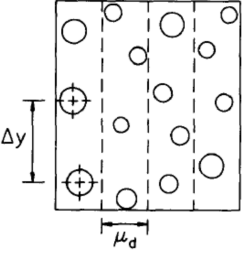
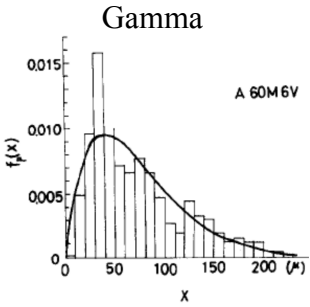
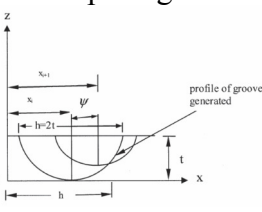
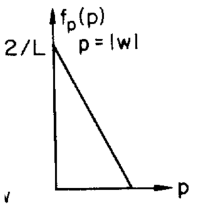
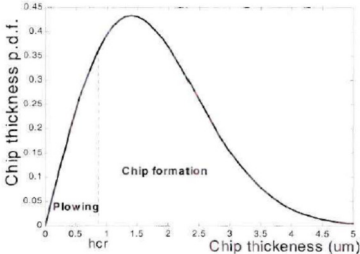
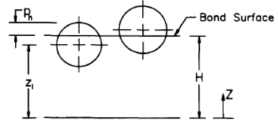
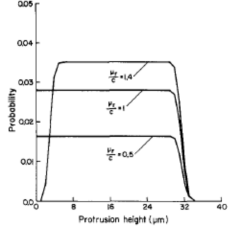
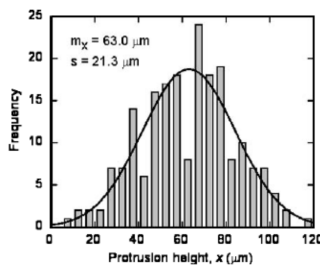
Characteristic	Model Distribution	Measurement Method	Study	
Static Circumferential Grit Spacings 	Negative Exponential $f_Y(\Delta y') = \frac{1}{\lambda} \exp(-\Delta y'/\lambda)$	Postulated from uniform $\theta$ pos. Stylus Profile Markov Chain Fitting	Law, 1973 [37] Orioka, 1961 [38] McAdams, 1964[39]	
	Gamma 	Monte Carlo Simulation Monte Carlo Simulation	Law and Wu, 1973[37] Koshy, 1997[32]	
	Rayleigh $f(h) = \begin{cases} \left(\frac{h}{\sigma^2}\right) e^{-h^2/2\sigma^2} & h \geq 0 \\ 0 & h < 0 \end{cases}$	Oscillating Stylus Profilometry	Hasegawa, 1974[29] Younis and Alawi, 1984[40]	
	Static Axial Grit Spacings 	Triangular 	Analytics from Uniform Axial Positions	Basuray, 1981[41]
		Parabolic $f_\psi(\psi) = 2 \frac{h - \psi}{h^2}$	Analytics from Uniform Axial Positions	Agarwal and Rao, 2005[42]
Static Grit Protrusion Spacings 	Rayleigh Distribution	Oscillating Stylus Profilometry	Younis and Alawi, 1984[40]	

Table 2.1 - continued

Characteristic	Model Distribution	Measurement Method	Study
<p>Static Grit Protrusion Height</p> 	<p>Uniform for Macro-Wheels, Gaussian for Micro-Wheels</p> 	Monte Carlo Simulation	Koshy, 1993[31]
	<p>Gaussian</p> 	Differential Optical Focusing	Hwang, Evans and Malkin, 2000[36]
		Optical Microscopy	Shi and Malkin, 2003[43]
		White Light Interferometry	Huo, 2009[35]
Static Grit Density	Parabolic	Knife-Edge Tracing	Orioka, 1961[38]

### 2.3 WHEEL MODEL

The grinding wheels considered in this study are single-layered, electroplated diamond grit wheels. These wheels are of a grind pin architecture utilizing a 1/8” shank with wheel diameters ranging from 0.5mm to 15mm. Figure 2.2 shows a model of such a wheel with a 1mm bond OD. The grits are assumed to be spherical with a bounded diameter and inconsequential orientation [18, 31, 32, 44]. They are positioned above the surface of a wheel core while suspended in an electroplated nickel bond. Figure 2.2 also shows a side view and end view of a 1mm, #220 grit wheel after the end has been diced off with a diamond grinding wheel and then sanded with CBN sandpaper. The end view

show the thin layer of diamond grits, and the approximate measurement can be made of the base core diameter and outer wheel diameter at the bond layer. The core diameter is consistent with the diameter of the wheel shank.

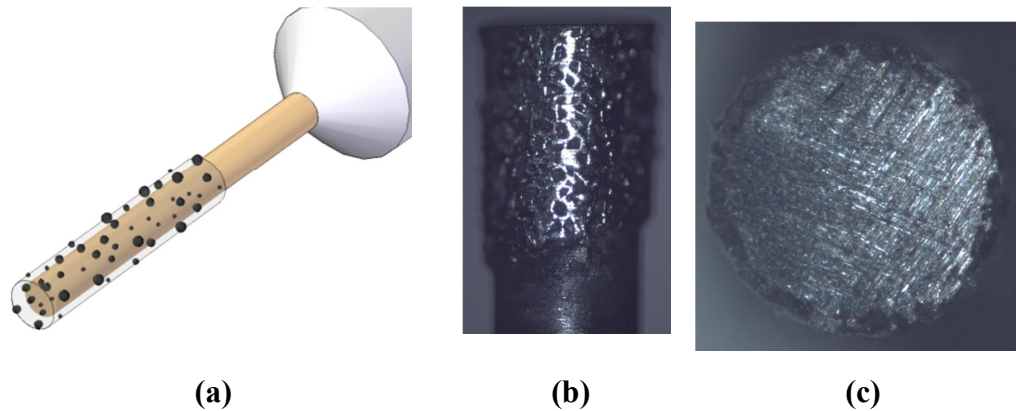


**Figure 2.2 – (a) Model of single-layered, spherical grit microgrinding wheel with a low concentration number, (b) diced microgrinding wheel with clean edge, and (c) end view of the diced wheel**

## 2.4 ANALYTIC ABRASIVE MODEL

The abrasive grits in a diamond wheel have diameters governed by the two sieves used to sort them for wheel production. The upper and lower bounds of the grit diameters are known to be 60% of the linear spacing between the sieve wires as governed by the sieve numbers as detailed in Equation 2.1 and Equation 2.2 [2]. The grits in the wheel have diameters that fit in between these two sizes. It has been shown that the distribution of grit diameters between the two sizes can be modeled using a Gaussian distribution [2]. The mean for this distribution is known to be the average of the upper and lower grit diameter bounds while the standard deviation allows for  $6\sigma$  of the grit diameters to occur between the bounds as detailed in Equation 2.3 and Equation 2.4. A single grit  $i$  has a diameter  $D_i$  that is a continuous random variable. The probability density function (PDF)

of a single diameter is governed by a Gaussian distribution as defined in Equation 2.5. The cumulative density function (CDF), shown in Equation 2.6, represents the probability that the value of the diameter falls below a certain value. The expected value for random variable  $D_i$  is defined by Equation 2.7 where it is calculated to be equivalent to the Gaussian mean.

$$f_{D_i}(d_i) = \frac{1}{\sigma_D \sqrt{2\pi}} \exp \left[ -\frac{1}{2} \left( \frac{d_i - \mu_D}{\sigma_D} \right)^2 \right] \quad \text{Equation 2.5}$$

$$F_{D_i}(d_i) = Pr(D_i \leq d_i) = \int_{-\infty}^{d_i} f_{D_i}(x) dx \quad \text{Equation 2.6}$$

$$E[D_i] = \int_{-\infty}^{\infty} x f_d(x) dx = \int_{-\infty}^{\infty} \frac{x}{\sigma_D \sqrt{2\pi}} \exp \left[ -\frac{1}{2} \left( \frac{x - \mu_D}{\sigma_D} \right)^2 \right] dx = \mu_D \quad \text{Equation 2.7}$$

Table 2.2 shows the calculated grit size numbers for two grit sizes: #220 and #1200 which bound the range of standard sizes available for grinding pins. Figure 2.3(a) shows the probability density function and expected value for grit diameters in the #220 grit wheel, and Figure 2.3(b) shows the same for a #1200 grit wheel.

**Table 2.2 – Grit size distribution data for sample grits**

<b>Grit Number</b>	<b>G#</b>	<b>220</b>	<b>1200</b>
Upper Sift Number	$S_U$	180	1000
Lower Sift Number	$S_L$	260	1400
Upper Grit Diameter	$d_U$	84.6 $\mu\text{m}$	15.2 $\mu\text{m}$
Lower Grit Diameter	$d_L$	58.6 $\mu\text{m}$	10.9 $\mu\text{m}$
Grit Diameter Mean	$M_D$	71.6 $\mu\text{m}$	13.1 $\mu\text{m}$
Grit Diameter Standard Deviation	$\Sigma_D$	4.34 $\mu\text{m}$	0.73 $\mu\text{m}$

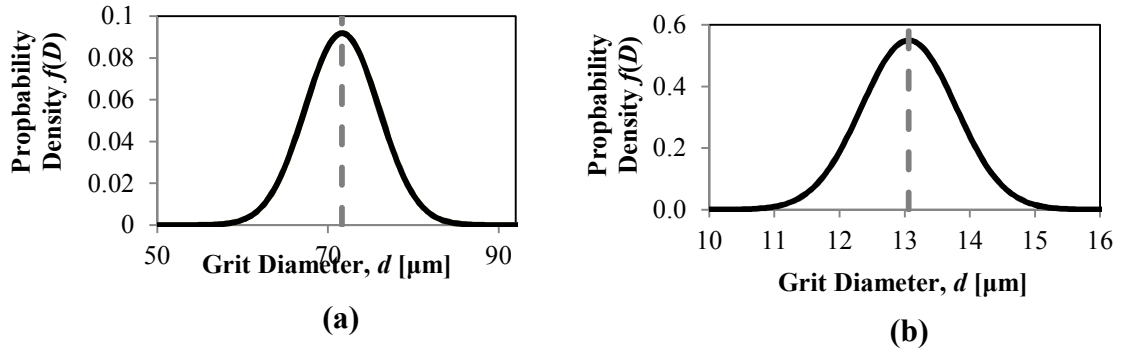


Figure 2.3 – PDF for the grit diameters in (a) #220 and (b) #1200 wheels

## 2.5 ANALYTIC CALCULATION OF THE NUMBER OF GRITS IN THE WHEEL

For a single-layered wheel, the volume available for grit occupation is determined by the wheel outer diameter, the core diameter, and the wheel width. The wheel concentration represents the expected ratio of abrasive volume to total available volume. The total volume of abrasive in a given wheel,  $V_a$ , is a random variable. The expectation of this random variable is the total available volume multiplied by the volumetric ratio. This computation is shown as Equation 2.9 where  $d_w$  and  $d_c$  are the diameters of the wheel and the core respectively,  $w$  is the axial width of the wheel,  $C$  is the wheel concentration number, and the denominator constant is a scaling factor for the concentration number.

$$E[V_a] = \frac{E[C]w\pi \left( \frac{d_w^2 - d_c^2}{4} \right)}{400} \quad \text{Equation 2.8}$$

The volume  $V_i$  of an individual grit is a function of the grit diameter  $D_i$  as calculated in Equation 2.9. It is therefore another continuous random variable. It is known that since  $V_i$  is a measurable function of  $D_i$ , the cumulative density function (CDF) of  $V_i$  can be

calculated from that of  $D_i$  using Equation 2.10[45]. The PDF of the grit volume  $V_i$  can then be calculated by utilizing the Fundamental Theorem of Calculus and definition of CDF as Equation 2.11[45]. These equations can then be combined as shown by the derivation in Equation 2.12 yielding the final PDF of an individual grit volume shown in Equation 2.13.

$$V_i = h(D_i) = \frac{\pi}{6} D_i^3 \quad \text{Equation 2.9}$$

$$F_{V_i}(v_i) = Pr(h(D_i) \leq v_i) = Pr(D_i \leq h^{-1}(v_i)) = F_{D_i}(h^{-1}(v_i)) \quad \text{Equation 2.10}$$

$$f_{V_i}(v_i) = \frac{d}{dv_i} F_{V_i}(v_i) \quad \text{Equation 2.11}$$

$$\begin{aligned} f_{V_i}(v_i) &= F_{D_i}(h^{-1}(v_i)) \cdot \frac{d}{dv_i} = F_{D_i}(h^{-1}(v_i)) \cdot \frac{d}{dv_i} \cdot \frac{dd_i}{dd_i} = F_{D_i}(h^{-1}(v_i)) \cdot \frac{d}{dd_i} \cdot \frac{dd_i}{dv_i} \\ &= f_{D_i}(h^{-1}(v_i)) \cdot \frac{dd_i}{dv_i} = f_{D_i} \left( \sqrt[3]{\frac{6v_i}{\pi}} \right) \cdot \frac{d \sqrt[3]{\frac{6v_i}{\pi}}}{dv_i} \end{aligned} \quad \text{Equation 2.12}$$

$$f_{V_i}(v_i) = \frac{1}{\sigma_D \sqrt{2\pi}} \exp \left[ -\frac{1}{2} \left( \frac{\sqrt[3]{\frac{6v_i}{\pi}} - \mu_D}{\sigma_D} \right)^2 \right] \sqrt[3]{\frac{2}{9\pi v_i^2}} \quad \text{Equation 2.13}$$

The PDF in Equation 2.13 cannot be rearranged to obtain a normal distribution for the grit volume with a unique distribution mean and variance. The expectation and variance of the random variable  $V_i$  can be calculated from the PDF of the individual volume using the Law of the Unconscious Statistician as shown in Equation 2.14 and Equation 2.15 respectively[46].

$$E[V_i] = \int_{-\infty}^{\infty} v_i f_{V_i}(v_i) dv_i = \int_{-\infty}^{\infty} v_i \frac{\sqrt[3]{\frac{2}{9\pi v_i^2}}}{\sigma_{D_i} \sqrt{2\pi}} \exp \left[ -\frac{1}{2} \left( \frac{\sqrt[3]{\frac{6v_i}{\pi}} - \mu_D}{\sigma_D} \right)^2 \right] dv_i = \frac{\pi}{6} \mu_D (\mu_D^2 + 3\sigma_D^2) \quad \text{Equation 2.14}$$

$$\begin{aligned} \text{Var}[V_i] &= \int_{-\infty}^{\infty} (v_i - E[V_i])^2 f_{V_i}(v_i) dv_i = \int_{-\infty}^{\infty} (v_i - E[V_i])^2 \frac{\sqrt[3]{\frac{2}{9\pi v_i^2}}}{\sigma_D \sqrt{2\pi}} \exp\left[-\frac{1}{2} \left(\frac{\sqrt[3]{\frac{6v_i}{\pi}} - \mu_D}{\sigma_D}\right)^2\right] dv_i \\ &= \frac{\pi^2 \sigma_D^2}{12} (3\mu_D^4 + 12\mu_D^2 \sigma_D^2 + 5\sigma_D^4) \end{aligned} \quad \text{Equation 2.15}$$

Figure 2.4 shows the calculated PDF obtained using Equation 2.13 along with the expected value of the grit volume as calculated using Equation 2.14. Notice how the expected value is not the peak of the PDF due to the skewness of the distribution.

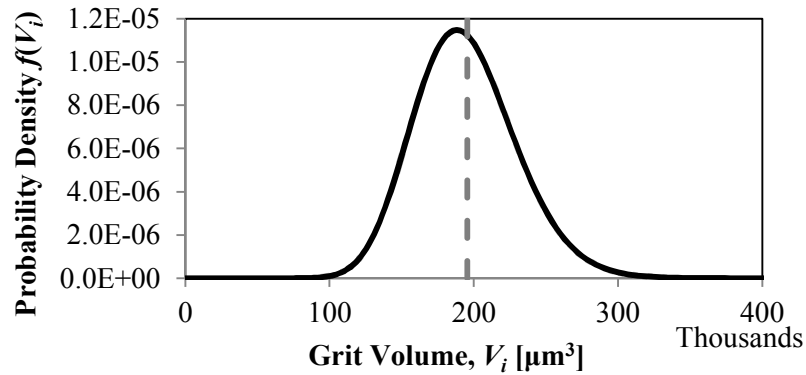


**Figure 2.4 – Individual grit volume probability density distribution for #220 grits**

Suppose that the given volume has random variable number of grits  $N_a$  where each grit has volume  $V_i$ . The sum of volumes of the individual grits is equal to the expected total abrasive volume  $V_a$ . This is the summation of independent random variables  $V_i$  where  $i = 1, 2, \dots, N_a$  which is shown in Equation 2.16.

$$V_a = g(V_i) = \sum_{i=1}^{N_a} V_i \quad \text{Equation 2.16}$$

First, the Law of the Unconscious Statistician is applied to the expected value for a function of independent random variables as shown in Equation 2.17 [45]. However,

since each independent random variable  $V_i$  has the same PDF and expected value, this can be further simplified in Equation 2.18 which can be rearranged to find the expected value for the number of grits in the wheel as seen in Equation 2.19.

$$E[V_a] = E[g(V_i)] = E[V_1 + V_2 + \dots + V_{N_a}] = E[V_1] + E[V_2] + \dots + E[V_{N_a}] \quad \text{Equation 2.17}$$

$$E[V_a] = E[V_i] + E[V_i] + \dots + E[V_{N_a}] = E[N_a]E[V_i] \quad \text{Equation 2.18}$$

$$E[N_a] = \frac{E[V_a]}{E[V_i]} \quad \text{Equation 2.19}$$

Similarly, the same can be done with the variable variances as shown in Equation 2.20 and Equation 2.21 [45].

$$\text{Var}[V_a] = \text{Var}\left[\sum_{i=1}^{N_a} V_i\right] = E[N_a]\text{Var}[V_i] + (E[V_i])^2\text{Var}[N_a] \quad \text{Equation 2.20}$$

$$\text{Var}[N_a] = \frac{\text{Var}[V_a] + E[N_a]\text{Var}[V_i]}{(E[V_i])^2} \quad \text{Equation 2.21}$$

It is seen that the variance in the total volume of abrasives in the wheel originates from the variance in the measured total volume of abrasive that will be put into the wheel,  $\text{Var}[V_a]$ . However, conventional grind wheel specification only provides the expected value of the volume of abrasive in the wheel and not its variance. A summary of the necessary steps for calculating the distribution for the number of grits in a grind wheel is shown in Figure 2.5.

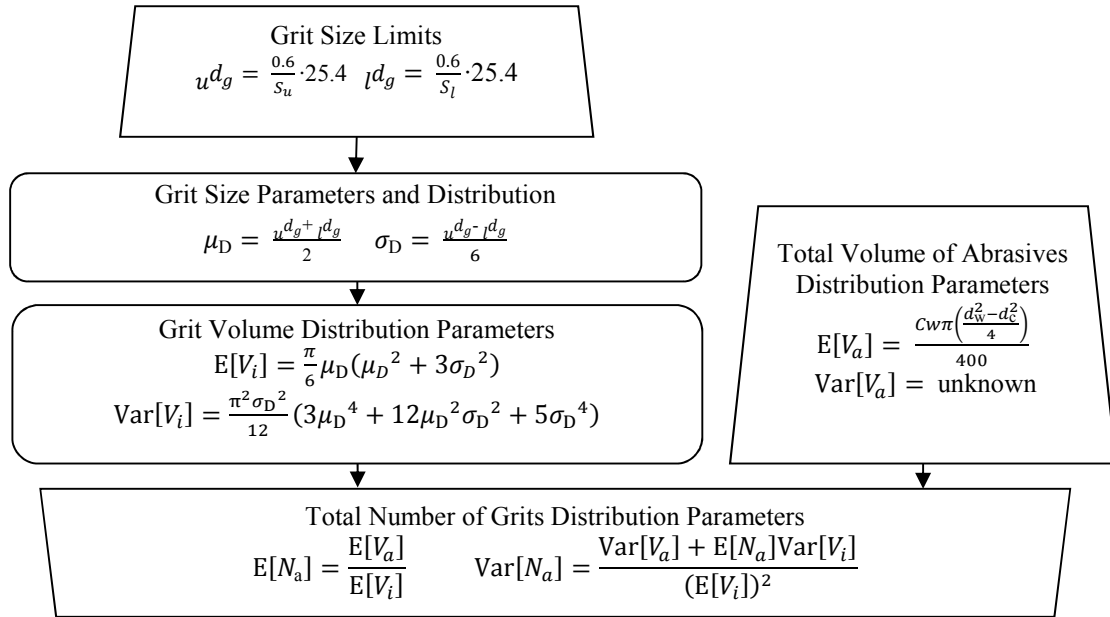


**Figure 2.5 – Summary of method for analytical calculation of number of grits in a grinding wheel**

## 2.6 NUMERICAL SIMULATION OF THE NUMBER OF GRITS IN THE WHEEL

A statistical simulation was conducted to investigate the probability distribution of the number of grits needed to occupy the wheel volume since an explicit solution was not obtained. This was achieved by creating a set of grits whose diameters are governed by Equation 2.5. Grits were added to the dataset until the total volume of abrasive in the wheel was greater than the expected value shown in Equation 2.8. The number of grits in the dataset required to meet the constraint are the number of grits present in the simulated wheel. The simulation algorithm is outlined in Figure 2.6.

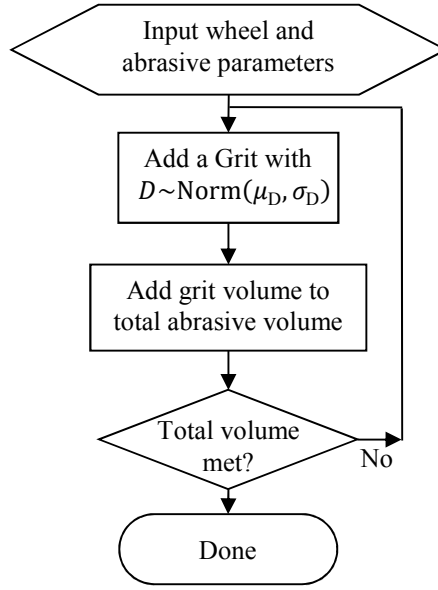


**Figure 2.6 – Numerical simulation algorithm to verify number of grits in wheel model**

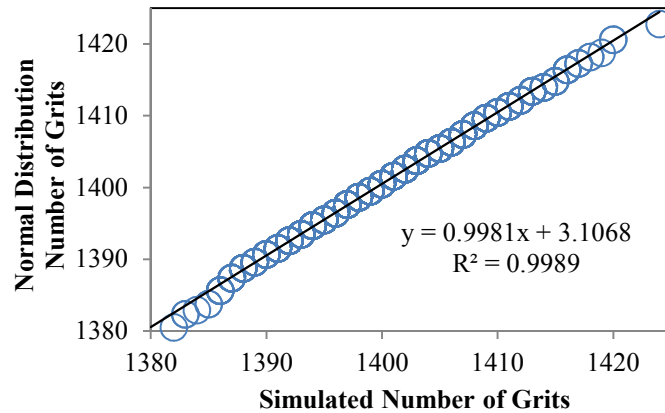
Table 2.2 presents the parameters used for the simulation. The wheel width for the #1200 grit simulation was chosen to be much smaller than that for the #220 simulation since the smaller grits will have a much larger population size in the same space. This was needed to decrease computation time for the #1200 simulation.

**Table 2.3 – Data for simulation of number of grits in a #220 and #1200 wheel**

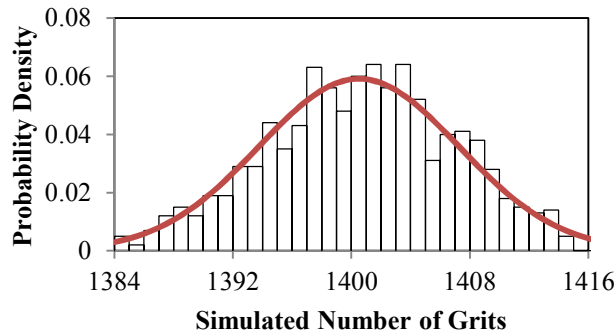
Grit Number	$G\#$	#220	#1200
Number of Simulations	$n$	1,000	
Core Diameter	$D_c$	0.85 mm	
Outer Diameter	$D_g$	1.00 mm	
Concentration	$C$	50	
Wheel Width	$w_w$	10.00 mm	0.1 mm

Figure 2.7 presents the normal probability plot for the simulation along with the linear correlation line. The fitted correlation has a coefficient of determination,  $R^2$ , of 0.9989

and the largest deviations occur at the outliers. This leads to the conclusion that the distribution is Gaussian. A histogram of the simulated number of grits across all of the simulations along with the Gaussian PDF is shown in Figure 2.8.



**Figure 2.7 – Normal probability plot of the simulated number of grits required to fill a #1200 wheel**



**Figure 2.8 - Simulation PDF of the number of grits required to fill a #220 wheel**

Table 2.4 shows the distribution characteristics for the #220 and #1200 grit wheels as calculated using the analytic model and the numerical simulation. It is seen that the simulated number of grits required varied slightly from the expected values calculated analytically using Equation 2.19. Also, note that the simulated values of the mean number of grits were both greater than the expected values. This is caused by the simulation

requiring that the total volume of the abrasive always be greater than the expected values. This is merely an artifact of the simulation algorithm in which the termination condition for adding grits to the wheel is that the total abrasive volume requirement is exceeded. The simulation values, although always slightly higher than the analytical ones, still agree strongly.

**Table 2.4 – Number of grits distribution data for simulations**

		<b>Analytic Prediction</b>	<b>Simulation Result</b>	<b>Analytic Prediction</b>	<b>Simulation Result</b>
<b>Grit Number</b>	<b>G#</b>	<b>#220</b>		<b>#1200</b>	
Number of Grits Mean	$\mu_N$	1,394	1,400	2,306	2,313
Number of Grits Variance	$\sigma_N^2$	45.58	45.83	63.47	64.37

## **2.7 ANALYTICAL CALCULATION OF GRIT LOCATION IN THE WHEEL**

It is assumed that the placement of abrasives within the bond zone is a completely random process as has been shown to be true for narrow grit size bands [47]. As a result, the volumetric distribution of the grits within the wheel has a Cartesian uniform distribution [32]. However, the location of a grit within the bond zone is subject to certain boundary conditions. First, it is assumed that grit retainment is maintained for grits imbedded by at least 10% of their diameter as shown in Figure 2.9. This assumption is adopted from prior numerical simulation studies conducted by Koshy in order to allow for direct comparison to the results of those studies [32]. Next, the location of a single grit cannot allow its outer boundary to extend into the wheel core. The grind wheel can be assigned a cylindrical coordinate system as shown in Figure 2.10.

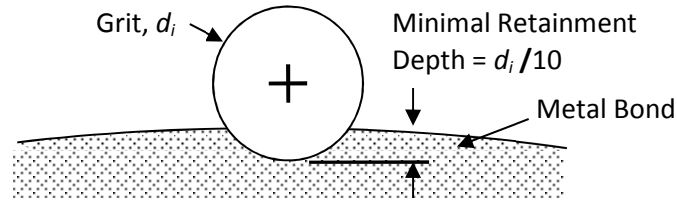


**Figure 2.9 – Boundary condition for grit retention on wheel surface**

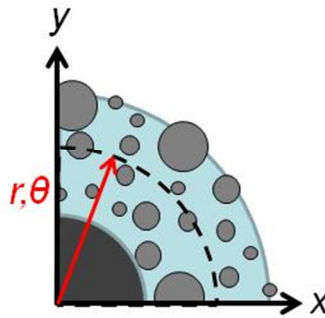


**Figure 2.10 - Grit position coordinate systems**

An arbitrary individual grit,  $g_i$ , then has a centroid location which can be any continuous value in a sample space  $\mathcal{S}$ . The centroid can be described by three independent random variables: its radial distance from the axis of rotation  $R_i$ , its angular position  $\Theta_i$ , and its axial position  $Z_i$ . These variables belong within individual sample spaces  $\mathcal{S}_R$ ,  $\mathcal{S}_\Theta$ , and  $\mathcal{S}_Z$  respectively which are defined in Equation 2.22.

$$\begin{aligned} \mathcal{S}_R &\equiv \left\{ r \left| \frac{D_c}{2} + \frac{D_i}{2} < r < \frac{D_w}{2} + \frac{4D_i}{10} \right. \right\} \\ \mathcal{S}_\Theta &\equiv \{ \theta | 0 \leq \theta < 2\pi \} \\ \mathcal{S}_Z &\equiv \{ z | 0 < z < w_w \} \end{aligned} \quad \text{Equation 2.22}$$

The assumption of a random grit placement process results in the Cartesian coordinates of a given grit being random variables having independent uniform distributions within the acceptable sample space boundaries. Figure 2.11 shows the boundaries of the Cartesian coordinate system that encompass all possible grit locations.

The PDF for the uniformly distributed grit position variables in Cartesian coordinates are shown in Equation 2.23, Equation 2.24, and Equation 2.25.

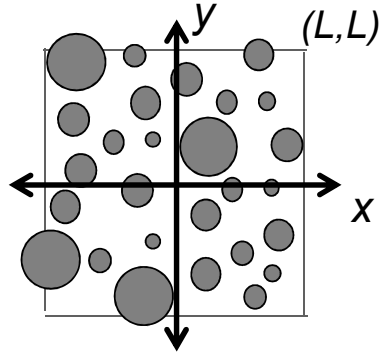


**Figure 2.11 – Grind wheel Cartesian coordinate system boundaries**

$$f_{x_i}(x_i) = \frac{1}{(L) - (-L)} = \frac{1}{2L} \quad \text{Equation 2.23}$$

$$f_{y_i}(y_i) = \frac{1}{(L) - (-L)} = \frac{1}{2L} \quad \text{Equation 2.24}$$

$$f_{z_i}(z_i) = \frac{1}{(w_w) - (0)} = \frac{1}{w_w} \quad \text{Equation 2.25}$$

These must be mapped into the cylindrical coordinate space. First, the  $z_i$  coordinate is identical between the two coordinate systems so its PDF is identical in both. The planar transformation from Cartesian to polar coordinates requires analysis of the bivariate joint probability of  $x_i$  and  $y_i$ . The independence of the two variables results in the joint PDF being the product of the two independent PDFs. The joint PDF is shown as Equation 2.26. The individual transformations of the Cartesian variables into polar variables are shown in Equation 2.27. Now the joint probability can be computed in terms of the polar coordinates as shown in Equation 2.28[45].

$$f_{x_i y_i}(x_i, y_i) = \frac{1}{4L^2} \quad \text{Equation 2.26}$$

$$x_i = r_i \cos(\theta_i) ; y_i = r_i \sin(\theta_i) \quad \text{Equation 2.27}$$

$$f_{R_i\theta_i}(r_i, \theta_i) = f_{X_iY_i}(r_i \cos(\theta_i), r_i \sin(\theta_i)) \begin{vmatrix} \partial x_i / \partial r_i & \partial x_i / \partial \theta_i \\ \partial y_i / \partial r_i & \partial y_i / \partial \theta_i \end{vmatrix} = \frac{1}{4L^2} \begin{vmatrix} \cos(\theta_i) & -r_i \sin(\theta_i) \\ \sin(\theta_i) & r_i \cos(\theta_i) \end{vmatrix} \quad \text{Equation 2.28}$$

$$= \frac{r_i}{4L^2}$$

The individual PDF for each polar variable can then be computed by taking the integral of the joint PDF with respect to the opposite variable. Care must be taken, however, to integrate across the variable range as mapped from the original Cartesian coordinate system. This is shown for the radial position in Equation 2.29 and the angular position in Equation 2.30.

$$f_{R_i}(r_i) = \int_{-\pi/2}^{\pi/2} f_{R_i\theta_i}(r_i, \theta_i) d\theta_i = \int_{-\pi/2}^{\pi/2} \frac{r_i}{4L^2} d\theta_i = \frac{\pi r_i}{4L^2} \quad \text{Equation 2.29}$$

$$f_{\theta_i}(\theta_i) = \int_0^{\sqrt{2}L} f_{R_i\theta_i}(r_i, \theta_i) dr_i = \int_0^{\sqrt{2}L} \frac{r_i}{4L^2} dr_i = \frac{1}{4} \quad \text{Equation 2.30}$$

The individual distributions for the radial and angular variables are not complete since the newly defined domains of the polar variables do not match those for the actual grits as shown in Equation 2.22. The PDF for each variable must be scaled to satisfy the definition of the PDF functions set in Equation 2.31 and Equation 2.32. The final scaled versions of the PDF and CDF for the radial and angular position variables are shown in Equation 2.33 and Equation 2.34 along with their domains.

$$\int_{\frac{D_c + d_i}{2}}^{\frac{D_g + 4d_i}{2} + \frac{4d_i}{10}} f_{R_i}(r_i) dr_i = 1 \quad \text{Equation 2.31}$$

$$\int_0^{2\pi} f_{\theta_i}(\theta_i) d\theta_i = 1 \quad \text{Equation 2.32}$$

$$f_{R_i|D_i}(r_i|d_i) = \frac{2r_i}{\left(\frac{D_g}{2} + \frac{4d_i}{10}\right)^2 - \left(\frac{D_c}{2} + \frac{d_i}{2}\right)^2}; \quad F_{R_i|D_i}(r_i|d_i) = \frac{r_i^2 - \left(\frac{D_c}{2} + \frac{d_i}{2}\right)^2}{\left(\frac{D_g}{2} + \frac{4d_i}{10}\right)^2 - \left(\frac{D_c}{2} + \frac{d_i}{2}\right)^2}; \quad \text{Equation 2.33}$$

$$\frac{D_c}{2} + \frac{d_i}{2} < r_i < \frac{D_g}{2} + \frac{4d_i}{10}$$

$$f_{\Theta_i}(\theta_i) = \frac{1}{2\pi} \quad ; \quad F_{\Theta_i}(\theta_i) = \frac{\theta_i}{2\pi} \quad ; \quad 0 \leq \theta_i < 2\pi \quad \text{Equation 2.34}$$

Notice in Equation 2.33 that the distribution of the radial position of a grit is a function of the grit diameter. The PDF shown is actually a conditional PDF of a joint probability given a known diameter. The relationship between the conditional PDF and the joint PDF is shown in Equation 2.35. It is desired, however, to know the probability distribution of the radial position of a grit regardless of its diameter. This can be calculated by integrating the joint PDF across the domain of the grit diameters as shown in Equation 2.36 [48].

$$f_{R_i|D_i}(r_i|d_i) = \frac{f_{R_i D_i}(r_i, d_i)}{f_{D_i}(d_i)} \quad \forall \left(\frac{D_c}{2} + \frac{d_i}{2} < r_i < \frac{D_g}{2} + \frac{4d_i}{10}\right) \quad \text{Equation 2.35}$$

$$f_{R_i}(r_i) = \int_{-\infty}^{\infty} f_{R_i D_i}(r_i, d_i) dd_i = \int_{-\infty}^{\infty} f_{R_i|D_i}(r_i|d_i) f_{D_i}(d_i) dd_i \quad \forall \left(\frac{D_c}{2} + \frac{d_i}{2} < r_i < \frac{D_g}{2} + \frac{4d_i}{10}\right) \quad \text{Equation 2.36}$$

The PDF of a particular radial position is still subject to the boundary conditions of that particular grit, which is also shown in Equation 2.36. It is desired to acquire the PDF of the radial position of any grit so the probability of a grit meeting the boundary conditions must be addressed. It is first assumed that the probability of a grit meeting either boundary condition is independent of the probability of the radial position of the grit within its valid boundary condition. Therefore, the total probability is the product of the probability of each boundary condition being met and the probability of the radial position of a grit as shown in Equation 2.37. The individual probabilities of the boundary conditions being met by any grit are calculated from the probability of the grit diameters

as shown in Equation 2.38 and Equation 2.39. The final probability density function for any grit having a radial position  $r$  is compiled into Equation 2.40.

$$f_R(r) \forall (-\infty < D < \infty) = f_{R_i}(r) \Pr\left(\frac{D_c}{2} + \frac{D}{2} < r\right) \Pr\left(r < \frac{D_g}{2} + \frac{4D}{10}\right) \quad \text{Equation 2.37}$$

$$\Pr\left(\frac{D_c}{2} + \frac{D}{2} < r\right) = \Pr(-\infty < D < 2r - D_c) = F_{D_i}(2r - D_c) \quad \text{Equation 2.38}$$

$$\begin{aligned} \Pr\left(r < \frac{D_g}{2} + \frac{4D}{10}\right) &= \Pr\left(\frac{10r}{4} - \frac{10D_g}{8} < D < \infty\right) = 1 - \Pr\left(-\infty < D < \frac{10r}{4} - \frac{10D_g}{8}\right) \\ &= 1 - F_{D_i}\left(\frac{10r}{4} - \frac{10D_g}{8}\right) \end{aligned} \quad \text{Equation 2.39}$$

$$f_R(r) = \left( \int_{-\infty}^{\infty} \frac{2r}{\left(\frac{D_g}{2} + \frac{4d}{10}\right)^2 - \left(\frac{D_c}{2} + \frac{d}{2}\right)^2} f_{D_i}(d) dd \right) \left( F_{D_i}(2r - D_c) \right) \left( 1 - F_{D_i}\left(\frac{10r}{4} - \frac{10D_g}{8}\right) \right) \quad \text{Equation 2.40}$$

The indefinite integral in Equation 2.40 does not have a closed form solution. Rather than using numerical integration, a faster method is to approximate the integration by evaluating the conditional probability at the mean of the grit diameters. This approximation results in the simplified probability density function for the radial position of any grit shown in Equation 2.41.

$$\begin{aligned} f_R(r) &\cong f_{R_i|\mu_d}(r|\mu_d) \left( F_{D_i}(2r - D_c) \right) \left( 1 - F_{D_i}\left(\frac{10r}{4} - \frac{10D_g}{8}\right) \right) \\ &= \frac{2r}{\left(\frac{D_g}{2} + \frac{4\mu_d}{10}\right)^2 - \left(\frac{D_c}{2} + \frac{\mu_d}{2}\right)^2} \left( F_{D_i}(2r - D_c) \right) \left( 1 - F_{D_i}\left(\frac{10r}{4} - \frac{10D_g}{8}\right) \right) \end{aligned} \quad \text{Equation 2.41}$$

The accuracy of these distributions is investigated by simulating a set of 50,000 grits from a #220 wheel. Their locations are generated in the Cartesian coordinates and are then converted to cylindrical coordinates. The positions of the grits in cylindrical coordinates are then plotted as occurrence frequencies. The cumulative distribution results are shown in Figure 2.12a for the radial position and Figure 2.12b for the angular position. The probability density results are shown in Figure 2.12c and Figure 2.12d for  $r$

and  $\theta$  respectively. The analytically calculated distributions for the grit locations closely match that from the simulations.

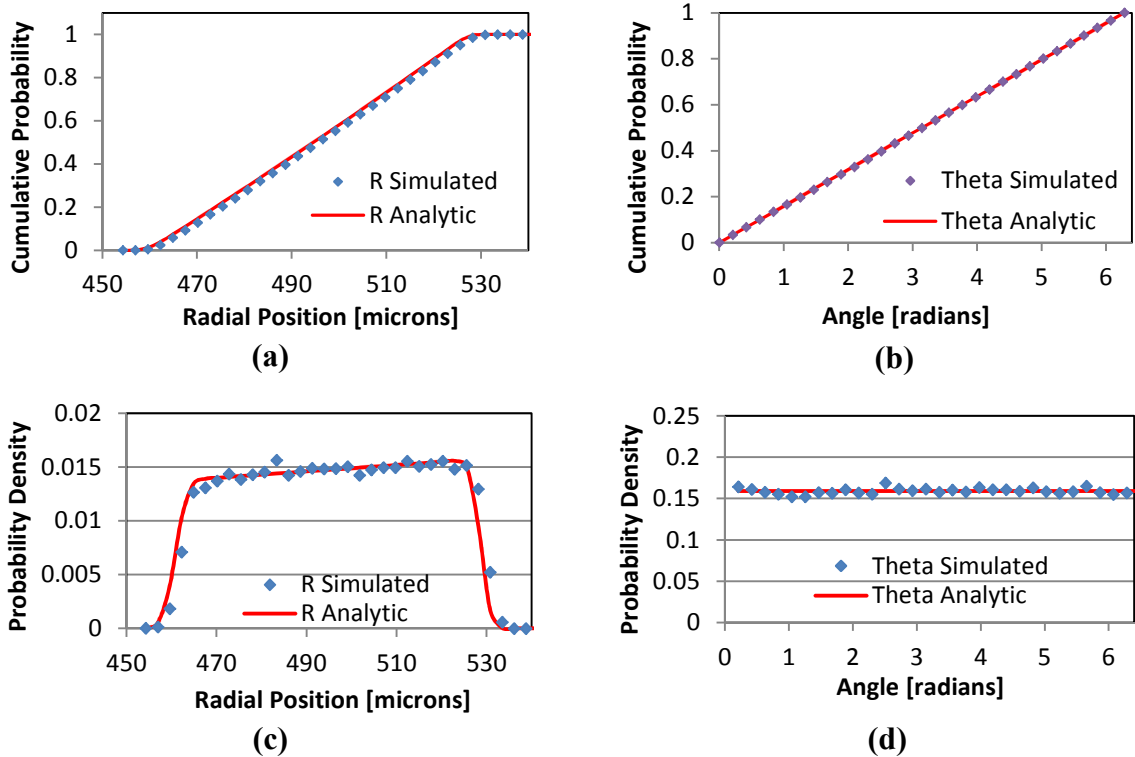


**Figure 2.12 – Simulation of 50,000 grits yielded the CDF for the (a) radial and (b) angular grit positions along with the PDF for the (c) radial and (d) position**

## 2.8 ANALYTICAL CALCULATION OF STATIC GRIT DENSITY IN THE WHEEL

The static grit density for the wheel is a measurement of how many grits intersect a wheel surface per unit area. The outer cylindrical surface of the wheel contains the grits that could participate in grinding so the calculation of the static grit density will consider the intersection of grits with a cylindrical surface, event  $\mathcal{C}$ . The intersection event  $\mathcal{C}$  is a discrete event which is either true or false and is described by a Bernoulli distribution. An individual grit either intersects the surface or does not intersect it. The surface containing

grits that could participate in a grinding operation would form a full cylinder that spans the full space of the angle variable  $\Theta$ . In addition, the surface will only occur at a single radius  $R_c$ . The intersection event  $\mathcal{C}$  is composed of individual variable events  $\mathcal{C}_r, \mathcal{C}_\theta$ , and  $\mathcal{C}_z$ . Event  $\mathcal{C}$  can then be defined as a set composed of the union of the set of individual coordinate events shown in Equation 2.42.

$$\mathcal{C} \equiv \mathcal{C}_r \cup \mathcal{C}_\theta \cup \mathcal{C}_z \quad \text{Equation 2.42}$$

By definition, the cylindrical surface intersection event  $\mathcal{C}$  is selected such that it is always a subset of the sample space  $\mathcal{S}$ . This sample space is the group of all possible surfaces that the grits could intersect which can be rewritten as Equation 2.43.

$$\mathcal{C} \in \mathcal{S} \therefore \mathcal{C}_R \in \mathcal{S}_R; \mathcal{C}_\Theta \in \mathcal{S}_\Theta; \mathcal{C}_Z \in \mathcal{S}_Z \quad \text{Equation 2.43}$$

Each individual coordinate variable event has a range of grit and surface parameters that must be satisfied for the individual event to be true. This parameter range, shown in Equation 2.44, is merely the condition that must be met in order for the grit to intersect the surface along that particular coordinate vector.

$$\begin{aligned} \mathcal{C}_R &\equiv \left\{ r \left| R_c - \frac{d_i}{2} < r < R_c + \frac{d_i}{2} \right. \right\} \\ \mathcal{C}_\Theta &\equiv \{ \theta \mid 0 \leq \theta < 2\pi \} \\ \mathcal{C}_Z &\equiv \left\{ z \left| Z_a - \frac{d_i}{2} < z < Z_b + \frac{d_i}{2} \right. \right\} \end{aligned} \quad \text{Equation 2.44}$$

### 2.8.1 Probability of a Grit Intersecting in the Angular and Axial Domains

The probability of a particular grit  $i$  intersecting the angular position range of the surface is a certain occurrence since the range of the surface covers the entire domain of the angular position. This probability is shown in Equation 2.45.

$$\Pr(\mathcal{C}_{\theta_i} = \text{true}) = f_{\mathcal{C}_{\theta_i}}(\text{true}) = F_{\Theta_i}(0 \leq \theta < 2\pi) = \frac{2\pi}{2\pi} - \frac{0}{2\pi} = 1 \quad \text{Equation 2.45}$$

The probability of a particular grit  $i$  intersecting the axial position range of the surface can be obtained by finding the valid domain of the grit center point position  $z_i$  that would cause the grit to intersect the axial position range. The probability of the location of the axial position of the grit can then be integrated across this domain. This results in the probability of the grit intersecting the axial component of the surface which is shown in Equation 2.46. This probability, however, is based on the diameter of a particular grit. It can be generalized to any grit by utilizing the definition of a conditional and joint probability. Then the joint probability can be integrated across the full domain of grit diameters to obtain the probability of any grit intersecting in the  $z$  domain independent of its diameter as shown in Equation 2.47.

$$\begin{aligned} \Pr(\mathcal{C}_Z = \text{true} | d_i) &= f_{\mathcal{C}_{z_i} | D_i}(\text{true} | d_i) = \Pr\left(Z_a + \frac{d_i}{2} < z_i < Z_b - \frac{d_i}{2}\right) = \int_{Z_a + \frac{d_i}{2}}^{Z_b - \frac{d_i}{2}} f_{z_i}(z_i) dz_i \\ &= \frac{\left(Z_b - \frac{d_i}{2}\right) - \left(Z_a + \frac{d_i}{2}\right)}{w_w} = \frac{Z_b - Z_a - d_i}{w_w} \end{aligned} \quad \text{Equation 2.46}$$

$$\begin{aligned} \Pr(\mathcal{C}_Z = \text{true}) &= f_{\mathcal{C}_{z_i}}(\text{true}) = \int_{-\infty}^{\infty} f_{\mathcal{C}_{z_i}, D_i}(\text{true}, d_i) dd_i = \int_{-\infty}^{\infty} f_{\mathcal{C}_{z_i} | D_i}(\text{true} | d_i) f_{D_i}(d_i) dd_i \\ &= \int_{-\infty}^{\infty} \frac{Z_b - Z_a - d_i}{w_w} f_{D_i}(d_i) dd_i \end{aligned} \quad \text{Equation 2.47}$$

### 2.8.2 Probability of a Grit Intersecting in the Radial Domain

The calculation of the probability of the radial position  $r_i$  of arbitrary grit  $g_i$  is more complicated. Consider the diameter  $D_i$  of grit  $g_i$ . The radial position of the centroid of this grit must be between the boundary conditions and must follow the probability distribution set forth in Equation 2.33. A sampling of some of the possible locations of this grit is shown in Figure 2.13. Notice how the areas where the grits overlap appear darker in the center of the figure since the likelihood of a grit intersecting a particular radial surface is lower at the edges of the domain than at the center.

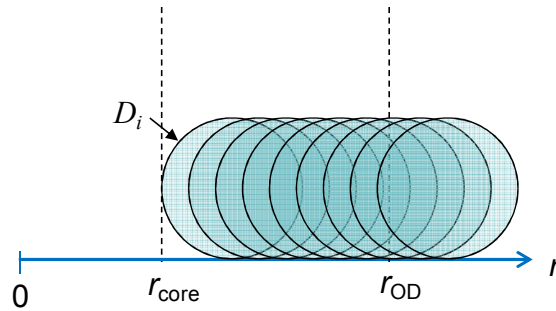


**Figure 2.13 – Sampling of possible locations of grit  $i$  with known diameter  $D_i$**

This visualization can be further simplified by reducing the circular grit representations in Figure 2.13 to the bar representation in the top of Figure 2.14 where each bar has a width of  $D_i$ . The bottom half of Figure 2.14 shows a plot of how many grits are intersecting at a given radius. Notice that there are ramp regions on the edges of the domain and a constant region in the center. These regions are labeled Region 1, 2, and 3.

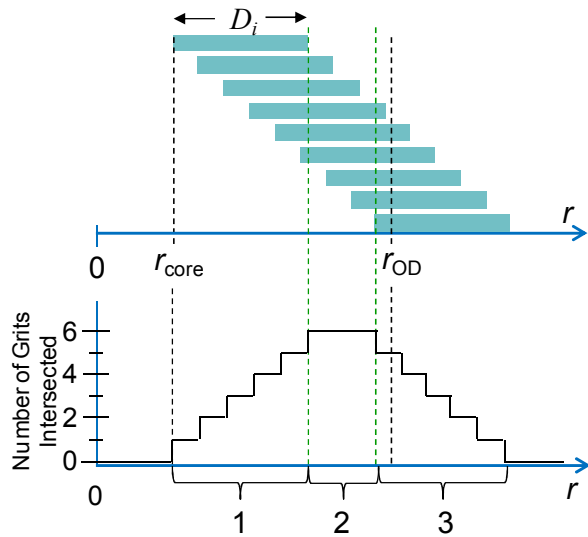


**Figure 2.14 – Bar representation of the intersection of grit  $i$  with a cylindrical surface**

The boundary conditions that define the three distinct regions are shown in Equation 2.48, Equation 2.49, and Equation 2.50.

$$\text{Region 1:} \quad \left( \frac{D_c}{2} < R_c < \frac{D_c}{2} + d_i \right) \quad \text{Equation 2.48}$$

$$\text{Region 2:} \quad \left( \frac{D_c}{2} + d_i < R_c < \frac{D_g}{2} - \frac{d_i}{10} \right) \quad \text{Equation 2.49}$$

$$\text{Region 3:} \quad \left( \frac{D_g}{2} - \frac{d_i}{10} < R_c < \frac{D_g}{2} + \frac{9d_i}{10} \right) \quad \text{Equation 2.50}$$

Knowledge of the probability of a grit intersecting a particular surface at radius  $R_c$  can be obtained from the knowledge of the radial position  $r_i$  of the grit centroid. Each region identified has a unique range of  $r_i$  that would cause an individual grit to intersect the surface. These ranges are shown in Equation 2.51, Equation 2.52, and Equation 2.53 for Region 1, 2, and 3 respectively.

$$\text{Region 1:} \quad \left( \frac{D_c}{2} + \frac{d_i}{2} < r_i < R_c + \frac{d_i}{2} \right) \quad \text{Equation 2.51}$$

$$\text{Region 2:} \quad \left( R_c - \frac{d_i}{2} < r_i < R_c + \frac{d_i}{2} \right) \quad \text{Equation 2.52}$$

$$\text{Region 3:} \quad \left( R_c - \frac{d_i}{2} < r_i < \frac{D_g}{2} + \frac{4d_i}{10} \right) \quad \text{Equation 2.53}$$

It is noticed, however, that this scenario only holds if the inner-most grits and outer-most grits in Figure 2.13 and Figure 2.14 do not overlap. The condition for this to be true for a particular grit diameter is shown in Equation 2.54. The condition can be extended to cover 99.7% of all grit diameters using the distribution parameters for grit diameters, shown in Equation 2.55, defining a wheel in which a grit located at its outermost possible position would not overlap a grit at its innermost position.

$$\left( \frac{D_c}{2} + d_i < \frac{D_g}{2} - \frac{d_i}{10} \right) = \left( \frac{11d_i}{10} < \frac{D_g - D_c}{2} \right) \quad \text{Equation 2.54}$$

$$\left( \frac{11(\mu_d + 3\sigma_d)}{10} < \frac{D_g - D_c}{2} \right) \quad \text{Equation 2.55}$$

However, the possibility of the inner-most grit overlapping the outer-most grit arises when the grit diameters are large in comparison to the thickness of the bond layer. This

occurs in single-layered superabrasive microgrinding wheels. Therefore, Equation 2.55 can be considered the threshold between single-layered and multi-layered grind wheels. The exact inequality in Equation 2.55 indicates true for a multi-layered wheel. A schematic of this scenario is shown in Figure 2.15.

The single-layered wheel scenario has three distinct regions like the conventional wheel scenario. However, the boundary conditions that define these regions are slightly different. The boundary conditions for Regions 1, 2, and 3 in a single-layered wheel are shown in Equation 2.56, Equation 2.57, and Equation 2.58 respectively.

Region 1:  $\left(\frac{D_c}{2} < R_c < \frac{D_g}{2} - \frac{d_i}{10}\right)$  Equation 2.56

Region 2:  $\left(\frac{D_g}{2} - \frac{d_i}{10} < R_c < \frac{D_c}{2} + d_i\right)$  Equation 2.57

Region 3:  $\left(\frac{D_c}{2} + d_i < R_c < \frac{D_g}{2} + \frac{9d_i}{10}\right)$  Equation 2.58

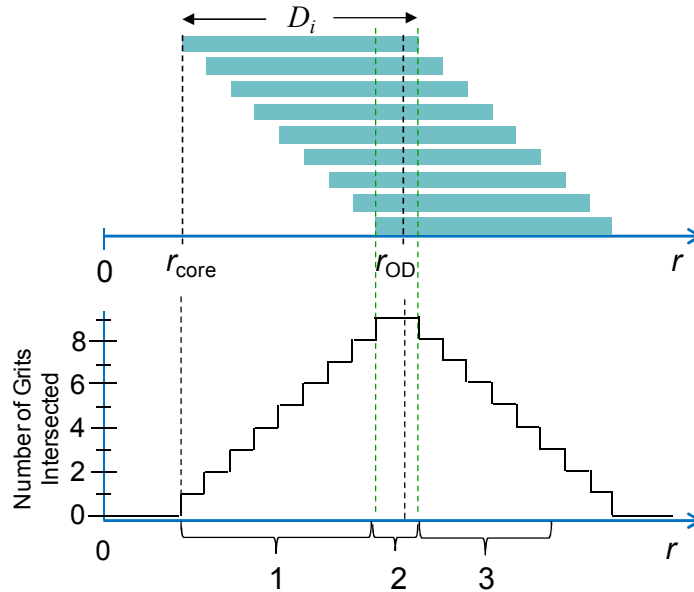


**Figure 2.15 – Bar representation of the intersection of grit  $i$  with a cylindrical surface in a single-layered wheel**

The single-layered wheel scenario regions also have unique ranges of the radial position  $r_i$  of the grit centroid that would result in a grit intersecting the surface of interest. These ranges are shown in Equation 2.59, Equation 2.60, and Equation 2.61 for the three regions of a large-grit wheel.

$$\text{Region 1:} \quad \left( \frac{D_c}{2} + \frac{d_i}{2} < r_i < R_c + \frac{d_i}{2} \right) \quad \text{Equation 2.59}$$

$$\text{Region 2:} \quad \left( \frac{D_c}{2} + \frac{d_i}{2} < r_i < \frac{D_g}{2} + \frac{4d_i}{10} \right) \quad \text{Equation 2.60}$$

$$\text{Region 3:} \quad \left( R_c - \frac{d_i}{2} < r_i < \frac{D_g}{2} + \frac{4d_i}{10} \right) \quad \text{Equation 2.61}$$

The probability of a grit interesting the radial component of the cylindrical surface can be found by integrating the probability of the radial position of the grit centroid across the range that would cause some part of the grit to intersect the radius of the surface. This has to be calculated for each region individually since they have different integration limits. In addition, the probability of a grit intersection the surface within each region must convolved with the probability of the radius  $R_c$  of the surface falling within the boundaries of that region. The probability of the surface being within a region is independent of the probability of a grit intersecting the surface within that region so this convolution is merely a product of the two probabilities as summarized in Equation 2.62 [48]. Analytically this is shown in Equation 2.63 for an arbitrary region  $j$  with region lower and upper boundaries  ${}_{j_{\text{lower}}}R_c$  and  ${}_{j_{\text{upper}}}R_c$  respectively and integration limit lower and upper bounds  ${}_{j_{\text{lower}}}r_i$  and  ${}_{j_{\text{upper}}}r_i$  .

$$= \sum_{\substack{\text{over} \\ \text{all regions}}} \Pr \left( \begin{array}{c} \Pr(C_R = \text{true}|R_c) \\ \text{grit intersecting the surface} \\ \text{radius within the region} \end{array} \right) \Pr \left( \begin{array}{c} \text{the surface radius occurring} \\ \text{within the region} \end{array} \right) \quad \text{Equation 2.62}$$

$$\Pr(\mathcal{C}_R = \text{true} | R_c) = \sum_{j=1}^3 \Pr(j_{\text{lower}} r < r < j_{\text{upper}} r) \Pr(j_{\text{lower}} R_c < R_c < j_{\text{upper}} R_c) \quad \text{Equation 2.63}$$

The first term in Equation 2.63, the probability of a particular grit with a given diameter  $d_i$  intersecting within a particular region, is calculated using the conditional probability in Equation 2.64. A generalization of this to any grit within the wheel can be generated by accounting for the probability of the occurrence of the grit diameters. The joint probability of a grit intersecting the surface and of the grit diameter is calculated using Equation 2.65. The independent probability of any grit intersecting with the region can then be calculated by integrating the joint probability across the full domain of the grit diameters as shown in Equation 2.66.

$$\begin{aligned} \Pr(r_{i\text{intersecting}} | d_i) &= f_{R_{i\text{intersecting}} | D_i}(r_{i\text{intersecting}} | d_i) = \Pr(j_{\text{lower}} r_i < r < j_{\text{upper}} r_i | d_i) \\ &= \int_{j_{\text{lower}} r_i}^{j_{\text{upper}} r_i} f_R(r) dr_i \end{aligned} \quad \text{Equation 2.64}$$

$$\begin{aligned} &= \int_{j_{\text{lower}} r_i}^{j_{\text{upper}} r_i} \frac{2r}{\left(\frac{D_g}{2} + \frac{4\mu_d}{10}\right)^2 - \left(\frac{D_c}{2} + \frac{\mu_d}{2}\right)^2} (F_{D_i}(2r - D_c)) \left(1 - F_{D_i}\left(\frac{10r}{4} - \frac{10D_g}{8}\right)\right) dr_i \\ f_{R_{i\text{intersecting}} | D_i}(r_{i\text{intersecting}} | d_i) &= \frac{f_{R_{i\text{intersecting}} | D_i}(r_{i\text{intersecting}}, d_i)}{f_{D_i}(d)} \end{aligned} \quad \text{Equation 2.65}$$

$$\begin{aligned} \Pr(j_{\text{lower}} r < r < j_{\text{upper}} r) &= \int_{-\infty}^{\infty} f_{R_{i\text{intersecting}} | D_i}(r_{i\text{intersecting}} | d_i) f_{D_i}(d) dd \\ &= \int_{-\infty}^{\infty} \left( \int_{j_{\text{lower}} r_i}^{j_{\text{upper}} r_i} f_R(r) dr_i \right) f_{D_i}(d) dd \end{aligned} \quad \text{Equation 2.66}$$

Similar to the calculation of the position of a grit, the integration of the joint probability across all grit diameters is approximated by evaluating the conditional probability at the mean of the grit diameters. This approximation results in the simplified

probability density function for the radial position intersection of any grit shown in Equation 2.67.

$$\Pr(j_{\text{lower}}r < r < j_{\text{upper}}r) \cong f_{R_{i_{\text{intersecting}}}|D_i}(r_{i_{\text{intersecting}}}|\mu_d) \quad \text{Equation 2.67}$$

The second term in Equation 2.63 calculates the probability of a cylindrical surface of interest falling within one of the specified three regions. First, it is assumed that the probability of the surface radius meeting the lower bound criteria is independent of its probability of meeting the upper bound criteria. This leads to the joint probability of both satisfying criteria being the product of the two individual criteria which is shown in Equation 2.68.

$$\Pr(j_{\text{lower}}R_c < R_c < j_{\text{upper}}R_c) = \Pr(j_{\text{lower}}R_c < R_c)\Pr(R_c < j_{\text{upper}}R_c) \quad \text{Equation 2.68}$$

The boundaries for the surface radius criteria are functions of the diameter of a particular grit. Therefore, the probability of a criteria being met is the probability that the grit diameter meets the inverse of this function imparted on the surface radius. This probability can be calculated using the CDF for any grit diameter which is shown in Equation 2.69. Similarly, the upper bound probability can be calculated using the grit diameter CDF. However, since the inequality is inverted, the remainder of the CDF is needed so it is subtracted from 1 as shown in Equation 2.70.

$$\Pr(j_{\text{lower}}R_c < R_c) = \Pr(h(d_i) < R_c) = \Pr(d_i < h^{-1}(R_c)) = F_{D_i}(h^{-1}(R_c)) \quad \text{Equation 2.69}$$

$$\Pr(R_c < j_{\text{upper}}R_c) = \Pr(R_c < g(d_i)) = \Pr(g^{-1}(R_c) < d_i) = 1 - F_{D_i}(h^{-1}(R_c)) \quad \text{Equation 2.70}$$

The complete algorithm for calculating the grit intersection probability in the radial direction is shown in Figure 2.16 with the boundaries.

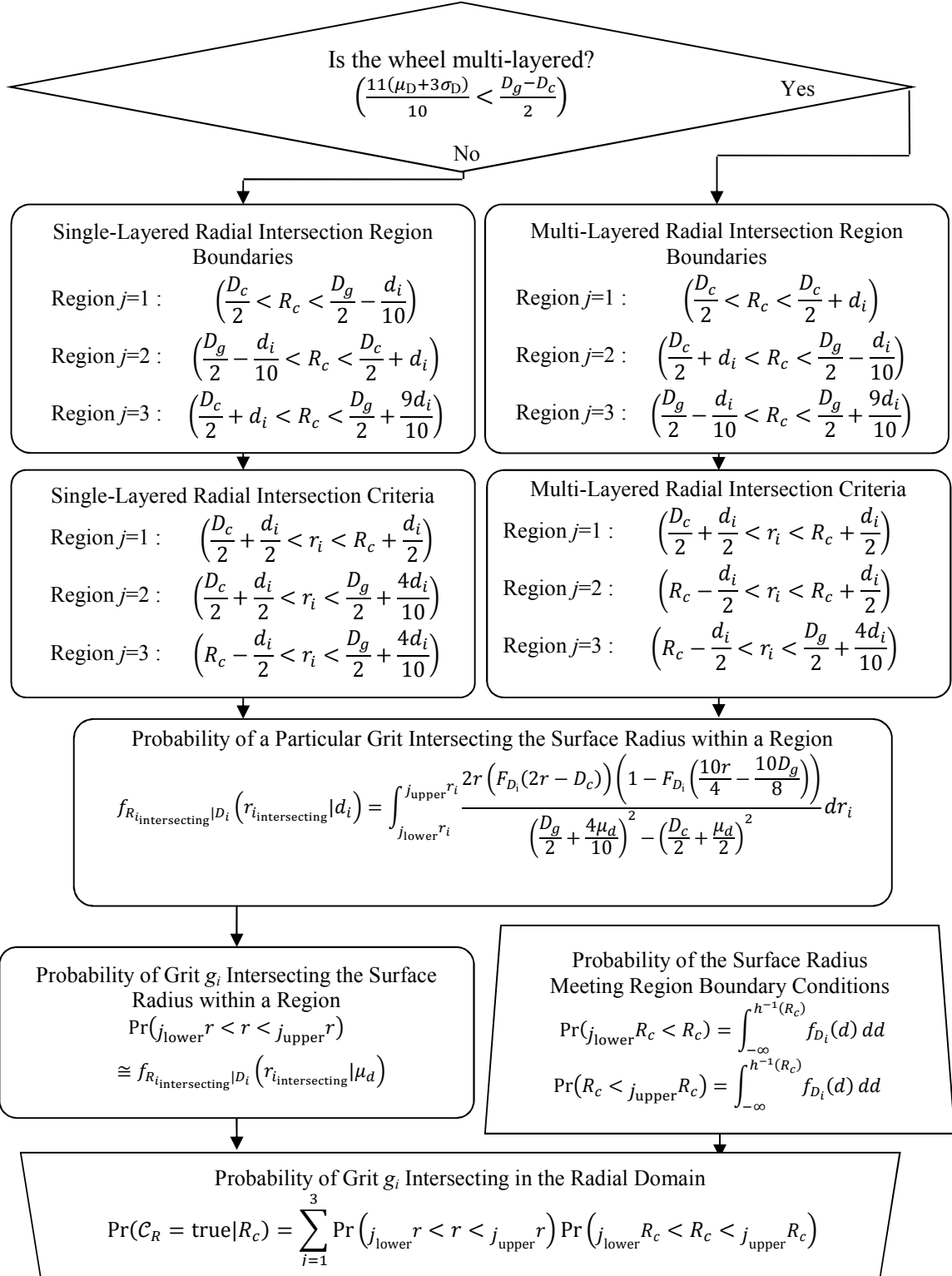


**Figure 2.16 – Method for analytical calculation of a the probability of a grit intersecting a surface with radius  $R_c$**

### 2.8.3 Combined Probability of a Single Grit Intersecting the Surface

The independence of the occurrences of the grit location coordinates results in the total probability of all three parameters falling within the examined region being the product of the individual probabilities. Again, this is the discrete probability that any single grit intersects the surface in event  $\mathcal{C}$  as shown in Equation 2.42. Since the three individual coordinate events are independent, the probability of their intersection is the product of their individual probabilities as shown in Equation 2.71. The probability of a grit intersecting has an outcome of either success or failure. Therefore, the intersection of a grit with a cylindrical surface is a Bernoulli trial. The expectation and variance of the probability of a grit intersecting are given by the known properties of a Bernoulli distribution which are shown in Equation 2.72 and Equation 2.73 respectively.

$$\Pr(\mathcal{C}|R_c) = \Pr(\mathcal{C}_R|R_c)\Pr(\mathcal{C}_\theta)\Pr(\mathcal{C}_Z) \sim \text{Bern}(\Pr(\mathcal{C}_R|R_c)\Pr(\mathcal{C}_\theta)\Pr(\mathcal{C}_Z)) \quad \text{Equation 2.71}$$

$$E(\mathcal{C}) = \Pr(\mathcal{C}_R|R_c)\Pr(\mathcal{C}_\theta)\Pr(\mathcal{C}_Z) \quad \text{Equation 2.72}$$

$$\text{Var}(\mathcal{C}) = (\Pr(\mathcal{C}_R|R_c)\Pr(\mathcal{C}_\theta)\Pr(\mathcal{C}_Z))(1 - \Pr(\mathcal{C}_R|R_c)\Pr(\mathcal{C}_\theta)\Pr(\mathcal{C}_Z)) \quad \text{Equation 2.73}$$

### 2.8.4 Static Grit Density using the Probability of a Particular Grit Intersecting the Surface

The static grit density is defined as the number of grits that intersect the surface divided by the surface area. The area of this cylindrical surface is given by Equation 2.74. This static grit density is defined in Equation 2.75.

$$A_{c_r} = 2\pi R_c(Z_b - Z_a) \quad \text{Equation 2.74}$$

$$C_s = \frac{N_g}{A} = \frac{\# \text{ of grits in } \mathcal{C}}{A_{c_r}} = \frac{g(\mathcal{C})}{A_{c_r}} \quad \text{Equation 2.75}$$

The random variable event  $\mathcal{C}$  of any individual grit intersecting the cylindrical surface is a Bernoulli trial in this model since each trial has either a success or failure outcome and the outcome for each grit is independent of the outcome of the other grits. The number of grits that reside in the wheel that have a success in random variable  $\mathcal{C}$  can be represented by another random variable  $N$ . The static grit density can therefore be represented as a function of this new random variable as shown in Equation 2.76.

$$\Pr(C_s = c_s) = \frac{\Pr(N = n)}{A_{c_r}} \quad \text{Equation 2.76}$$

The random variable  $N$  can be described as the sum of independent, identical Bernoulli trials. This distribution is therefore an ordinary Binomial Distribution [48]. The probability mass function for this variable is shown as Equation 2.77. Here, each  $\Pr(\mathcal{C})$  within the summation is the probability that a particular grit  $g_i$  with a particular diameter  $D_i$  intersects the surface. Notice that this distribution is contingent on the condition of a known number of abrasives in the wheel. The expectation and variance are given by Equation 2.78 and Equation 2.79.

$$\Pr(N = n|N_a) = f(n|N_a) = \binom{N_a}{n} \Pr(\mathcal{C})^n (1 - \Pr(\mathcal{C}))^{N_a - n} = \frac{N_a!}{n! (N_a - n)!} \Pr(\mathcal{C})^n (1 - \Pr(\mathcal{C}))^{N_a - n} \quad \text{Equation 2.77}$$

$$E[N|N_a] = N_a \Pr(\mathcal{C}) \quad \text{Equation 2.78}$$

$$\text{Var}[N|N_a] = N_a \Pr(\mathcal{C}) (1 - \Pr(\mathcal{C})) \quad \text{Equation 2.79}$$

The distribution of the number of grits intersected regardless of the number of grits in the wheel is obtained by utilizing the definition of the conditional probability as shown in Equation 2.80.

$$\Pr(N = n) = f(n) = \int_{-\infty}^{\infty} f(n, N_a) dN_a = \int_{-\infty}^{\infty} f(n|N_a) f(N_a) dN_a \quad \text{Equation 2.80}$$

The expectation of the number of grits that intersect independent of the exact number of grits in the wheel can be calculated by the double expectation as shown in Equation 2.81. Similarly, the variance in the number of abrasives intersecting the surface is given by Equation 2.82.

$$\begin{aligned} E[N] &= E[E[N|N_a]] = \int_{-\infty}^{\infty} E[N|N_a] f(N_a) dN_a = \int_{-\infty}^{\infty} N_a E[C] f(N_a) dN_a \\ &= E[C] \int_{-\infty}^{\infty} N_a f(N_a) dN_a = E[C] E[N_a] \end{aligned} \quad \text{Equation 2.81}$$

$$\text{Var}[N] = E[N_a] \text{Var}[C] + (E[C])^2 \text{Var}[N_a] \quad \text{Equation 2.82}$$

The mean and variance in the static grit density can now be calculated using Equation 2.83 and Equation 2.84.

$$E[C_s] = \frac{E[N]}{A_{c_r}} \quad \text{Equation 2.83}$$

$$\text{Var}[C_s] = \frac{\text{Var}[N]}{(A_{c_r})^2} \quad \text{Equation 2.84}$$

A final summary of the algorithm for calculating the probability of the static grit density in a grind wheel is presented in Figure 2.17.

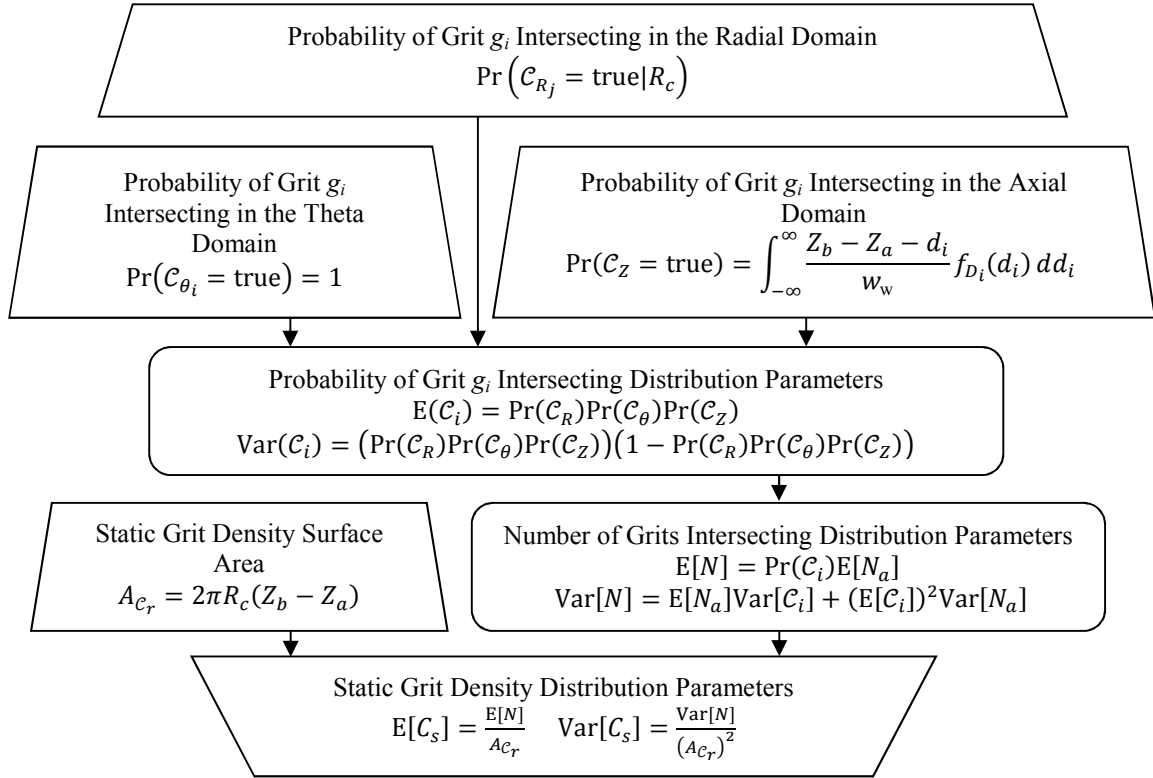


**Figure 2.17 - Summary of method for analytical calculation of a microgrinding wheel static grit density**

## 2.9 ANALYTIC STATIC GRIT DENSITY MODEL RESULTS

The analytic model for the probability of static grit densities in grinding wheels provides a method to quickly predict not only mean static grit densities but also its variance in any wheel. Appendix A details a more complete solution of the calculation of the static grits density by substituting and solving the equations presented in the algorithm. The analytical solution of the static grit density distribution parameters was calculated for a #220 and #1200 grinding wheel as shown in Figure 2.18.

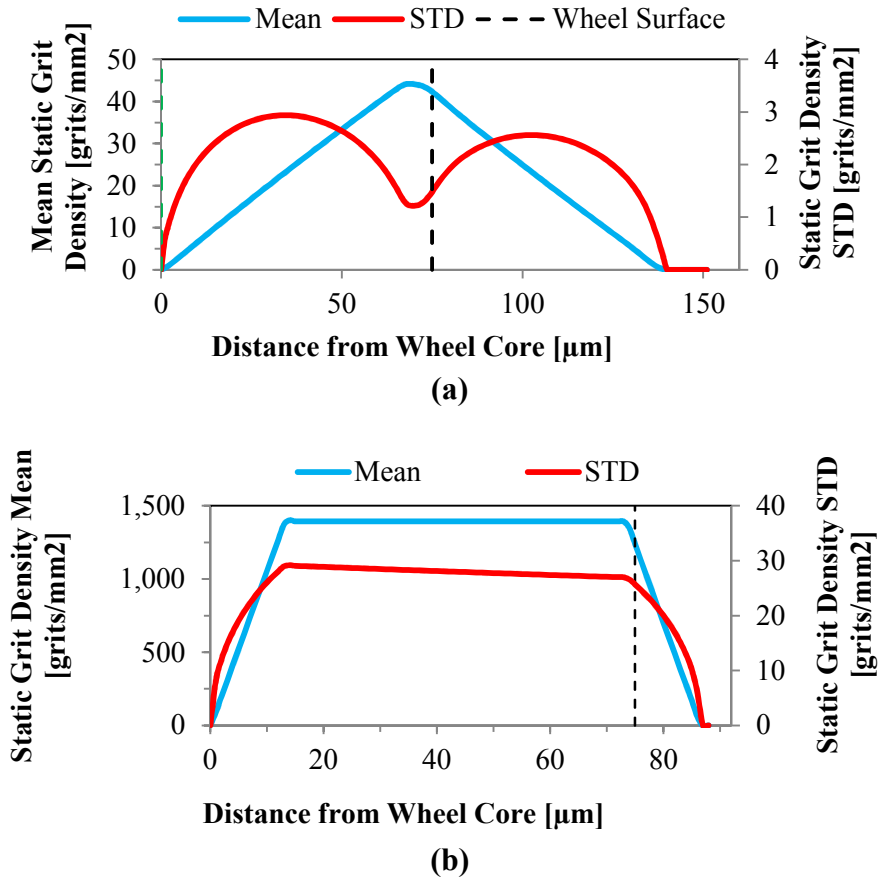
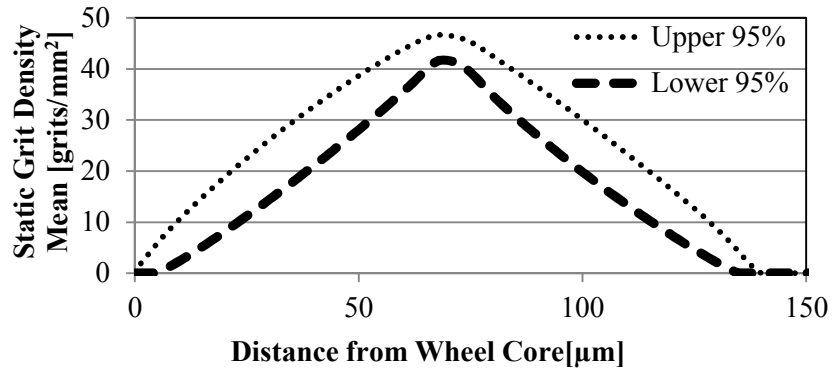
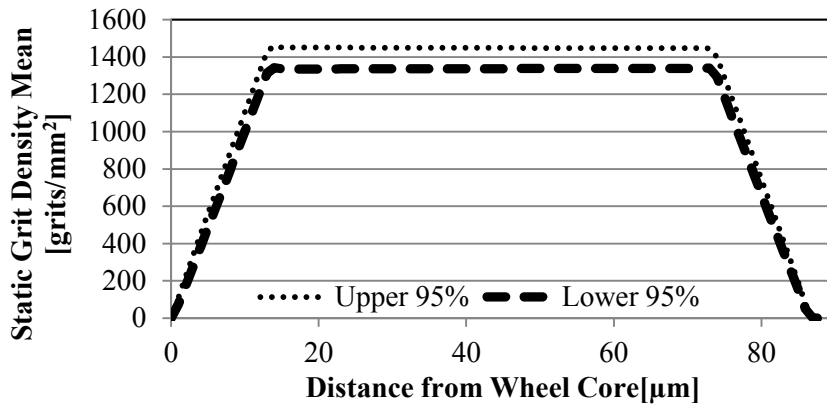


**Figure 2.18 – Static grit density distribution parameters from analytic model for (a) #220 and (b) #1200 microgrinding wheels**

The mean and variance of the static grit density can be used to analytically generate boundaries of the range of possible static grit densities as a function of a surface's distance from the core of the grind wheel as shown in Figure 2.19 for a #220 and #1200 grit wheel.



(a)



(b)

**Figure 2.19 - Boundary range of 95% of the possible static grit densities of in (a) #220 and (b) #1200 microgrinding wheels**

## 2.10 DISCUSSION

The analytic model for the wheel consists of complex statistical descriptions. Some of the model parameters have distinct probability density functions while others require numerical integration. This requires some costly computation time. Other parameters can only be analytically modeled by calculating their distribution parameter estimators. For example, the number of grits in the wheel is only analytically modeled by their expected mean and variance. A full description of the PDF and CDF are not obtainable. However, use of numerical simulation showed that the probability of the number of grits in the wheel can be modeled using a Gaussian distribution governed by the analytically

generated estimators. This allows a much faster method of calculating the probability of how many grits are in a wheel.

The accuracy of the model to predict the topography of actual grinding wheels stems from the accuracy of the initial assumptions in the simplification of the wheel. The assumed shape of the abrasive particles can have a significant effect on the outcomes of the model. This was investigated by Kramer and Wagenheim in 2008 by using different abrasive shapes in a model of wheel topography that located the abrasives uniformly in a simple cubic lattice structure [49]. The shapes compared were spheres, twin cones, twin pyramids, and twin pyramidal frustrums as shown in Figure 2.20.

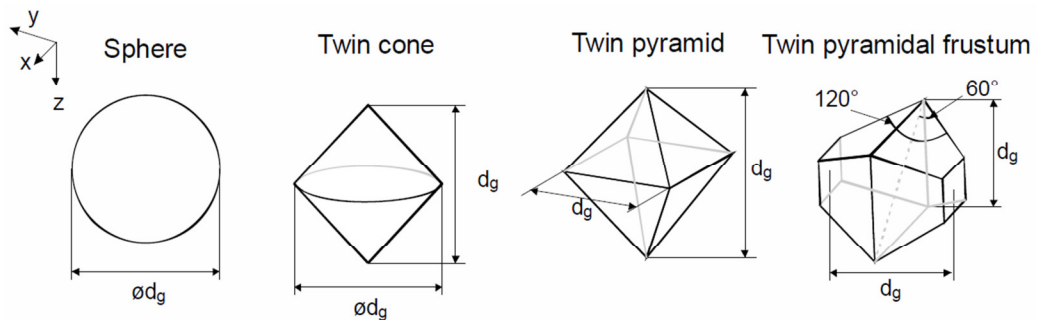


**Figure 2.20 – Abrasive shapes investigated by Kramer and Wagenheim<sup>[49]</sup>**

The results of the study on the impact of grit size are shown in Figure 2.21 where the ratio between abrasive and bond area is displayed as a function of the radial depth of the analyzed surface into the wheel. It is seen that none of the model results computed using the simple cubic packing structure matched that of the measured wheel. However, it is observed that the sphere and twin pyramidal assumptions provide the most accurate model results. In addition, it is observed that the spherical grit model represents an average result within the set assumed abrasive shapes.

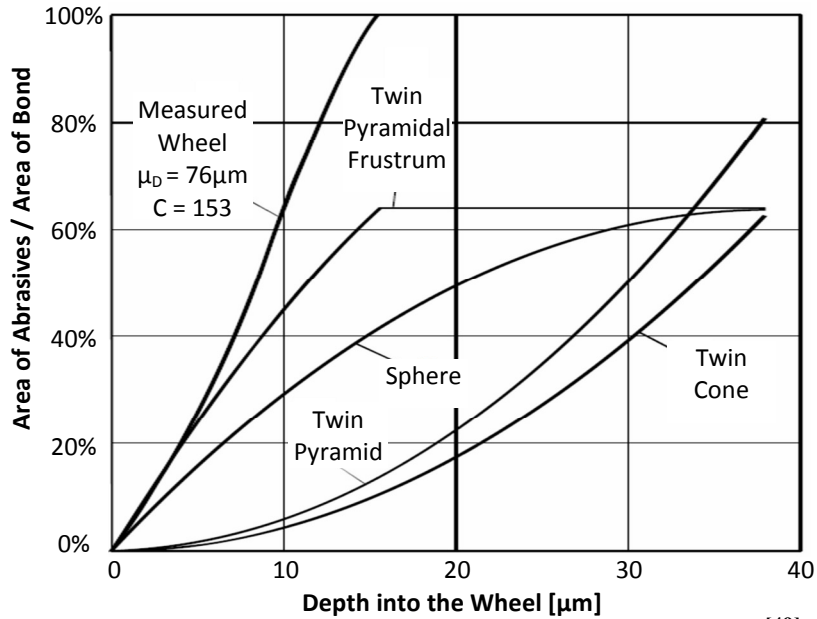


**Figure 2.21 – Impact of modeled abrasive shapes<sup>[49]</sup>**

It is noted that the spherical grit assumption also does not require additional model dimensionality to capture the grit orientation. The spherical grit assumption therefore simplifies the complexity of the probabilistic model leading to faster computation times using both the analytic formulation and current numerical simulation techniques. The results acquired with this simplification come with minimal loss of model accuracy.

## 2.11 SUMMARY

The analytic wheel modeling technique developed in this chapter provides a method to model key aspects of superabrasive grinding wheel static topography such as the distribution of grit radial positions and the expectation and variance of the static grit density. Derivation and simulation showed that the number of grits residing in a wheel can be modeled as having a Gaussian probability with parameters calculated analytically from the wheel specifications and manufacturing variances. The locations of the grits

within the wheel were shown to have distinct regions of different probability functions based on the boundary conditions of grit placement within a wheel. A mathematical description of the difference between single-layered and multi-layered grind wheels was defined. Finally, the analytic model for the static grit density allows the quick calculation of the mean and variance of the number of grits available to participate in grinding.

The large grit sizes relative to the grind wheel sizes at the micro scale presents unique challenges in the ability to accurately predict wheel topographies. The limited number of grits that exist in such wheels has a significant impact on the variances in the static topography from wheel to wheel. The analytic model generated here can be used to bound these uncertainties in order to provide more accurate predictions of wheel topographies and microgrinding behavior. The stochastic distributions of the grit locations can be used in dynamic grinding simulations and analytics to acquire distributions of the process forces. This model, however, is expected to have some limitations in its ability to accurately predict real grind wheel topography due to differences in manufacturing methods and accuracy. The accuracy of the model is limited by the basis on uniform grit position distributions in Cartesian space which relies on the ability of the manufacturing process to un-biasedly place grits within the wheel bond

The accuracy of the statistics used in the analytic model will be verified in CHAPTER 3 using numerical simulation while its ability to accurately model real microgrinding wheels will be validated in CHAPTER 4. This probabilistic model will be used to perform a scaling study on microgrinding wheel topographies in CHAPTER 5.

## **CHAPTER 3 – NUMERICAL VALIDATION OF ANALYTIC MODEL**

### **3.1 INTRODUCTION**

Numerical simulation of grit size and placement within a microgrinding wheel allows for an analysis of the accuracy of the statistical propagation used in the analytical stochastic model generated in CHAPTER 2. Numerical simulation is a widely accepted technique for modeling grinding wheel topography and has been shown to provide results that closely predict real wheel topography. In order to establish the verification of the statistical propagation, initial numerical simulations were constrained to match the assumptions and boundary conditions of the analytic model. Further simulation techniques were subsequently established that improve the efficacy of the numerical simulation by utilizing more realistic assumptions about grit location. Particularly, the more realistic simulation will limit the ability of grits to overlap in the simulated wheel bond. This will allow for an investigation into the possible deviation of the analytic model from real grind wheel topography.

### **3.2 REVIEW OF SALIENT LITERATURE**

Numerical simulation has been used for many years to model grinding action along with static wheel topography. An early review of the different techniques used was present by Tönshoff as a keynote paper of CIRP in 1992[50]. Stochastic representations of several aspects of static wheel topography have been generated using this technique as is outlined in Table 2.1. These simulations use varying techniques to generate the static wheel topography. Most techniques for simulating grit locations within a wheel define

the volume space of a wheel and populate it one-grit-at-a-time [31, 32, 37]. One of the earliest simulations, conducted by Law in 1972, randomly assigned each simulated grit a uniformly distributed position in the axial and radial direction of the grind wheel along with a uniformly distributed circumferential spacing between each grit [51]. Any grit locations that caused overlapping were reassigned new random locations until the overlapping was resolved[32]. Others place grits in a defined lattice space and then shifted them slightly from that position using a random displacement distance. The random displacement for each grit was re-generated if that grit overlapped another grit. This was repeated until zero grits overlapped each other [44, 52]. Both of these methods of alleviating grit overlap are time consuming as they rely on blind location reassignment to eliminate the overlaps.

### **3.3 NUMERICAL SIMULATION OF STATIC WHEEL**

#### **TOPOGRAPHY WITHOUT CONSIDERING GRIT OVERLAP**

The simulation of the grind wheels will model the abrasive grits as perfect spheres whose diameters follow a Gaussian occurrence distribution as outlined in CHAPTER 2. The locations of the grits within the wheel will follow the same boundary conditions setup for the analytical model in Equation 2.22. The numerical simulation used here first assigns each grit a random, independent position in a Cartesian space that includes the desired wheel geometry. The grit locations are then converted to cylindrical space so that the static grit density at different radial positions can be calculated. Each grit is then checked for a violation of the boundary conditions in Equation 2.22. Grits that violate the boundary condition are then assigned a new random position. Note, however, that this

method allows for grits to overlap. A summary of the algorithm used to simulate each grind wheel is shown in Figure 3.1.

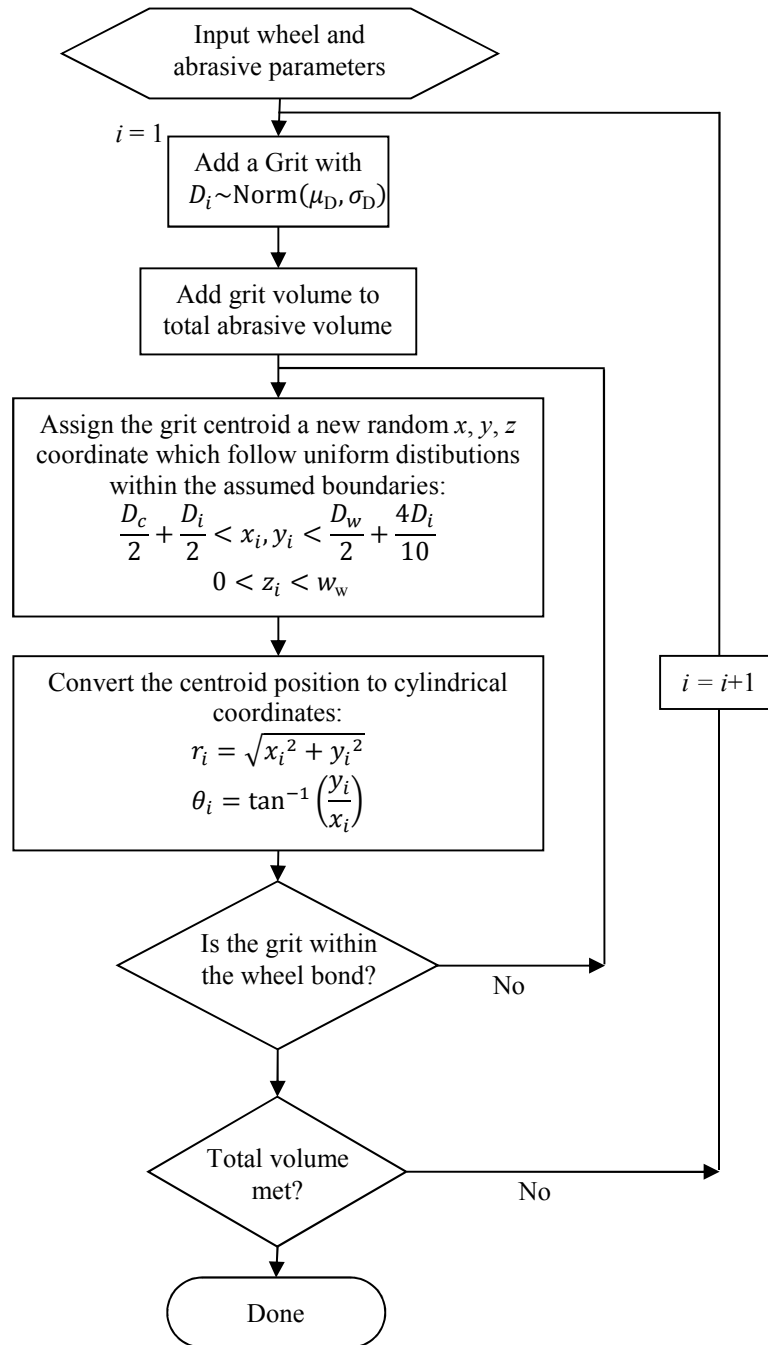


**Figure 3.1 – Numerical simulation algorithm to model grits within a grind wheel**

The simulated grind wheel is then examined for information about the number of grits within the wheel, the static grit density, the grit protrusion height, etc. This is achieved by merely examining each grit and performing a check on its diameter and position to measure the desired wheel attribute.

It has already been shown in Section 2.6 that the number of grits that reside in a wheel can be modeled using a normal distribution. It was also shown that the analytic model for the distribution parameters for the number of grits in the wheel accurately describes wheels governed by the assumed behavior.

A subjective evaluation of the grit placement within a wheel generated using the simulation algorithm can be conducted by plotting the simulated wheel surface. This is shown in Figure 3.2 for four separate simulation incidences. Notice the significant grit overlay caused by the algorithm not accounting for previous grit locations when adding a new grit.

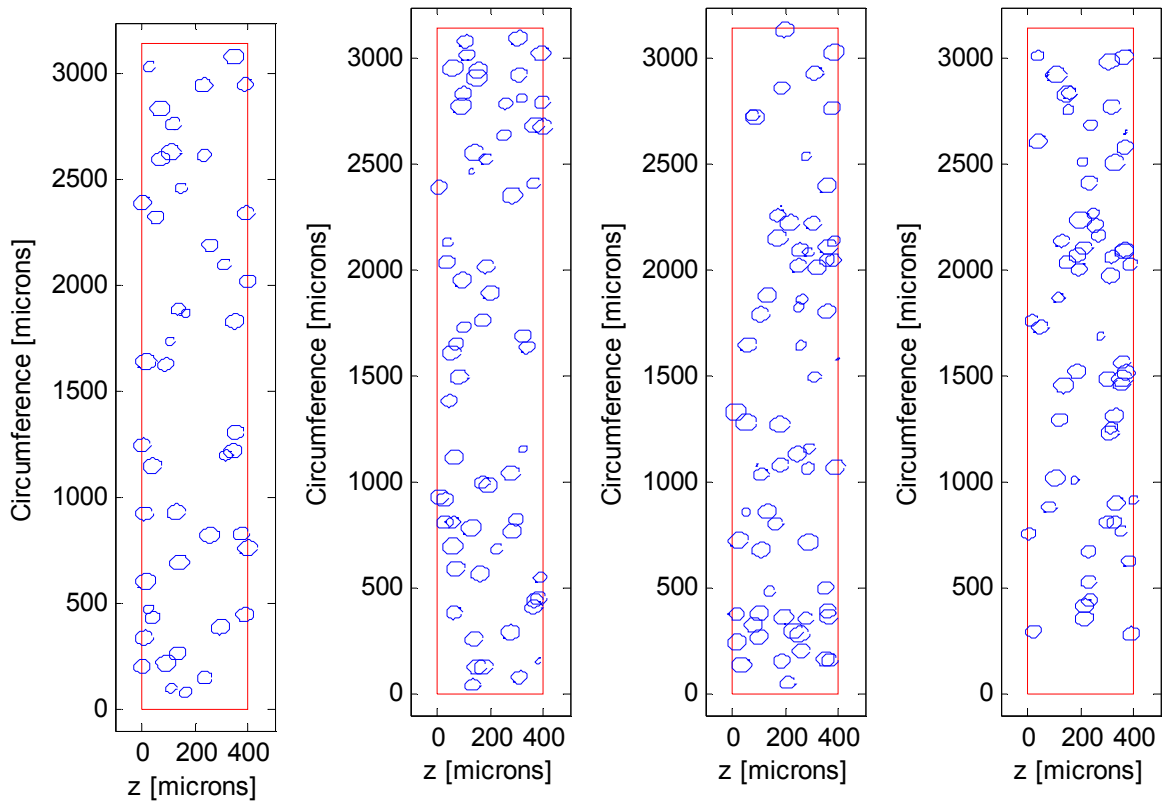
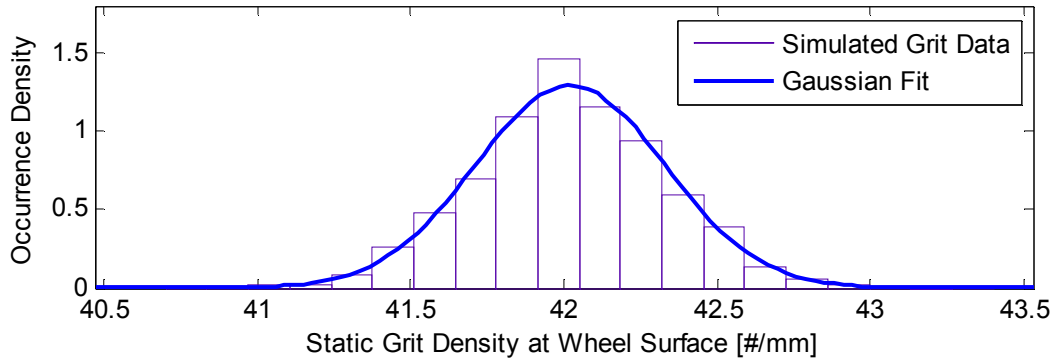
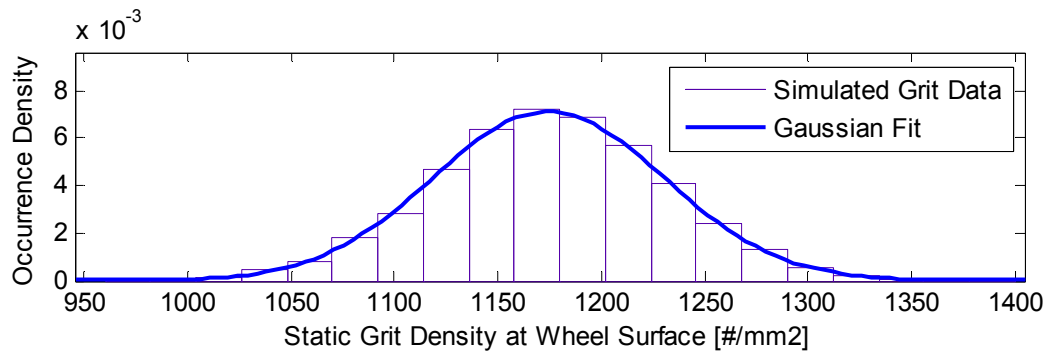


**Figure 3.2 – Plots of simulated wheel surfaces for #220 wheel with grit overlap**

The simulation was executed for 1,000 wheels. Figure 3.3 shows the static grit density at the wheel surface for the simulated #220 and #1200 grit wheels. This is calculated by counting the number of grits that break the surface of the wheel and dividing that by the outer surface area of the wheel. It is seen that the distribution of static grit densities closely matches that of a Gaussian distribution. Note these results do not address the issue of grits randomly overlapping one another.



(a)



(b)

**Figure 3.3 - Static grit density distribution on the wheel surface simulated with grit overlap for (a) #220 and (b) #1200 wheels**

Figure 3.4 show the calculated static grit density at different radial distances from the wheel core for the #220 and #1200 grit simulations. The distinct regions of static grit density dependence on the radius of the examined surface resemble those identified in Section 2.8.2. There is evidence also of variation between simulations. The dotted lines in the plots represent the wheel bond surface.

Here, the static grit density is calculated by counting the number of grits that are intersected between their maximum protrusion point and their minimal retainment depth by the cylindrical surface generated using the radius of interest. The surface area used for the calculation utilizes the radius of interest as well.

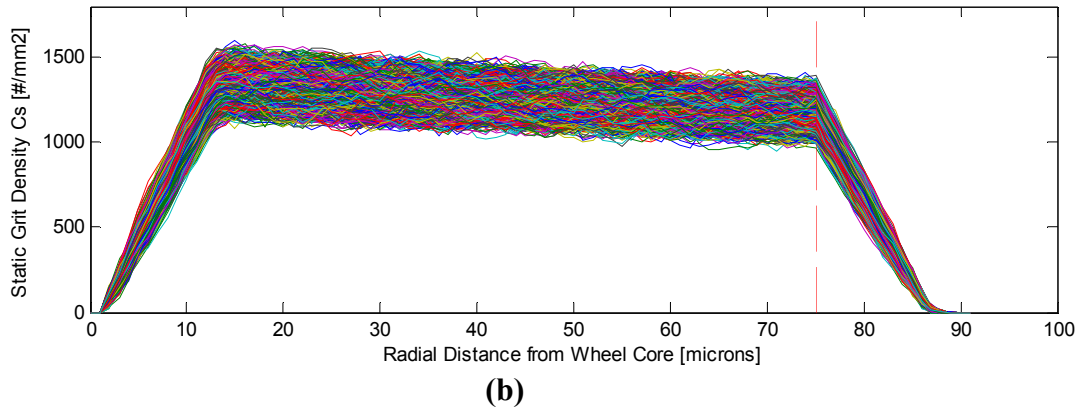
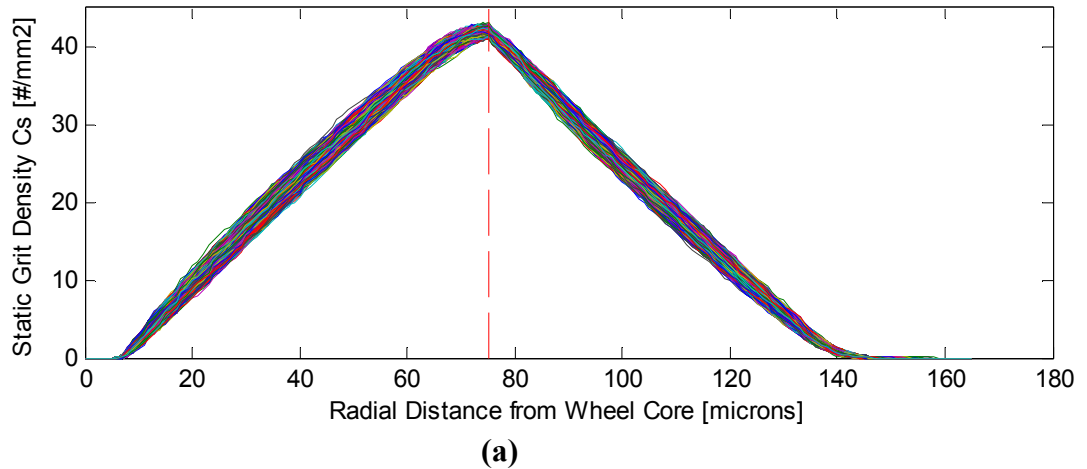
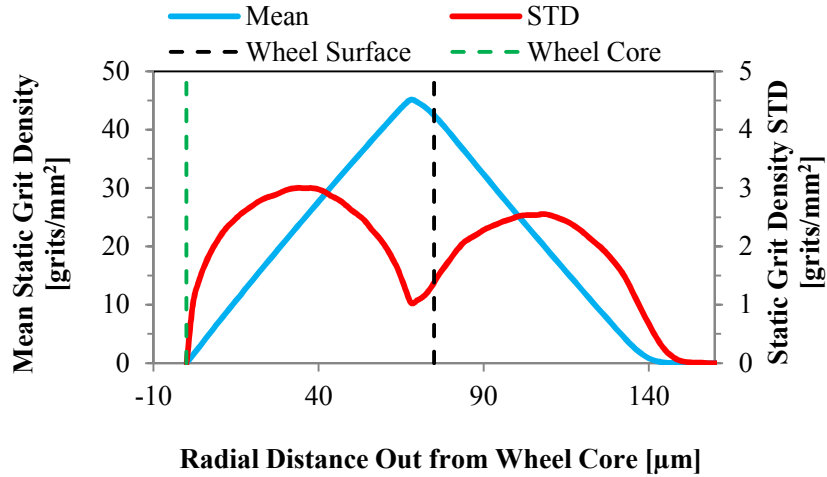
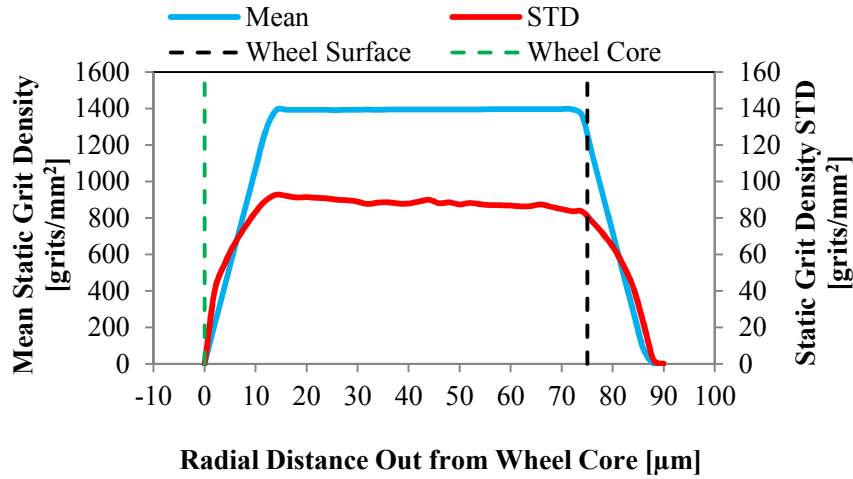


**Figure 3.4 - Static grit density as a function of the distance from the wheel core simulated with grit overlap in (a) #220 and (b) #1220 grit wheels**

The variations along the plots of the static grit density versus radial position can be quantified by fitting a normal distribution to the static grit density at each radius. Figure 3.5 shows the calculated sample mean and standard deviation of the static grit density for the #220 and #1200 grit wheels. It is interesting to note how the location of the middle region for the #220 grit wheel forms a point where the variance between simulations decreases.



(a)



(b)

Figure 3.5 - Static grit density normal distribution parameters as a function of distance from the wheel core simulated with grit overlap in (a) #220 and (b) #1200 grit wheels

### 3.4 PLACING THE GRITS IN THE WHEEL CONSIDERING GRIT OVERLAP

In an actual grind wheel, however, the location of grit  $g_i$  is subject to positional limitations imposed by the other grits placed in the simulation since no two grits can occupy the same space and overlap one another. This phenomenon is not accounted for in

the current simulation algorithm. This constraint is shown as Equation 3.1 for two spherical grits  $i$  and  $j$ . A second numerical simulation that limits the number of grits that violate this constraint can show how this impacts the simulated wheel topography. However, current techniques of enforcing the grit overlap constraint merely regenerate a grit location. Instead, the method used here will linearly relocate the overlapping grits to the closest position in which the grits are merely in contact with one another.

$$d_{ij} = \sqrt{r_i^2 + r_j^2 - 2r_i r_j \cos(\theta_i - \theta_j) + (z_i - z_j)^2} > \frac{d_i + d_j}{2}; j = 1 \text{ to } i - 1 \quad \text{Equation 3.1}$$

### 3.4.1 Algorithm of Grit Relocation to Minimize Grit Overlap

This method is essentially a particle packing simulation which is a large area of active research. The loose packing nature of this problem lends it to need less computationally heavy algorithms. The proposed technique, which uses Monte Carlo simulation, will utilize collective rearrangement as the method of relocating the grits to positions that minimize or eliminate grit overlap [53]. Figure 3.6 shows two grits  $i$  and  $j$  in a Cartesian plane with grit  $j$  overlapping grit  $i$ . This overlap is removed by moving particle  $i$  in the direction that is governed by the line between the two grit centers.

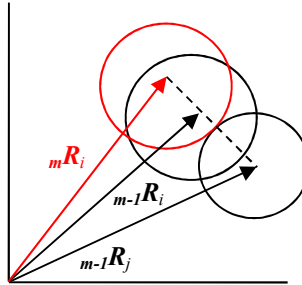


**Figure 3.6 – Calculation for the separation between particles  $i$  and  $j$**

The  $m^{\text{th}}$  new grit  $i$  position,  ${}_mR_i$ , is calculated using the previous positions  ${}_{m-1}R_i$  and  ${}_{m-1}R_j$ . This is shown in vector form in Equation 3.2. The cylindrical coordinate component version to calculate the new position in Cartesian coordinates is shown in Equation 3.3, Equation 3.4, and Equation 3.5. The conversion to cylindrical coordinates is shown in Equation 3.6 and Equation 3.7.

$${}_mR_i = {}_{m-1}R_i + \left( \frac{{}_{m-1}R_i - {}_{m-1}R_j}{{}_{m-1}d_{ij}} \right) (r_i + r_j - {}_{m-1}d_{ij}) \quad \text{Equation 3.2}$$

$${}_m x_i = {}_{m-1}r_i \cos {}_{m-1}\theta_i + \left( \frac{{}_{m-1}r_i \cos {}_{m-1}\theta_i - {}_{m-1}r_j \cos {}_{m-1}\theta_j}{{}_{m-1}d_{ij}} \right) (r_i + r_j - {}_{m-1}d_{ij}) \quad \text{Equation 3.3}$$

$${}_m y_i = {}_{m-1}r_i \sin {}_{m-1}\theta_i + \left( \frac{{}_{m-1}r_i \sin {}_{m-1}\theta_i - {}_{m-1}r_j \sin {}_{m-1}\theta_j}{{}_{m-1}d_{ij}} \right) (r_i + r_j - {}_{m-1}d_{ij}) \quad \text{Equation 3.4}$$

$${}_m z_i = {}_{m-1}z_i + \left( \frac{{}_{m-1}z_i - {}_{m-1}z_j}{{}_{m-1}d_{ij}} \right) (r_i + r_j - {}_{m-1}d_{ij}) \quad \text{Equation 3.5}$$

$${}_m r_i = \sqrt{{}_m x_i^2 + {}_m y_i^2} \quad \text{Equation 3.6}$$

$${}_m \theta_i = \tan^{-1} \left( \frac{{}_m y_i}{{}_m x_i} \right) \quad \text{Equation 3.7}$$

Multiple overlaps of one grit requires a method of combining the displacement vectors into a single vector for grit  $i$ . Figure 3.7 shows the desired relocation of a grit that is overlapped by three other grits.

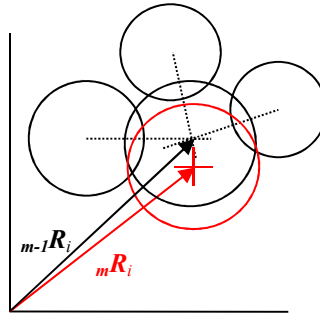


**Figure 3.7 – Visualization of the repositioning of an overlapping particle**

The new position vector for grit  $i$  is generated by summing up the relocation vectors generated by each overlapping grit which is governed by Equation 3.8.

$${}^m\mathbf{R}_i = \sum_{j=1}^{n_i} \left( {}^{m-1}\mathbf{R}_i + \left( \frac{{}^{m-1}\mathbf{R}_i - {}^{m-1}\mathbf{R}_j}{{}^{m-1}d_{ij}} \right) (r_i + r_j - {}^{m-1}d_{ij}) \right) \quad \text{Equation 3.8}$$

However, it is noted moving the grits could result in some grits no longer satisfying the boundary conditions of the grind wheel set forth in Equation 2.22. It is also noted that a single implementation of the algorithm does not necessarily relocate a grit from all of its overlapping neighbors. In addition, moving a grit from one overlap situation may introduce a new overlap situation. Therefore, the process must be repeated until there are no instances of grit overlap within the wheel. This could be computationally burdensome so a limiting criterion is implemented that relocates grits until less than 5% of the grits overlap one another. The selection of which overlapped grit is moved in each iteration is selected randomly in order to minimize the repeated boundary condition violations.

A summary of the final grit relocation algorithm is shown in Figure 3.8 which accounts for the boundary conditions by not allowing any relocation that would introduce a violation. The algorithm repeats until the number of grits that are overlapping is reduced below a specified threshold. A simulated surface plot of a grind wheel after the implementation of the final algorithm is shown in Figure 3.9 for a wheel with less than 5% overlapping grits.

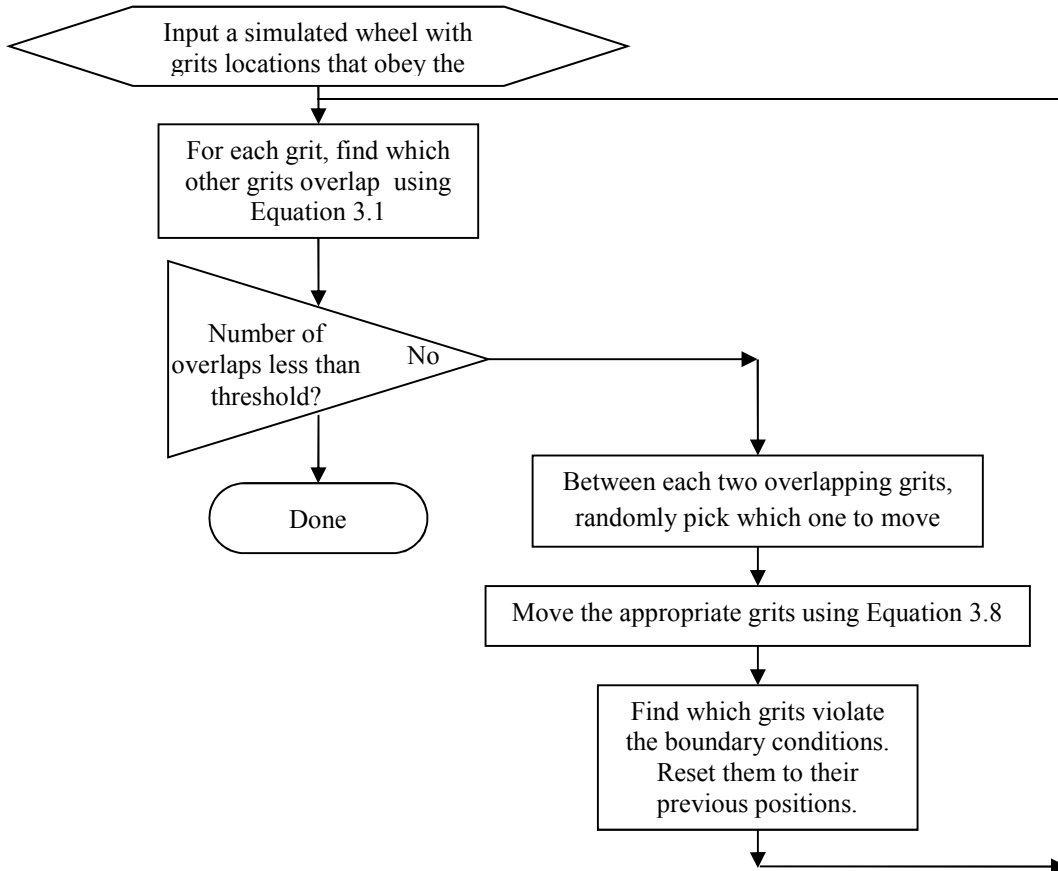


**Figure 3.8 – Grit relocation algorithm to minimize grit overlap within a grind wheel**

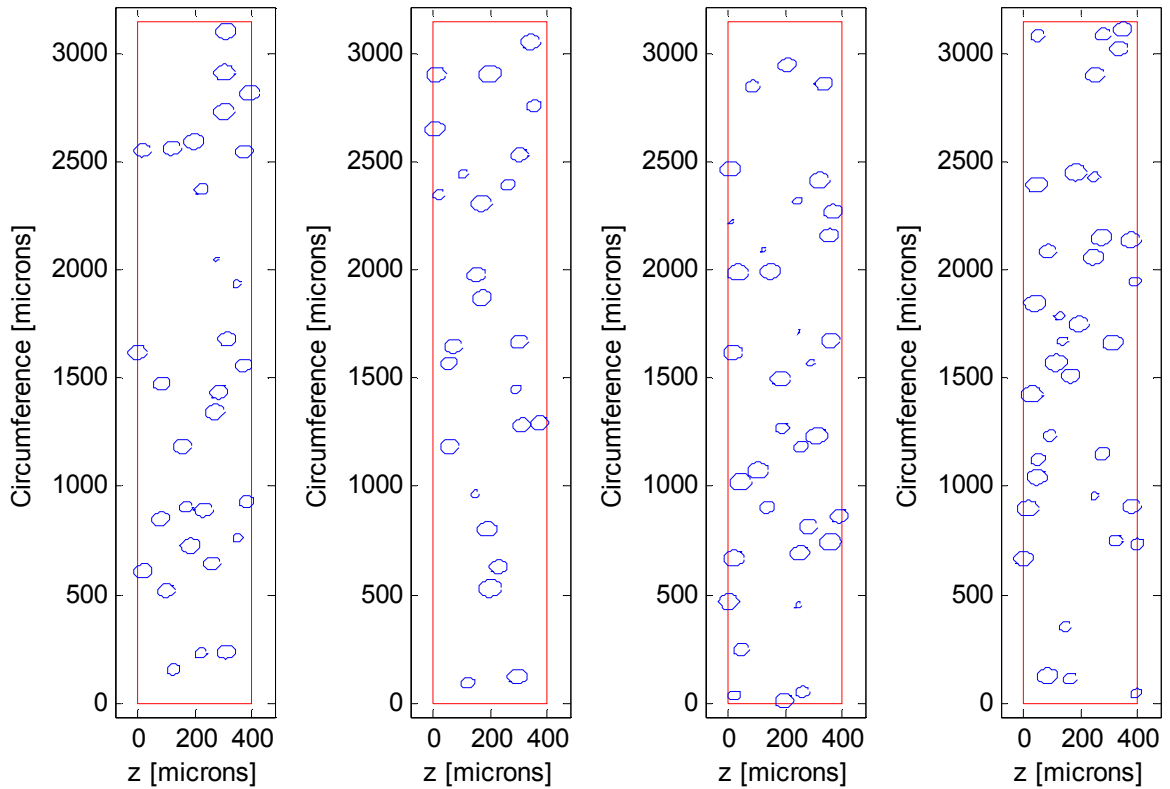


**Figure 3.9 - Plots of simulated wheel surfaces for #220 wheel with no grit overlap without verifying BC**

### 3.4.2 Effect of Grit Overlap Reduction on Grit Position Probabilities

The grit location algorithm modifies the locations of the individual grits and therefore the occurrence frequencies of the coordinate locations of the grit centroids. The cumulative probability plots for the grit radial and angular positions are shown in Figure 3.10 along with the CDF provided by the analytic model which does not account for grit relocation. Figure 3.10 also show the probability density plots for the coordinates.

It is seen that the grit relocation does not affect the occurrence probability of the angular position coordinates. However, relocation does slightly modify the radial position probability by shifting more grits towards the edges of the range as seen by the deviation

peaks around 470 and 530  $\mu\text{m}$ . The analytic model does still approximate the occurrence probability of the grit radial position well in that the locations of the slopes at the edges of the wheel are still accurate.

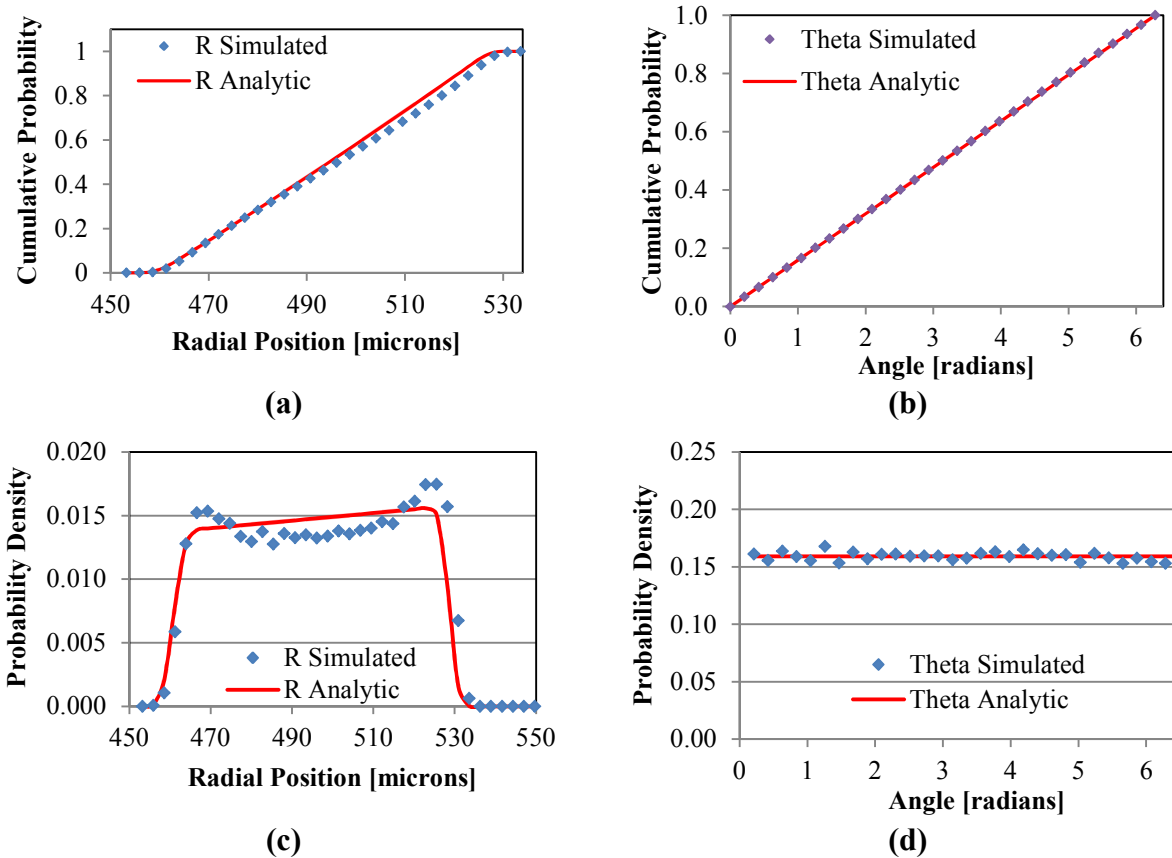


**Figure 3.10 – Simulation of 50,000 #220 grits with reduced overlap produced the CDF of the (a) radial and (b) angular grit positions along with the PDF of the (c) radial and (d) angular positions**

### 3.4.3 Effect of Grit Overlap Reduction on Static Grit Density

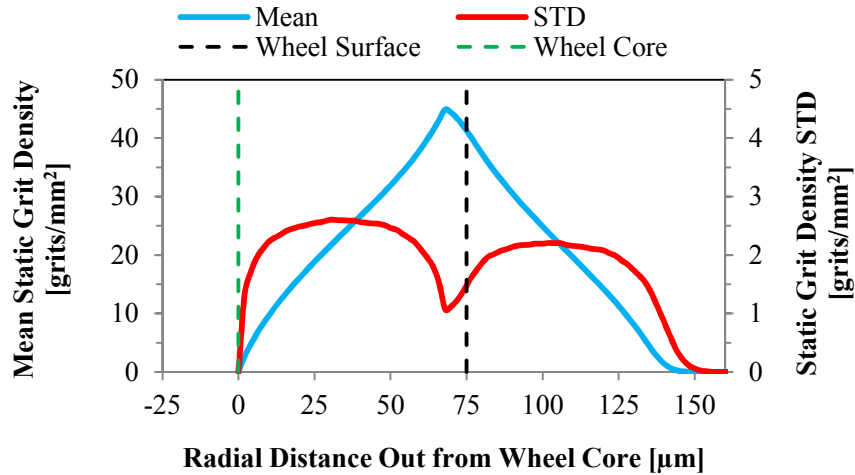
Table 3.1 presents the tabulated results for static grit density distribution with and without the overlay adjustment algorithms. The results are based on #220 and #1200 grits governed by the abrasive parameters in Table 2.2 and wheel parameters outlined in Table 2.3. The width of the grind wheels and the number of iterations computed were reduced

in order decrease computation time. The static grit density is seen to be reduced once the grits are relocated. This is attributed to the grits moving outside of the valid wheel boundary conditions.

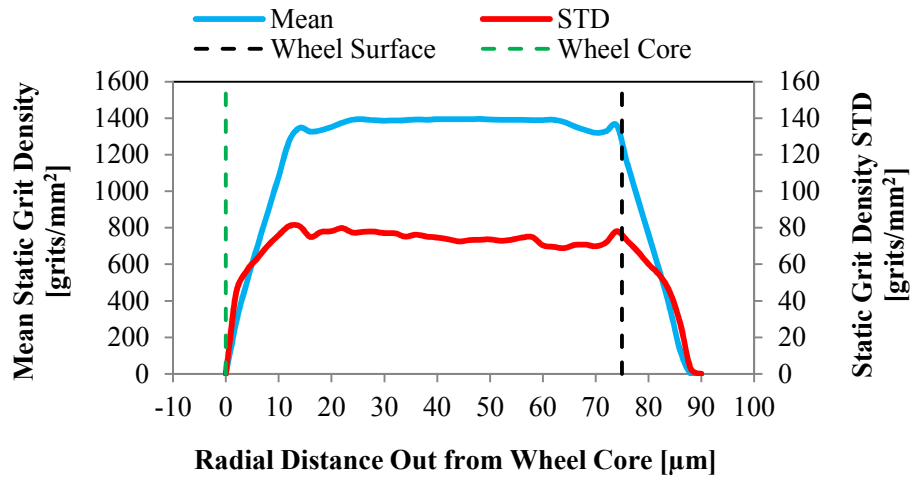
**Table 3.1 – Simulation results for the static grit density at the wheel Surface**

<b>Grit Number</b>	<b>G#</b>	<b>220</b>		<b>1200</b>	
<b>Grit Overlap</b>		<b>Allowed</b>	<b>Reduced (&lt; 5%)</b>	<b>Allowed</b>	<b>Reduced (&lt; 5%)</b>
Number of Simulations	$n$	1,000	1,000	1,000	1,000
Wheel Width	$w$	0.5 mm	0.5 mm	0.05 mm	0.05 mm
Number of Grits Mean	$\mu_N$	70.45	70.48	1,157.4	1,156.9
Static Grit Density Mean at Bond Surface	$\mu_N$	41.84	40.53	1146.35	1150.24
Static Grit Density STD at Bond Surface	$\sigma_N$	1.44	1.59	78.43	72.86
Solve Time with 4-Core Parallel Processing	$t$	4.67 sec	7.48 sec	99.97 sec	1341.04 sec

The static grit densities for the #220 and #1200 grit wheel with grit relocation are shown in Figure 3.11 where it is seen that profiles differ slightly from that observed in the overlapping-grit scenarios.



(a)



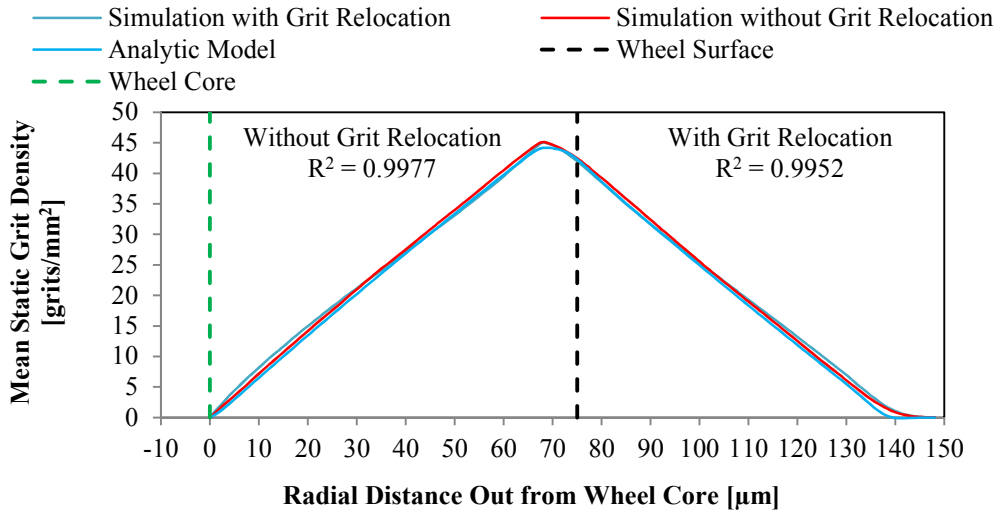
(b)

Figure 3.11 - Static grit density normal distribution parameters as a function of radial distance from the core simulated with grit overlap reduced to 5% in (a) #220 and (b) #1200 grit wheels

### 3.5 COMPARISON BETWEEN THE ANALYTIC MODEL AND NUMERICAL SIMULATION

A comparison of the expectation of the static grit density at different radii within a #220, 1mm OD single-layered grind wheel as predicted by the analytic model and as

calculated from the numerical simulation with and without grit relocation is shown in Figure 3.12. The coefficients of determination were calculated by comparing the individual numerical simulation outputs to the analytic model prediction. It is seen that the analytic model predicts the expected mean static grit density well for both cases and that the overlapping of grits does not have a significant impact on the static grit density mean. A more detailed view of how well the analytic model agrees with the numerical simulations can be seen in Figure 3.13 where the deviation between model prediction and the output of the two simulations is plotted for each radial surface in the wheel. Notice that the model maintains an accuracy of 2 grits/mm<sup>2</sup> for both with and without overlapping grits.



**Figure 3.12 - Static grit density expectation for #220 wheel from analytic and simulation models**

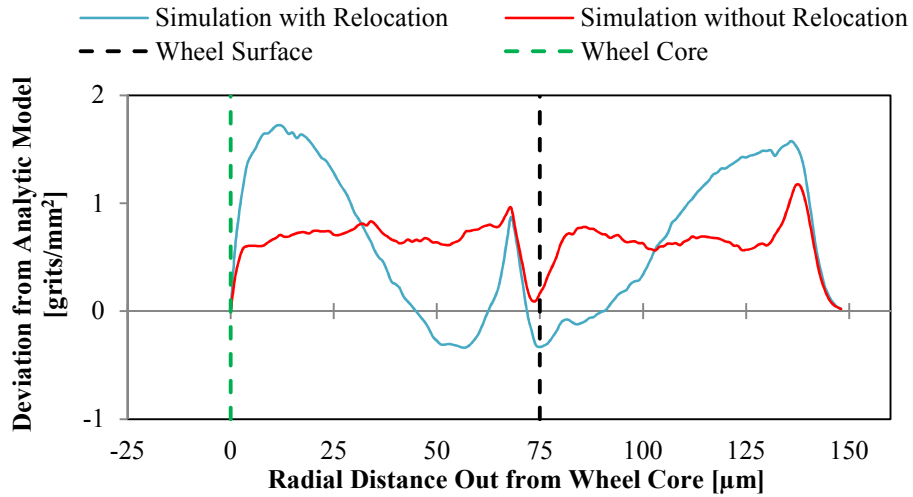


**Figure 3.13 - Static grit density expectation deviation from analytic model for #220 wheel**

A comparison between the predicted standard deviation of the static grit density in the analytic model and that calculated by the two numerical simulation methods is shown in Figure 3.14. The coefficient of determination is worse in the case of the standard deviation than it was in the expectation. Also, the effect of overlapping grits is more significant in the prediction of the static grit density standard deviation. The numerical difference between the predicted and simulated std. dev. are shown in Figure 3.15. It is observed that the analytic model does maintain a prediction accuracy of 0.6 grits/mm<sup>2</sup>.

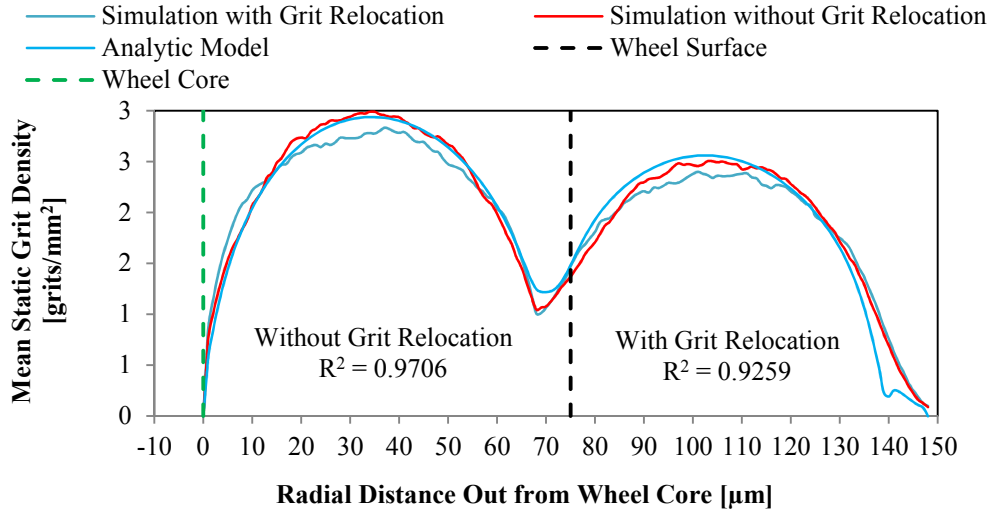


**Figure 3.14 - Static grit density std. dev. for #220 wheel from analytic and simulation models**

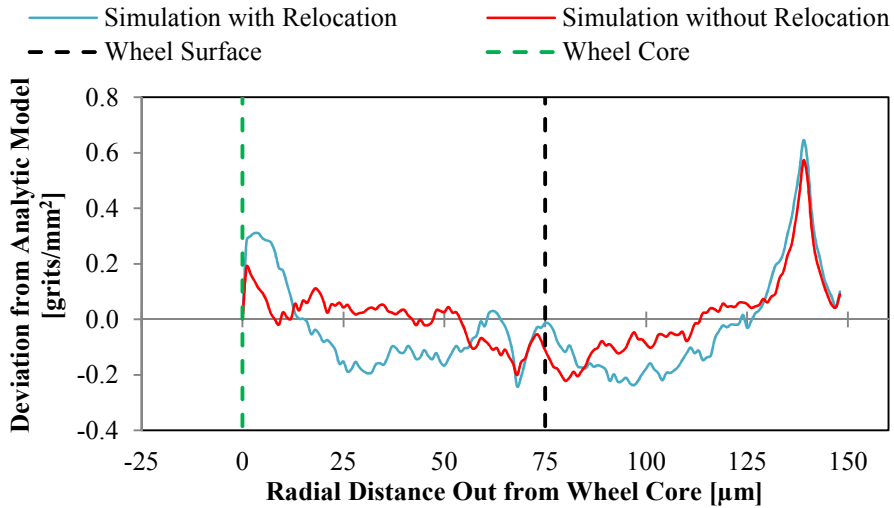


**Figure 3.15 - Static grit density std. dev. deviation from analytic model for #220 wheel**

Similar comparisons were made for a multi-layered #1200 wheel as seen in Figure 3.16 and Figure 3.17 for the static grit density mean and standard deviation respectively.

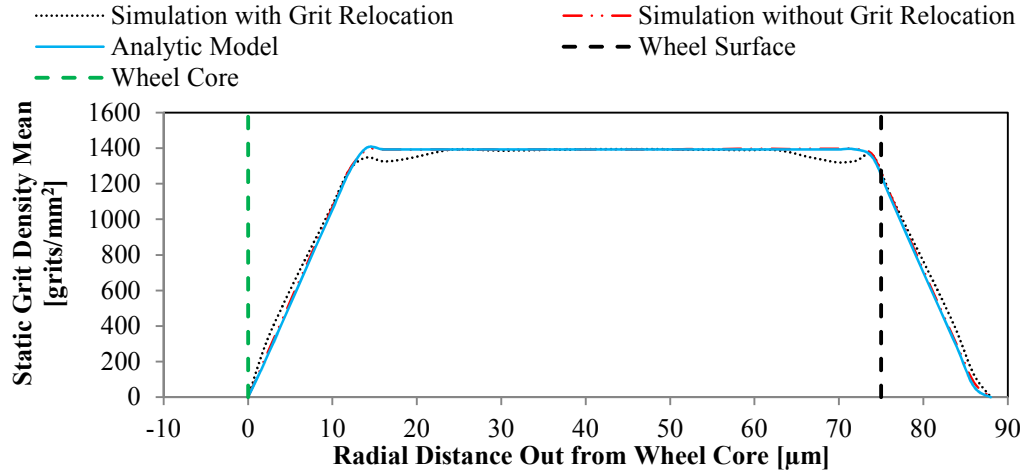


**Figure 3.16 – Static grit density mean from analytic and simulation models for a #1200, 1mm OD multi-layered grinding wheel**

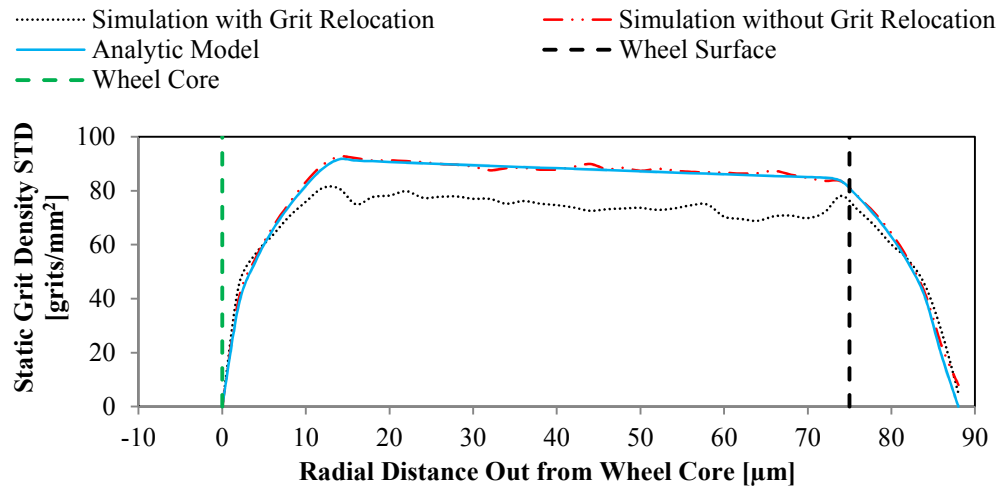


**Figure 3.17 – Static grit density std. dev. from analytic and simulation models for a #1200, 1mm OD multi-layered grinding wheel**

### 3.6 STATISTICAL DISTRIBUTION OF STATIC GRIT DENSITY

The analytic model for grind wheels presented in CHAPTER 2 yields a method for calculating the expected mean and variance of the static grit density on any cylindrical surface of a wheel with a known geometry and abrasive size. However, the model does not produce a distribution of the static grit density as a random variable. It is

hypothesized that the random nature of the process produces a final static grit density that follows a standard distribution such as a normal Gaussian. The appropriate distribution can be selected by examining the results from the numerical simulation of the grind wheels.

The Chi-Squared Goodness of Fit test is used on the static grit density distributions for the #220 and #1200 grit wheels generated using the two numerical simulation methods. The test tries to reject the null hypothesis that the static grit density at a specified wheel radius can be represented by a normal distribution. The significance level for these tests will be set at  $\alpha = 5\%$ . The test statistic for the Chi-Squared Goodness of Fit test is shown in Equation 3.9.

$$\chi^2 = \sum_{k=1}^n \frac{(O_k - E_k)^2}{E_k} \quad \text{Equation 3.9}$$

The test involves separating the simulated wheel static grit densities into occurrence frequency bins such as in a histogram. Each bin has an index  $k$  with  $n$  bins in the data set to be tested.  $O_k$  is the frequency of observed outcomes within the dataset bin while  $E_k$  is the theoretical frequency of outcomes from an identical bin in the test distribution. The distribution being tested is the Gaussian distribution with a mean and standard deviation estimated from the sample mean and variance of the simulated wheels in the radius bin. These tests utilized a large sampling of 5000 wheels to provide a better estimate of the distribution parameters.

The chi squared goodness of fit test rejected the hypothesis that a Gaussian distribution describes the static grit density for both grind wheels. This is due to the large number of simulated samples available to evaluate the test. However, a more qualitative assessment of the actual distribution can be examined using the skewness and kurtosis

values for the dataset. Figure 3.18 shows this for the #220 simulated grinding wheels while Figure 3.19 shows it for the #1200 wheel. It is seen that the distribution of static grit density is mostly symmetrical and has a kurtosis shape that is similar to that of a Gaussian distribution, zero.

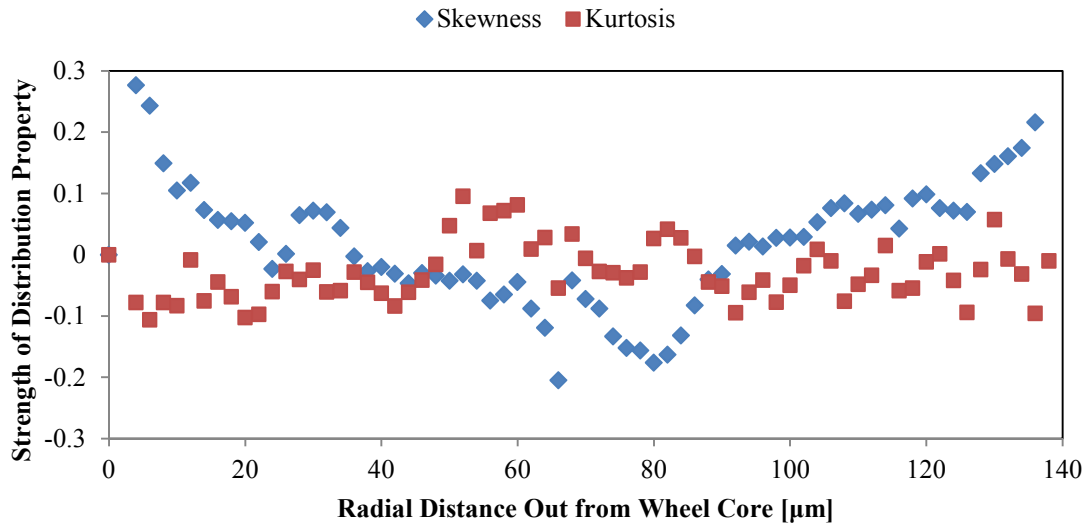


**Figure 3.18 - Skewness and kurtosis for the distribution of static grit density at various radii in #220 wheels**

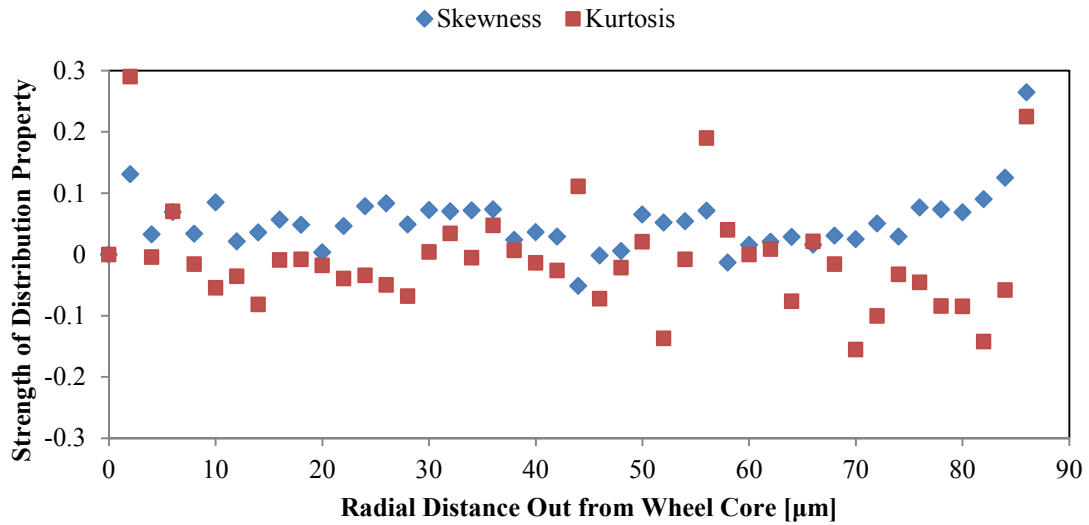


**Figure 3.19 – Skewness and kurtosis for the distribution of static grit density at various radii in #1200 wheels**

Another subjective method of testing the hypothesis of Gaussian distributed static grit densities is to visualize the simulated occurrence frequencies against what a Gaussian distribution would yield. This is done in a normal probability plot in Figure 3.20. It is seen that the correspondence between the simulated static grit densities and what would be expected from a normal distribution are very similar since both the measured slope of a linear fit and its fit correlation are very close to 1. This was repeated across the various wheel radii and also for the simulated #220 grit wheel. The results consistently showed that a normal distribution is very similar to the actual static grit density distribution.

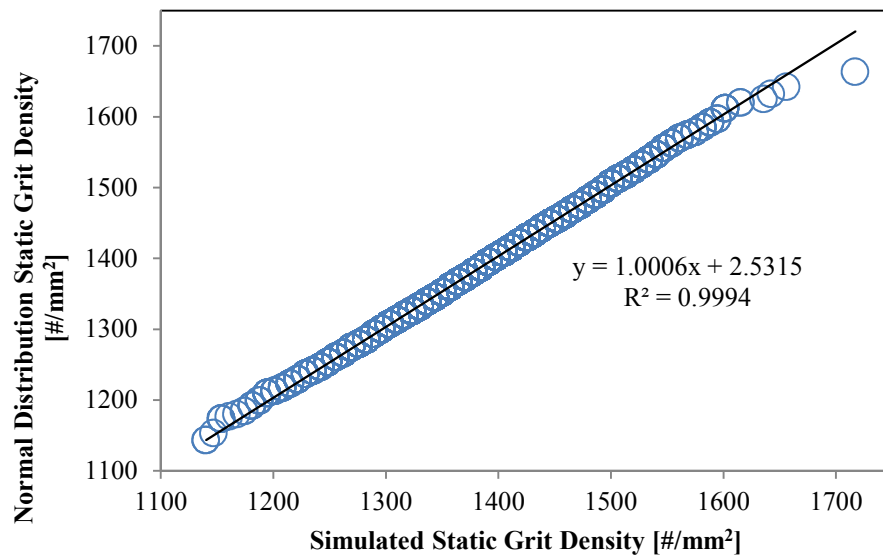


**Figure 3.20 – Normal probability plot for static grit density at the bond surface of a #1200 wheel**

### 3.7 DISCUSSION

The analytic model for the wheel consists of complex statistical descriptions. Some of the model parameters have distinct probability density functions but the cumulative

density functions must be numerically integrated. This requires some costly computation time. Other parameters can only be analytically modeled by calculating their distribution estimators. For example, the number of grits in the wheel is only analytically modeled by their expected mean and variance. A full description of the PDF and CDF are not obtainable. However, use of numerical simulation showed that the probability of the number of grits in the wheel can modeled using a Gaussian distribution governed by the analytically generated estimators. This allows a much faster method of calculating the probability of how many grits are in a wheel.

Comparison between the analytical stochastic model and the numerical simulations show that the analytic model accurately captures the behavior of the grinding wheels given the assumptions made. However, the assumptions of allowing the abrasives to overlap one another would not hold in actual grinding. The new numerical simulation technique accounts for this by limiting abrasive overlap. Comparison between the analytic model and the relocated grit positions showed that the relocation did radially shift grits from the center of the bond layer to its edges while it did not affect the angular positions of the grits. The analytic model was seen, however, to provide an adequate method to estimate grit positions.

A comparison between the analytic model, simple simulation with grit overlap, and new simulation with reduced grit overlap is shown in Table 3.2. It is seen that the analytic model closely arrives at similar estimations for the static grit density distribution parameters as those provided by the Monte Carlo simulation. The analytic method, however, did consistently over-predict the static grit density expectation and variance. It

is suspected that this arises from the method of simulating how many grits are in the wheel since this was consistently over predicted in the simulation.

**Table 3.2 - Comparison of analytical and simulated wheel topography models**

Grit Number	G#	#220			#1200		
Method		Analytic	Numerical Simulation		Analytic	Numerical Simulation	
			With Grit Overlap	Reduced Overlap (< 5%)		With Grit Overlap	Reduced Overlap (< 5%)
Number of Simulations	$n$	1,000			1,000		
Wheel Width	$w$	0.5 mm			0.05 mm		
Number of Grits Mean	$\mu_N$	69.98	70.45	70.48	1,156.4	1,157.4	1,156.9
Static Grit Density Mean at Bond Surface	$\mu_N$	42.31	41.83	40.52	1239.6	1146.3	1150.2
Static Grit Density STD at Bond Surface	$\sigma_N$	1.481	1.441	1.586	81.23	78.43	72.85
Solve Time with 4-Core Parallel Processing	$t$ [sec]	1.71	5.01	9.47	0.72	99.97	1341.04

It is noticed, however, that the analytic method is significantly faster than the simulation methods. For wheels with many grits in them such as the #1200 wheels, the analytical model is over 2 orders of magnitude faster. The real strength in the model is that a large number of wheels do not have to be simulated to estimate the static grit density parameters. One calculation provides the information for any wheel of the same geometry and abrasive characteristics. Improvements to the analytic calculation time could be made through refinement of the techniques used to calculate the necessary integrals in the stochastic propagation.

### **3.8 SUMMARY**

Numerical simulation techniques were used to validate the behavior and accuracy of the analytical model. The two major outcomes of this investigation are the new vectorized displacement method of grit relocation to minimize overlap in the simulation and the verification of the probabilistic model developed in CHAPTER 2. The statistical propagation in the analytic model was shown to accurately capture the stochastic nature of the wheel topography based on the assumptions made. The new technique of numerical simulation using grit relocation utilizes the knowledge of the amount of overlap that is occurring to displace the grits to the closest location that eliminates the interference. The new technique of grit relocation showed that grit overlap has a minor but definite impact on the predicted wheel topography distributions.

The static grit density of a cylindrical surface within the wheel was shown to have a Gaussian distribution. The static grit density can modeled using the mean and variance predicted by the analytic model. The analytic model was shown to calculate the statistical parameters for the static grit density distribution over 3 times faster than the numerical simulation for wheels with small grit populations and 2 orders of magnitude faster for large population wheels. This makes the analytic model better suited for the prediction of stochastic wheel topography in advanced process control with the greatest benefits occurring for multi-layered wheels with large numbers of grits. The ability of the analytic model and numerical simulation technique to predict the static topography of actual microgrinding wheels will be reviewed in CHAPTER 4 through comparison to measured wheel surface topography.

# CHAPTER 4 – STATIC MEASUREMENT OF MICROGRINDING WHEELS

## 4.1 INTRODUCTION

The ability of the probabilistic model to accurately predict real grinding wheel topography needs to be verified using experimental measurement. The surface topography of microgrinding wheels needs to be measured for the distribution of static grit density across multiple wheels of the same specification. The analytic model and numerical simulations have shown that there is variance in static topography between different wheels, and it is hypothesized that this variance is exacerbated in microgrinding because there are so few grits in each wheel. Therefore, it is desired for the measurement technique to provide a quick estimate of the distribution of the static topography characteristics for each microgrinding wheel before it is used in a grinding operation. A technique that can be easily implemented on the grinding machine tool for *in situ* measurement will fill this need.

This chapter presents a machine vision approach for simple, non-contact measurement *in situ* of microgrinding wheels. The measurements recorded using the measurement technique are used to verify the accuracy of the topography models. In addition, the variance in microgrinding wheel specifications is investigated to characterize manufacturing variability as a source to topography variance. Finally, the scaling effect that the limited number of abrasives in each microgrinding wheel has on the topography variance is measured.

## 4.2 REVIEW OF SALIENT LITERATURE

Many methods of measuring grinding wheel topography have been developed and documented. Due to difficulties in the measurement of individual grit cutting forces in a grinding operation, the preferred method of generating models for the dynamic cutting action of individual abrasives is to measure the static wheel topography and empirically relate the two [2, 54, 55]. The traditional technique for measuring grind wheel surface topography is time-consuming measurement with a scanning electron microscope. An overview of the other methods used to measure conventional grinding wheel topographies including the source studies is provided by Malkin and Guo and are listed in Table 4.1 [2]. The analysis of static topography data for wheel characterization has included discrete autoregressive moving average of profiles [34], fast Fourier transform [54], and power spectral density [56].

**Table 4.1 – Methods for characterizing conventional grind wheel topographies**

1-D Profilometry methods [54]
Imprint Methods [18, 24, 57]
Scratch Methods[44, 58, 59]
Measurement of reflected surfaces of wear-flats as wheel is rotated [60]
Angled and Vertical Microscopy Differential Focusing [36, 43]

Recently reported literature shows attempts at specifically characterizing microgrinding wheels. Many of these studies have tried to use conventional techniques [18]. These have limited applicability though because they are slow and not conducive to repetitive *in situ* measurement. In 2008, Park [18] used a machine vision approach that viewed the end of a grinding pin and traced the outline of the wheel. This outline was

then analyzed for grit spacing content. However, this method limited the measurements to one data sample per wheel. Also, the technique analyzed only the projected image of the peripheral grits closest to the end of the wheel. This provides no information about the axial spacing of these grits. Grits observed from the end of the wheel could appear to be inline circumferentially but could actually have axial offsets.

Profilometers are a popular method for measuring the surface topography of conventional grinding wheels and could be implemented in a machine tool for *in situ* microgrinding wheel measurement. However, conventional profilometers are not well suited for small diameter wheels. Figure 4.1 shows an image of a conventional 2 $\mu$ m diamond profilometer probe in contact with a #220 microgrinding wheel with an outer diameter of 1mm. The large grits relative to the probe size requires that the probe travel up and down large distances along steep surfaces of the wheel grits. However, the probe tip tends to deflect out of the plane of measurement since the profilometer probe is less stiff in that direction. The case of a rotary profilometer as seen in Figure 4.1 rotates the grind wheel as the measurement of the probe along the major axis of its tip is measured. However, the probe arm has little lateral stiffness so the probe deflects in a direction tangential to the grind wheel surface rather than normal to the surface. This results in false readings of grit heights. This same scenario arises when a conventional linear profilometer is used such as the one shown in Figure 4.1. The probe is translated along the grind wheel axis while the vertical deflection of the probe is measured. However, the probe again deflects laterally as it encounters steep grit surfaces rather than deflecting upwards. This results in similar false readings.

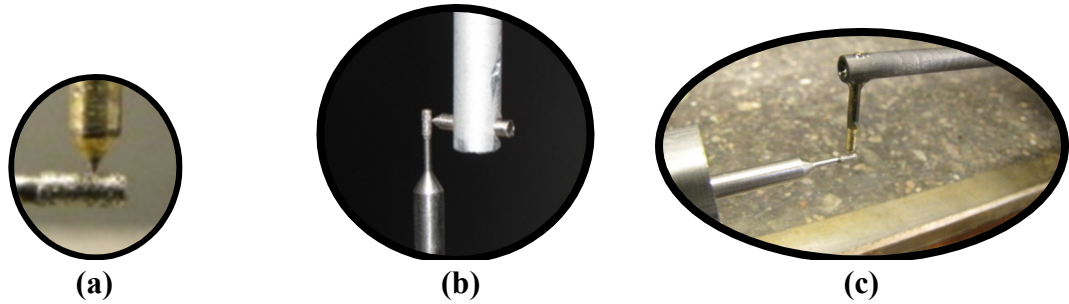


**Figure 4.1 - 1mm OD microgrinding wheel profilometry with (a) a conventional 2  $\mu\text{m}$  diamond probed, (b) conventional rotary profilometer and (c) conventional linear profilometer**

Sample traces of the #220, 1mm microgrinding wheel were taken to examine the nature of the profiles produced using rotary profilometry. The traces, shown in Figure 4.2, were taken at different axial positions on the wheel and measured the grit heights at the wheel was rotated. The lateral deflection of the probe tip was observed to cause the probe to roll off the surface of the wheel creating large decreases in the measured profile as seen in trace 1 and trace 2.

In addition, these profilometer methods provide information about grit protrusion height along a single line of travel around the grind wheel. Many time-consuming readings would need to be implemented to get an accurate depiction of the properties of the wheel topography.

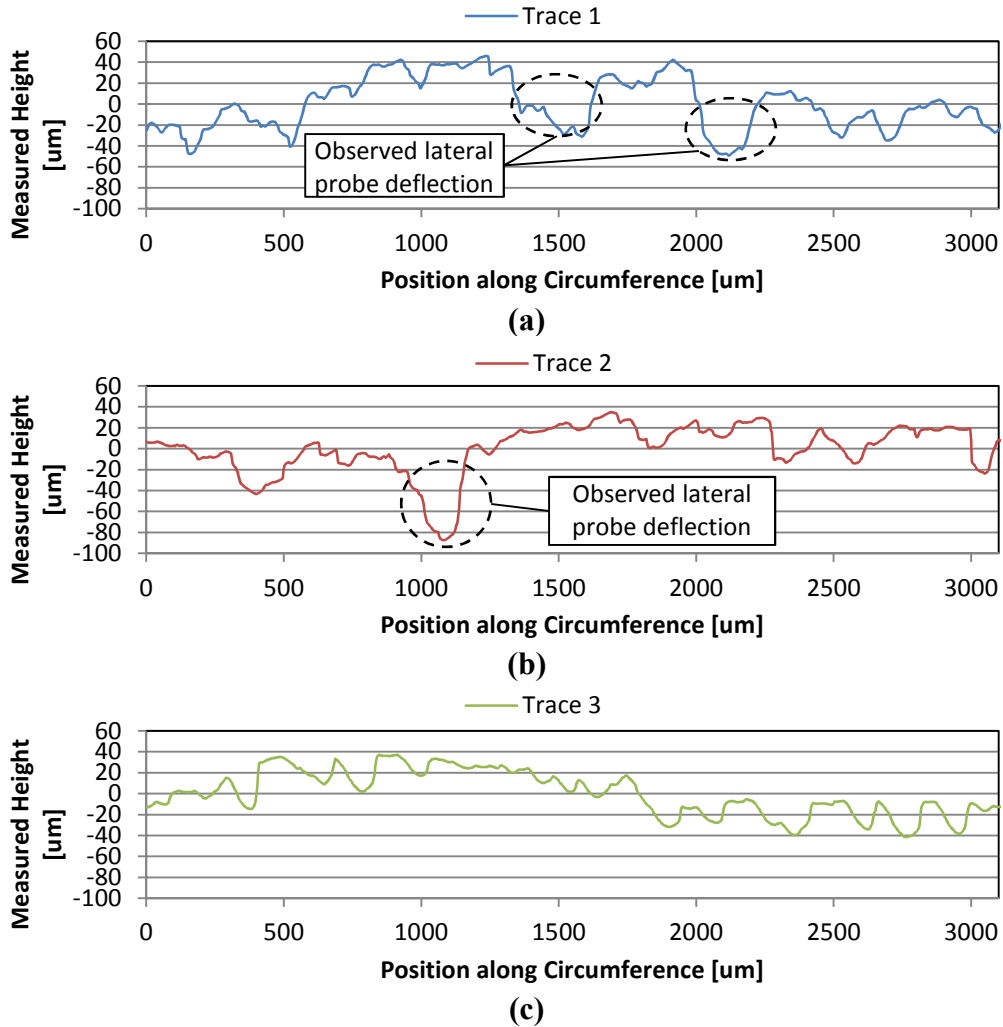


**Figure 4.2 – Rotary profilometry profiles for a #220, 1mm wheel using trace paths at 3 different axial positions (a), (b), and (c) on the wheel**

A white light interferometer is another possible method of measuring the surface topography of microgrinding wheels. Sample 3-D profiles of the surface of the same #220, 1mm wheel were taken using such a measurement tool made by Zygo. The measurements showed highly incomplete profile information as can be seen in the example shown in Figure 4.3. The large difference in the reflectivity of the dark industrial diamonds and the shiny metallic bond resulted large holes of missing information. The imprint method attempts to overcome this by transferring the surface profile to a soft

material which then has uniform reflectivity. However, similar results were seen when this was attempted using lead as the impression material. It is thought that the sharply faceted angles on the diamond abrasive make it difficult for the measurement device to interpret the reflection of the white light.

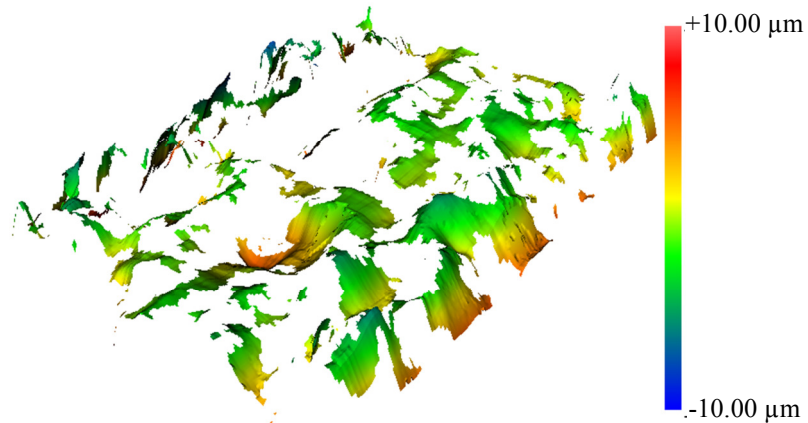


**Figure 4.3 – Surface of #220, 1mm wheel measured using white light interferometer**

A faster method of measuring the layout of the grits on the surface of microgrinding wheels is needed. In addition, the exact static wheel topography characteristic distributions needs to be measured specifically for microgrinding wheels. Many studies have presented varying distributions measured from the topography of conventional grind wheels, as reviewed in Table 2.1, but there is limited information on the topography of microgrinding wheels.

### 4.3 MACHINE VISION INSPECTION AND MEASUREMENT OF MICROGRINDING WHEELS

A machine vision method for measurement of the static grit density is a preferred solution, because it offers the easiest and cheapest solution for a system that could be integrated directly onto a microgrinding machine tool. A proposed structure for such a system is shown in Figure 4.4. This solution is non-intrusive, non-contact and can easily be incorporated in an existing system. It also allows for rapid, accurate *in-situ* surface measurement while broadening the capabilities of the machine tool as a whole.

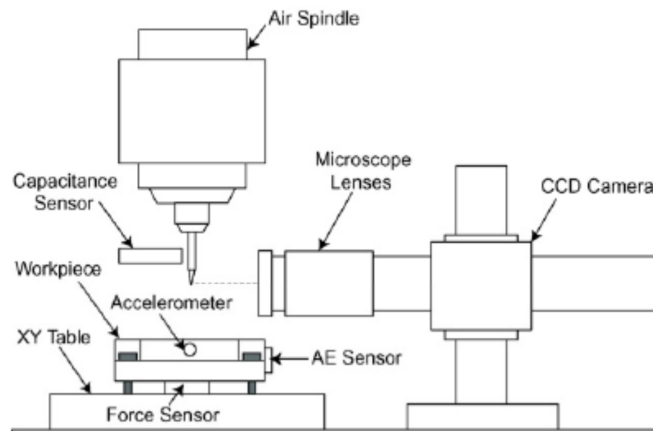


**Figure 4.4 – Potential setup for an *in-situ* microgrinding wheel topography measurement tool [61]**

#### 4.3.1 Imaging of the Wheel Surface

A test of the feasibility and accuracy of such a system was conducted by measuring microgrinding wheels on a microscope which has specifications that could easily be implemented in an *in-situ* vision system. The images for the machine vision measurements were taken on a Leica Type 301-371.01 microscope with a 10x optic. Medium intensity front-lighting conditions were used, and the light polarity was adjusted

to highlight the reflectivity of the metal bonding and limit reflectance from the grits. The setup for testing the approach is shown in Figure 4.5 while a resulting image of the microgrinding wheel is shown in Figure 4.6.

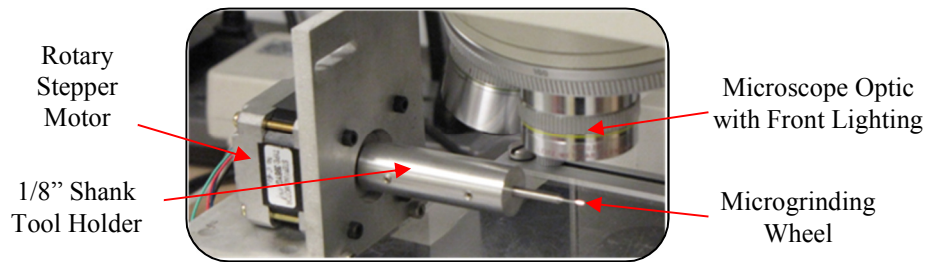


**Figure 4.5 – Setup for test Approach for *in-situ* machine vision measurement of microgrinding wheel topography**

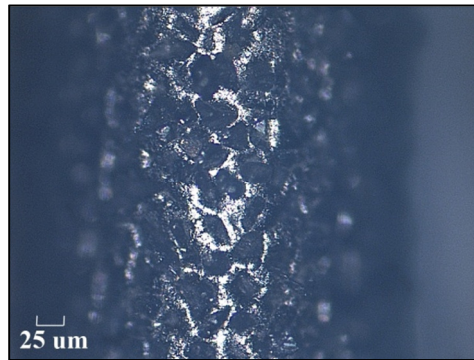


**Figure 4.6 - Image of a 1mm OD, #220 grit diamond microgrinding wheel in a microscope at 10x magnification**

The end-goal modeling of grinding force frequency requires measurement of the static grit density along with the circumferential grit spacing along the grind path. However, due to the small diameter of the grind wheel, the projected 2-D image contains significant distortion of the apparent distance between grits in the circumferential direction. This effect is illustrated in Figure 4.7 where the partitions on the cylindrical wheel are spaced equally along the circumference of the wheel but are distorted on the projected image plane. Therefore, there would be significant inaccuracy if the image was

processed by measuring grit spacing in the radial direction on a single image. Instead, a full image of the wheel was obtained by taken sequential images as the wheel was rotated under the microscope. The images were digitally stitched utilizing the commercial image stitching software AutoPano© by Kolor. The software utilizes a search algorithm to identify control points at the junctions of regions of contrasting pixels. Matching control points in adjacent images are identified allowing for automated stitching to occur. A resulting full surface image is shown in Figure 4.8 comprised of a single row of 61 stitched images. Wheels with large axial widths required multiple rows of images to be stitched together. The use of simplistic optics and a commercial stitching package was chosen to facilitate simple *in situ* measurement of a full wheel surface without the need for sophisticated metrology equipment.

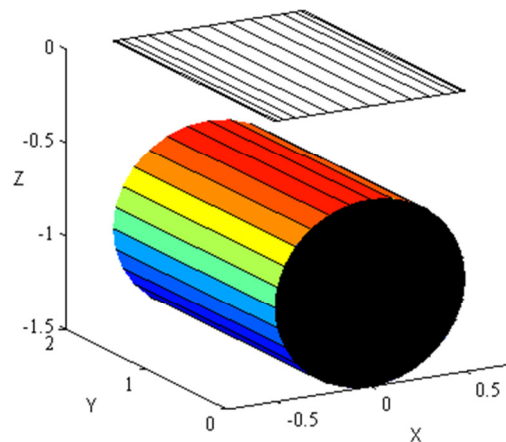


**Figure 4.7 - Illustration of space distortion in projected image due to grind wheel curvature**

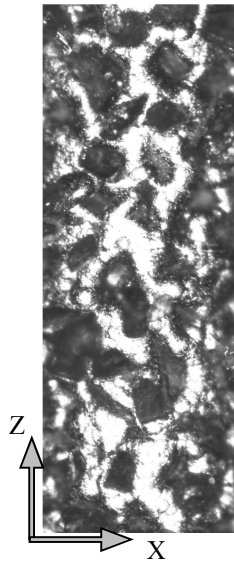


**Figure 4.8 - Stitched surface image of 0.5mm OD, #200 grit diamond grinding wheel composed from 61 individual images**

The grind wheels were also optically measured on the microscope for accuracy in specified diameter and length while the unknown specification of the bond thickness was measured. The repeatability of the optical measurement method was measured to be  $\pm 0.9$   $\mu\text{m}$  by repeated measurement of a gauge pin.

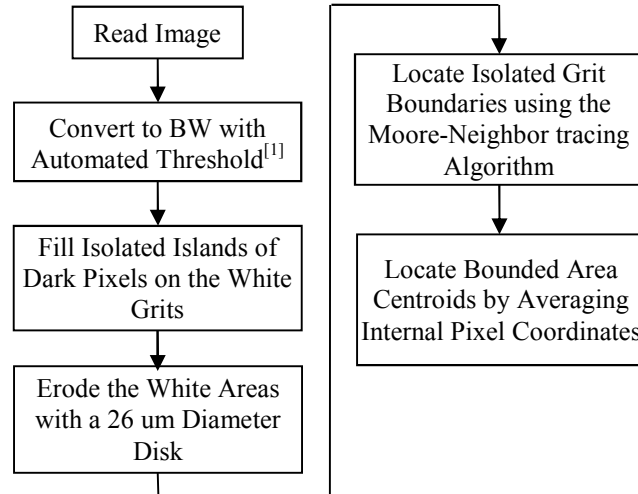
#### **4.3.2 Machine Vision Analysis of Fully Imaged Wheels**

Image analysis was conducted in a grayscale format because of the lack of color variation in the original image. Figure 4.9 shows a sample raw image region after manual cropping. The surface shows dark grits scattered on a bright background. The labeled  $Z$ -direction is along the axis of rotation of the grind wheel while the  $X$ -direction is tangential to the wheel surface in the circumferential direction.



**Figure 4.9 - Raw grayscale image of #220 grit diamond wheel used for machine vision analysis**

Figure 4.10 shows the machine vision algorithm used to isolate individual grits and locate their centroids while Figure 4.11 presents sample results after each step in the algorithm. The algorithm begins with the conversion of the grayscale image into a binary black-and-white image using an automated threshold. Next, stray background pixels that are surrounded by white foreground pixels are eliminated. The white areas are then eroded using a structuring element that approximates a disk with a 26  $\mu\text{m}$  diameter. This separates white areas that are connected with thin bridges resulting in the isolation of individual grits. The boundaries of the isolated grits are then located using the Moore-Neighbor tracing algorithm [62]. Grit centroids are then calculated by averaging the coordinate locations of all of the pixels contained within each boundary separately.



**Figure 4.10 - Machine vision algorithm for locating individual grits**

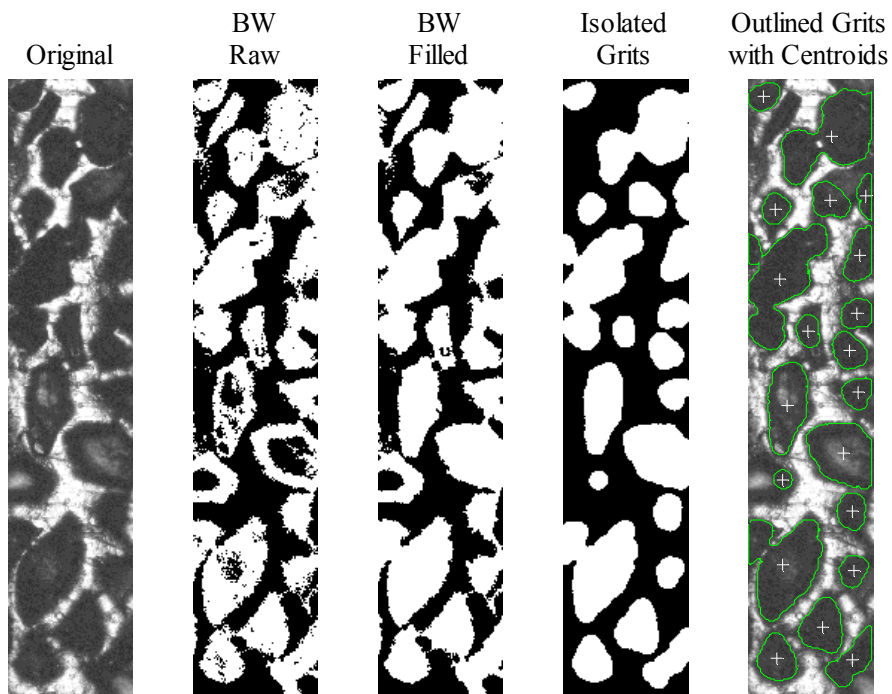


**Figure 4.11 - Effects of machine vision algorithm steps on select region of a #220 microgrinding wheel**

### 4.3.3 Measurement of Wheel Specifications

The visual inspect of the wheels also provides a method to measure the geometric specifications of the wheel. Images of the wheel shank and plated grits, such as that shown in Figure 4.12, allow for the wheel shank diameter and bond layer thickness to be measured. The width of the wheels was too large to measure in a single image so it was instead measured from the stitched image of the complete wheel surface as can be seen in the sample image in Figure 4.14. Calibration of the uncertainty in the accuracy of the measurements using the images was conducted by repeated measurement of the diameter of a known 1.0000 mm gauge pin. The technique was found to have an uncertainty of 0.9  $\mu\text{m}$ .

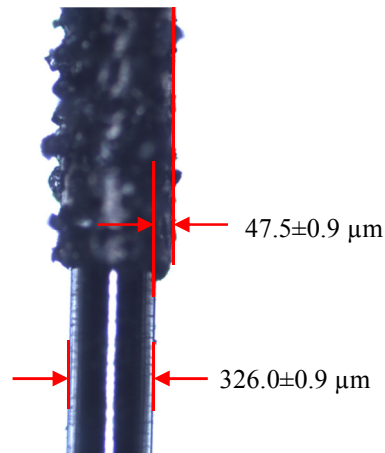


**Figure 4.12 – Inspection measurement of #200, 508 $\mu\text{m}$  wheel**



**Figure 4.13 - Inspection measurement of #200, 508μm wheel stitched surface image**

The machine vision algorithm was used to count the number of abrasives that resided in each wheel. It had to be assumed that all of the grits embedded into the wheel bond protruded the outer surface allowing them to be counted. The analytic modeling in CHAPTER 2 developed a relationship between the number of abrasives in the grind wheel to the concentration number by using the analytically expected individual grit volume. This analytic relationship, shown in Equation 4.1, was used to calculate the actual wheel concentration number based on the measured number of grits. Here,  $E[N_a]$  is the expected number of abrasives,  $w$  is the wheel axial width,  $d_w$  is the wheel bond diameter,  $d_c$  is the wheel core diameter,  $\mu_D$  is the mean of the grit diameters, and  $\sigma_D$  is the standard deviation of the grit diameters.

$$E[N_a] = \frac{3Cw \left( \frac{d_w^2 - d_c^2}{4} \right)}{200\mu_D(\mu_D^2 + 3\sigma_D^2)} \quad \text{Equation 4.1}$$

The uncertainty in the calculated concentration numbers was determined using Kline-McIntock error propagation with the dimensional errors set as the  $\pm 0.9 \mu\text{m}$  repeatability

of the measurement system. The uncertainty in the measured concentration numbers was calculated to be an average of 1.08 across all measured wheels.

#### **4.4 COMPARISON OF MACHINE VISION ALGORITHM TO MANUAL INSPECTION**

A comparison of the ability of the vision algorithm to locate grit centroids was conducted by manually identifying centroids. This involved a user viewing the original image and placing identifying dots on what appeared to be the grit centroids. The differences between the machine vision centroids and the manually observed centroids highlight the ability of the vision method to separate grits effectively without eroding smaller grits from the image. The microgrinding wheels were specified to be #220 diamond grit with a 1.0 mm OD and concentration of 50.

Statistics of the axial grit spacings identified using the two methods were compared. A total of 33 non-stitched images were used from 3 different wheels for a total of 99 images. The spacings between adjacent grits within the same axial strip of the wheel were calculated for comparison. The width of the axial strip was mean grit diameter, 75  $\mu\text{m}$ . Table 4.2 presents the results from the analysis of the axial grit spacing using both the machine vision and manual inspection approaches.

**Table 4.2 - Results from machine vision and manual inspection of #220 grit, 50 concentration diamond microgrinding wheels**

<b>Method</b>	<b>Total Number of Grits</b>	<b>Axial Spacing Mean [μm]</b>	<b>Axial Spacing STD [μm]</b>	<b>C<sub>s</sub> [grits/mm<sup>2</sup>]</b>
Manual Inspection	512	91.6	52.8	13.9
Machine Vision	513	100.0	63.7	13.2

The numbers of grits found in total were almost identical. However, the mean grit spacing and its standard deviation within each strip varied slightly between the methods. Comparison between the mean measured static grit density  $C_s$  for the two methods also showed close agreement and is similar to that measured by other studies [32].

#### **4.5 MEASUREMENT OF MICROGRINDING WHEEL SPECIFICATION ACCURACY**

A thorough investigation of microgrinding wheel topography was conducted through the measurement of wheels of differing diameters, axial widths, and grit sizes as shown in the experimental plan in Table 4.3. The single manufacturer provided the target specifications for the wheel geometry along with the expected concentration number  $C$  achieved by the electroplating process.

**Table 4.3 – Experimental plan of inspected wheels**

Wheel Set #	# of replicates	G#	OD [ $\mu\text{m}$ ]	w [ $\mu\text{m}$ ]	C
1	3	#200	508	1588	140
2	3	#400	508	3175	140
3	15	#400	1016	1588	140
4	6	#800	1016	1588	140
5	3	#400	1016	3175	140
6	3	#800	1016	3175	140
7	3	#400	1524	1588	140
8	3	#200	1524	3175	140

The complete results of the measured wheel specifications are shown in Table 4.4. The most influential discrepancy between manufacturing specification and measured specification occurred with wheel sets 4 and 6 which were specified to be #800 grit. However, measurements showed them to have #400 grit. The manufacturer explained that it was not possible to electroplate finer than #400 grit so the ordered #800 wheels were merely #400 wheels that had been diamond trued in order to fracture abrasive tips so that the wheel machined surface finishes as fine as #800 wheels. This is indicated with the abrasive size #400\* in the results in Table 4.4.

**Table 4.4 – Experimentally measured specifications of microgrinding wheels**

Wheel #	Manufacturer Specifications			Measured Specifications				Measured Characteristics		K-S Test P-value	
	$\hat{G}\#$	$\hat{D}$ [ $\mu\text{m}$ ]	$\hat{w}$ [ $\mu\text{m}$ ]	$\hat{C}$	$D_{\text{shank}}$ [ $\mu\text{m}$ ]	$t_{\text{bond}}$ [ $\mu\text{m}$ ]	$w$ [ $\mu\text{m}$ ]	$C$	$N_a$		$C_s$ [ $\#/\text{mm}^2$ ]
1.1	#200	508	1588	140	326.0	47.5	1545	160.39	182	89.49	0.392
1.2					291.5	48.7	1789	140.08	172	79.28	0.642
1.3					332.2	50.8	1260	141.90	144	85.47	0.911
2.1	#400	508	3175	140	399.5	41.3	2830	177.22	989	228.51	0.127
2.2					388.1	47.0	3024	149.34	1000	217.47	0.264
2.3					396.8	45.2	2986	155.31	1005	219.92	0.866
3.1	#400	1016	1588	140	903.4	43.3	1317	136.28	798	194.78	0.142
3.2					907.2	50.1	1419	127.74	943	209.92	0.237
3.3					895.4	46.6	1459	115.93	805	177.69	0.275
3.4					921.8	40.1	1309	141.30	774	187.75	0.263
3.5					906.0	42.2	1406	130.15	794	181.50	0.807
3.6					903.4	44.8	1384	122.50	781	180.88	0.047
3.7					895.5	44.4	1581	133.42	953	195.04	0.316
3.8					900.6	42.6	1496	128.42	836	180.47	0.304
3.9					918.4	48.3	1406	105.32	749	167.07	0.146
3.10					893.4	43.4	1478	110.68	720	158.28	0.248
3.11					909.6	42.6	1432	125.59	790	176.57	0.646
3.12					912.2	43.9	1459	134.20	891	194.42	0.020
3.13					900.8	48.3	1442	106.99	767	169.74	0.136
3.14					909.6	42.4	1451	127.22	807	178.05	0.511
3.15					910.0	43.0	1454	136.09	878	193.06	0.005
4.1	#400*	1016	1588	140	954.6	42.9	1518	139.26	981	195.18	0.183
4.2					961.8	45.0	1585	110.71	862	166.94	0.640
4.3					952.2	45.4	1454	135.54	969	203.50	0.891
4.4					940.2	46.6	1731	105.28	908	154.74	0.069
4.5					940.9	48.9	1679	116.34	1025	180.49	0.083
4.6					938.6	43.9	1461	109.91	750	160.10	0.201
5.1	#400	1016	3175	140	897.2	40.2	2863	135.63	1587	180.53	0.657
5.2					909.6	37.3	2881	152.33	1678	188.48	0.486
5.3					899.4	38.8	2798	152.11	1678	186.92	0.250
6.1	#400*	1016	3175	140	932.8	44.6	2817	119.71	1592	173.43	0.776
6.2					947.3	36.7	3042	145.26	1728	174.14	0.173
6.3					942.9	33.0	2956	163.00	1680	175.36	0.549
7.1	#400	1524"	1588	140	1417.0	41.3	1227	138.18	1107	191.24	0.044
7.2					1422.3	42.2	1326	114.50	1016	161.31	0.057
7.3					1420.5	40.9	1128	116.71	853	165.22	0.089
8.1	#200	1524	3175	140	1361.7	45.2	2727	136.57	981	79.25	0.244
8.2					1337.5	52.6	2604	122.81	968	83.16	0.254
8.3					1346.9	45.4	2844	140.42	1046	81.84	0.593

An ANOVA analysis of the measured microgrinding wheel specifications examined the relationships between the specifications set by the manufacturer, or the input factors, and the measured specification errors, or responses. An example of a single relationship analysis is the impact of the nominal wheel diameter on the bond thickness as shown in Figure 4.14. The 95% confidence intervals of the estimated mean bond thickness for each group are seen to overlap one another indicating that no conclusion can be made that the mean bond thickness is different for wheels of different diameters. A Tukey-Kramer test showed that the actual probability of the mean bond thickness being different for different wheel diameters (a Type I error has occurred) is 1.9% [63]. The chosen family error rate limit for this study is chosen to be 5% so it is concluded that the bond thickness does not differ between wheels of different diameters. Similar results were seen with respect to wheel axial widths and grit size as seen in Figure 4.15 and Figure 4.16 respectively. It is concluded that the bond thickness is not definitively affected by the wheel or grit size within the range of the wheels studied.

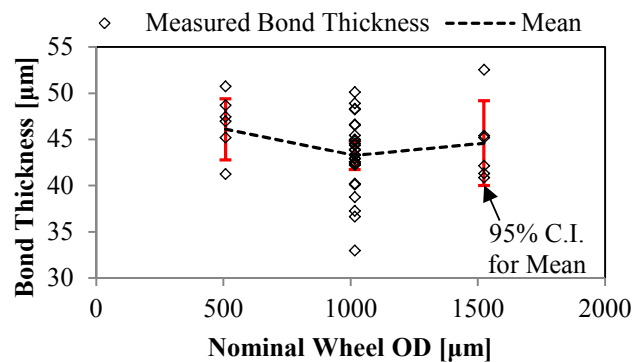


**Figure 4.14 - Bond thickness measurements showing no definite variation across different wheel diameters**

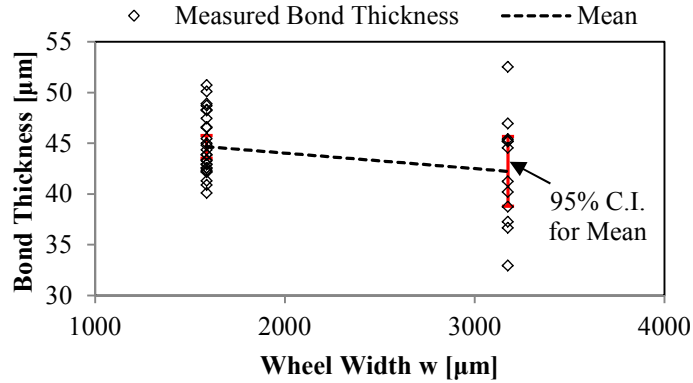


**Figure 4.15 - Bond thickness measurements showed no definite variation across different wheel widths**

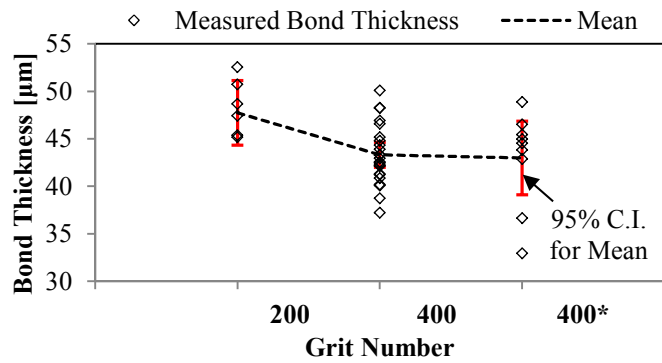


**Figure 4.16 - Bond thickness measurements showed no definite variation across different grit sizes**

The ANOVA analysis was executed to determine the impact of each factor on the wheel specification responses. The results are summarized in Table 4.5 where the response directions of the measured wheel specifications for increasing input factors are shown. Only four out of twelve interactions were seen to have significant impact according to the Tukey-Kramer test criteria. It was observed that the axial width error of the wheels decreased for larger wheels. The concentration number error also decreased for larger diameter wheels but increased for larger width wheels.

**Table 4.5 – Measured specification interactions and distribution parameters**

		Manufacturer Specification			$\mu$	$\sigma$	
		Grit #	OD	Width			
		$\hat{G}\uparrow$	$\hat{D}\uparrow$	$\hat{w}\uparrow$			
Measured Specification	Shank OD error	$\mathcal{E}_{\text{shank}} [\mu\text{m}]$	-	-	-	-5.2	10.1
	Axial Width error	$\mathcal{E}_{\text{width}} [\mu\text{m}]$	-	↓	↓	-189.6	160.6
	Bond Thickness	$t [\mu\text{m}]$	-	-	-	43.8	3.7
	Concentration # error	$\mathcal{E}_C$	-	↓	↑	-7.7	17.1

The mean and standard deviation were also calculated for each wheel specification across the entire set of wheels. An Anderson-Darling statistical test for each measured specification showed that they could each be described by a Gaussian distribution despite the four significant factor effects. An example of one of the tests is shown in Figure 4.17a with all of the measured concentration numbers falling within the envelope of error on the normal probability plot. The Anderson-Darling statistic for this particular test was 0.28 while the probability value (p-value) for the test was 63%, well above the chosen 5% threshold, indicating that the Gaussian distribution cannot be rejected as the underlying distribution of this population. Tests of the other measured wheel specifications returned similar results as seen in Figure 4.17 for the bond thickness, wheel shank diameter error, and wheel width error respectively. This allows each of them to be modeled with Gaussian distributions independent of the input factors. A summary of the mean and standard deviation of each measured wheel specification is presented in Table 4.5.

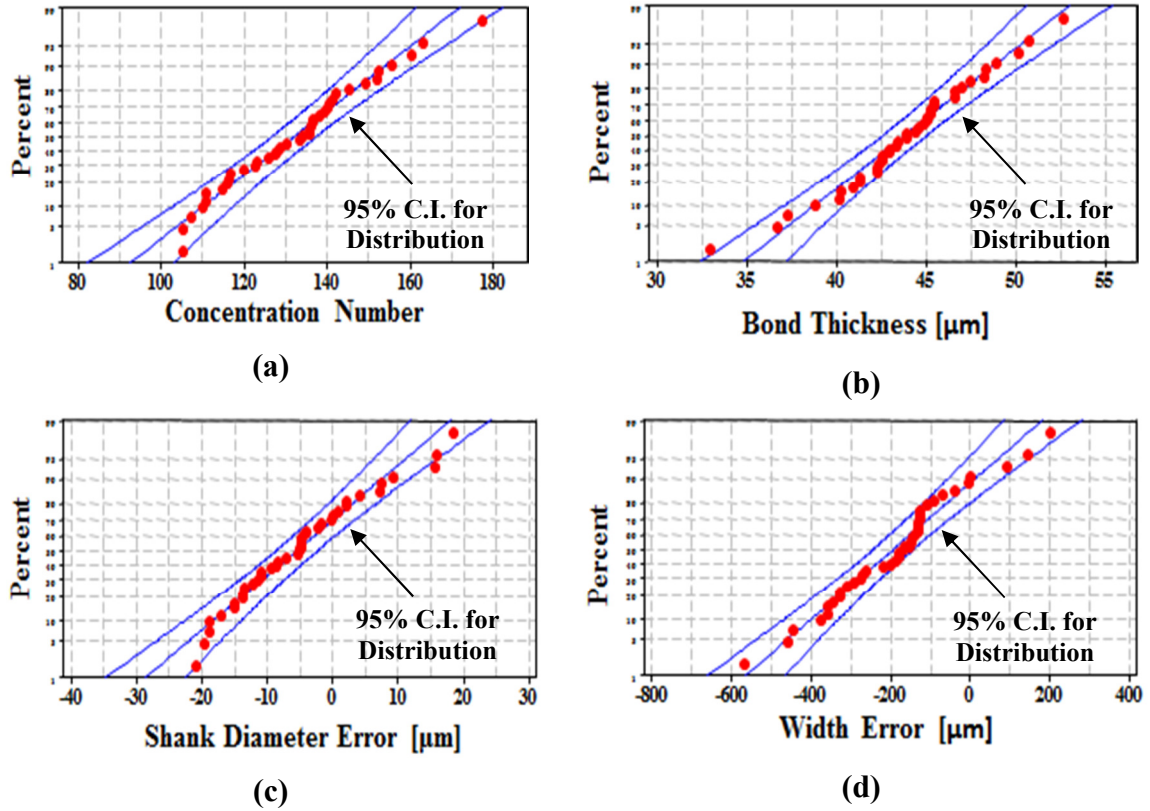


**Figure 4.17 - Normal probability plots for the measured wheel (a) concentration number, (b) bond thickness, (c) shank diameter error, and (d) wheel width error across all wheels**

## 4.6 STATIC GRIT DENSITY MODEL ACCURACY

The static grit density  $C_s$  was calculated for each measured wheel using the number of abrasives identified by the machine vision algorithm along with the measured wheel geometry specifications as shown in Equation 4.2. Here,  $t$  is the measured bond thickness. The measured number of grits and static grit density for each wheel are included in Table 4.4.

$$C_s = \frac{N_a}{\pi(D_c + 2t)w} \quad \text{Equation 4.2}$$

The accuracy of the analytic and numerical simulation models for the static wheel topography was measured by calculating the residual  $\hat{\epsilon}_i$  between the measured values and

the values from both the numerical simulation and analytic stochastic propagation models. This is shown in Equation 4.3 where  $\hat{\mu}_{c_s,i}$  is the modeled mean static grit density for wheel  $i$  and  $y_{c_s,i}$  is the measured value.

$$\hat{\varepsilon}_i = \hat{\mu}_{c_s,i} - y_{c_s,i} \quad \text{Equation 4.3}$$

The analytic and numerical simulation models show that for identical wheel geometries with identical concentration numbers, the static grit density for the separate wheels has a Gaussian distribution. The distribution of static grit densities is caused by the stochastic nature of the grit sizes and locations. The modeled value used in Equation 4.3 is the mean of the modeled static grit density distribution.

The calculated residual for each wheel for the numerical simulation and analytic models are shown in Table 4.6. The histogram of the numerical simulation residual is shown in Figure 4.18a while that for the analytic model is shown in Figure 4.18b. It is observed that both residual sets are distributed around zero but in general the numerical simulation over-estimates the static grit density while the analytic model under-estimates it.

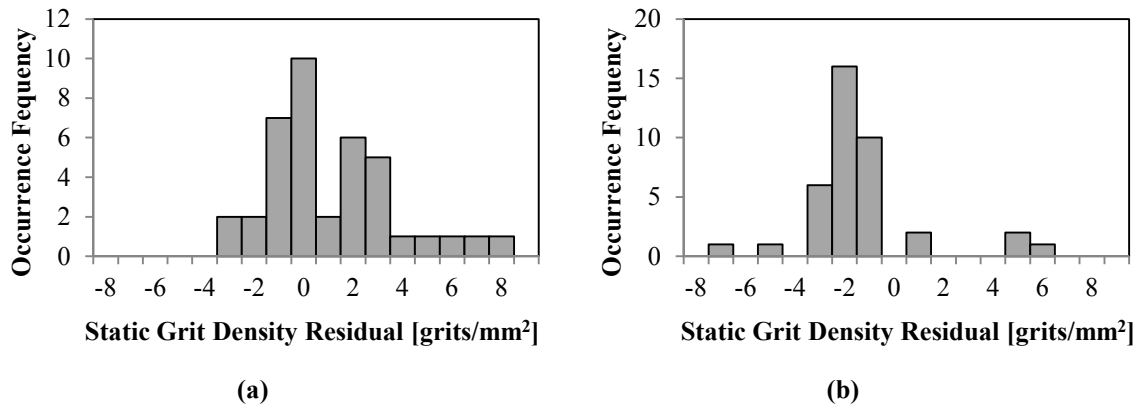


**Figure 4.18 - Histogram of static grit density residual error between experimental measurement and (a) numerical simulation model and (b) probabilistic model**

**Table 4.6 – Static Grit Density Model Residuals and Experimentally Measured Circumferential Static Grit Spacing Distribution Parameters**

Wheel #	$\hat{G}\#$	Measured Static Grit Density Residuals		Grit Spacing Loglogistic Distribution Parameters			
		Numerical Simulation Model	Probabilistic Model	Location	Scale	Location Standard Error	Scale Standard Error
1.1	#200	-0.22	-1.38	5.107	0.335	0.049	0.021
1.2		-0.37	-1.65	5.163	0.345	0.054	0.023
1.3		-1.35	-3.14	5.127	0.349	0.060	0.026
2.1	#400	2.91	-1.61	4.310	0.340	0.020	0.009
2.2		0.87	-2.06	4.335	0.342	0.020	0.009
2.3		2.14	-2.22	4.337	0.321	0.019	0.009
3.1	#400	-1.41	-3.94	4.495	0.319	0.020	0.009
3.2		-0.94	-3.00	4.416	0.346	0.021	0.010
3.3		2.65	-1.71	4.544	0.335	0.021	0.010
3.4		-2.06	-2.83	4.500	0.359	0.023	0.011
3.5		-0.96	-2.32	4.514	0.333	0.021	0.010
3.6		2.43	-2.46	4.509	0.365	0.023	0.011
3.7		-0.74	-2.98	4.449	0.333	0.020	0.009
3.8		-2.76	-2.08	4.504	0.365	0.022	0.010
3.9		1.45	-2.44	4.568	0.354	0.023	0.011
3.10		0.35	-2.66	4.622	0.349	0.023	0.011
3.11		-0.25	-2.39	4.538	0.341	0.022	0.010
3.12		-1.30	-3.09	4.477	0.328	0.020	0.009
3.13		-1.73	-2.11	4.589	0.325	0.021	0.010
3.14		1.09	-2.49	4.500	0.343	0.022	0.010
3.15		-0.04	-2.55	4.458	0.344	0.021	0.010
4.1	#400*	3.42	-1.03	4.434	0.354	0.020	0.010
4.2		-1.20	-5.24	4.612	0.329	0.020	0.009
4.3		1.83	-2.26	4.383	0.334	0.019	0.009
4.4		5.22	4.68	4.635	0.352	0.021	0.010
4.5		6.35	4.39	4.495	0.348	0.020	0.009
4.6		-0.26	-3.41	4.610	0.363	0.024	0.011
5.1	#400	-1.25	-3.65	4.498	0.356	0.016	0.007
5.2		-3.90	-3.86	4.458	0.342	0.015	0.007
5.3		7.12	5.88	4.475	0.339	0.015	0.007
6.1	#400*	1.93	0.61	4.530	0.357	0.016	0.007
6.2		2.10	-1.02	4.535	0.342	0.015	0.007
6.3		4.90	0.51	4.508	0.383	0.017	0.008
7.1	#400	1.52	-2.44	4.473	0.327	0.018	0.008
7.2		1.25	-1.04	4.629	0.345	0.020	0.009
7.3		-3.23	-7.31	4.598	0.336	0.021	0.010
8.1	#200	-0.32	-1.73	5.269	0.380	0.022	0.010
8.2		-1.20	-1.96	5.204	0.386	0.023	0.010
8.3		-0.37	-1.98	5.222	0.386	0.022	0.010

The numerical simulation and analytic model provide distributions of the static grit density caused by the stochastic nature of the grit size and locations. The deviation of the measured static grit density values from the means of these distributions could still lie within the range predicted by the model standard deviations. An investigation of this was conducted by calculating the probability that the residual between the models and measured value (or a more extreme residual) could come from the distributions provided by the models. The Gaussian distribution of the predicted static grit densities allows the use of the complimentary error function to compute the two-sided tail probability as shown in Equation 4.4. Here,  $\hat{\sigma}_{c_s,i}$  is the standard deviation of the distribution of the static grit density as predicted by the models, and  $P$  is the p-value for the two-tail test.

$$P = \text{erfc} \left| \frac{\hat{\mu}_{c_s,i} - \gamma_{c_s}}{\hat{\sigma}_{c_s,i} \sqrt{2}} \right| \quad \text{Equation 4.4}$$

The significance level selected for the test p-value test is 5%. If the value calculated using Equation 4.4 is less than 5%, then it is determined that the distribution provided by the model did not accurately predict the measured static grit density. Results showed that the numerical simulation predicted the static grit density in only 12 of the 39 wheels measured with significance greater than chance. The analytic model only predicted the value in 6 of the 39. However, there is uncertainty in the measured values of the wheel actual specifications of the concentration number, bond thickness, wheel width, and core diameter. Utilization of the uncertainties in the wheel numerical simulation and analytic models broadens the Gaussian distribution estimate of the static grit density. Incorporating this uncertainty into the models showed that static grit density was correctly predicted in all 39 wheels using both models.

## 4.7 STATIC GRIT DENSITY VARIANCE SCALE EFFECT

It is proposed that small number of abrasive grits that reside in microgrinding wheels can lead to scale effects in which there is larger wheel-to-wheel variation in the wheel topography due purely to statistical sampling. This scale effect is investigated by examining the relationship between the static grit density relative standard deviation across each wheel-set to the average number of grits in the wheels within the set. This is plotted in Figure 4.19 where it is seen that there is a definite trend towards more variation in wheels with fewer grits. The small number of wheels sampled limits the possibility of quantifying the scale effect, but it is observed that the static grit density standard deviation approaches as high as 3.6% of its mean. Analysis of the wheel specifications showed no definite dependence of the manufacturing specification errors on the number of grits in the wheel. Therefore, the dependence of the static grit density variation must be attributed to statistical effects associated with nature of small wheels with larger grit sizes.

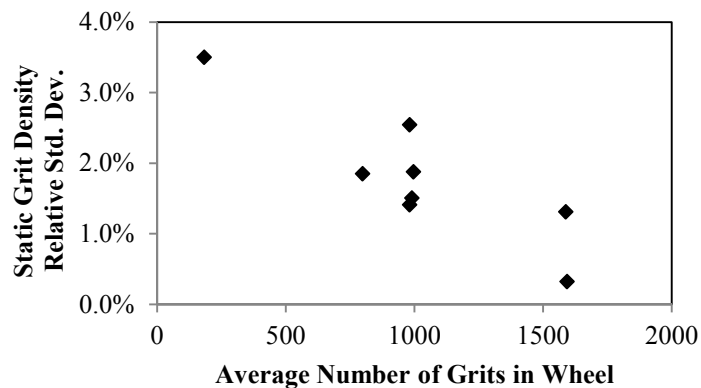


**Figure 4.19 – Potential scale effect of higher static grit density relative standard deviation in microgrinding wheels due to the few number of grits in the wheel**

## 4.8 STATIC GRIT POSITIONS

The machine vision algorithm identified individual grits and calculated their centroid locations within each image. The occurrence frequency of the grit locations was analyzed in order to validate the underlying model assumption that the grits are position probabilities are uniformly distributed in Cartesian space. The analytic model in CHAPTER 2 was based on this assumption and calculates uniformly distributed grit position in the angular and axial directions of the cylindrical coordinate system of the wheel. Therefore, the grit positions in these two cylindrical coordinates were analyzed for the 15 identical wheels comprising wheel set 3. The domain of possible locations of grit positions in the angular direction is 0 to  $2\pi$  while in the axial direction it is 0 to 1.5875mm. The occurrence frequency for the angular grit positions is shown in Figure 4.20 while that for the axial positions is shown in Figure 4.21.

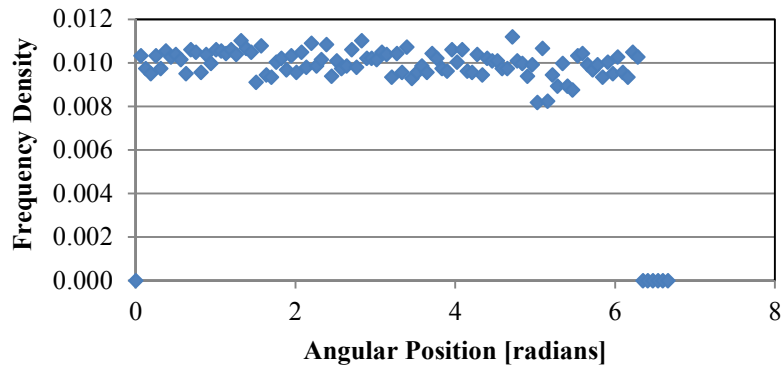


**Figure 4.20 – Occurrence frequency of angular grit position in wheel set 3**

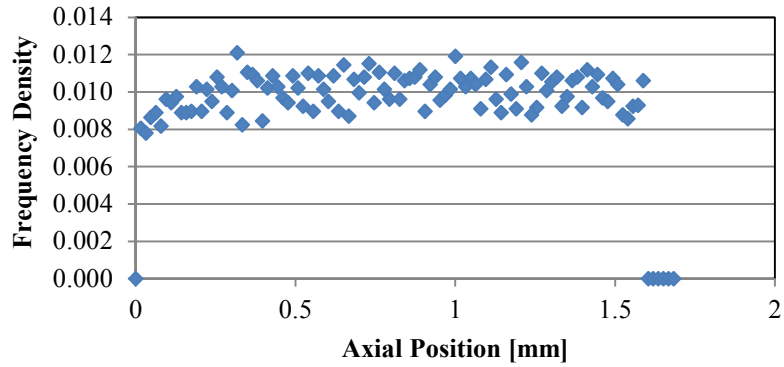


**Figure 4.21 - Occurrence frequency of axial grit position in wheel set 3**

It is observed that the occurrence frequencies are approximately uniform in both directions although there is slight divergence in the lowest axial positions. These occurrence frequencies are taken to verify the underlying assumption of uniform probability of grit positions in Cartesian space.

#### **4.9 STATIC GRIT SPACINGS**

The machine vision algorithm was used to measure the spacings between the grits in both the axial direction and the circumferential direction of the wheel. These two strip directions are shown in Figure 4.22. The spacings measured are between grits that would remove material along the same line of action in the specified direction. Therefore, the wheel surface was divided into strips in each direction with the strip widths equal to the mean grit diameter for the wheel. The spacings between sequential grits within the same strip were then calculated using the identified grit centroids from the machine vision analysis. Wheel 6.2 has the largest number of grits and grit spacings which lends it to the best visualization of the static grit spacings. A sample histogram of the measured circumferential spacings in wheel 6.2 is shown in Figure 4.23.

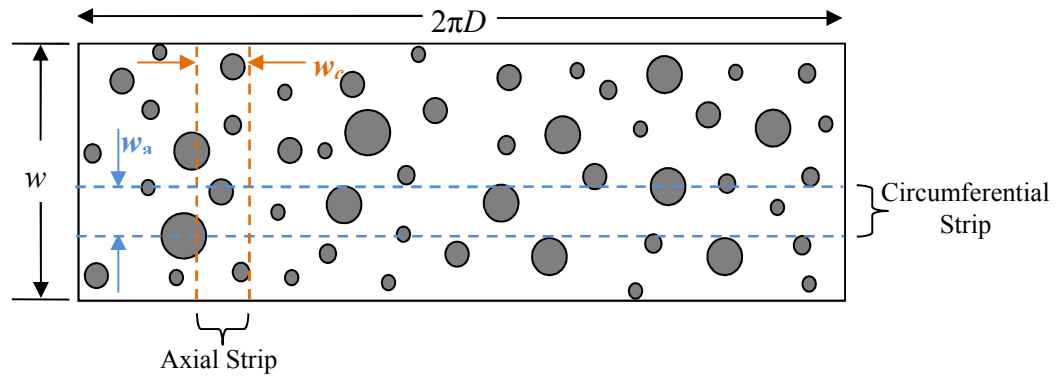


**Figure 4.22 – Measurement strips used to verify that static grit density is independent of the strip direction**

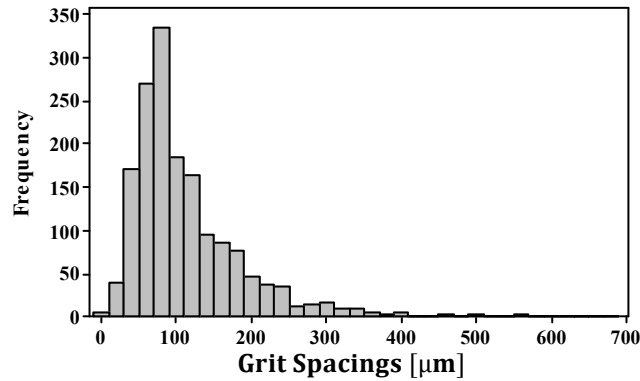


**Figure 4.23 – Histogram of the circumferential grit spacings in wheel 6.2**

Measurement of a wheel with the machine vision method facilitates grit spacing in the axial direction more easily than in the circumferential direction as there is no need for image stitching. If the spacings in the two directions, which are independent, belong to the same probability distribution, then axial spacing measurement can serve as a more efficient way to estimate the distribution in the circumferential direction which is of most interest in the modeling of grinding action. The distributions of the spacings in the two directions were tested against each other using the Kolmogorov-Smirnov test to determine if they were identical [64]. The probability-value from the test is required to be

above the 5% threshold to conclude that the samples could come from the same continuous distribution. The results of the test are shown in Table 4.4 where it is seen that 35 of the 39 wheels measured passed the test.

The distribution of the spacings was also investigated as current knowledge proposes three different distributions: exponential, gamma, and Rayleigh with the latter being the most popular as outlined in Table 2.1. The goodness-of-fit of these distributions to the measured spacings was evaluated along with two additional distributions, lognormal and loglogistic, as these exhibit similar shapes to the established distributions. The governing parameters for each distribution were estimated for the grit spacings in both directions for all of the measured wheels. Again, wheel 6.2 provides the best visualization of the distribution fitting due to its large number of grit spacings. Comparisons of the fitted distributions for wheel 6.2 are shown in Figure 4.24a for the Rayleigh and lognormal distributions and in Figure 4.24b for the Rayleigh and loglogistic distributions.

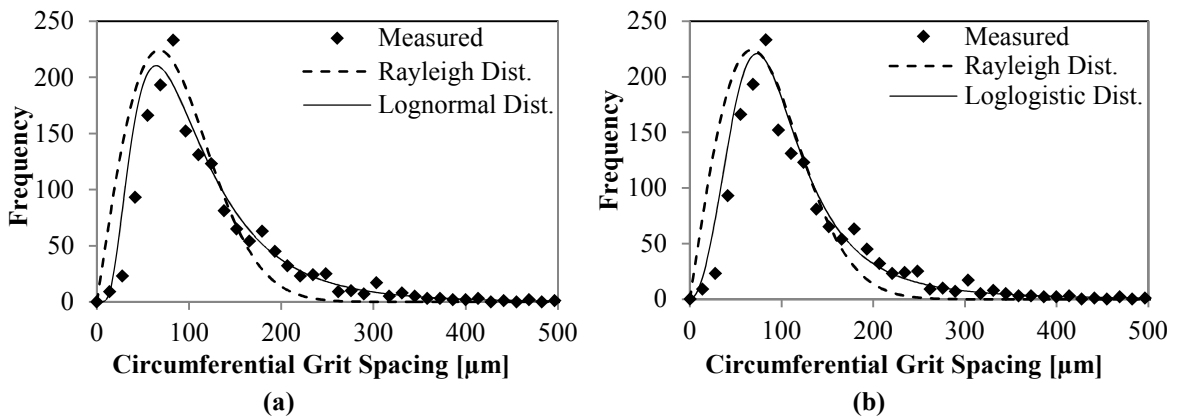


**Figure 4.24 – Frequency PDF of measured circumferential grit spacings in wheel 6.2 with fitted distribution comparison between the currently used Rayleigh distribution and proposed (a) lognormal distribution and (b) loglogistic distribution**

It is seen that both of the newly proposed distributions are improvements over the Rayleigh distribution with the loglogistic distribution marginally fitting the dataset better than the lognormal distribution graphically. The goodness-of-fit for each distribution was evaluated by calculating the p-value and Anderson-Darling statistic each fit. The Anderson-Darling statistic measures the area between the fitted distribution and cumulative data step function. The areas near the tails of the distribution are weighted more heavily providing better differentiation between similar distributions [65]. Lower Anderson-Darling statistics indicate a better goodness-of-fit evaluation for a given distribution.

The results of the distribution evaluation are shown in Table 4.7 where it is seen that of the established distributions, the gamma distribution has the best average Anderson-Darling statistic. However, the newly proposed lognormal and loglogistic distributions are seen to better describe the data with both better Anderson-Darling and p-value statistics. The two new distributions show similar potential to describe the distribution best as they split superiority between the two metrics. A third statistic, the correlation coefficient ( $R^2$ ), was calculated to differentiate the two distributions. The correlation coefficient is calculated based on the error between data and the one-to-one line of the corresponding probability plot for each distribution. It is seen that the loglogistic distribution provides better results in two of the three test statistics showing that it best describes the grit spacing probability out of the distributions examined. The estimated loglogistic distribution parameters and the associated standard errors of the parameters are tabulated for each wheel in Table 4.6.

**Table 4.7 – Grit spacing distribution results**

<b>Distribution</b>	<b>Mean Anderson-Darling Statistic</b>	<b>Mean P-value</b>	<b>Mean Correlation Coefficient <math>R^2</math></b>
Exponential	75.23	0.003	-
Gamma	7.40	0.005	-
Rayleigh	34.12	0.003	-
Lognormal	2.41	0.009	0.982
Loglogistic	2.50	0.014	0.985

#### **4.10 DISCUSSION**

The analysis of the microgrinding wheel specifications showed that there is significant error between the target values specified by the manufacturer and the values measured in the final products. The shank diameter errors can be attributed to variations in the turning process used to create the steel shanks of the grinding wheels. This source of overall uncertainty can be easily reduced by tightening the tolerances used to machine the shank. The bond thickness variation arises from the nature of the plating process governed mostly by electroplating time. The wheel width and concentration error come from the method in which the grits are adhered to the shank before the wheel is submerged for electroplating.

The comparison between the model and the measured static grit density showed that when using only the mean static grit density reported by the models, the measured static grit density residuals are as high as 7.31 grits/mm<sup>2</sup>. However, utilizing the expanded stochastic considerations in the analytic and numerical simulation models allows for a predicted distribution of values for the static grit density while accounting for the uncertainty in the measurement of the wheel specifications. The probability analysis showed that when accounting for the measurement uncertainty of the exact wheel

specifications, both the numerical simulation and probabilistic model accurately predicted the static grit density in all 39 wheels with a significance level of 5%.

The ability to use the models to predict the static grit density of microgrinding wheels can be explored by utilizing only the manufacturer-provided wheel specifications as *a priori* information. The numerical simulation model showed that the average residual between the mean static grit density predicted by the simulation and the measured values was only 0.81 grits/mm<sup>2</sup>. However, the worst *a priori* estimate was 25.3% larger than the measured value. This demonstrates that microgrinding wheel topography modeling needs metrology inspection of the wheel geometry to have any confidence in the modeled static grit density. Manufacturer specifications have errors that compound to yield a final product that deviates too significantly. Instead, distributions for the predicted errors in each manufacturer specification can be generated by a set of metrology experiments. This study showed that these distributions can be modeled as Gaussian for the manufacturer chosen.

The investigation into the statistical scale effects associated with small numbers of grits in microgrinding wheels showed that such wheels possess inherently more variation in wheel topography than larger grit population wheels. This demonstrates the need for microgrinding modeling to include stochastic descriptions to bound potential process characteristics as mere average-value do not fully capture the potential process outcomes.

The best solution for acquiring accurate static wheel topography information is *in situ* wheel measurement. The machine vision technique used in this study is easily adaptable to be performed using an inexpensive camera system in the actual microgrinding machine tool. The algorithm can quickly and autonomously provide full wheel surface

characterization or, by utilizing sampling statistics, measure only a small portion of the wheel and predict the topography characteristics. The measurement of the grit spacings in axial and circumferential directions of the grinding wheels showed that they can be modeled with the same distributions. This allows the machine vision technique to only need to measure the axial grit spacings without needing to stitch together full images of the wheel surface.

The examination of the grit spacing distributions led to the conclusion that the loglogistic distribution describes the superabrasive grit spacings better than the currently used distributions. However, examination of the statistics of the fitted loglogistic distributions showed that only 7% of the measured spacing sets had p-values large enough for 95% confidence in the distribution. Therefore the loglogistic distribution does not fully explain or capture the distribution of the grit spacings. More complex analytic modeling of the grit spacing probabilities or fitting of more complex distributions is needed to improve the model.

#### **4.11 SUMMARY**

A machine vision measurement technique has been established as a method of quickly measuring the static wheel topography on the surface of the microgrinding wheels *in situ*. The probabilistic and numerical simulation models developed in CHAPTER 2 and CHAPTER 3 provide probability distributions for the static grit density of a particular microgrinding wheel. Analysis of the static grit density values measured on the microgrinding wheels showed that the distributions provided by both the analytic and numerical simulation models accurately predicted the static grit density within a

significance level of 5%. It is important to understand that the comparison of a single measured value to a distribution of probable values can only yield the probability that the measurement did in fact come from the distribution.

The use of the models to predict the static grit density using only *a priori* manufacturer specifications was seen to have predicted static grit density errors of as much as 25.3% of the measured static grit density. This demonstrates that the accurate prediction of the distributions of the static wheel topography characteristics cannot rely on manufacturer specifications of the grind wheel geometry.

The grit spacings on the wheel surfaces were shown to be identical in the axial and circumferential directions lending the machine vision measurement method for easy implementation as *in situ* measurement of the wheel surface without the need for image stitching. The grit spacing probabilities were shown to be better described by a loglogistic distribution than the currently used Rayleigh distribution. In addition, it was shown that microgrinding wheels suffer from increased wheel topography variation due to statistical population size effects associated with the small number of abrasives involved. Future work is required to develop a comprehensive description of grit spacing probabilities.

# CHAPTER 5 – STATIC WHEEL TOPOGRAPHY SCALE EFFECTS

## 5.1 INTRODUCTION

The limited number of abrasives in microgrinding wheels is hypothesized to increase the variance in the distributions of wheel topography characteristics thereby increasing the variability in process force attributes. Results from the measurement of microgrinding wheels in CHAPTER 4 have already showed that the variability in the static grit density increases in wheels with fewer grits. This potential scale effect could be detrimental to the integrity of the microgrinding of HAR ceramic micro-features. Improved understanding of the nature of grind wheel topography at the micro-scale is needed to mitigate the possibilities of excessive depth of cut of individual grits and cutting frequencies that could dynamically excite the receptive micro-features.

The nature of increased variance in microgrinding wheels will be investigated using the analytic topography model to calculate distribution parameters in various size wheels. The scaling parameter which most impacts the topography variance is identified. Microgrinding topography measurements in CHAPTER 4 showed that microgrinding wheel specifications have large variability and deviation from manufacturer specifications. The impact of this on wheel topography distributions is explored. Finally, the ability to use *in situ* measurement of microgrinding wheels to acquire a more accurate prediction of the wheel topography is investigated.

## 5.2 REVIEW OF SALIENT LITERATURE

Limited research has been conducted on the scale effects associated with microgrinding wheels. There are multiple definitions of microgrinding but the most robust definition, put forth by Park, involves both the wheel size and process parameters. Microgrinding wheels are typically two or more orders of magnitude smaller than conventional grinding wheels as is illustrated in Figure 5.1. The microgrinding definition extends to the grinding process parameters as there are distinct workpiece interaction characteristics as is outlined in Table 5.1 [18].

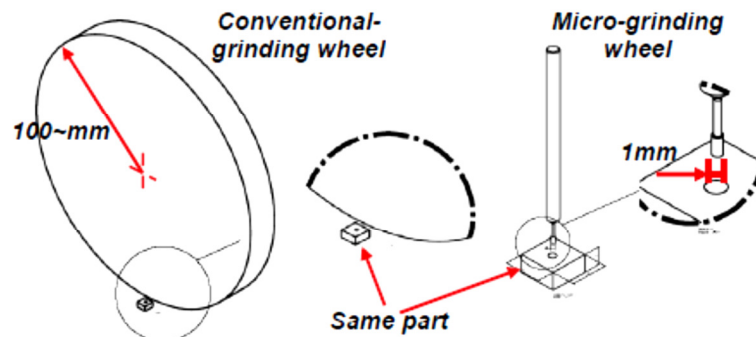


Figure 5.1 – Microgrinding as defined by the size of the grinding wheel[18]

Table 5.1 – Microgrinding as defined by distinct process characteristics[18]

	Conventional Grinding	Microgrinding
<b>Depth-of-Cut to Grit Diameter Ratio</b>	50-100	0.1-1
<b>Ploughing Effect</b>	Not Significant $\approx 0\%$	Significant $\approx 10\text{-}30\%$
<b>Interfacial Friction</b>	$\mu = \mu_c$	$\mu = \mu_c(\text{depth of cut}) + \mu_p$
<b>Chip Formation Rake Angle</b>	Constant Negative	Vairable Negative
<b>Material Removal Rate</b>	$10^0 \sim 10^1 \text{ mm}^3 / \text{mm}\cdot\text{sec}$	$10^{-1} \sim 10^{-3} \text{ mm}^3 / \text{mm}\cdot\text{sec}$

### 5.3 INVESTIGATION OF SCALE EFFECT ASSOCIATED WITH STOCHASTIC DISTRIBUTIONS USING ANALYTIC TOPOGRAPHY MODEL

The characterization of the scale effects in microgrinding wheel topography requires an investigation of the nature of static grit density as grind wheels decrease in size to the micro-scale. This can be conducted by utilizing the analytic model for the static grit density in superabrasive grinding wheels developed in CHAPTER 2. The definition of microgrinding wheel structure requires the investigation to merely vary the wheel diameter and observe the effect on the static grit density distribution. Several simplifications and assumptions must be made, however, to facilitate the study. These are summarized in Table 5.2.

**Table 5.2 – Parameters for scaling study of static grit density**

	Conventional Grind Wheel	Microgrinding Wheel
<b>Wheel Bond Diameter</b>	100 mm $\rightarrow D_g \rightarrow 0$ mm	
<b>Grit Mesh Size</b>	#100, #220, #440	
<b>Wheel Width</b>	30 mm $\rightarrow D_g \rightarrow 0.1$ mm	
<b>Fully Sampled Wheel Width</b>	$(Z_a, Z_b) = (0, w)$	
<b>Single-Layered Grits</b>	$\frac{D_g - D_c}{2} = \mu_D$	
<b>Static Grit Density Measured at Wheel Surface</b>	$R_c = \frac{D_g}{2}$	
<b>No Variance in the Total Volume of Abrasive in the Wheels (Perfect Manufacturing)</b>	$\text{Var}[V_a] = 0$	

The results of the analytic study for #220 wheels with a fixed axial width of 10mm are shown in Figure 5.2a where the expected static grit density and standard deviation of

the static grit density are shown as the outer wheel diameter is decreased. It is noticed that the expected mean static grit density decreases at the micro scale while the variation in the static grit density increases. The decrease in expected static grit density is attributed to the effects of decreasing surface area of the wheel while the increase in static grit density variance is attributed to the statistical effects.

The opposing trends in the static grit density expected mean and standard deviation can be better captured by utilizing the relative standard deviation (RSD) of the distribution as defined in Equation 5.1. The relationship between the wheel outer bond diameter and the RSD of the static grit density are shown in Figure 5.2b. Notice how microgrinding wheels have static grit density standard deviations that are up to 3% of their expected mean values.

$$RSD_{C_s} = \frac{\sqrt{\text{Var}[C_s]}}{E[C_s]} \quad \text{Equation 5.1}$$

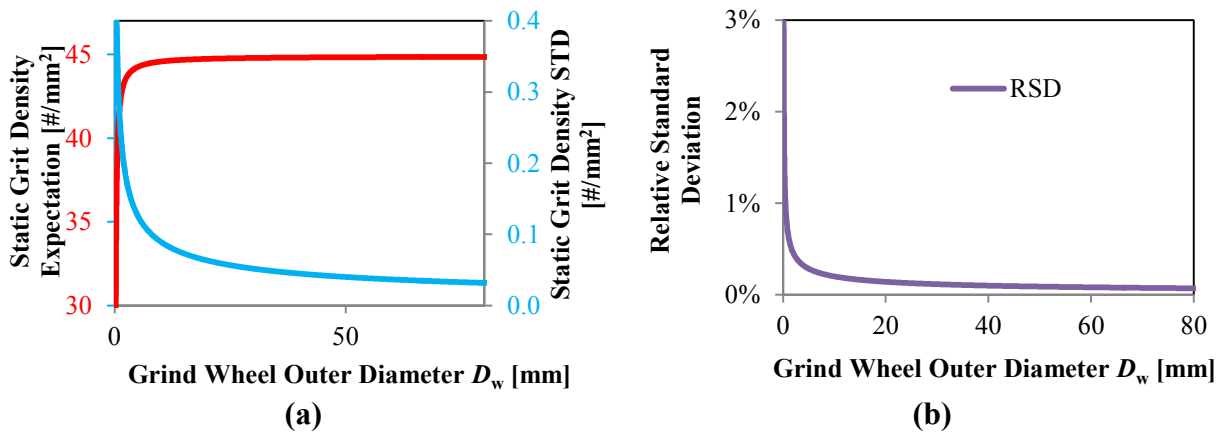


**Figure 5.2 –Variation of static grit density in #220 single-layered grind wheels as a function of the outer bond diameter formed as the (a) expectations and standard deviation and (b) as the relative standard deviation**

Another investigation into the effects of the size of the grind wheel on the static grit density can be conducted by using a constant wheel diameter but a varying grind wheel width. Figure 5.3a shows that the expected mean and standard deviation of the static grit density of a single-layered grind wheel with a fixed outer diameter of 1.0 mm and a wheel width that varies from 0.1 to 30 mm. It is seen that although the expected static grit density remains constant, the standard deviation in its distribution increases significantly as the wheel size decreases. Figure 5.3b shows that the RSD significantly increases in thin wheels as well.

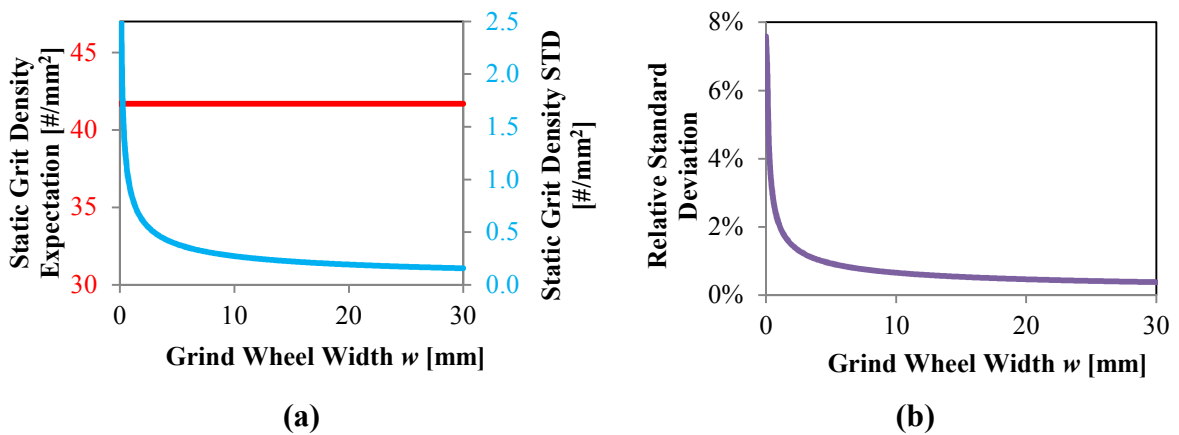


**Figure 5.3 –Variation of static grit density in #220 single-layered grind wheels as a function of the wheel width formed as the (a) expectations and standard deviation and (b) as the relative standard deviation**

It is hypothesized that the increase in the relative variation of the static grit density can be attributed to the size of the grits relative to the wheel. Figure 5.4 shows the RSD for three single-layered wheels with a 10 mm width and varying outer diameter and grit size. It is seen that both have an effect on the RSD. Increasing the grit size and decreasing the wheel diameter has a net effect of increasing the RSD. Here, the core diameter of the

wheel is adjusted for each grit size and outer diameter to maintain the single-layered wheel structure by requiring the bond thickness to be equal to the average grit diameter.

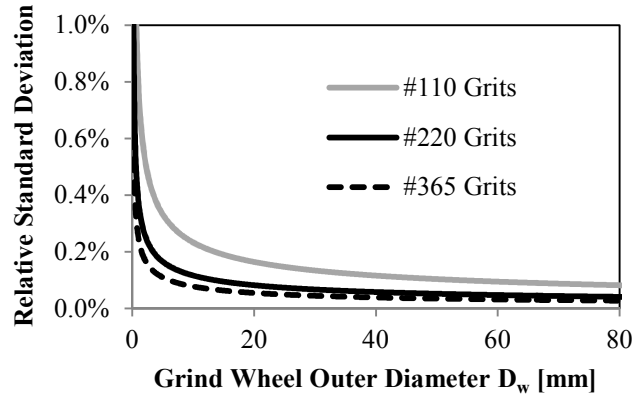


**Figure 5.4 - Variation of static grit density in single-layered grind wheels as a function of the outer bond diameter and grit size**

The RSD can also be investigated as a function of the wheel outer diameter normalized by the mean grit diameter as seen in Figure 5.5. The normalization to the mean grit diameter provides better correspondence between the wheels, but it does not completely capture the micro-scale trend.

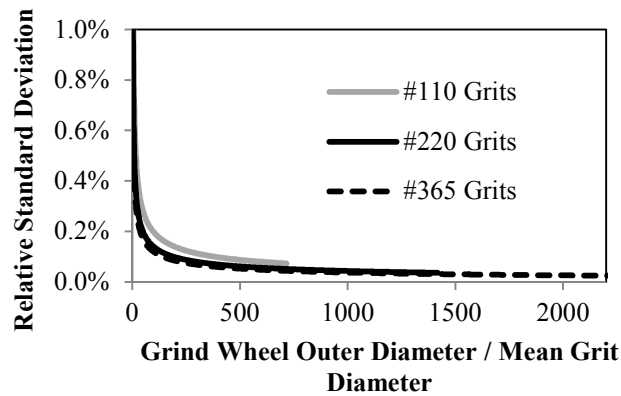


**Figure 5.5- Variation of static grit density in single-layered grind wheels as a function of the outer bond diameter divided by the mean grit diameter**

The expected number of abrasives in the wheel can also be used to normalize the RSD between different wheels as shown in Figure 5.6. It is seen that the expected number of abrasives in the wheels normalizes the RSD so that there is no dependence on abrasive size or wheel size. Therefore, this is taken to be a better scaling parameter than the standard wheel outer diameter when the scale effect of interest is the variance in the location and number of abrasives within microgrinding wheels.

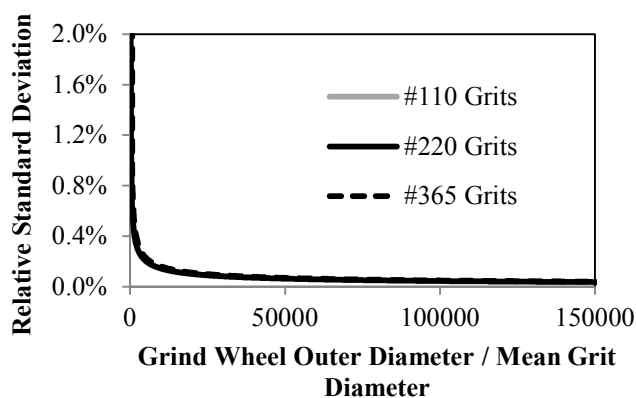


**Figure 5.6- Variation of static grit density in single-layered grind wheels as a function of the outer bond diameter divided by the mean grit diameter**

## **5.4 EFFECT OF MANUFACTURING VARIANCE AT THE MICROSCALE**

The measurement of the microgrinding wheel specifications presented in CHAPTER 4 showed that wheels that are manufactured to be identical in fact have large variability in geometry and concentration number. It is desired to know how this variability impacts the wheel topography distributions. It is hypothesized that wheel specification variability exacerbates the statistical variation in wheel topography at the micro-scale.

The scaling study has shown that the relative standard deviation of microgrinding wheel static grit density increases significantly when the expected number of abrasives in a single-layered wheel drops below 2000. However, the wheel topography has a large dependence on the expected mean and variance in the number of abrasives that are in a wheel. The manufacturer specifies a wheel concentration number which is a representation of the expected mean number of grits. However, the variance in the number of grits is not stated as a representation of how closely the manufacturing process meets the targeted concentration number.

An investigation of the effect of manufacturing variance in the concentration number can be conducted by first defining a relative standard deviation in the concentration number as shown in Equation 5.2. Combining the definition of the expected concentration number in Equation 2.8 and the analytic expectation of the number of abrasives in the grind wheel shown in Equation 2.19 yields a condensed form of the expected number of abrasives as shown in Equation 5.3.

$$RSD_c = \frac{\sqrt{\text{Var}[C]}}{E[C]} \quad \text{Equation 5.2}$$

$$E[N_a] = \frac{E[C]w\pi \left( \frac{d_w^2 - d_c^2}{4} \right)}{400E[V_i]} \quad \text{Equation 5.3}$$

The variance in the number of abrasives in a grind wheel is a function of both the expectation and variance in the number of abrasives in the wheel. This was derived in Equation 2.21 and is duplicated in Equation 5.4 for convenience. It is seen that a variance in the total volume of abrasive in the wheel needs to be derived. This can be calculated from the definition of the concentration number as shown in Equation 5.5.

$$\text{Var}[N_a] = \frac{\text{Var}[V_a] + E[N_a]\text{Var}[V_i]}{(E[V_i])^2} \quad \text{Equation 5.4}$$

$$\text{Var}[V_a] = \text{Var}[C] \left( \frac{w\pi \left( \frac{d_w^2 - d_c^2}{4} \right)}{400} \right)^2 \quad \text{Equation 5.5}$$

This can be rearranged in terms of the RSD of the concentration number using Equation 5.2 as shown in Equation 5.6.

$$\begin{aligned} \text{Var}[V_a] &= (\mathbf{RSD}_c E[C])^2 \left( \frac{w\pi \left( \frac{d_w^2 - d_c^2}{4} \right)}{400} \right)^2 = \left( \mathbf{RSD}_c \frac{E[C]w\pi \left( \frac{d_w^2 - d_c^2}{4} \right)}{400} \right)^2 \\ &= (\mathbf{RSD}_c E[N_a] E[V_i])^2 \end{aligned} \quad \text{Equation 5.6}$$

The equations can now be combined to produce a final variance in the number of grits within a wheel as shown in Equation 5.7. It is seen that the number of grits in the wheel has a variance which is the sum of the contribution from the variance in the concentration number (1st term) and from the variance in abrasive sizes (2nd term).

$$\begin{aligned} \text{Var}[N_a] &= \frac{(\mathbf{RSD}_c E[N_a] E[V_i])^2 + E[N_a]\text{Var}[V_i]}{(E[V_i])^2} \\ &= (\mathbf{RSD}_c E[N_a])^2 + \frac{E[N_a]\text{Var}[V_i]}{(E[V_i])^2} \end{aligned} \quad \text{Equation 5.7}$$

The relative standard deviation of the number of abrasives in a grind wheel can be formed using Equation 5.7 and Equation 5.4 as shown in Equation 5.8.

$$\mathbf{RSD}_{N_a} = \frac{\sqrt{\text{Var}[N_a]}}{E[N_a]} = \sqrt{\frac{(\mathbf{RSD}_c E[N_a])^2 + \frac{E[N_a]\text{Var}[V_i]}{(E[V_i])^2}}{E[N_a]^2}} = \sqrt{\mathbf{RSD}_c^2 + \frac{\text{Var}[V_i]}{E[N_a](E[V_i])^2}} \quad \text{Equation 5.8}$$

It is desired to know the impact of the variability of the static grit density as a function of the variability in the concentration number. The analytic wheel topography model calculates the expectation and variance in the static grit density as shown in Equation 5.9 and Equation 5.10 using the wheel surface area  $A_{e_r}$  and the expectation and variance in the number of grits that intersect the surface,  $N$ .

$$E[C_s] = \frac{E[N]}{A_{c_r}} \quad \text{Equation 5.9}$$

$$\text{Var}[C_s] = \frac{\text{Var}[N]}{(A_{c_r})^2} \quad \text{Equation 5.10}$$

The relative standard deviation of the static grit density can now be defined and calculated using the analytic model and relationships derived in this section. The final form of the relative standard deviation in the static grit density is shown in Equation 5.11.

$$\begin{aligned} \mathbf{RSD}_{C_s} &= \frac{\sqrt{\text{Var}[C_s]}}{E[C_s]} = \frac{\sqrt{\text{Var}[N]}}{E[N]} = \frac{\sqrt{E[N_a]\text{Var}[C] + (E[C])^2\text{Var}[N_a]}}{E(C)E[N_a]} \\ &= \sqrt{\frac{E[N_a]\text{Var}[C] + (E[C])^2\text{Var}[N_a]}{E(C)^2E[N_a]^2}} = \sqrt{\frac{\text{Var}[C]}{E(C)^2E[N_a]} + \frac{\text{Var}[N_a]}{E[N_a]^2}} \\ &= \frac{\mathbf{RSD}_c}{\sqrt{E[N_a]}} + \mathbf{RSD}_{N_a} = \frac{\mathbf{RSD}_c}{\sqrt{E[N_a]}} + \sqrt{\mathbf{RSD}_c + \frac{\text{Var}[V_i]}{E[N_a](E[V_i])^2}} \\ &= \mathbf{RSD}_c + \frac{\mathbf{RSD}_c + \mathbf{RSD}_{V_i}}{\sqrt{E[N_a]}} \end{aligned} \quad \text{Equation 5.11}$$

It is seen that the RSD in the static grit density is equivalent to the RSD in the concentration number at the conventional scale where there is a large number of abrasives in the wheel. However, as the number of grits in the wheel decreases, the RSD in the volume of an individual grit and the RSD of the probability of a grit intersecting the surface of the grinding wheel have more effect.

The calculated impact of the concentration number variability on the variability in the static grit density is difficult to visualize in Equation 5.11. Figure 5.7 shows the effect of the concentration number RSD on the static grit density RSD in #220 grinding wheels. It is seen that the RSD of the concentration number dominates the static grit density variability in conventional grind wheels. The grit density variability is not impacted by scaling effects until the expected number of abrasives reaches a very small value. Re-

examination of Equation 5.11 shows that this is caused by square root of the expected number of abrasives in the denominator of the second term.

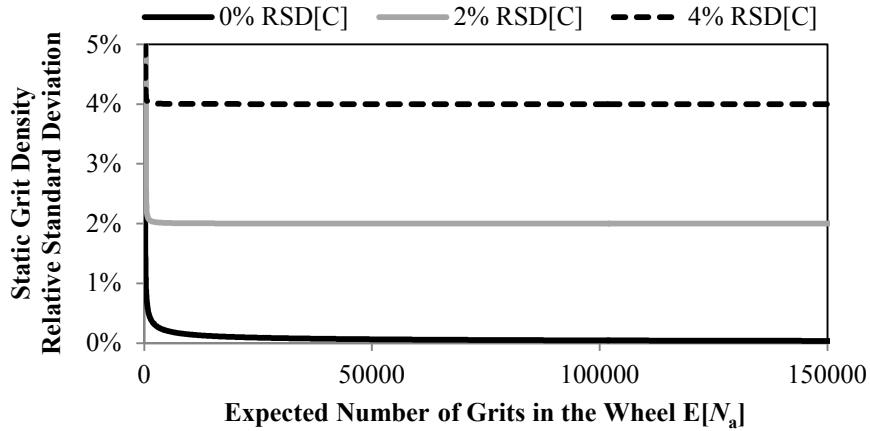


**Figure 5.7 – Effect of concentration number relative standard deviation on static grit density variance**

## 5.5 STATIC GRIT DENSITY MEASUREMENT AT THE MICROSCALE

The *in-situ* measurement of surface topography in microgrinding wheels can allow for the tuning and calibration of the probabilistic model of the wheel topography. The machine vision measurement technique presented in CHAPTER 4 samples images of individual axial segments of the microgrinding wheel. Sampling of the entire wheel surface is not necessary to obtain an accurate prediction of the surface topography and calculation of the minimum number of samples that are needed will reduce the amount time needed for measurement.

### 5.5.1 Static Grit Density Sample Measurement to Estimate Static Grit Density of a Single Wheel

Suppose that a grind wheel has a total surface area of  $A_{e_r}$  over which the total number of contained grits  $Y$  needs to be estimated. The maximum area sample size of a given measurement method can be designated as  $A_{\text{sample}}$ . The total population of independent samples that reside in the wheel can be designated as  $N$  and can be determined by Equation 5.12. For simplicity, it is assumed that the sample area is altered such that the total sample population is an integer.

$$N = \frac{A_{e_r}}{A_{\text{sample}}} \quad \text{Equation 5.12}$$

The most efficient sampling method requires that each sample taken from the wheel be independent and non-overlapping. The number of samples used to estimate the total number of grits on the surface can be designated as  $n$ . Therefore, there will be samples  $i = 1, 2, 3, \dots, n$ , each of which will yield an individual count of the number of grits  $y_1, y_2, y_3, \dots, y_n$  within its sample area. This process is designated as a “simple random sampling scheme without replacement” in that the actual sample areas used for the estimation are randomly chosen from the available population and no sample is used more than once. It has been shown through numerical simulation that the static grit density on a wheel is normally distributed. As the static grit density is proportional to the number of surface grits on a wheel by the total surface area, the total number of surface grits on the wheel is also normally distributed [45].

This process is well described in literature, and statistical descriptions of the estimation of the total number of grits  $Y$  are common knowledge [66]. The unbiased, consistent estimator of the total number of grits,  $\hat{Y}$ , is the arithmetic mean of the sample

outcomes,  $\bar{y}$ , multiplied by the population size  $N$  which is shown in Equation 5.13. This estimator is consistent in that if the total population was sampled, i.e.  $n = N$ , then  $\hat{Y} = Y$ .

$$\hat{Y} = N\bar{y} = \frac{N}{n} \sum_{i=1}^n y_i \quad \text{Equation 5.13}$$

This provides the estimate of the total number of grits. However, the variance of this estimation is also needed in order to choose the number of samples needed to reach certain accuracy in the estimation. First, the mean squared error (MSE) of the population measures the average of the square of the difference between the number of grits counted in a sample and the average of the number of grits in all samples. The MSE is designated as  $S^2$  and is shown as Equation 5.14.

$$S^2 = \frac{1}{N-1} \sum_{i=1}^N (y_i - \bar{Y})^2 = \frac{1}{N-1} \sum_{i=1}^N \left( y_i - \frac{1}{N} \sum_{i=1}^N y_i \right)^2 \quad \text{Equation 5.14}$$

However, the actual MSE of the population is not available unless the entire population is sampled. Therefore,  $S^2$  can be estimated using the unbiased estimator  $s^2$  which can be calculated according to Equation 5.15.

$$s^2 = \frac{1}{n-1} \sum_{i=1}^n (y_i - \bar{y})^2 = \frac{1}{n-1} \sum_{i=1}^n \left( y_i - \frac{1}{n} \sum_{i=1}^n y_i \right)^2 \quad \text{Equation 5.15}$$

This unbiased estimate of the population MSE can now be used to estimate the variance in the predicted total number of grits. This variance in the predicted total number of grits is shown in Equation 5.16.

$$\text{Var}[\hat{Y}] = N(N-n) \frac{s^2}{n} \quad \text{Equation 5.16}$$

The expectation and variance in the estimated total number of grits on a wheel surface assume that the prediction can be described by a normal distribution. Therefore, a confidence interval can be generated for the estimation based on a desired accuracy

probability  $1-\alpha$ . It is chosen by convention that the confidence interval CI of the estimate needs to be within 95%. This confidence interval can be generated using a student  $t$ -distribution as shown in Equation 5.17. Here,  $t_{n-1,\alpha/2}$  denotes the  $1-\alpha$  quantile of the  $t$ -distribution with  $n-1$  degrees of freedom. Values for this quantile can be found in tabulations in most statistical references.

$$P \left[ \hat{Y} - t_{n-1,\alpha/2} \sqrt{\text{Var}[\hat{Y}]} \leq Y \leq \hat{Y} + t_{n-1,\alpha/2} \sqrt{\text{Var}[\hat{Y}]} \right] = 1 - \alpha \quad \text{Equation 5.17}$$

Here, the actual total number of grits lies within a confidence half-width of the estimated total number of grits with a probability of  $1-\alpha$ . This confidence half-width  $H$  is shown in Equation 5.18.

$$H = t_{n-1,\alpha/2} \sqrt{\text{Var}[\hat{Y}]} = t_{n-1,\alpha/2} S \sqrt{N(N-n) \frac{s^2}{n}} \quad \text{Equation 5.18}$$

### 5.5.2 Sample Size to Estimate Static Grit Density of a Single Wheel

The calculation of the number of wheel surface measurement samples needed to predict the total number of abrasives requires that an accuracy half-width first be chosen. Here, it is selected that the tolerable range needs to be approximately 5% of the actual number of grits as is shown in Equation 5.19.

$$H \leq 0.05Y \quad \text{Equation 5.19}$$

However, the actual number of grits in the wheel is unknown as it is the goal of the estimation. Standard techniques involve a pre-sampling of the population in order to estimate the actual number of grits for this calculation of the number of samples needed in future sampling [67]. However, this study will utilize the numerical simulation for static grit density to investigate the effects of sampling on the estimation of the total number of grits on a wheel surface.

The numerical simulation provides an estimated number of grits on a wheel surface,  $\hat{Y}_{\text{analytic}}$ . In the case of a single-layered, #220 grit wheel with a surface diameter of 1.0mm and a width of 10 mm, the predicted static grit density is 42.31 grits/mm<sup>2</sup> and therefore  $\hat{Y}_{\text{analytic}}$  is 1,329 grits. The half-width of for 5% accuracy needs to therefore be less than 66 grits.

The confidence interval half-width is dependent on the  $t$ -distribution value with  $n-1$  degrees of freedom, the number of samples  $n$ , the population size  $N$ , and the sample variance  $s^2$ . An estimate for the sample variance can be obtained by analyzing the probability of grits on the wheel surface being located within a sample area. If the total population of i.i.d. sample areas on the wheel surface is  $N$ , then the probability of a single grit  $i$  being located within the area is  $1/N$  with the assumption that the grits are uniformly distributed across the surface as shown in Equation 5.20. The number of grits actually residing in a sample area  $y_{\text{sample}}$  is a random variable with a distribution equal to the sum of the probabilities of each grit on the wheel surface being located within the sample area. Therefore, the number of grits located in the sample is Binomially Distributed with  $Y$  total number of grits being the number of Bernoulli trials and a probability occurrence of  $1/N$  as shown in Equation 5.21.

$$P[i \in \text{sample area}] = \frac{1}{N} \quad \text{Equation 5.20}$$

$$y_{\text{sample}} \sim \sum_{i=1}^Y P[i \in \text{sample area}] = B\left(Y, \frac{1}{N}\right) \quad \text{Equation 5.21}$$

The mean and variance in the number of grits residing in a sample are given by Equation 5.22 and Equation 5.23 respectively. The ratio between the variance and the mean is given by Equation 5.24.

$$\mu_{y_{\text{sample}}} = \frac{Y}{N} \quad \text{Equation 5.22}$$

$$\sigma_{y_{\text{sample}}}^2 = \frac{Y}{N} \left(1 - \frac{1}{N}\right) \quad \text{Equation 5.23}$$

$$\frac{\sigma_{y_{\text{sample}}}^2}{\mu_{y_{\text{sample}}}} = \left(1 - \frac{1}{N}\right) \quad \text{Equation 5.24}$$

It is seen that for large values of  $N$ , the variance is approximately equal to the mean. This relationship will be used to approximate the sample variance when selecting the sample size needed to estimate the total number of grits in a wheel to within 5% accuracy.

The machine vision approach used to measure the surface topography of the microgrinding wheels has a limited field-of-view due to resolution, magnification, and distortion. It was determined that this view size is approximately 0.175 mm in the circumferential direction and 0.833 mm in the axial direction. This sample area will be used in a study to determine the number of samples that need to be taken of a grinding wheel to predict its static grit density to within 5% accuracy with 95% confidence. This study will vary the wheel and grit size in order to investigate if there are any micro-scale effects associated with the sampling.

Figure 5.8 shows the estimated number of samples needed to estimate the total number of grits on a wheel surface to within 5% with 95% confidence. Each wheel is 10 mm wide and is single-layered. It is observed that number of samples needed increases as the wheel diameter increases. This effect asymptotically decreases as the outer diameter, and therefore total number of samples available in each wheel, increase.

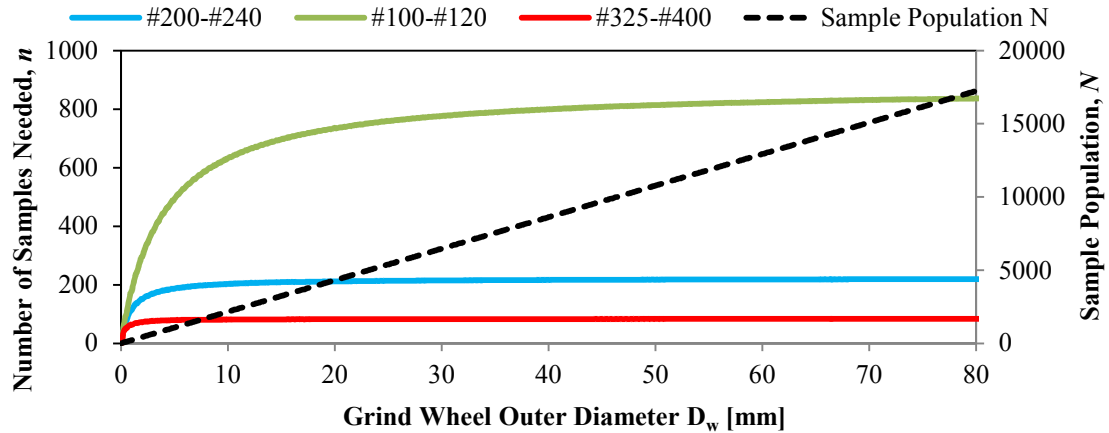


**Figure 5.8 – Total sample population and number of samples needed to estimate the total number of surface grits on single-layered grind wheels**

It is observed that the total population size increases as the wheel size increases but the total number of samples does not. A useful parameter for analyzing this effect is the sampling ratio  $f$  which is defined in Equation 5.25. The sampling ratio needed can then be used to analyze the scale effects in wheel measurement sampling. It is seen in Figure 5.9 that as the wheel diameter decreases, the sampling ratio increases. It is also observed that larger grits require a larger sampling ratio as well.

$$f = \frac{n}{N} \quad \text{Equation 5.25}$$

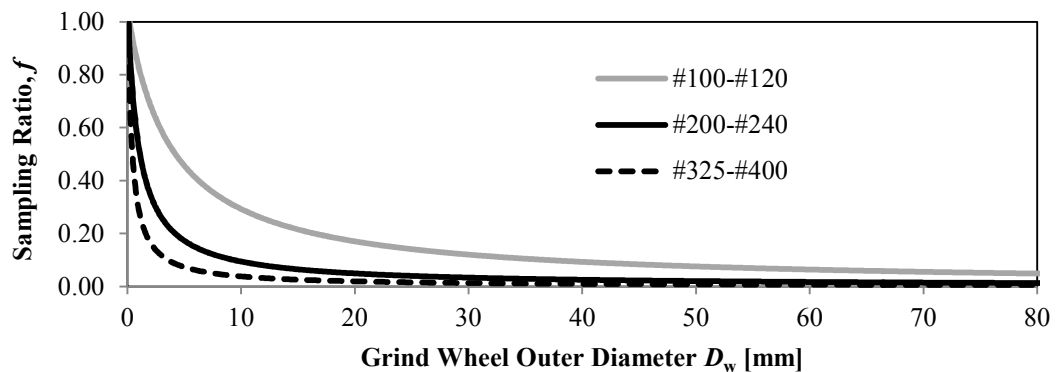


**Figure 5.9 – Sampling ratio required on varying OD single-layered grind wheels to estimate the total number of surface grits and static grit density to within 5% with 95% confidence**

A better descriptor of the scaling effect is the expected total number of grits in the wheel. This parameter captures both the wheel size and grit size. It is seen in Figure 5.10 that the sampling ratios of the three grit sizes are equalized by plotting it against the expected total number of grits in the wheels.

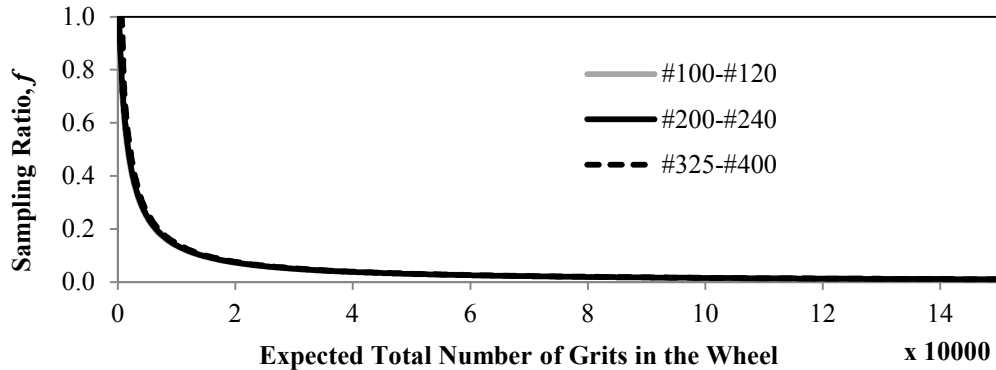


**Figure 5.10 – Sampling ratio required to estimate the total number of surface grits and static grit density to within 5% with 95% confidence**

The total number of surface grits on a grind wheel is proportional to its static grit density by the surface area. Therefore, the sampling ratio needed to maintain a 5% accuracy estimation on the static grit density is identical to that needed for total number of surface grits.

### **5.5.3 Static Grit Density Sample Measurement to Estimate Static Grit Densities across a Set of Wheels from the Same Manufacturer**

Manufacturers do not provide the variance in the concentration number causing inaccuracy in analytic prediction of the variance in the static grit density. The concentration number variance needs to be estimated from measurements in order to bound the distribution of static grit densities to a confidence interval that allows for accurate process prediction.

In this case of measuring wheels to calculate the variance in the concentration number for a given manufacturer, it is assumed that each sample is taken of an entire wheel which comes from an infinitely large population of wheels. All of the wheels in the population have the same nominal dimensions and were produced similarly from a single batch process. The sampling process under consideration will involve the full measurement of each wheel used as a sample  $i$ . Each sample  $i$  will yield a single static grit density value  $c_{si}$  for the entire wheel. The goal of the sampling is to estimate the true mean and variance of the static grit density across separate wheels within the population. Given  $n$  wheel samples, the estimated mean static grit density and the variance of that estimate are given by Equation 5.26 and Equation 5.27 respectively.

$$\widehat{C}_s = \bar{c}_s = \frac{1}{n} \sum_{i=1}^n c_{si} \quad \text{Equation 5.26}$$

$$\text{Var}[\widehat{C}_s] = \frac{s^2}{n} \quad \text{Equation 5.27}$$

The estimated static grit density variance and the variance of that estimate are given by Equation 5.28 and Equation 5.29 respectively.

$$\widehat{\text{Var}}[C_s] = s^2 \quad \text{Equation 5.28}$$

$$\text{Var}[\widehat{\text{Var}}[C_s]] = \frac{2s^4}{n-1} \quad \text{Equation 5.29}$$

The confidence interval half-width for the estimated static grit density mean is given by a student  $t$ -distribution as shown in Equation 5.30.

$$H_{\widehat{C}_s} = t_{n-1, \alpha/2} \sqrt{\widehat{\text{Var}}[C_s]} = t_{n-1, \alpha/2} \sqrt{\frac{s^2}{n}} \quad \text{Equation 5.30}$$

The confidence interval half-width can be used to calculate the number of wheels that need to be sampled in order to estimate the mean static grit density for identical wheels from the same manufacturing process. Figure 5.11 shows that the variance in static grit

density from the expected number of grits in a wheel does not affect the number of samples needed to accurately predict static grit density across different wheels. Figure 5.12 shows that the actual manufacturing variance does have a significant impact on the number of samples needed. It is seen that in general, the number of samples needed is proportional to the concentration number variance.

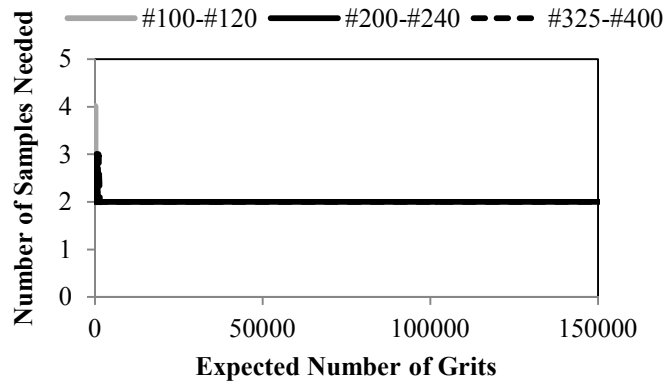


**Figure 5.11 – Effect of the number of grits in a wheel on the number of wheel measurements needed to estimate static grit density to within 5%**

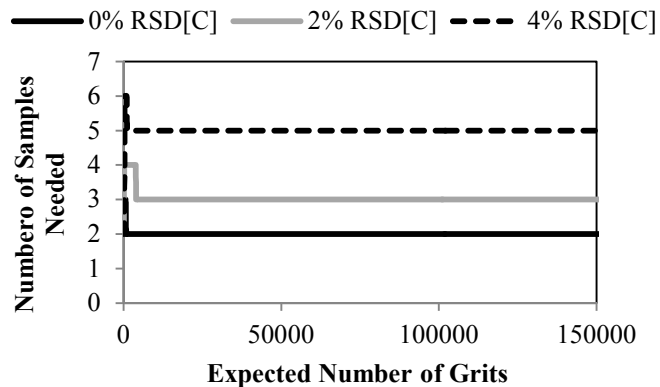


**Figure 5.12 – Effect of manufacturing variance on the number of wheel measurements needed to estimate static grit density to within 5%**

## 5.6 SUMMARY

The scale effect study identified that the wheel specification that has the most impact on wheel topography variance is the number of grits that reside in the wheel. It was seen that both static grit density mean and variance are functions of the wheel size. However, the variance in the manufactured concentration number of the wheel was seen to have a more significant impact on the topography distribution than that caused by purely statistical effects alone. Analytic calculation showed that the impact of the concentration number variance does not significantly increase in microgrinding wheels. The measurements conducted in CHAPTER 4 of the manufacturing variance in microgrinding wheels showed that wheels specified by the manufacturer to be the same have large variances in the wheel specifications. Therefore, accurate *a priori* prediction of the wheel topography distributions is not feasible without measurement of the actual wheel concentration number or at least a statistical description of its variance between wheels. The ability to use the machine vision technique of CHAPTER 4 to conduct *in situ* measurement of each grinding wheel to predict the static grit density and concentration number was investigated. It was shown that only limited sampling of the grind wheel is needed to accurately capture the pertinent parameters. However, it was shown that the proportion of the surface area of the wheel that needs to be measured to accurately predict the global static grit density and concentration number increases exponentially at the micro scale.

# CHAPTER 6 –DYNAMIC TOPOGRAPHY IN STRAIGHT TRAVERSE GRINDING

## 6.1 INTRODUCTION

Process control in the HAR microgrinding of ceramics requires accurate modeling of the probabilities of grit cutting forces and frequencies. A probabilistic model of the grinding force as a probability of its occurrence based on the statistical description of the grind wheel topography, generated using either direct measurement or advanced models, is proposed. The convolution method of Chang can be used to create a probability of the grinding force by convolving the probability of the dynamic grit density and the probability of the cutting force of an individual grit as shown in Equation 6.1 [48].

$$\Pr(f(\Phi)) = \Pr(C_d(\Phi)) * \Pr\left\{\begin{matrix} p_x(\Phi) \\ p_y(\Phi) \end{matrix}\right\} \quad \text{Equation 6.1}$$

The key link between static grits on the wheel surface and the dynamically active grits that remove material is the grit shadowing phenomenon [53]. This shadowing occurs when the path of a grit through the grind zone follows a previous grit that removed all the interfering material resulting in no interaction with the workpiece. This chapter presents a probabilistic model of the dynamic grit density in straight traverse microgrinding. This grinding approach is the one most commonly used for jig grinding arrays of micro-features. Numerical simulation is used to verify the accuracy of the probabilistic model constructed using the analytical statistical propagation technique first introduced in CHAPTER 2. An investigation into the dominant force frequencies in a microgrinding process is conducted on a micro-machining tool.

## 6.2 REVIEW OF SALIENT LITERATURE

Modeling of actual grinding forces requires knowledge of the frequency of individual cutting edges of the grind wheel as they move through the grind zone. The pioneering work of Verkerk identified that grit cutting frequency is caused by the dynamic cutting edge density,  $C_d$ , on the wheel [54]. The  $C_d$  represents the number of active cutting edges per unit area of the grind wheel that participate in material removal during a given process. The  $C_d$  is related to the static cutting edge density  $C_s$  which represents the number of cutting edges per unit area that are observed on the surface of a stationary grind wheel. The difference between the static and dynamic densities is caused by grit shadowing phenomena where one grit will kinematically shadow out the effects of the cutting edges of a subsequent grit [54].

The basic analysis of grind wheel geometry and theoretical cutting parameters of topographically uniform wheels can be found in Malkin's book as a summary of conventional grind wheel modeling [2]. The analysis addresses a surface grinding operation using the geometric and process parameters shown in Figure 6.1 where the region of detailed analysis is in the grind zone along the zone length  $l_c$ .

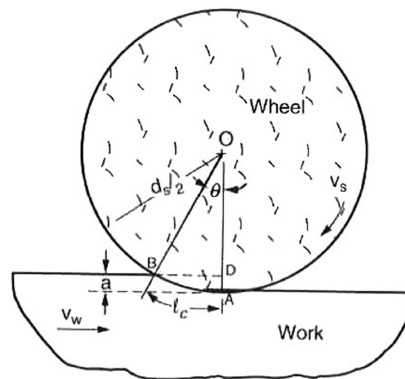
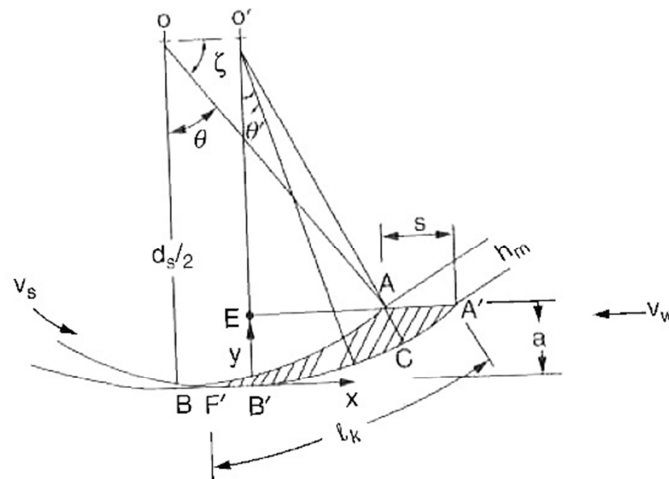


Figure 6.1 – Grinding process geometry and parameters <sup>[2]</sup>

The detailed analysis models the geometry of a removed chip when grinding with a wheel that has uniform grit diameter, protrusion height, and circumferential spacing on the wheel as seen in Figure 6.2. The model calculates the average maximum undeformed chip thickness,  $h_m$ , given the constant protrusion height of the grit from the wheel center,  $d_s/2$ , and the constant axial displacement of the wheel from the point of initial grit contact,  $O$ , and the point of exiting the grind zone,  $O'$ .



**Figure 6.2 – Single cutting chip geometry in a topographically uniform wheel** <sup>[2]</sup>

The small number of grits in microgrinding wheels requires a force model that accounts for variations in grit size, protrusion height, and spacing since the law of large numbers does not apply and the average characteristics cannot be used exclusively. Malkin presents a method for calculating the maximum undeformed chip thickness for a particular grit given its protrusion height along with the protrusion height and spacing to the next grit on the wheel. A sketch of the geometry in this calculation is shown in Figure 6.3. The sketch shows the cutting path of three consecutive grits. It is seen that the three

grits have different protrusion heights,  $a_1$ ,  $a_2$ , and  $a_3$ , in addition to different wheel advancement distances,  $s_1$  and  $s_2$ .

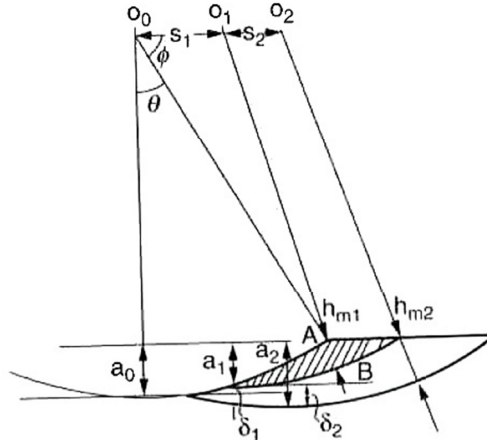


**Figure 6.3 – Maximum undeformed chip thickness of grits in a wheel with varying grit protrusion height and linear spacing [2]**

The cutting paths of the grits are modeled in a quasi-static state. The grind wheel is assumed to be fixed at a central location  $O_0$  at which the first grit,  $\theta$ , would be located at the bottom of the wheel. The wheel then rotates to move the grit along a circular path to remove a chip with maximum undeformed thickness  $h_m$ . The wheel then displaces linearly to the next central location at which the next grit would be at the bottom of the wheel. The displacement between the two central locations is designated  $s_1$  and is calculated from the wheel speed, feedrate, and angle between the consecutive grits on the wheel. A circular cutting path is then generated for grit 1 at this location. It is seen in the sketch that the variations in the grit spacing and protrusion height cause a variation between the penetration depths of each grit into the wheel designated as  $\delta$ . These parameters are all then used to calculate the maximum undeformed chip thickness for each grit,  $h_m$ . This model also allows accounting for grit shadowing since any grit with a calculated negative chip thickness is in fact removing no material.

The limitation of Malkin's grit cutting model is its limitation to the approximation of the *average* undeformed chip thickness as the goal of the model is to calculate the *average* dynamic grit density. Approximations of the variations in the wheel are made by first assuming an *average* value for the grit protrusion height. A statistical model for the dynamic grit density at a certain protrusion depth is then used to calculate the *average* number of grits along a circumferential path on the wheel that has a width equal to the average measured chip width. The *average* spacing between the grits is then calculated from the number of grits along the circumferential path and the path length itself [2].

The ability to model the total grinding force of a process requires the modeling of two distinct phenomena: the nature of the cutting parameters of the wheel on a grit-by-grit basis and the actual interaction of individual grits with material deformation and removal in the workpiece. It was reasoned by Chang that the nature of the grinding allows for the combining of the individual grit force model with the model for the number of grits cutting through the use of a convolution of the two functions over time as shown in Equation 6.1 [48]. The modeled used for each were dependent only on the position of the grind wheel in space. This is shown in Equation 6.2 where the force of an individual grit cutting is decomposed into Cartesian directions in the workpiece reference frame. The angle  $\Phi$  is the rotation angle of the wheel as it spins while  $\theta$  is the angle of an arbitrary grit within the grind zone. The rotation angle of the wheel can be transformed to a time variable by using the known wheel speed.

$$f(\Phi) = \int_0^{\pi} C_d(\Phi - \theta) \begin{Bmatrix} p_x(\theta) \\ p_y(\theta) \end{Bmatrix} d\theta = C_d(\Phi) * \begin{Bmatrix} p_x(\Phi) \\ p_y(\Phi) \end{Bmatrix} \quad \text{Equation 6.2}$$

Chang used a stationary model for the force of a single grit as a function of its position in the grind zone. This force function was calculated using an *average* value of

the maximum undeformed chip thickness, a circular cutting path, and a fixed value of specific cutting energy. This stationary model allowed Chang to measure grinding forces and convert both the stable grind signal and model into a power spectrum density. The dynamic grit density could then be obtained by comparison of the two.

A methodology of linking static grit position distributions with dynamic grit density distributions is needed to complete a single stochastic description of grinding from wheel manufacturing to workpiece material removal. Such a statistical model would allow the input of arbitrary grit size, height, and placement distributions and yield a corresponding dynamic grit distribution that is not merely a fit to a fixed distribution model. The technique would enable fast computation of wheel topography without needing numerous iterations to eliminate sampling effects. The fast modeling method would allow for rapid bounding of cutting force frequencies and magnitudes based on *a priori* information. Such a fast and robust model would facilitate improved process control techniques to address the challenges of emerging specialty grinding methods such as microgrinding.

The aim of this chapter is to generate an analytic dynamic wheel topography model for the undeformed chip thickness and dynamic grit density. This model will be based on stochastic models of the static wheel topography that are generated from *a priori* manufacturer specifications. The stochastic analytics will be verified utilizing Monte Carlo simulation that is based on the same set of fundamental specifications and static topography distributions. The grinding process modeled is straight in-feed grinding.

### 6.3 ANALYTIC MODEL OF DYNAMIC WHEEL TOPOGRAPHY

The probability of the dynamic grit density in a grinding process can be derived from the static wheel topography model by accounting grit shadowing phenomena. It is first noted that the wheel model assumes that the grits are uniformly distributed circumferentially on the wheel. Therefore, the probability of a dynamic grit density is independent of the angular position of the wheel with respect to the workpiece. The wheel model statistically predicts the number of grits in a given wheel. The probability of the number of grits in the wheel must be augmented, however, by the probability of any single grit actually participating in the grinding action by not being overshadowed by the previous grit. The dynamic grit density is therefore shown as a function  $h$  of the not-being-overshadowed probabilities as seen in Equation 6.3.

$$\Pr(C_d|d_r) = h\left(\Pr\left(\begin{array}{c} \text{any single grit not being} \\ \text{overshadowed by the previous grit} \end{array}\right)\right) \quad \text{Equation 6.3}$$

The condition necessary for a grit not to be overshadowed is presented by Malkin in the form shown in Equation 6.4. Here, the variables correspond to those in Figure 6.3.

$$\begin{aligned} \Pr\left(\begin{array}{c} \text{any single grit not being} \\ \text{overshadowed by another grit} \end{array}\right) &= \Pr\left(\begin{array}{c} \text{any single grit having} \\ \text{a positive undeformed chip thickness} \end{array}\right) \\ &= \Pr\left(\frac{\delta}{s} < 2\sqrt{\frac{a}{d_w}}\right) \end{aligned} \quad \text{Equation 6.4}$$

The displacement  $s$  of the grind wheel between consecutive grits can be obtained from the wheel speed  $V_s$ , feedrate  $V_w$ , and circumferential distance between the grits on the wheel  $L$ . This is shown in Equation 6.5.

$$\Pr\left(\begin{array}{c} \text{any single grit not being} \\ \text{overshadowed by another grit} \end{array}\right) = \Pr\left(\frac{\delta}{L} < 2\frac{V_w}{V_s}\sqrt{\frac{a}{d_w}}\right) \quad \text{Equation 6.5}$$

The condition for a grit not to be overshadowed can be obtained from the cumulative density function of the parameter  $\frac{\delta}{L}$  as seen in Equation 6.6.

$$\Pr\left(\begin{array}{l} \text{any single grit not being} \\ \text{overshadowed by another grit} \end{array}\right) = F_{\frac{\delta}{L}}\left(2\frac{V_w}{V_s}\sqrt{\frac{a}{d_w}}\right) \quad \text{Equation 6.6}$$

Individual probability distributions for the penetration depth difference  $\delta$  and the spacing between grits on the wheel surface  $L$  need to be obtained.

### 6.3.1 Probability of the Penetration Depth Difference between Two Grits

The penetration depth difference is the difference of the penetration depths  $a$  of two grits. Each grit in the wheel has contact radius  $r_c$  which designates its outermost point of contact as is depicted in Figure 6.4.

The contact radius is a random variable whose probability function can be calculated from the probability of the radial position and diameter of a grit is shown in Equation 6.7

$$r_c = r + \frac{d}{2} \quad \text{Equation 6.7}$$

The sum of such two random variables is solved through the known convolution method in which a variable transformation is made to eliminate one of the domain random variables inside the joint probability of the grit radial position and spherical radius as shown in Equation 6.8.

$$f_{R_c}(r_c) = \int_{-\infty}^{\infty} f_{R, \frac{D}{2}}\left(r_c - \frac{d}{2}, \frac{d}{2}\right) d\frac{d}{2} \quad \text{Equation 6.8}$$

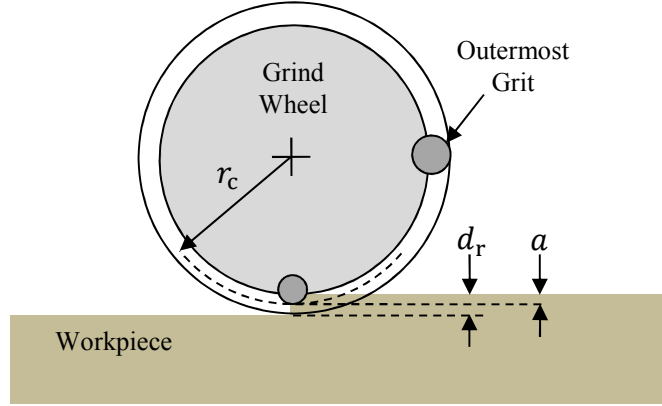


**Figure 6.4 – Grit penetration depth as defined from the radial depth of cut and position of the outermost grit**

First, the individual PDF for the spherical radius of a grit is obtained by transforming the PDF of the grit diameter as seen in Equation 6.9.

$$f_{\frac{D}{2}}\left(\frac{d}{2}\right) = \frac{1}{\frac{\sigma_D}{4}\sqrt{2\pi}} \exp\left[-\frac{1}{2}\left(\frac{\frac{d}{2} - \frac{\mu_D}{2}}{\frac{\sigma_D}{4}}\right)^2\right] = \frac{4}{\sigma_D\sqrt{2\pi}} \exp\left[-8\left(\frac{\frac{d}{2} - \frac{\mu_D}{2}}{\sigma_D}\right)^2\right] \quad \text{Equation 6.9}$$

The joint PDF of the radial position and spherical radius of a grit can then be calculated using the conditional probability of the radial position which is given in Equation 2.33. The resulting joint PDF is shown in Equation 6.10. The probability of the contact radius of any grit can now be calculated using Equation 6.11.

$$f_{R,\frac{D}{2}}\left(r, \frac{d}{2}\right) = f_R(r) f_{\frac{D}{2}}\left(\frac{d}{2}\right) = \frac{2r}{\left(\frac{D_g}{2} + \frac{4\mu_d}{10}\right)^2 - \left(\frac{D_c}{2} + \frac{\mu_d}{2}\right)^2} (F_{D_i}(2r - D_c)) \left(1 - F_{D_i}\left(\frac{10r}{4} - \frac{10D_g}{8}\right)\right) \frac{4}{\sigma_D\sqrt{2\pi}} \exp\left[-8\left(\frac{\frac{d}{2} - \frac{\mu_D}{2}}{\sigma_D}\right)^2\right] \quad \text{Equation 6.10}$$

$$f_{R_c}(r_c) = \int_{-\infty}^{\infty} f_R\left(r_c - \frac{d}{2}\right) f_{\frac{D}{2}}\left(\frac{d}{2}\right) d\frac{d}{2} \quad \text{Equation 6.11}$$

The penetration depth difference  $\delta$  between two grits is the difference between their outer contact radii as given in Equation 6.12 for random grits  $i$  and  $j$ .

$$\delta = r_{c_i} - r_{c_j} \quad \text{Equation 6.12}$$

The PDF of the penetration depth difference can be obtained by again performing a convolution method of the joint probability along with a variable transformation. Here, it is noted that the contact radii of two grits are independent of one another so their joint probability is the product of their individual probabilities. This is shown in Equation 6.13 as the final form of the PDF of the difference in penetration depth of two grits.

$$f_{\Delta}(\delta) = \int_{-\infty}^{\infty} f_{R_c, R_c}(\delta + r_c, r_c) dr_c = \int_{-\infty}^{\infty} f_{R_c}(\delta + r_c) f_{R_c}(r_c) dr_c \quad \text{Equation 6.13}$$

### 6.3.2 Probability of the Arc Length between Two Grits

The circumferential spacing between two grits on the wheel surface  $L$  needs to be obtained in order to complete an expression for Equation 6.6. The circumferential distance between two grits is only of interest in the grind zone. Since the grind wheel rotates much faster than it progresses across the workpiece, the grind zone is modeled as a circular cutting path. The radius of this cutting path is taken to be the contact radius of the outermost grit. This is shown in Equation 6.14 where the contact radius is simplified to be from a grit with an upper 95% diameter located at its minimal retainment depth in the wheel.

$$r_{\text{outermost grit}} = \frac{d_w}{2} + \frac{9}{10}(\mu_D + 3\sigma_D) \quad \text{Equation 6.14}$$

The spacing along the grinding zone arc of two individual grits  $i$  and  $j$  can be calculated using Equation 6.15. Here,  $\Delta_{\theta}$  is used to represent the angular difference between two grits.

$$L_{ij} = (\theta_i - \theta_j) r_{\text{outermost grit}} = \Delta_{\theta} r_{\text{outermost grit}} = \Delta_{\theta} \left( \frac{d_w}{2} + \frac{9}{10}(\mu_D + 3\sigma_D) \right) \quad \text{Equation 6.15}$$

The PDF of the grit spacing can be generated from Equation 6.15. First, the PDF of the difference between two grit angular positions can be calculated in Equation 6.16. It is assumed that the angular position of two grits is independent so the PDF of their positions is merely the product of the two individual PDFs. It is seen that the probability of the angular difference between two grits is uniform with the same probability of the angular position of the individual grit.

$$\begin{aligned} f_{\Delta\theta}(\Delta\theta) &= \int_{-\infty}^{\infty} f_{\theta,\theta}(\Delta\theta + \theta, \theta) d\theta = \int_{-\infty}^{\infty} f_{\theta}(\Delta\theta + \theta) f_{\theta}(\theta) d\theta = \int_{-\infty}^{\infty} \left(\frac{1}{2\pi}\right) \left(\frac{1}{2\pi}\right) d\theta \\ &= \int_0^{2\pi} \frac{1}{4\pi^2} d\theta = \frac{1}{2\pi} \end{aligned} \quad \text{Equation 6.16}$$

The PDF of the arc length between two grits along the contact radius of the grind wheel can now be generated using variable transformation as shown in Equation 6.17.

$$\begin{aligned} f_L(l) &= F_L(l) \frac{d}{dl} = \Pr\{L \leq l\} \frac{d}{dl} = \Pr\left\{\Delta\theta \left(\frac{d_w}{2} + \frac{9}{10}(\mu_D + 3\sigma_D)\right) \leq l\right\} \frac{d}{dl} \\ &= \Pr\left\{\Delta\theta \leq \frac{l}{\left(\frac{d_w}{2} + \frac{9}{10}(\mu_D + 3\sigma_D)\right)}\right\} \frac{d}{dl} = F_{\Delta\theta}\left(\frac{l}{\left(\frac{d_w}{2} + \frac{9}{10}(\mu_D + 3\sigma_D)\right)}\right) \frac{d}{dl} \\ &= \int_0^{\frac{l}{\left(\frac{d_w}{2} + \frac{9}{10}(\mu_D + 3\sigma_D)\right)}} f_{\Delta\theta}(x) dx \frac{d}{dl} = \frac{\left(\frac{d_w}{2} + \frac{9}{10}(\mu_D + 3\sigma_D)\right)}{2\pi} \frac{d}{dl} \\ &= \frac{1}{2\pi \left(\frac{d_w}{2} + \frac{9}{10}(\mu_D + 3\sigma_D)\right)} \end{aligned} \quad \text{Equation 6.17}$$

### 6.3.3 Probability of a Grit Not Being Overshadowed

An expression can now be generated for the probability of a grit not being overshadowed by another in the wheel as needed for Equation 6.6. First, the CDF of the ratio between the difference of penetration depths and arc length between any two grits in the wheel can be calculated from its PDF as shown in Equation 6.18.

$$F_{\frac{\Delta}{L}}\left(\frac{\delta}{l}\right) = \int_{-\infty}^{\frac{\delta}{l}} f_{\frac{\Delta}{L}}(x) dx \quad \text{Equation 6.18}$$

Next, the PDF of the ratio is calculated using the individual PDFs of the difference of penetration depths and arc length between any two grits in the wheel which is shown in Equation 6.19. Here, the substitution  $z = \frac{\delta}{l}$  is made for simplicity.

$$\begin{aligned} f_{\frac{\Delta}{L}}\left(\frac{\delta}{l}\right) &= f_{\frac{\Delta}{L}}(z) = \int_{-\infty}^{\infty} |l|f_{\Delta,L}(\delta, l)dl = \int_{-\infty}^{\infty} |l|f_{\Delta,L}(zl, l)dl = \int_{-\infty}^{\infty} lf_{\Delta}(zl)f_L(l)dl \\ &= \frac{1}{2\pi\left(\frac{d_w}{2} + \frac{9}{10}(\mu_D + 3\sigma_D)\right)} \int_{-\infty}^{\infty} lf_{\Delta}(zl)dl \end{aligned} \quad \text{Equation 6.19}$$

The probability of a grit not being overshadowed is again shown in Equation 6.20. The inequality must now be evaluated using an evaluation parameter that is a function of the wheel geometry, process parameters, and grit penetration depth  $a$  which is a random variable. This evaluation parameter will be simplified into a new random variable  $a'$  which is defined in Equation 6.21.

$$\Pr\left(\begin{array}{c} \text{any single grit not being} \\ \text{overshadowed by the previous grit} \end{array}\right) = \Pr\left(\frac{\delta}{L} < 2\frac{V_w}{V_s}\sqrt{\frac{a}{d_w}}\right) \quad \text{Equation 6.20}$$

$$a' = 2\frac{V_w}{V_s}\sqrt{\frac{a}{d_w}} \quad \text{Equation 6.21}$$

The definition of this penetration depth  $a$  is shown in Figure 6.4 and its calculation is shown in Equation 6.22. The evaluation parameter  $a'$  can now be written in terms of the random variable  $r_c$  which has a known PDF calculated in Equation 6.11.

$$a = d_r - (r_{c_{\text{outermost grit}}} - r_c) = d_r - \left(\frac{d_w}{2} + \frac{9}{10}(\mu_D + 3\sigma_D) - r_c\right) \quad \text{Equation 6.22}$$

$$a' = g(a) = 2\frac{V_w}{V_s}\sqrt{\frac{d_r - \left(\frac{d_w}{2} + \frac{9}{10}(\mu_D + 3\sigma_D) - r_c\right)}{d_w}} \quad \text{Equation 6.23}$$

The CDF of  $a'$  can now be calculated using Equation 6.24, and its PDF can be calculated using Equation 6.25.

$$F_{A'}(a') = F_{R_c}(g^{-1}(a')) = F_{R_c}\left(d_w\left(\frac{V_s a'}{2V_w}\right)^2 - d_r + \frac{d_w}{2} + \frac{9}{10}(\mu_D + 3\sigma_D)\right) \quad \text{Equation 6.24}$$

$$f_{A'}(a') = F_{A'}(a') \frac{d}{da'} \quad \text{Equation 6.25}$$

The probability of a grit not being overshadowed can now be calculated using Equation 6.26. The random variable  $A_g$  is introduced to represent this probability of a grit being active.

$$\Pr\left(\begin{array}{c} \text{any single grit not being} \\ \text{overshadowed by the previous grit} \end{array}\right) = \Pr(A_g) = \Pr\left(\frac{\delta}{L} < a'\right) = \int_{-\infty}^{\infty} F_{\frac{\delta}{L}}(a') f_{A'}(a') da' \quad \text{Equation 6.26}$$

The distribution of the probability of a grit being active is a Bernoulli trial whose expectation and variance are given by Equation 6.27 and Equation 6.28 respectively.

$$E(A_g) = \Pr(A_g) \quad \text{Equation 6.27}$$

$$\text{Var}(A_g) = \Pr(A_g) (1 - \Pr(A_g)) \quad \text{Equation 6.28}$$

### 6.3.4 Dynamic Grit Density using the Probability of a Positive Chip Thickness

This dynamic grit density is defined in Equation 6.29 as the number of dynamically active grits  $N_d$  divided by the wheel surface area  $A_{c_r}$ .

$$C_d = \frac{N_d}{A_{c_r}} = \frac{\# \text{ of active grits}}{A_{c_r}} = \frac{h(A_g)}{A_{c_r}} \quad \text{Equation 6.29}$$

The probability of any individual grit intersecting the cylindrical surface is a Bernoulli trial in this model since each trial has either a success or failure outcome and the outcome for each grit is independent of the outcome of the other grits. The number of grits that reside in the wheel that have a success in not being overshadowed can be represented by another random variable  $N_d$ . The dynamic grit density can therefore be represented as a function of this new random variable as shown in Equation 6.30.

$$\Pr(C_d = c_d) = \frac{\Pr(N_d = n_d)}{A_{c_r}} \quad \text{Equation 6.30}$$

The random variable  $N_d$  can be described as the sum of independent, identical Bernoulli trials. This distribution is therefore an ordinary Binomial Distribution [48]. The probability mass function for this variable is shown as Equation 6.31. Here, each  $\Pr(A_g)$  within the summation is the probability that a particular grit  $i$  actively removes material. Notice that this distribution is contingent on the condition of a known number of abrasives in the wheel. The expectation and variance are given by Equation 6.32 and Equation 6.33.

$$\begin{aligned} \Pr(N_d = n_d | N_a) = f(n_d | N_a) &= \binom{N_a}{n_d} \Pr(A_g)^{n_d} (1 - \Pr(A_g))^{N_a - n_d} \\ &= \frac{N_a!}{n_d! (N_a - n_d)!} \Pr(A_g)^{n_d} (1 - \Pr(A_g))^{N_a - n_d} \end{aligned} \quad \text{Equation 6.31}$$

$$E[N_d | N_a] = N_a E(A_g) \quad \text{Equation 6.32}$$

$$\text{Var}[N_d | N_a] = N_a E(A_g) (1 - E(A_g)) \quad \text{Equation 6.33}$$

The distribution of the number of grits participating regardless of the number of grits in the wheel is obtained by utilizing the definition of the conditional probability as shown in Equation 6.34.

$$\Pr(N_d = n_d) = f(n_d) = \int_{-\infty}^{\infty} f(n_d, N_a) dN_a = \int_{-\infty}^{\infty} f(n_d | N_a) f(N_a) dN_a \quad \text{Equation 6.34}$$

The expectation of the number of active grits independent of the exact number of grits in the wheel can be calculated by the double expectation. This is shown in Equation 6.35. Similarly, the variance in the number of active grits is given by Equation 6.36.

$$\begin{aligned} E[N_d] &= E[E[N_d | N_a]] = \int_{-\infty}^{\infty} E[N_d | N_a] f(N_a) dN_a = \int_{-\infty}^{\infty} N_a E(A_g) f(N_a) dN_a \\ &= E(A_g) \int_{-\infty}^{\infty} N_a f(N_a) dN_a = E(A_g) E[N_a] \end{aligned} \quad \text{Equation 6.35}$$

$$\text{Var}[N_d] = E[N_a] \text{Var}[A_g] + (E[A_g])^2 \text{Var}[N_a] \quad \text{Equation 6.36}$$

The expectation and variance in the dynamic grit density can now be calculated using Equation 6.37 and Equation 6.38.

$$E[C_d] = \frac{E[N_d]}{A} \quad \text{Equation 6.37}$$

$$\text{Var}[C_d] = \frac{\text{Var}[N_d]}{A^2} \quad \text{Equation 6.38}$$

## 6.4 ANALYTIC DYNAMIC GRIT DENSITY MODEL RESULTS

The analytic model for the probability of dynamic grit densities in grinding wheels provides a method to quickly predict not only mean dynamic grit densities but also its variance for a given traverse grinding process. The expectation and variance in the number of grits in a grinding wheel are needed in the calculation of the dynamic grit density. A summary of the necessary steps for calculating this is shown in Figure 2.5. A summary of the necessary steps for calculating the probability of the dynamic grit density of a grinding process is presented in Figure 2.16.

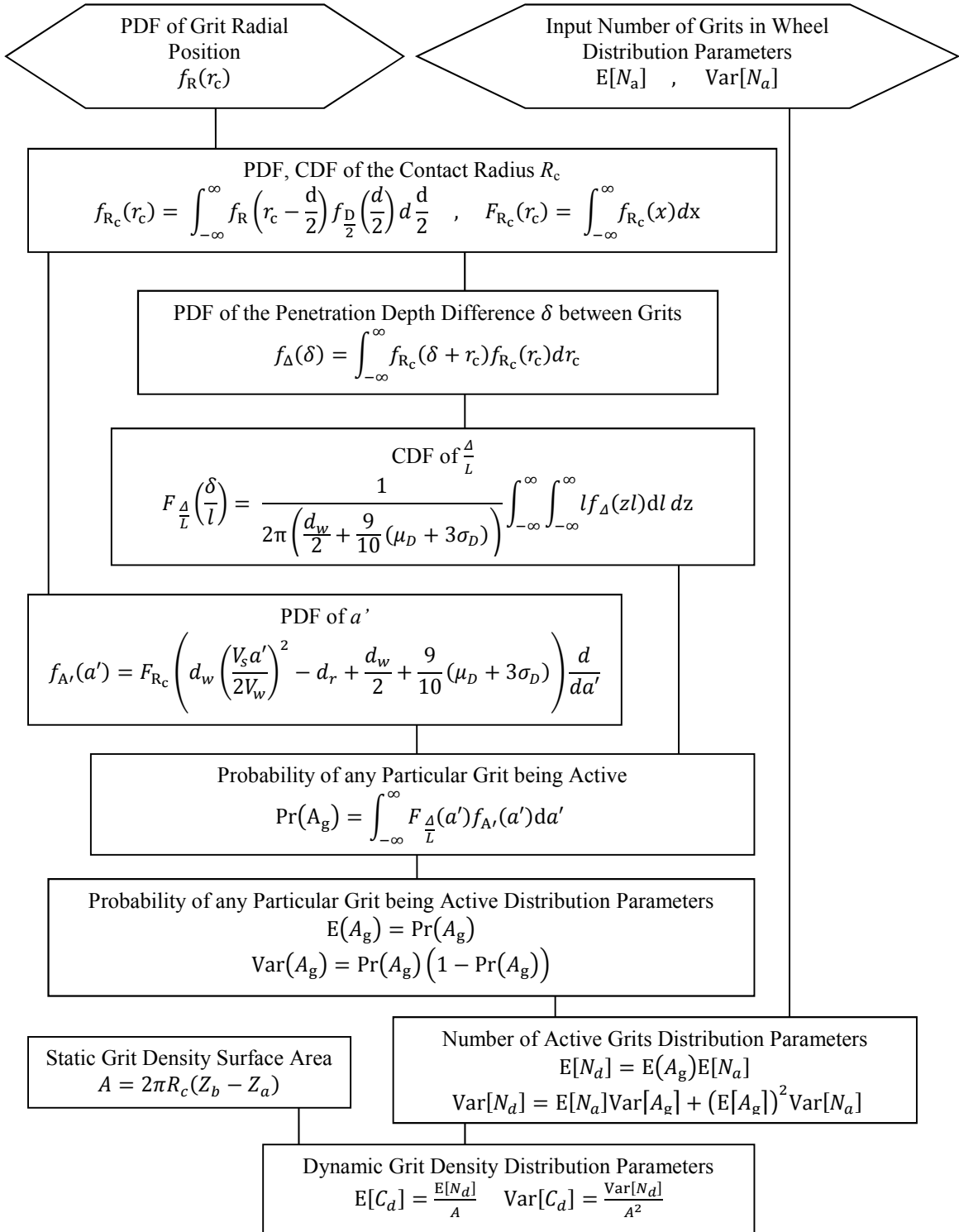


**Figure 6.5 – Summary of analytical calculation of number of grits in a grinding wheel**

A sampling of the expected dynamic grit density for a #220 grit microgrinding wheel with a 1mm OD is shown in Figure 6.6a while the variance is shown in Figure 6.6b. Here, the spindle speed is 10 krpm while the feedrate is varied. Figure 6.7 shows the same setup except the feedrate is fixed at 40 mm/sec and the spindle speed is varied.

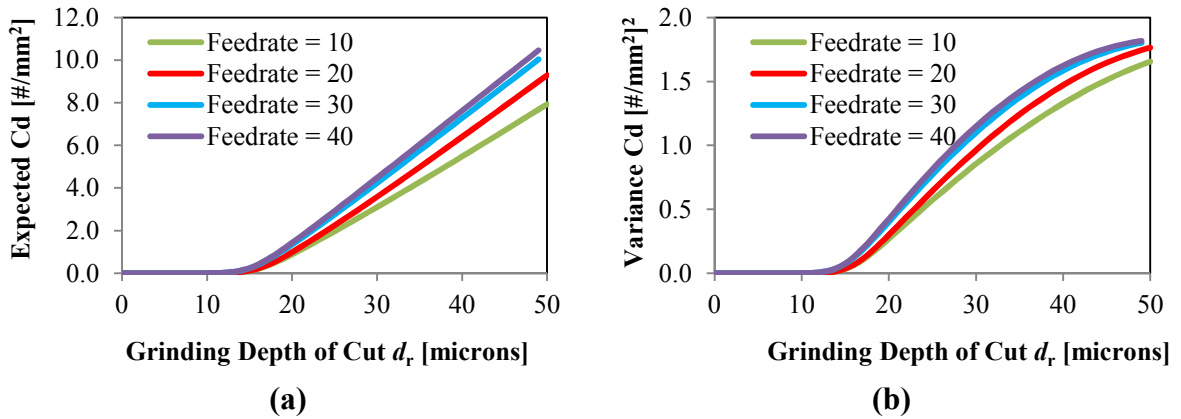


**Figure 6.6 – Analytically calculated  $C_d$  (a) expectation and (b) variance for a #220, 1mm OD wheel operating at 10 krpm (feedrate in mm/sec)**

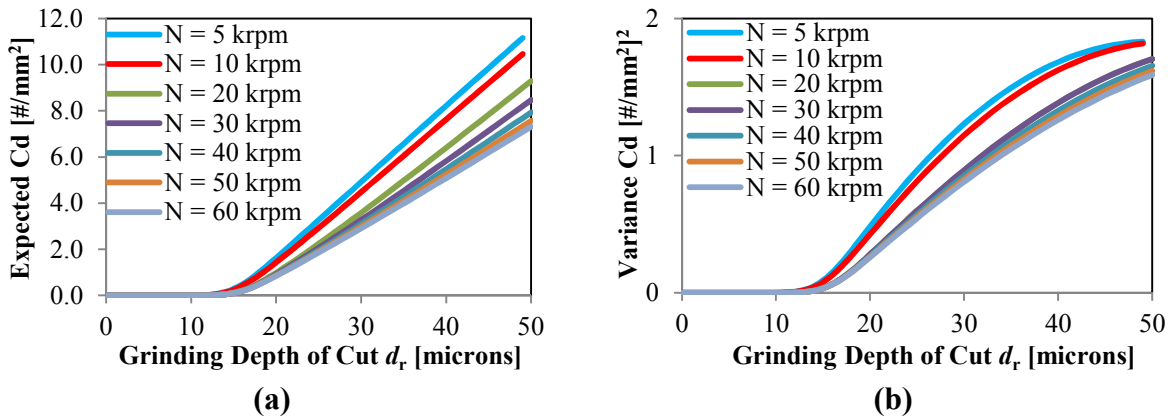


**Figure 6.7 – Analytically calculated  $C_d$  (a) expectation and (b) variance for a #220, 1mm OD wheel operating at a 40 mm/sec feedrate**

## **6.5 NUMERICAL SIMULATION OF STRAIGHT TRAVERSE GRINDING**

Numerical simulation will be used to verify the accuracy of the analytic statistics in the model of the dynamic grit density distribution parameters in straight traverse grinding. The numerical simulation presented is designed to first replicate the assumptions made to construct the analytic grinding force model. This will begin with a simulated wheel that is created using the algorithm presented in CHAPTER 3 where grits are allowed to overlap which matches the analytic model assumptions. Simulation will also be conducted using the grit relocation technique to allow investigation of the impact of the assumption of uniform grit distribution independent of other grits.

### **6.5.1 Simulation Algorithm**

The algorithm used to simulate the grinding action of a single wheel is shown in Figure 6.8.

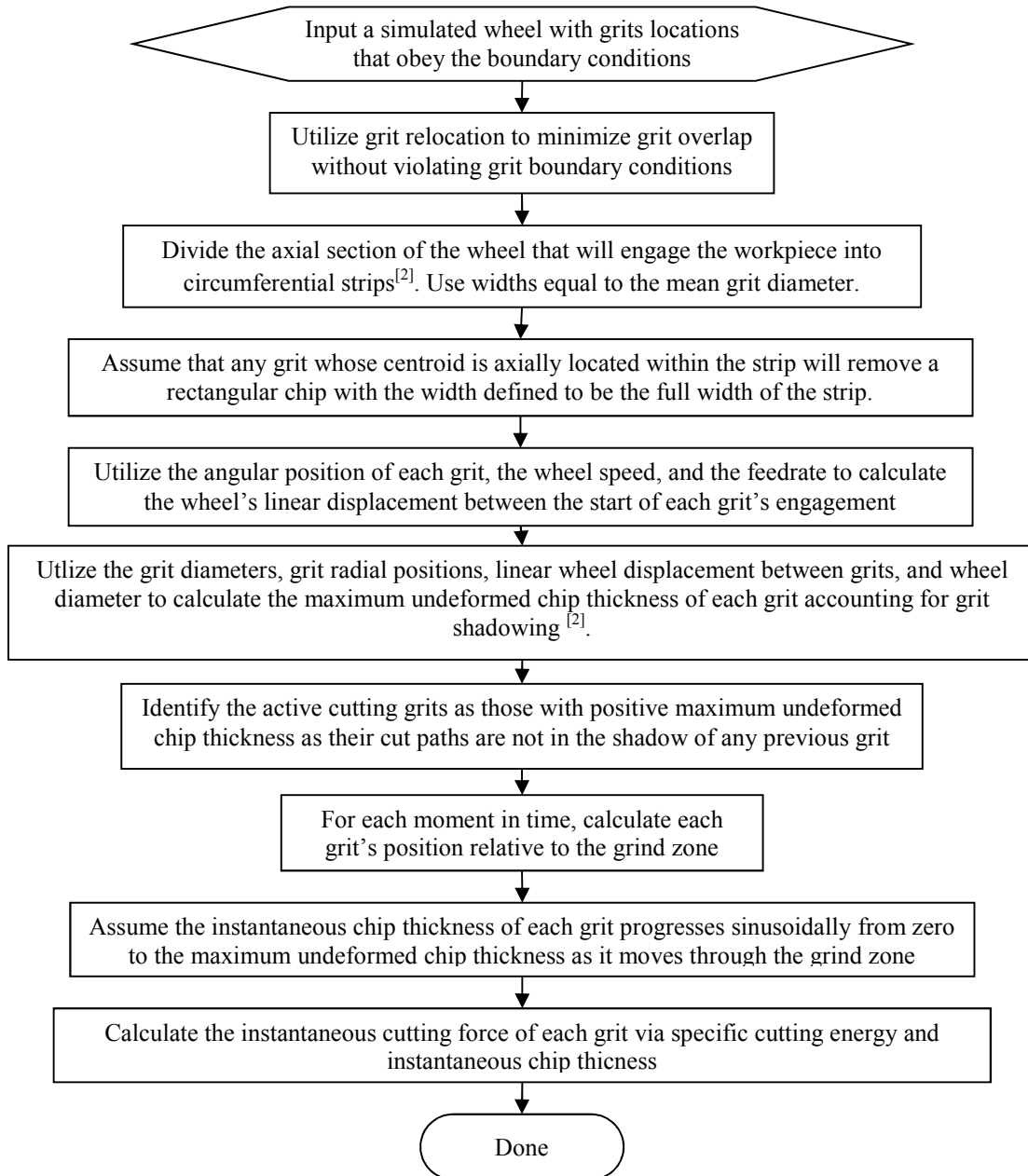


**Figure 6.8 – Algorithm to simulating the grind action of a single wheel**

### 6.5.2 Dynamic Grit Density Distribution Statistics

The numerical simulation first provides a validation of the analytic statistics for the prediction of the dynamic grit density distribution parameters. Figure 6.9a shows the comparison between the dynamic grit density predicted by the analytic model and that

from 1,000 simulations of a #220 grit, 1mm OD microgrinding wheel without the grit relocation algorithm. The selected spindle speed is 10 krpm and the feedrate is 40 mm/sec. It is observed that the analytic model predicts the dynamic grit density mean and variance very accurately.

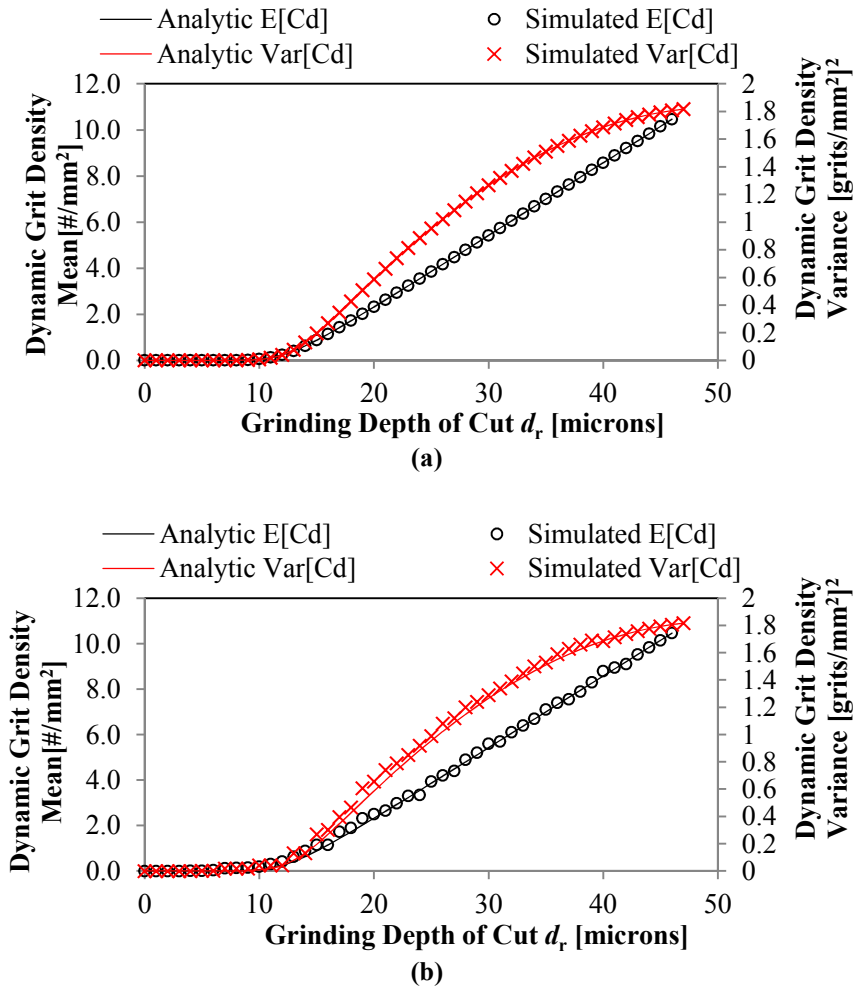


**Figure 6.9 – Comparison of the dynamic grit density mean and Std. Dev. as predicted by the analytic model and (a) numerical simulation with overlapping grits and (b) numerical simulation with grit relocation**

The simulation algorithm was also executed using the grit relocation technique to reduce overlap. The result of the dynamic grit density calculation is shown in Figure 6.9b

with a comparison to the analytic model prediction. It is observed that the relocation of the grits did alter the dynamic grit density mean and variance. The relocation of the grits served to slightly increase the mean and variance overall. This can be attributed to the algorithm moving more grits to outer surface of the wheel. Also, evidence is seen of statistical sampling effects in the non-smooth nature of the simulated profiles.

### 6.5.3 Dynamic Grit Density Probability Distribution

The probabilistic model provides a method to estimate the distribution parameters of the dynamic grit density. However, the model does not provide any information as to the form of the distribution itself. However, the Monte Carlo numerical simulation presented here does provide an occurrence frequency profile which can be used to determine an appropriate distribution. Figure 6.10 shows the cumulative occurrence frequency of the dynamic grit density in the numerical simulation at the wheel surface. The Gaussian fit was generated using the estimated mean and standard deviation from the data set. The Gaussian distribution appears to describe the dynamic grit density well which mirrors what was found for the static grit density.

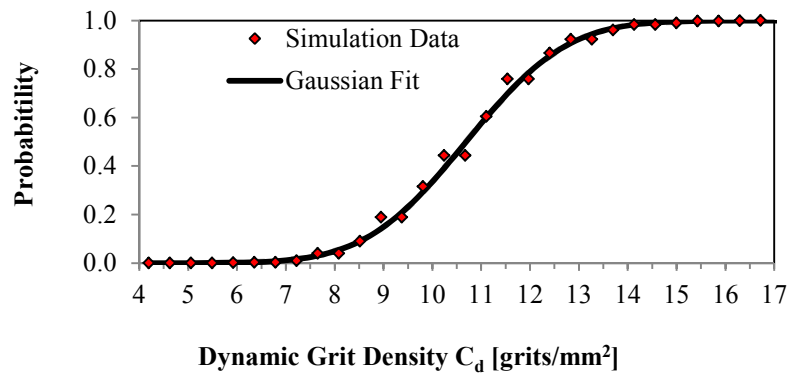


**Figure 6.10 - #220 wheel dynamic grit density distribution at wheel surface without grit overlap**

#### 6.5.4 Cutting Force Simulation

HAR microgrinding of ceramic micro-features needs to avoid modes of dynamic excitation of the receptive workpiece. Therefore, the nature of the grinding force frequencies for a microgrinding process needs to be investigated. The numerical simulation of straight traverse grinding was used to conduct this investigation. Figure 6.11 shows a simulation of a single #220 grind wheel with a 150  $\mu\text{m}$  grind width, which is equivalent to the twice the average diameter of a grit, a 40  $\mu\text{m}$  radial grind depth, a feedrate of 40 mm/sec and a spindle speed of 10 krpm. The individual forces of each grit is shown with grits 1-3 cutting within the first grind strip and grits 4-6 cutting in the second grind strip over one rotation of the grind wheel. The cutting force of each grit is simply modeled as having a force equal to the depth of cut times the specific grinding energy of 0.32 N/mm<sup>2</sup>. This model of the cutting force of each grit is selected because of its simplicity as it is this should have no impact on the frequency content of the force signal.

Figure 6.12 shows the cumulative grind force calculated by adding up the instantaneous forces of each grit over time. Notice that although 6 grits are participating, the final grind force signal has only 4 distinct force peaks.

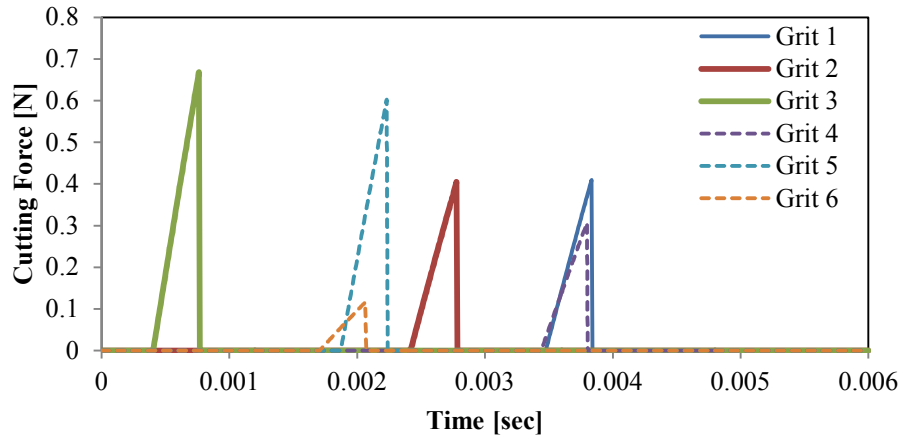


**Figure 6.11 – Simulated cutting force by individual grits in a #220 wheel with a 150 um grind width, 40 um radial depth of cut, 40mm/s feedrate, and 10krpm spindle speed**

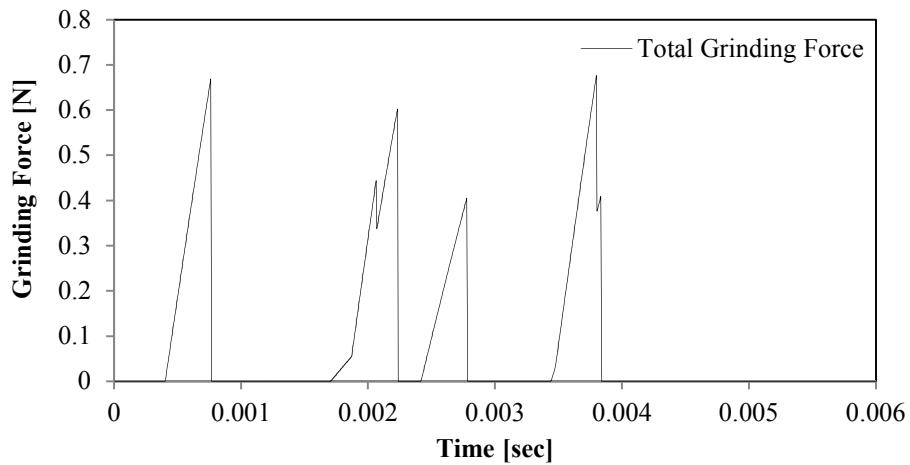


**Figure 6.12 – Total simulated cutting force as the sum of the force of each active grit**

The frequency content of the grinding force can be analyzed by taking the FFT of the grind signal as shown in Figure 6.13. The single rotation grind signal was repeated 10 times in order to match the periodic repetition of the grind force as the wheel rotates. Notice that the largest peak is at twice the fundamental spindle frequency while the second peak occurs at 4 times the speed of the spindle. All other peaks manifest at

harmonics of the spindle frequency but at magnitudes that can only be attributed to the spacings between the cutting force peaks.

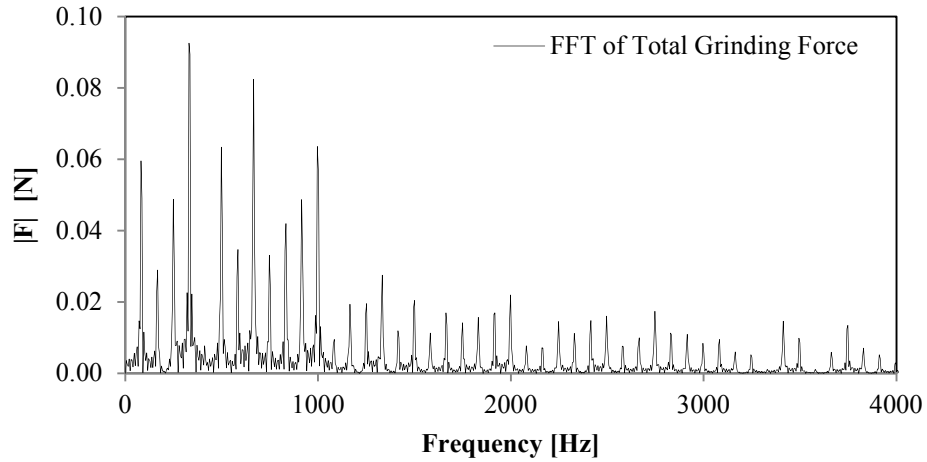


**Figure 6.13 – FFT of the total grinding force**

Figure 6.14, Figure 6.15, and Figure 6.16 show the same outcomes for a second simulation. Here, however, the 6 active grits created 6 distinct cutting force peaks.

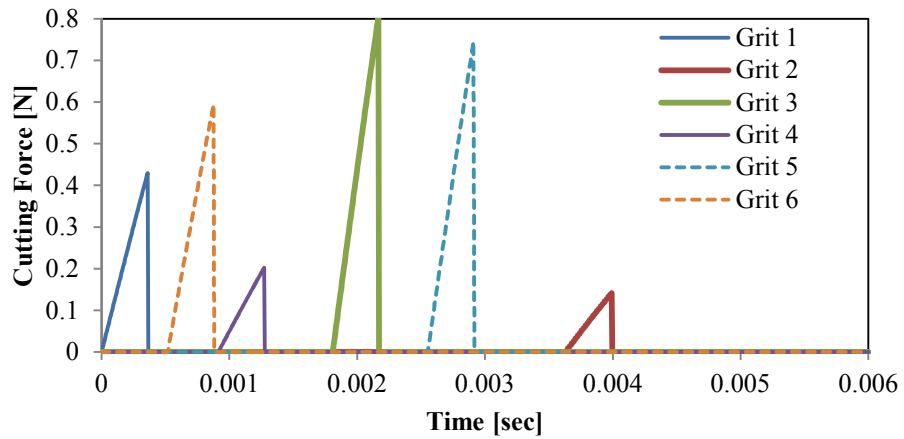


**Figure 6.14 – Simulated cutting force of individual grits in a #220 wheel with a 75  $\mu\text{m}$  grind width, 40  $\mu\text{m}$  radial depth of cut, 40mm/s feedrate, and 10krpm spindle speed**

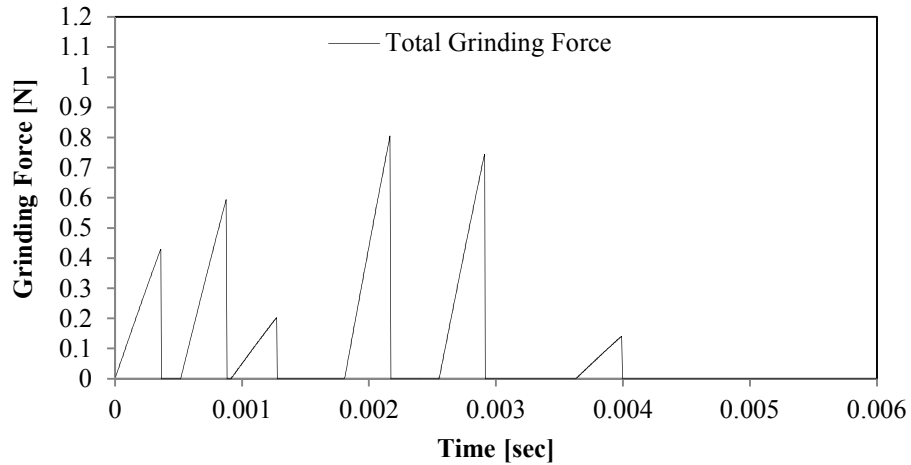


**Figure 6.15 – Total simulated cutting force as the sum of the force of each active grit**

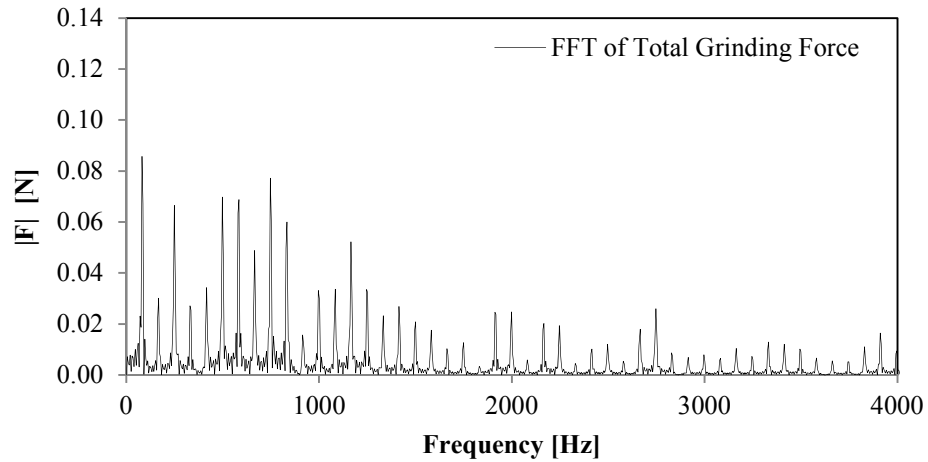


**Figure 6.16 – FFT of the total grinding force**

The frequency content from each simulation differs only in the relative magnitudes of the peaks. The frequency locations of the peaks are dependent only on the fundamental spindle frequency. All peaks occur at harmonic multiples of this frequency. There appears to be no discernible relationship, however, between the number of force peaks or the spacing between them that can explain the relative magnitudes of the frequency peaks.

A total of 1000 wheels were simulated in order to provide a general force frequency profile for the simulated grinding operations. Figure 6.17 shows the mean force contribution at each frequency over the 1000 simulations while Figure 6.18 shows the standard deviation of the peak magnitudes at the frequencies. It is observed that all of the signal power arises from the harmonics of the spindle speed as a result of the grind force signal repeating at that frequency.

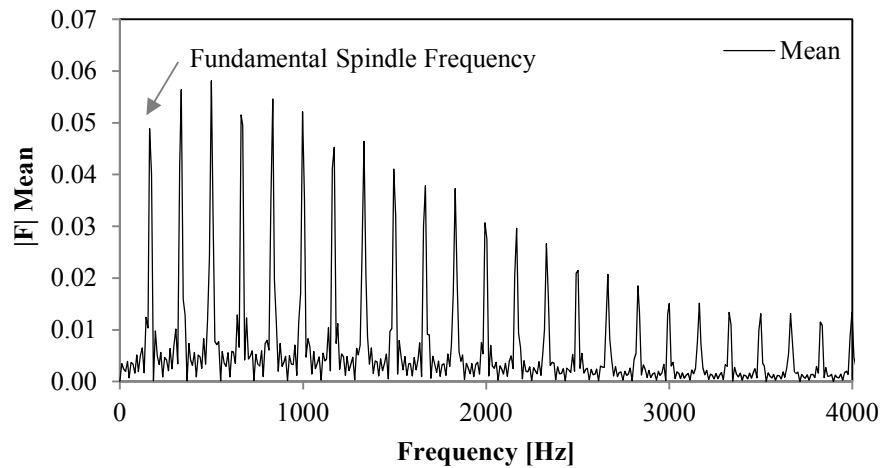


**Figure 6.17 – Mean FFT magnitude for 1,000 simulations of the grinding process**

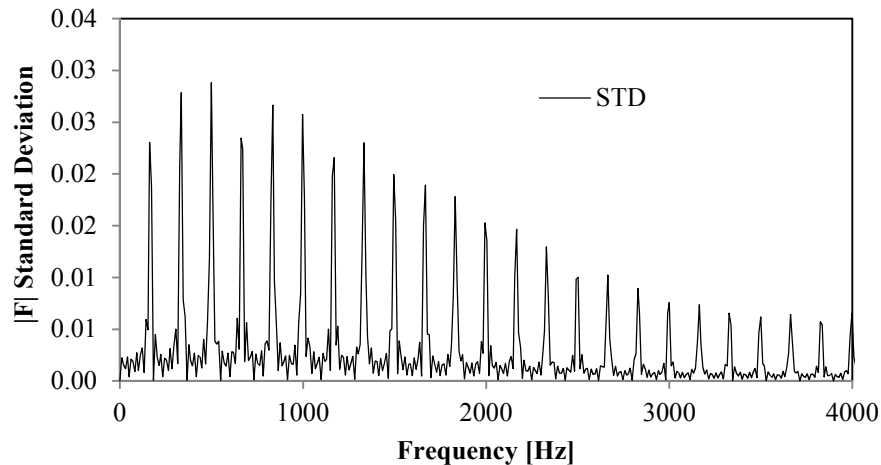


**Figure 6.18 – Standard deviation of FFT magnitude for 1,000 simulations of the grinding process**

A comparison can be made between the simulated grind signature of stochastic cutting points and that of the signature of a deterministic 5-flute cutting tool. Figure 6.19 shows the simulated force signal form one cutting rotation of a 5-flute, straight-toothed cutter. The simulation included sinusoidal tool runout resulting in varying depths of cut for each tooth.

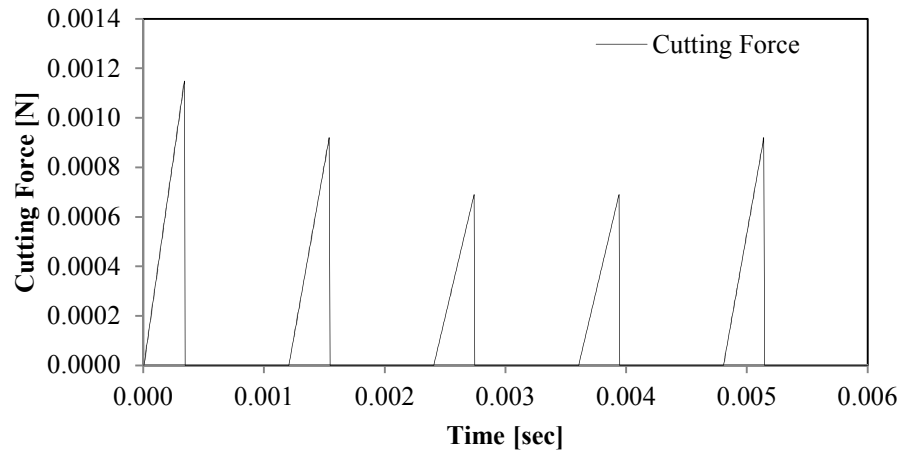


**Figure 6.19 – Simulation of a cutting force of a 5-flute cutting tool with tool-tip runout at 10 krpm**

The FFT of the cutting force repeated over 10 rotations is shown in Figure 6.20. It is observed that the fundamental spindle frequency is evident but not significant while most power comes from the tooth-passing frequency and the exponentially-decaying harmonics. This is similar to the grinding force simulation results.

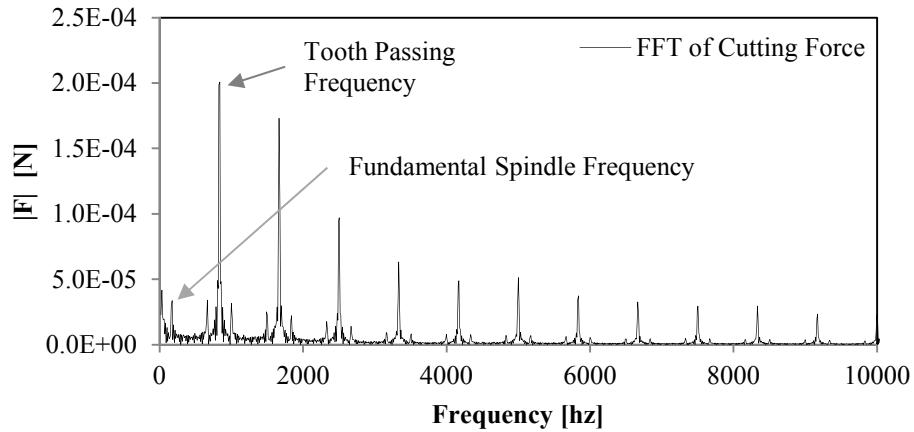


**Figure 6.20 – FFT of the 5-flute tool simulated cutting force**

## **6.6 EXPERIMENTAL MEASUREMENT OF MICROGRINDING FORCES**

### **6.6.1 Setup for Straight Traverse Razorblade Grinding**

The nature of microgrinding force frequencies in straight traverse microgrinding was investigated using a razorblade as a workpiece as has been done in other studies [2]. It is desired to know the major source of the dynamic forcing frequencies in the process in order understand the impact of the process on the vibrational response of the receptive workpieces in HAR microgrinding. The experimental setup, shown in Figure 6.21, is designed to closely imitate that of what would be used in profile jig grinding of HAR micro-features. An 80,000 rpm electric spindle is mounted on a vertical z-axis column in a micromachining tool. The x-y table holds a Kistler 5091A dynamometer, which has a 4.9 kHz natural frequency, onto which a workpiece fixture is mounted. The fixture holds a standard consumer steel razorblade such that the sharp edge of the blade lies close to perpendicular to the x-axis of travel. Two accelerometers, PCB 353B33 and PCB 352C68 with 2% linear measurement ranges of 0-4 kHz and 0-10 kHz and natural frequencies of

12 kHz and 20 kHz respectively, are mounted onto the workpiece fixture in order to measure the cross-feed movement of the grinding action.

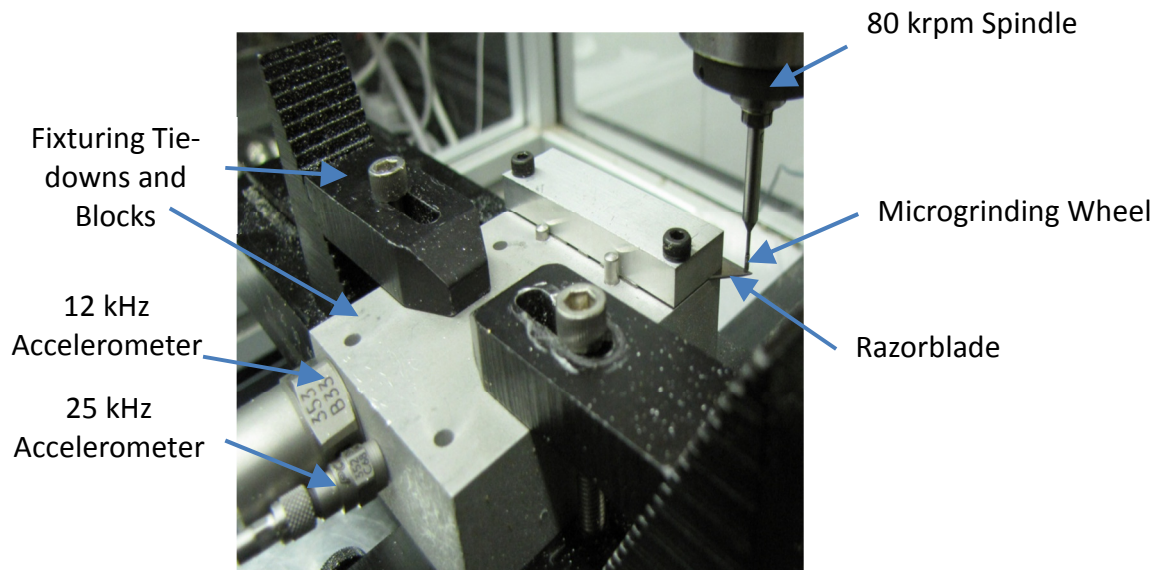


**Figure 6.21 – Setup for straight traverse microgrinding on a razorblade**

### 6.6.2 Characteristics of the System Free-Response

The ability to measure forces and movements using both accelerometers and the dynamometer was investigated by comparing the responses simultaneously to an impact force. Figure 6.22 shows the output response of the sensors to 95 N impact force. The results show a distinct free-response after the impact load has been removed. The damped natural frequency of the system was determined to be 2.14 kHz by utilizing the fast accelerometer and dynamometer responses. The response of the fast accelerometer and dynamometer were also used to calculate a system mass of 0.121 kg that relates the two in the free response of the system. This is an average over three individual tests.

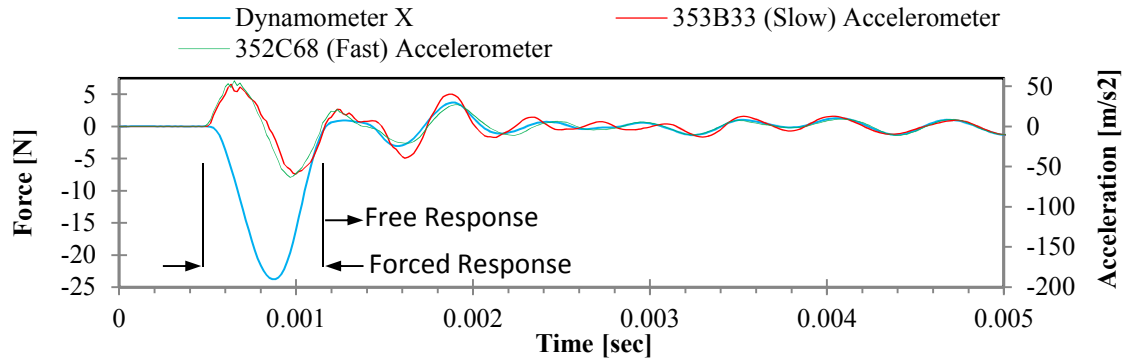


**Figure 6.22 – Impact response of the workpiece-fixture system measured with hammer load cell, 2 accelerometers, and dynamometer**

### 6.6.3 Characteristics of the System Forced-Response

The system consisting of the workpiece, fixture, dynamometer, and accelerometers has complex system dynamics which include not only significant response correlation between the x, y, and z directions, as seen by the response in Figure 6.22 which is not a strictly decaying sinusoid, but also forced responses whose magnitudes and phases are dependent on the excitation frequency. The frequency-dependency of the magnitude of the system response is of great interest since it will result in distortion of the measured forces in microgrinding experiments.

The forced response of the system was investigated by using an engraving tool in the spindle to exert a periodic rubbing frictional force onto the razorblade workpiece. Using the engraving tool adds the benefit of its increased stiffness over other cutting tools which will limit its deflection under the frictional force. The test was conducted by first slowly moving the cutting tool into contact with the workpiece as the spindle rotates at a slow 1,000 rpm. Initial contact is determined by a measured electrical continuity between the rotating tool and stationary workpiece. Then the spindle speed was increased stepwise to

81krpm as the FFT of the dynamometer and accelerometer outputs were measured over 2 second windows after the spindle speed was held stationary for 5 seconds at intervals of 3000 rpm.

Samples of the FFT data at 30 krpm are shown for the dynamometer and accelerometer respectively in Figure 6.23 and Figure 6.24 respectively. Notice the dominant peak at the spindle speed of 505 Hz along with the presence of the 2<sup>nd</sup>, 3<sup>rd</sup>, and 4<sup>th</sup> positive harmonics in both the data sets. Also, it is seen that the contribution of the harmonics decays exponentially as would be expected in a system with relatively low damping and many vibrationally-reflective surfaces.

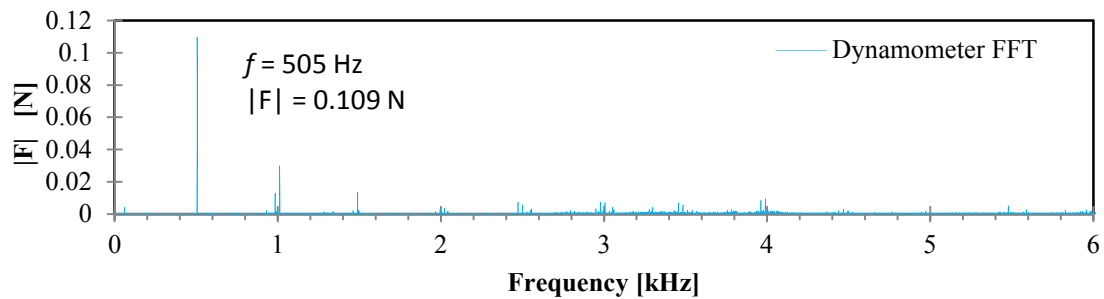


**Figure 6.23 – FFT of dynamometer signal of engraving tool rubbing at 30 krpm**

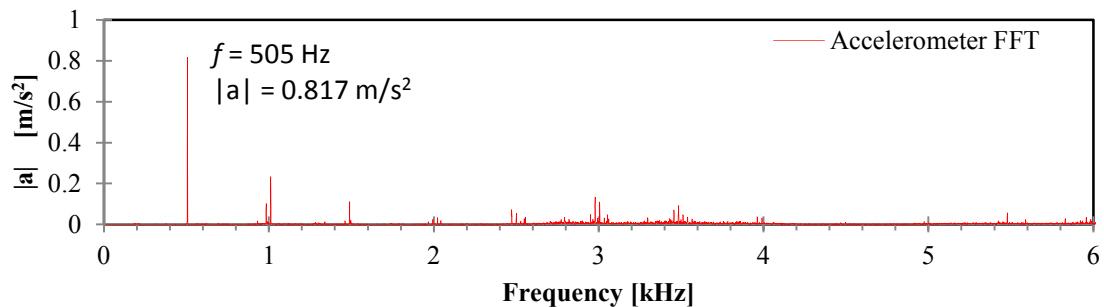


**Figure 6.24 - FFT of accelerometer signal of engraving tool rubbing at 30 krpm**

The resulting dominant peak frequencies from the tests at all spindle speeds are shown in Figure 6.25. It is observed that the dominant response corresponds to the

spindle speed. The magnitude of the dominant frequency peak at each forcing frequency is shown in Figure 6.26. The dynamometer and accelerometer responses were seen to match well in each test.

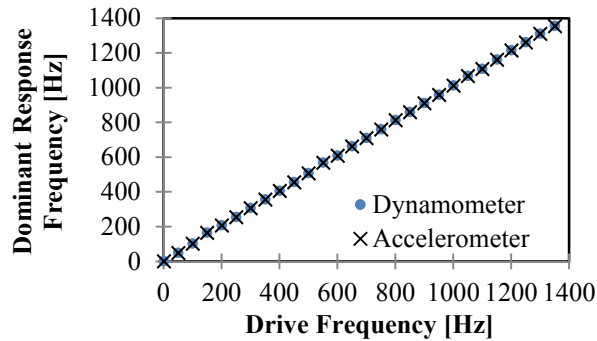


**Figure 6.25 – Dominant response peak frequency versus spindle drive frequency**

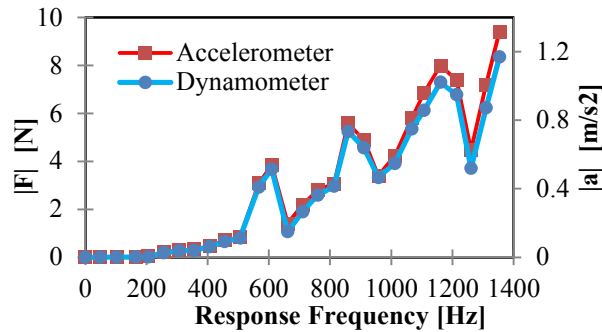


**Figure 6.26 – Dominant peak magnitude versus response frequency**

The magnitudes of the dominant response frequency were seen increase as the spindle speed increased. The response of the system is measured in the normal force direction of the rubbing action. The normal force can be represented as a linear elastic deformation of the workpiece therefore having a magnitude proportional to the interference depth of the tool-workpiece interaction. This model only holds, however, for small interference depths. The bearings of the spindle can also be simply modeled as having a linear elastic

stiffness. Therefore, the interference depth and corresponding rubbing normal force are proportional to the whirl force of the rotor system of the spindle. This relationship is shown in Equation 6.39.

$$F_N = k_{wp}\Delta_x = k_{wp}k_{bearings}F_{whirl} = k_{wp}k_{bearings}mr\omega^2 \quad \text{Equation 6.39}$$

The responses of the dynamometer and accelerometer can be adjusted to account for the increasing whirl force by dividing the square of the drive frequency as shown in Equation 6.40.

$$\frac{F_N}{\omega^2} = k_{wp}k_{bearings}mr \quad \text{Equation 6.40}$$

The normalized response forces shown in Figure 6.27 therefore show the excitation frequencies that result in resonating forced responses. It is observed that there is increased response with in the ranges of 500-650 Hz and 800-950 Hz. In addition, the calibration mass of the system which correlates the measured acceleration to the measured force was found to be 0.122 kg which agrees with the result of the free-response test.

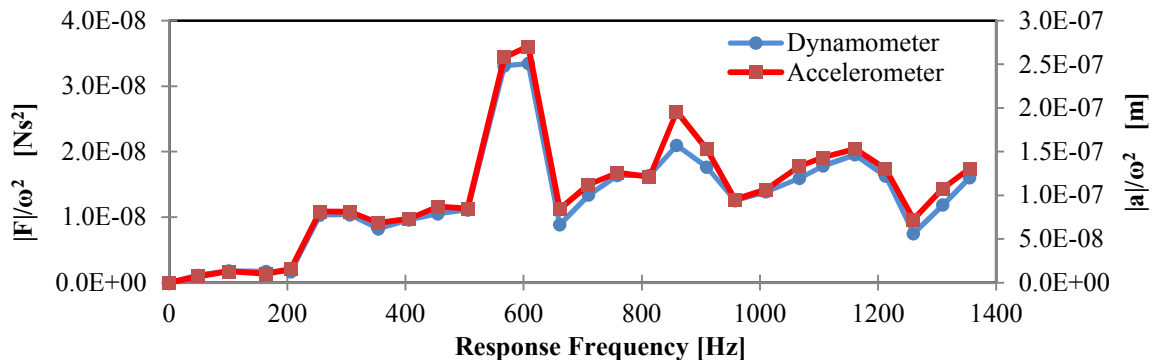


**Figure 6.27 - Dominant peak magnitude divided by spindle speed squared versus response frequency**

The frequency content of the system response also provides a qualitative method to evaluate the relative magnitudes of the harmonics of the forcing response. Figure 6.28 shows the magnitudes of the fundamental, 2<sup>nd</sup>, 3<sup>rd</sup>, and 4<sup>th</sup> harmonics at the driving spindle frequencies of the tests. It is observed that the magnitudes of the harmonic contributions remain consistently below half that of the fundamental frequency peak. This is further characterized in Figure 6.29 where the magnitude of each harmonic peak relative to the fundamental frequency peak is plotted for each driving spindle frequency. It is observed that the magnitudes of the harmonics do not decay exponentially in any consistent manner. In fact, there appears to not be dominance of any of the harmonics in relative contribution. This neglects the suggestive results of the single test at 30 krpm or 500 hz which show an exponential harmonic magnitude decay in Figure 6.23 and Figure 6.24. Notice that the harmonic magnitudes also appear to be independent of frequency.

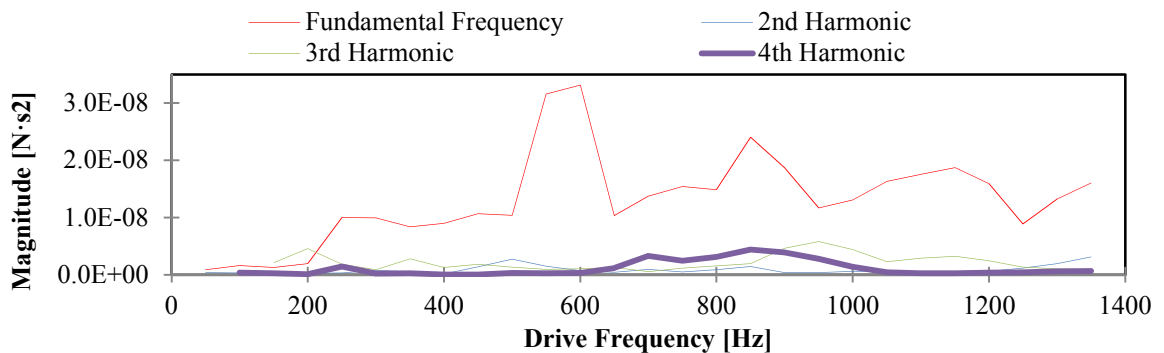


**Figure 6.28 - Dynamometer peak magnitudes divided by spindle speed squared versus driving spindle frequency**

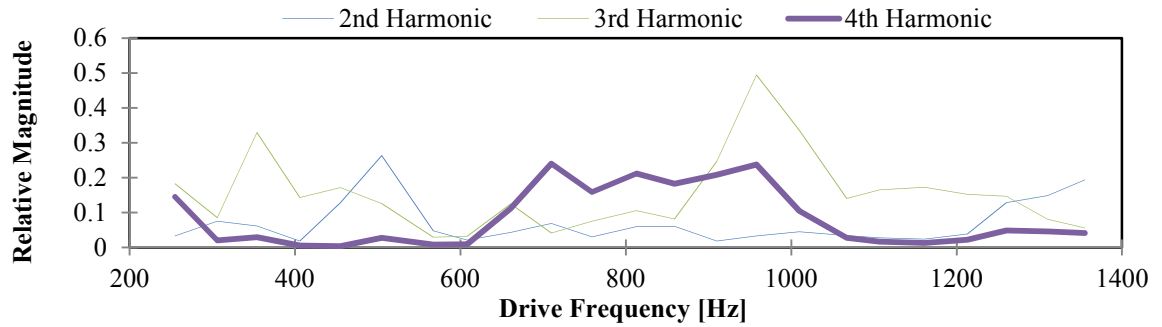


**Figure 6.29 – Harmonic peak magnitudes relative to fundamental peak as a function of driving spindle frequency**

#### 6.6.4 Measured Dynamic Cutting Forces

Preliminary grind tests were conducted to investigate the characteristics of micro-grinding force signatures. The tests utilized #220 diamond grit, 1mm OD microgrinding wheels on the razorblade workpiece. A preliminary test for system noise was conducted by measuring the dynamometer output when the grind wheel was rotating at 5 krpm but was not actually in contact with the workpiece. The FFT of the dynamometer signal, shown in Figure 6.30, showed that the signal amplifier failed to remove 60 Hz electrical noise and that the system possessed operational vibration peaks around 800, 3200, 4000, and 4800 Hz.

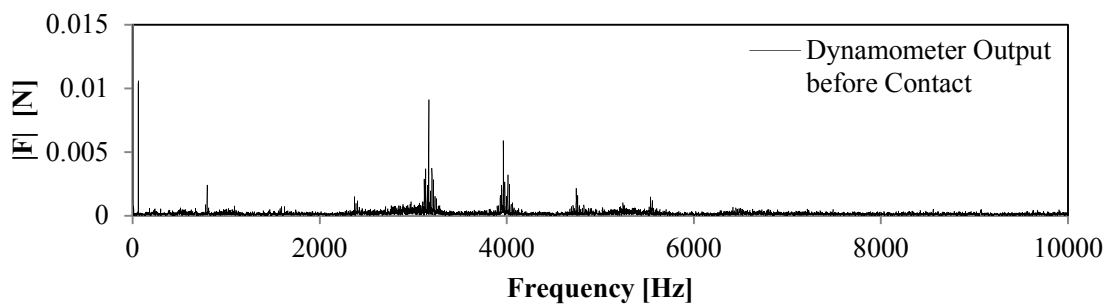


**Figure 6.30 – FFT of dynamometer output before grinding contact**

Several grinding tests were performed by slowly moving the grind wheel into contact with the workpiece until the accelerometer registered initial contact. The wheel then radially plunged into the workpiece to a depth of 15 $\mu$ m before traversing at a feedrate of 10 mm/sec. The frequency content of the force signals measured at spindle speeds of 4000, 5000, and 7000 rpm are shown in Figure 6.31, Figure 6.32, and Figure 6.33 respectively.

It was observed that the fundamental spindle frequency was not dominant in FFT signatures. The plots show that there was large signal contribution at approximately 50 times the spindle speed in all three tests. It is noticed, however, that these peaks have spacings that are consistently equal to twice the spindle speed suggesting that they are harmonics of the periodic repetition of the grinding force signal. The data plots also show that there is significant increase in the signal power in the fixed-frequency regions around 2800 and 5300 Hz as the spindle speed is increased. This can be explained as the excitation of natural system dynamics of the structure.

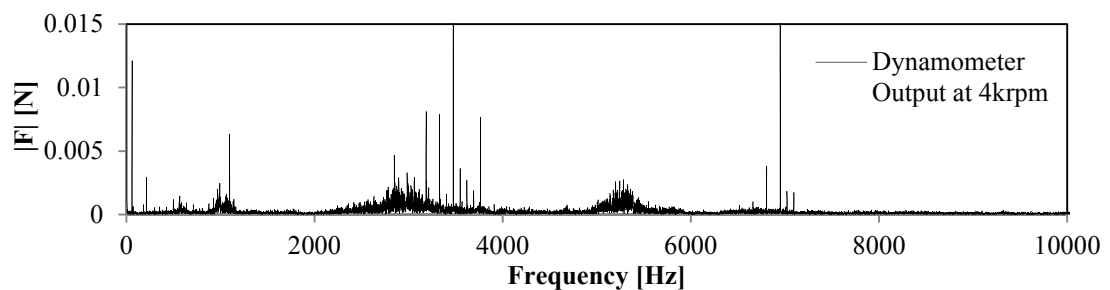


**Figure 6.31 – FFT of grinding force at 4krpm (66Hz) from dynamometer**

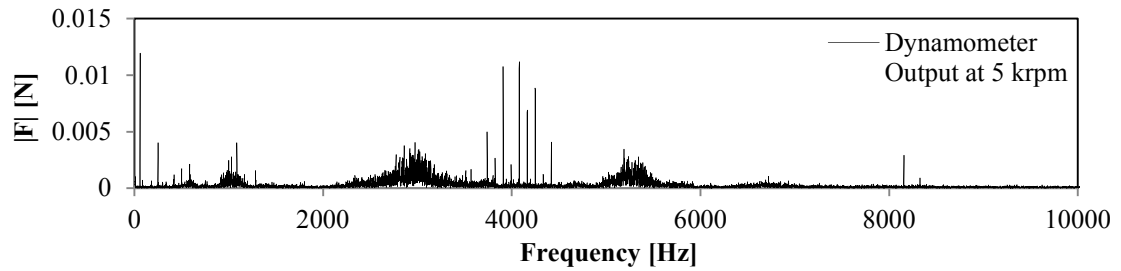


**Figure 6.32 – FFT of grinding force at 5krpm (83 Hz) from dynamometer**

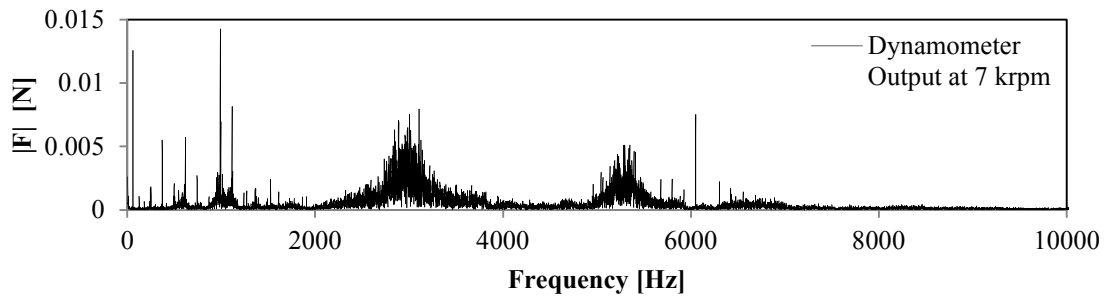


**Figure 6.33 - FFT of grinding force at 7krpm (117 Hz) from dynamometer**

The output from the accelerometer for the grind test showed similar measurements although the accelerometer did provide information at frequencies above the cutoff frequency of the dynamometer of approximately 9 kHz which is seen in Figure 6.34.

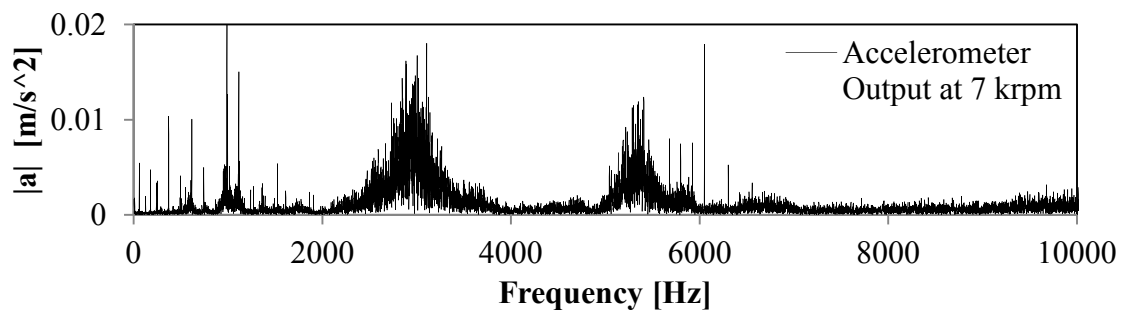


**Figure 6.34 – FFT of grinding workpiece acceleration at 7krpm from 20kHz accelerometer**

More grinding tests were conducted by increasing the spindle speed in a slow, step-wise manner as the wheel traversed the workpiece. A time-frequency plot of the FFT over time shows increasing peak frequencies as the spindle speed is increased. Figure 6.35 and Figure 6.36 show this for the dynamometer and accelerometer outputs respectively as the spindle speed is increased from 1,000-2,000 rpm. Notice the stationary natural dynamic response bands at 2,800 and 5,300 Hz.

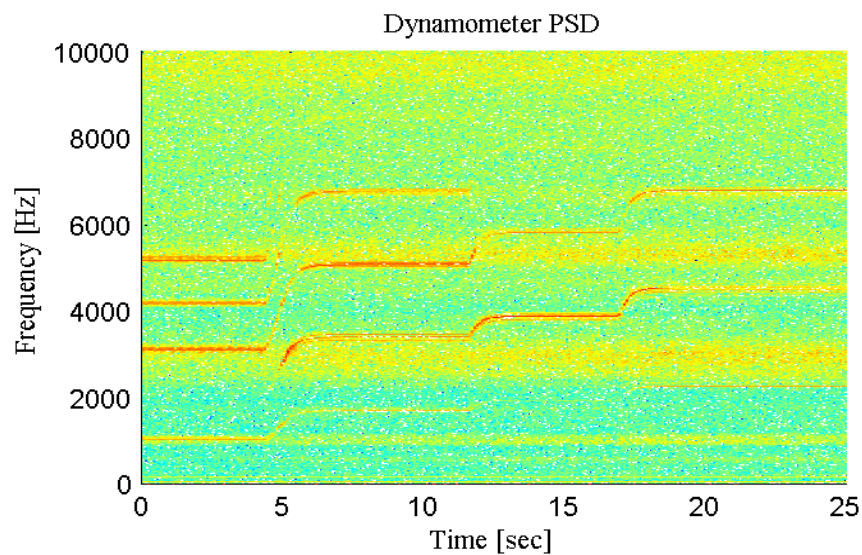


**Figure 6.35 – Time-frequency plot of force during microgrinding with a #220 grit wheel as it is accelerated from 1-2 krpm**

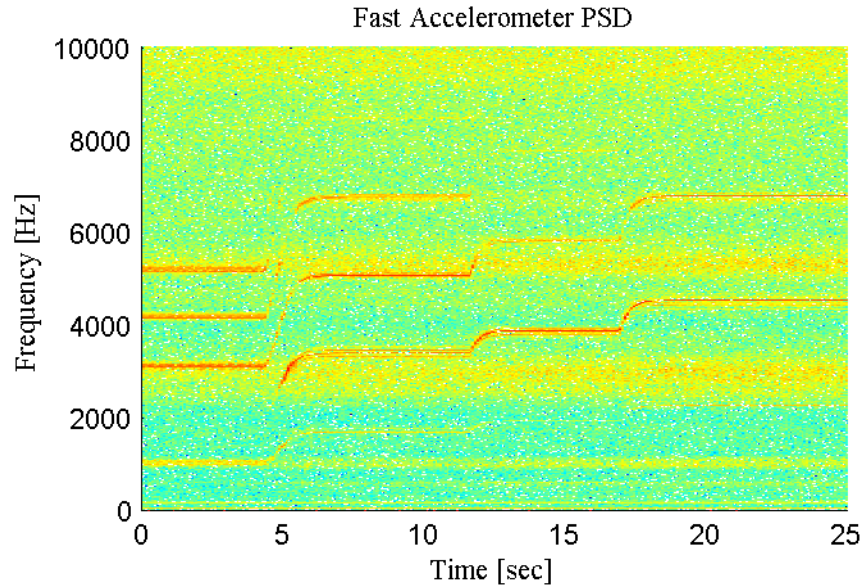


**Figure 6.36 – Time-frequency plot of acceleration during microgrinding with a #220 grit wheel as it is accelerated from 1-2 krpm**

The fixed response bands can be removed from the time-frequency plot by subtracting the time-averaged power at each frequency. This is shown in Figure 6.37 and Figure 6.38 for the dynamometer and accelerometer respectively. Notice that the frequency signatures of the grinding action are now more readily evident. It is observed that as the spindle speed increases over time the gap between the harmonic frequencies increase as expected. It is also seen that the second band contains the most power in each instrument.

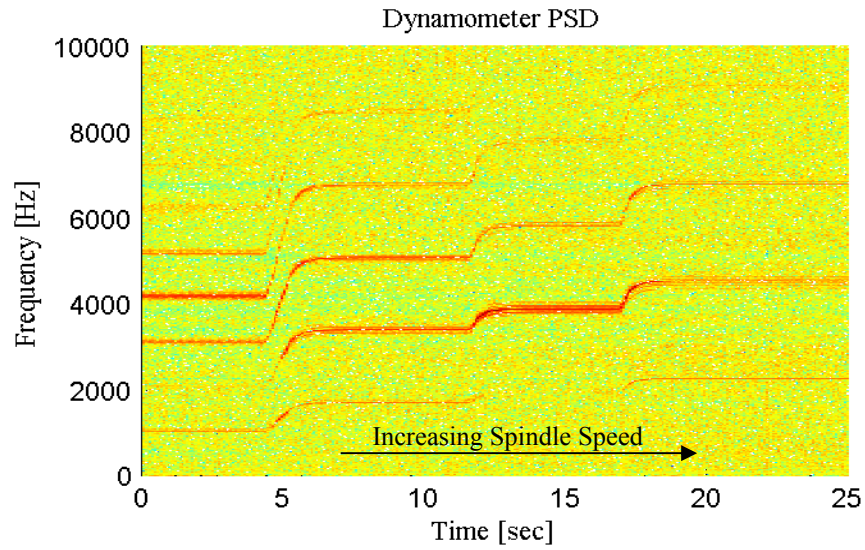


**Figure 6.37 – Time-frequency plot of force during microgrinding with a #220 grit wheel as it is accelerated from 1-2 krpm with mean power removed by frequency**

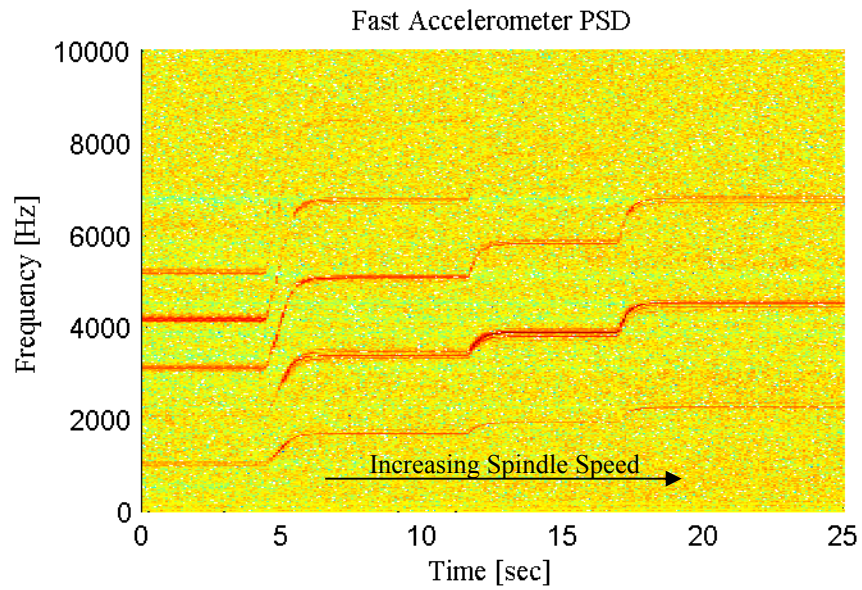


**Figure 6.38 – Time-frequency plot of acceleration during microgrinding with a #220 grit wheel as it is accelerated from 1-2 krpm with mean power removed by frequency**

## 6.7 DISCUSSION

The microgrinding forces measured using the straight traverse grinding on a razorblade yielded complicated force signatures that contained significant noise due to the high receptance and complicated dynamics in the micromachining tool. The varying undeformed chip thickness and dynamic grit density through the grind zone further complicated force profile. Therefore, the time-force signature could not be interpreted for analysis of individual grit cutting forces. The analytic model developed could therefore not be verified using experimental data.

Analysis of the frequency content of numerical simulation of straight traverse microgrinding predicted that the spindle speed and its harmonics would be the dominant driving frequencies in HAR microgrinding of ceramic micro-features. Tests conducted on the micromachining tool verified this to be the case. Simplified tool rubbing tests of the experimental setup showed that compensating for tool runout in the rubbing force yielded identification of a definite system dynamic natural frequency at 0.6 kHz although the only natural frequency identified through impact test occurred at 2.14 kHz. The rubbing force frequency peaks were analyzed at the dominant spindle harmonic frequencies to observe the nature of the decay in relative harmonic magnitude. However, it was observed none of the first 4 harmonics had a consistent magnitude relationship. This observation also held true for the frequency content in the grinding tests. It is also interesting to note that the harmonic frequencies failed to excite either of the natural frequencies identified by the impact test and peak forcing frequency response.

## 6.8 SUMMARY

The probabilistic model presented for straight traverse microgrinding was seen to predict the dynamic grit density mean and variance under varying grinding spindle speeds, feedrates, and depths of cut. Numerical simulation showed that the analytic model was significantly faster while yielding the same results. The nature of the force signature of traverse microgrinding in a micromachining tool was investigated using razorblade grinding. It was observed that even under slow spindle speeds and shallow infeed angles, the grit cutting pulses were not discernible in the force profile due to varying chip thickness through the grind zone and complicated dynamic response of the machine tool.

The grinding force frequency profile was investigated using both numerical simulation and razorblade grinding. Simulation showed that the dominant force frequency power occurred at the spindle frequency and its harmonics despite the presence of only a few grits participating in the grinding action. The variability in the force frequencies only arose in the relative magnitudes of the spindle harmonic frequencies.

Simple testing of the force contributions at harmonics of the spindle speed was conducted using a single-toothed engraving tool. Results showed that harmonic magnitudes do not consistently decay at increasing multiples of the spindle frequency and fail to excite the identified natural frequencies of the system. Experimental grinding forces on the razorblade edge showed that microgrinding force frequencies are similarly dominated by the spindle speed and varying magnitudes of its harmonics.

## **CHAPTER 7 –DYNAMIC TOPOGRAPHY IN INFEEED GRINDING**

### **7.1 INTRODUCTION**

The distributions of the parameters that govern the grinding force contribution of each cutting abrasive is needed to develop full understanding of the impact of statistical variation in the microgrinding process. In addition, HAR microgrinding of ceramic micro-features requires process control that can limit the probability of extreme undeformed chip thicknesses while not sacrificing material removal rates. This requires statistical models that can predict the probabilities of the abrasive cutting characteristics.

A probabilistic model was developed in CHAPTER 6 for the widely used straight traverse microgrinding, but the process has a varying infeed angle through the grind zone which results in more grits participating near the end of the grind zone than at the start. This makes it difficult to measure the dynamic grit density since it constantly varies. In addition, the ability to identify and measure the force contributions of individual grits is difficult as the force signal contains too few discernible peaks. A method of measuring dynamic grit interactions at specific infeed angles is needed for microgrinding in order to study the nature of the distributions of the material removal parameters. This will allow for the identification and measurement of the force contributions of individual grits. Such a technique will facilitate the validation of the probabilistic modeling of the distribution of dynamic grit density. This chapter presents a grinding approach that maintains a constant infeed angle through the grind. A probabilistic model of the dynamic grit density for this grinding approach is generated and validated using numerical simulation. Experimental validation of the model is conducted, and the distributions of grit cutting force attributes are investigated using this approach.

## 7.2 REVIEW OF SALIENT LITERATURE

Current techniques for the characterization of the dynamic wheel topography distributions have utilized numerical simulation and empirical modeling based on various measurement techniques. Measurements and analysis of the dynamic grit interaction of conventional grind wheels have yielded many distribution models for various attributes of grit engagement with the workpiece. A summary of these distributions is presented in Table 7.1.

Measurement of the interaction of individual grits with workpiece in microgrinding has been limited. The most noteworthy study by Park utilized grinding on a micro-thermocouple to measure grit force pulses through the heat pulse generated [18]. However, this does not provide direct information on the undeformed chip thickness distribution for the process. Instead, this modeling effort will investigate infeed grinding on a thin workpiece as shown Figure 7.1 following the work of Tigerstrom where the wheel is fed radially into a workpiece creating a small grinding zone angle  $\theta$  [68]. This grinding approach provides a method to evaluate dynamic topography characteristics without variation over time. Tigerstrom showed that the infeed angle through the grind zone is nearly constant for this geometry and is governed by the feedrate and wheel surface speed as shown in Equation 7.1 [68].

$$\tan \alpha = \frac{v_f}{v_s} \quad \text{Equation 7.1}$$

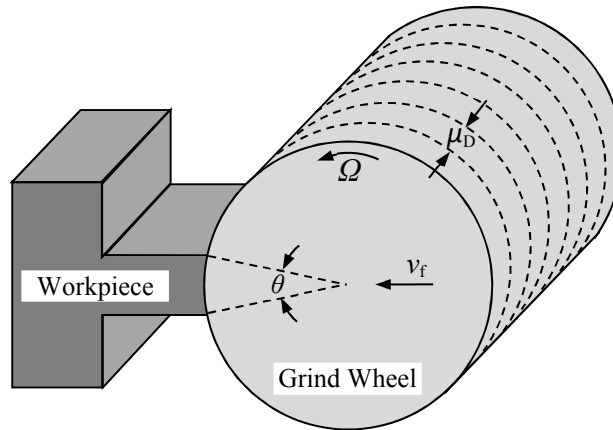
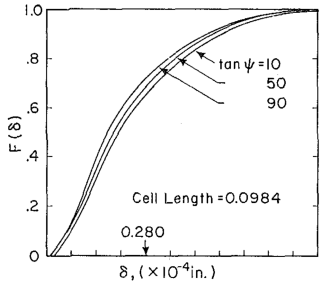
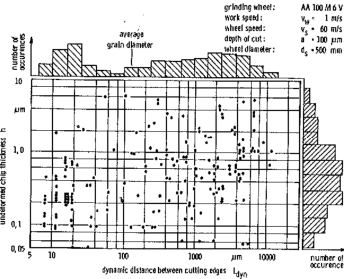
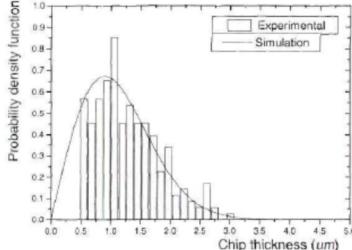
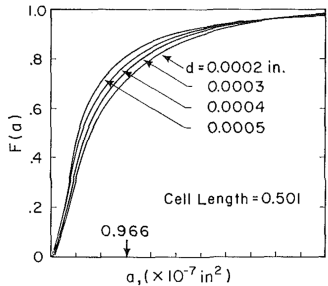
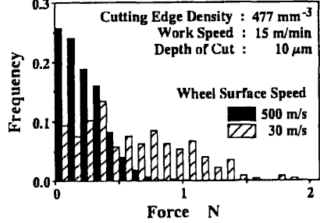


Figure 7.1 – Schematic of in-feed grinding approach: straight infeed grinding with a small grind zone angle

Table 7.1 – Stochastic models for dynamic grind wheel characteristics

Characteristic	Model Distribution	Measurement Method	Study
Dynamic Circumferential Grit Spacings	<p>Rayleigh Distribution</p> <p>Fig. 10(a) Histogram of grain spacings</p>	Monte Carlo Simulation	Law and Wu, 1972
	<p>Dual Agglomerations</p> <p>grinding wheels: AA 60 1.6 V work speed: v<sub>w</sub> = 1 m/s wheel speed: v<sub>s</sub> = 30 m/s depth of cut: a = 1 mm wheel diameter: d<sub>w</sub> = 500 mm</p>	Dynamic Stylus Profilometry	König and Aachen, 1975

**Table 7.1 (continued)**

		<p>Monte Carlo Simulation</p>	<p>Law and Wu, 1972</p>
<p>Dynamic Undeformed Chip Thickness</p>	<p>Logarithmic Distribution</p> 	<p>Dynamic Stylus Profilometry</p>	<p>König and Aachen, 1975</p>
	<p>Rayleigh Distribution</p> 	<p>Optical Measurement of Grinding Chips (Swarf)</p>	<p>Hecker, 2002</p>
<p>Dynamic Chip Cross Sectional Area</p>		<p>Monte Carlo Simulation</p>	<p>Law and Wu, 1972</p>
<p>Dynamic Tangential Cutting Force per Grit</p>		<p>Monte Carlo Simulation with Constant Specific Grinding Force</p>	<p>Inasaki, 1996</p>

## 7.3 ANALYTIC MODEL OF DYNAMIC WHEEL TOPOGRAPHY

### 7.3.1 Analysis of the Cutting Action of Individual Grits

The engagement depth  $h_{ij}$  of a grit  $i$ , as caused by the shadowing from a previous grit  $j$ , is constant across the grinding zone. The relationship between the two arbitrary grits is illustrated in Figure 7.2 where  $L_{ij}$  is circumferential spacing between the grits in question. The protrusion height difference between the grits  $\delta_{ij}$  is positive for a grit that protrudes more than the previous one and is a function of the protrusion height of each grit from the wheel center,  $R_c$ . The engagement depth can be calculated for a given grit using the kinematic relationship shown in Equation 7.2 where  $s_{ij}$  is the linear advancement of the grind wheel during the time interval between the engagements of grit  $i$  and  $j$ .

However, the grit engagement calculation only applies to grits that are in close proximity in the axial direction of the wheel. A grit can only be overshadowed by other grits that cut along the same circumferential line of action on the wheel surface.

$$h_{ij} = (s_{ij}) - (\delta_{ij}) = (L_{ij} \tan \alpha) - (R_{c_j} - R_{c_i}) \quad \text{Equation 7.2}$$

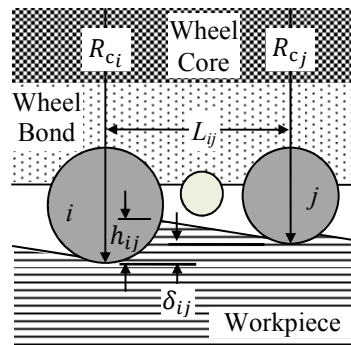


Figure 7.2 - Kinematically active grits overshadowing multiple inactive grits

### 7.3.2 Probabilistic Model of the Dynamic Grit Density

A probabilistic model of the dynamic grit density is generated by propagating the fundamental grit size and location distributions to a final stochastic description of the number of grits that are engaging the workpiece. This is achieved by calculating the general probability that any single grit  $i$  in the wheel has an overall positive engagement depth as caused by its relationship with each of the other grits  $j$  that could possibly overshadow it. This must account for the probability of the number of grits that cut along the same circumferential line of action on the wheel.

The possible grits  $j$  that could overshadow grit  $i$  are identified by axially dividing the grind wheel into cylindrical segments with widths equal to the mean grit diameter  $\mu_D$  defined in Figure 7.1. It is assumed that each grit  $j$  with a centroid located in a given segment removes a rectangular chip that has a width equal to the segment width. All of the grits  $j$  identified within the same segment as grit  $i$  must then be checked for causing overshadowing based on a positive engagement depth of grit  $i$  with respect to grit  $j$ .

In addition, the relationships between grit  $i$  and the other grits that could overshadow it must utilize constant properties of grit  $i$  but random properties of the other grits. The probability of grit  $i$  having an overall positive engagement depth can then be calculated as the probability that its engagement depth with respect to each other grit  $j$  are all individually positive.

### 7.3.3 Probability of the Dynamic Grit Density

The dynamic grit density in a grind wheel is a measurement of the number of active grits that participate in the grinding action per unit area on the wheel surface. The

stochastic nature of a grind wheel requires that this dynamic grit density  $C_d$  be a random variable with an unknown probability,  $\Pr(C_d)$ . It can be formed as the probability of the number of dynamically active grits  $N_d$  divided by the participating surface area  $S_a$  of the grind wheel as shown in Equation 7.3.

$$\Pr(C_d) = \frac{\Pr(N_d)}{S_a} \quad \text{Equation 7.3}$$

The expectation and variance of the dynamic grit density can be calculated from the expectation and variance of the number of active grits as shown in Equation 7.4 and Equation 7.5 respectively.

$$E[C_d] = \frac{E[N_d]}{S_a} \quad \text{Equation 7.4}$$

$$\text{Var}[C_d] = \frac{\text{Var}[N_d]}{S_a^2} \quad \text{Equation 7.5}$$

The random variable  $N_d$  can be described as the sum of independent, identical Bernoulli trials in which each trial is a test of whether or not a specific grit is active. The distribution of the number of active grits  $N_d$  is therefore a binomial Distribution [45]. The probability mass function for this variable is shown as Equation 7.6. Here, each  $\Pr(A_i)$  within the summation is the probability that a particular grit  $i$  actively removes material. Notice that this distribution is contingent on the condition of a known number of abrasives in the wheel  $N_a$ . The expectation and variance given the exact number of static grits available for grinding are given by Equation 7.7 and Equation 7.8.

$$\begin{aligned} \Pr(N_d = n_d | N_a) &= f(n_d | N_a) = \binom{N_a}{n_d} \Pr(A_i)^{n_d} (1 - \Pr(A_i))^{N_a - n_d} \\ &= \frac{N_a!}{n_d! (N_a - n_d)!} E(A_i)^{n_d} (1 - E(A_i))^{N_a - n_d} \end{aligned} \quad \text{Equation 7.6}$$

$$E[N_d | N_a] = N_a E(A_i) \quad \text{Equation 7.7}$$

$$\text{Var}[N_d|N_a] = N_a E(A_i)(1 - E(A_i)) \quad \text{Equation 7.8}$$

The number of trials in a given wheel is equal to the number of grits that reside in the grind zone portion of the wheel. This study assumes for simplicity that the full width of the grind wheel is used for grinding resulting in the number of trials being equal to the total number of grits within the wheel. This number of abrasive grits in a wheel is a random variable  $N_a$  since each wheel has a different number of grits. The distribution of the number of grits participating regardless of the number of grits in the wheel is obtained by utilizing the definition of the conditional probability as shown in Equation 7.9.

$$\Pr(N_d = n_d) = f(n_d) = \int_{-\infty}^{\infty} f(n_d, N_a) dN_a = \int_{-\infty}^{\infty} f(n_d|N_a) f(N_a) dN_a \quad \text{Equation 7.9}$$

The expectation of the number of active grits independent of the exact number of grits in the wheel can be calculated by the double expectation which is shown in Equation 7.10. Similarly, the variance in the number of active grits is given by Equation 7.11.

$$\begin{aligned} E[N_d] &= E[E[N_d|N_a]] = \int_{-\infty}^{\infty} E[N_d|N_a] f(N_a) dN_a = \int_{-\infty}^{\infty} N_a E(A_i) f(N_a) dN_a \\ &= E(A_i) \int_{-\infty}^{\infty} N_a f(N_a) dN_a = E(A_i) E[N_a] \end{aligned} \quad \text{Equation 7.10}$$

$$\text{Var}[N_d] = E[N_a] \text{Var}[A_i] + (E[A_i])^2 \text{Var}[N_a] \quad \text{Equation 7.11}$$

Each Bernoulli trial has a probability of being successful as each grit  $i$  has a specific probability of being active,  $\Pr(A_i)$ . The expectation and variance of each Bernoulli trial is shown in Equation 7.12 and Equation 7.13 respectively as calculated from the probability of a single grit being active.

$$E[A_i] = \Pr[A_i] \quad \text{Equation 7.12}$$

$$\text{Var}[A_i] = \Pr[A_i](1 - \Pr[A_i]) \quad \text{Equation 7.13}$$

Combining the results yields the final expectation and variance of the dynamic grit density based on the probability of any arbitrary grit  $i$  being active. The results are shown in Equation 7.14 and Equation 7.15.

$$E[C_d] = \frac{\Pr[A_i]E[N_a]}{S_a} \quad \text{Equation 7.14}$$

$$\text{Var}[C_d] = \frac{E[N_a]\Pr[A_i](1 - \Pr[A_i]) + (\Pr[A_i])^2\text{Var}[N_a]}{S_a^2} \quad \text{Equation 7.15}$$

### 7.3.4 Probability of Grit $i$ being Active

The probability of random grit  $i$  being active,  $\Pr(A_i)$ , is equivalent to the probability that it would not be overshadowed by any of the other grits that reside in the same axial segment. The probability of a grit being active can be written as the marginal distribution of the joint PDF  $f_{A_i,N}(a_i, n)$  between a random variable instance of a grit being active  $a_i$  and the random variable instance of the number of grits  $n$  within a single axial segment of the wheel as shown in Equation 7.16. This joint PDF can be determined using the definition of the conditional PDF of an active grit given the number of grits that reside within a particular segment  $f_{A_i|N}(a_i | n)$  and the independent PDF of this number of grits occurring,  $f_N(n)$ .

$$\Pr(A_i) = \int_{-\infty}^{\infty} f_{A_i,N}(a_i, n) dn = \int_{-\infty}^{\infty} f_{A_i|N}(a_i | n) f_N(n) dn \quad \text{Equation 7.16}$$

The condition needed for a grit to be active requires that its engagement caused by all the other grits within the same wheel segment be greater than zero. The conditional PDF of a grit being active  $f_{A_i|N}(a_i | n)$  is therefore also a function of the protrusion height of the grit in question,  $r_{c_i}$ . Therefore, the conditional PDF needs to be derived from the joint PDF with the random variable contact radius  $R_{c_i}$  of grit  $i$  as shown in Equation 7.17.

Again, this joint PDF  $f_{A_i|N,R_{c_i}}(a_i|n,r_{c_i})$  can be calculated from the definition of a conditional PDF. The PDF of a single grit  $i$  being active is now written as a double conditional probability in which it is dependent on a given number of grits within the same axial segment and the protrusion height of grit  $i$  from the wheel center.

$$f_{A_i|N}(a_i|n) = \int_{-\infty}^{\infty} f_{A_i|N,R_{c_i}}(a_i|n,r_{c_i}) dr_{c_i} = \int_{-\infty}^{\infty} f_{(A_i|N)|R_{c_i}}((a_i|n)|r_{c_i}) f_{R_{c_i}}(r_{c_i}) dr_{c_i} \quad \text{Equation 7.17}$$

The probability of this particular grit being active can now be derived from the condition that its engagement resulting from the shadowing caused by each of the other grits in the axial segment be greater than zero. It is assumed that the engagement caused by the other grits are independent of one another since the circumferential distance to each other grit  $j$  and the protrusion height of that grit is independent of the others. The total probability of the grit engagement being greater than zero when measured against all the other grits is merely the product of the individual engagement probabilities being greater than zero as shown in Equation 7.18 where  $n$  is the random variable instance of the number of grits within the axial segment.

$$f_{(A_i|N)|R_{c_i}}((a_i|n)|r_{c_i}) = [\Pr(h_{ij} > 0|r_{c_i})]^{n-1} \quad \text{Equation 7.18}$$

### 7.3.5 Probability of Grit $i$ not being Overshadowed by Grit $j$

The probability of the engagement of grit  $i$  created by the relationship with random grit  $j$  being greater than zero is the cumulative probability of all positive engagement values from zero to infinity as shown in Equation 7.19. The cumulative probability is defined by the integral of the PDF across the chosen range.

$$\Pr(h_{ij} > 0 | r_{c_i}) = \int_0^{\infty} f_{H_{ij}|R_{c_i}}(h_{ij}|r_{c_i}) dh_{ij}|r_{c_i} \quad \text{Equation 7.19}$$

The PDF of the engagement of grit  $i$  created by the relationship with random grit  $j$  can be calculated using the known relationship shown in Equation 7.2. The grit engagement is a function of both the random variable linear wheel advancement between the grits  $S_{ij}$  and the protrusion height of the random grit  $R_{c_j}$ . Therefore, the grit engagement PDF must be defined by the joint PDF of these two random variables as shown in Equation 7.20. A manipulation of Equation 7.2 allows for a variable transformation to take the place of the random grit protrusion height. The independence of the linear wheel advancement between the two grits and the protrusion height of the second grit allows for the joint PDF to be rewritten as the product of the two individual PDFs.

$$f_{H_{ij}|R_{c_i}}(h_{ij}|r_{c_i}) = \int_{-\infty}^{\infty} f_{S_{ij},R_{c_j}}(s_{ij}, s_{ij} - h_{ij}) ds_{ij} = \int_{-\infty}^{\infty} f_{S_{ij}}(s_{ij})f_{R_{c_j}}(s_{ij} - h_{ij}) ds_{ij} \quad \text{Equation 7.20}$$

The analytic static wheel model developed in CHAPTER 2 showed that grit location along the circumference of a wheel is random with a uniform distribution [69]. Therefore, the circumferential distance  $L_{ij}$  between grit  $i$  and  $j$  also has a uniform distribution as shown in Equation 7.21. Here the circumferential distance is equally likely to be any value between zero and the maximum possible distance,  $L_{\max}$ , which is the circumference of the wheel.

The infeed angle for a given operation is a constant, and therefore the linear wheel advancement between the grits also has a uniform distribution as derived in Equation

7.22 using a standard PDF transformation [45]. Here,  $\Omega$  is the spindle speed in revolutions per minute.

$$f_{L_{ij}}(l_{ij}) = \frac{1}{L_{\max}} = \frac{1}{\pi d_w} \quad \text{Equation 7.21}$$

$$f_{S_{ij}}(s_{ij}) = f_{L_{ij}}\left(\frac{s_{ij}}{\tan \alpha}\right) \left(\frac{dL_{ij}}{dS_{ij}}\right) = \frac{1}{L_{\max}} \left(\frac{1}{\tan \alpha}\right) = \frac{1}{(\pi d_w) \left(\frac{v_f}{v_s}\right)} = \frac{\left(\frac{\Omega}{60}\right) \frac{d_w}{2}}{(\pi d_w) v_f} = \frac{\Omega}{60 v_f} \quad \text{Equation 7.22}$$

The probability distribution of the protrusion height of a random static grit has been measured to be a Gaussian distribution and simulated to be Rayleigh distribution [36, 40, 70]. Here, the distribution chosen is stochastically derived from the original uniform distributions of the grit Cartesian location and the Gaussian distribution of the grit diameter [69]. A sample of this analytic PDF is shown in Figure 7.3 for a #400 wheel with a 1mm OD and 0.9mm core.

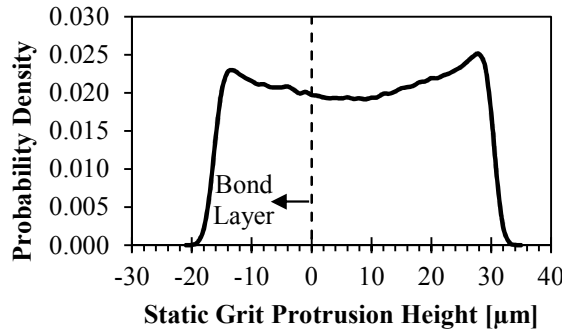


**Figure 7.3 - Probability density of grit radial protrusion height above the bond surface in the simulations of a #400, 1mm single-layered wheel**

The numerical calculations of the PDF integrals were the main source of computation time in the dynamic grinding calculation. The algorithm was executed using Matlab 7.12.0 on an Intel i7 Dual Core microprocessor. The simulation setup for the static wheel

grit protrusion height PDF took an average of 6.23 seconds. This same function could then be used for different dynamic scenarios. The calculation of the dynamic grit density characteristics for any given spindle speed and feedrate took an average of 16.3 additional seconds.

## **7.4 NUMERICAL SIMULATION OF DYNAMIC WHEEL TOPOGRAPHY**

The numerical simulation is designed to replicate the assumptions made to construct the analytic infeed grinding force model. This will serve to verify the accuracy of the analytic model. The simulation begins with a simulated wheel that is created using the algorithm presented in CHAPTER 3. The algorithm for simulating the cutting action of the wheel is identical that used in CHAPTER 6 for straight traverse grinding with only slight modifications to account for the change in grinding approach. The simulations will use overlapping grits which matches the analytic model assumptions.

## **7.5 COMPARISON BETWEEN ANALYTIC MODEL AND NUMERICAL SIMULATION**

The analysis was conducted for a #400, single-layered microgrinding wheels with a 1mm outer diameter. The thickness of the workpiece was selected to be 135  $\mu\text{m}$  which creates a grind zone angle  $\theta$  of approximately  $15^\circ$ .

### 7.5.1 Probability of the Engagement of a Single Grit Caused by the Shadowing of another Grit

The foundation of the analytic formulation of the probability of a grit being active rests on the condition that needs to be met in order for a single grit not to be overshadowed by another individual grit,  $h_{ij} > 0$ . Figure 7.4 shows a comparison between the probability density function of the engagement depth of grit  $i$  after the shadowing caused by grit  $j$  as calculated by the analytic model and the numerical simulation.

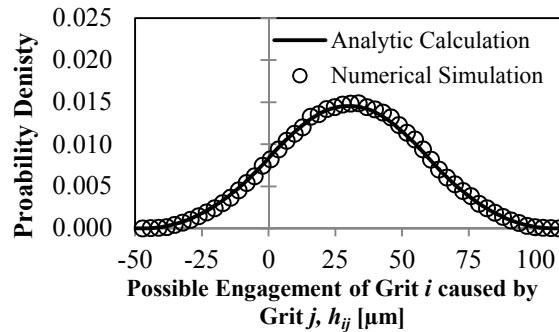


**Figure 7.4 - Probability density of the engagement of a single grit caused by the possible overshadowing by another individual grit  $f_{H_{ij}}(h_{ij})$  shows a Gaussian distribution,  $\Omega = 30\text{krpm}$  ,  $v_f = 30\text{m/s}$ .**

It is seen that the profile is approximately Gaussian with a positive mean. The analytic solution is seen to closely capture the stochastic properties observed by the numerical simulation technique. The probability of overshadowing not being caused by this single other grit is the area beneath the curve above zero engagement.

### 7.5.2 Probability of a Single Grit being Active

The probability of a grit being active was derived to be the product of the probabilities that it is not overshadowed by each of the other grits that act along the same

circumferential grind path. Figure 7.5 shows that the probability of grit  $i$  not being overshadowed by grit  $j$  is always greater than 50%. However, the final analytic probability that the grit is not overshadowed any other grit and is active is much smaller. The analytic probability of a grit being active is compared to the mean probability observed in 1,000 iterations of numerical simulation at each infeed angle operating condition. The plot shows that the probability of a grit being active increases significantly at higher infeed angles.

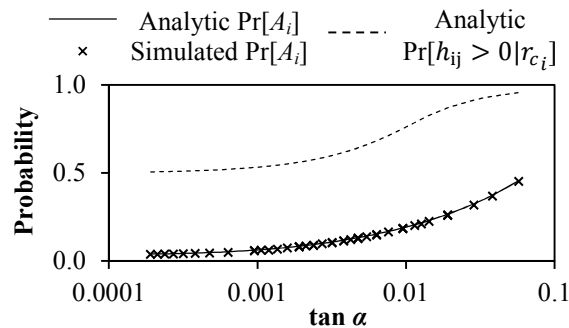


**Figure 7.5 -Analytic calculations of the probability of a grit being active matching well with numerical simulation results**

### 7.5.3 Dynamic Grit Density

The analytic model was used to predict the dynamic grit density mean and standard deviation under different grinding infeed angles. Figure 7.6 shows that the analytic model accurately captures the behavior seen in the numerical simulation. The dynamic grit density mean is seen to increase with larger infeed angles which agrees with measured dynamic wheel topographies in literature [71, 72]. The standard deviation is observed to be significantly large ranging to a maximum of 45% of the mean.

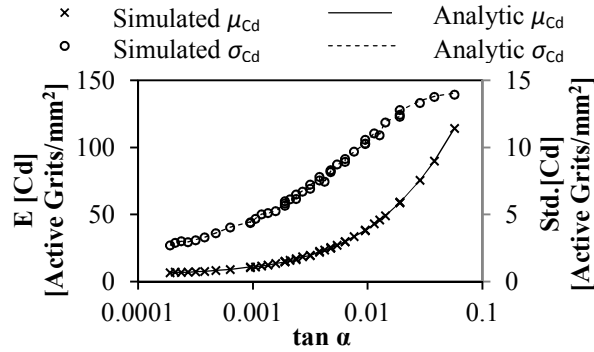


**Figure 7.6 - Statistical nature of expectation and mean of the dynamic grit density are seen to be well modeled by the analytic solution**

An examination of the ability of the analytic model to predict the behavior of actual wheels in which grits cannot overlap can be conducted by comparison to the unmodified numerical simulation that implements grit relocation to remove overlap. The results from that comparison, seen in Figure 7.7, indicate that the numerical simulations that eliminate grit overlap are still consistently predicted by the analytic model. However, the results do diverge slightly at high infeed angles. This is expected to be caused by the deviation of the grit protrusion height PDF between the two simulations having more effect when such a large number of grits are active.

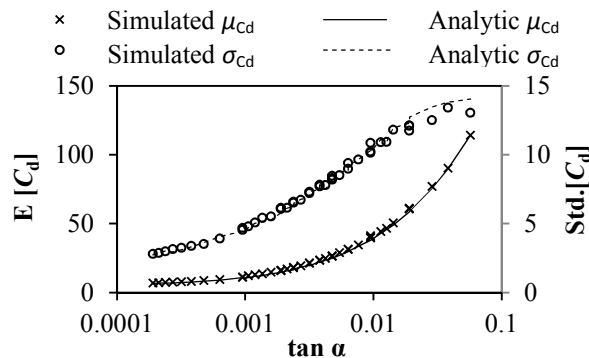


**Figure 7.7 - Results from the numerical simulation technique that eliminates overlapping grits shows that the approximations made by the analytic model allow it to accurately predict the more realistic dynamic grit density characteristics.**

## 7.6 MEASUREMENT OF DYNAMIC MICROGRINDING WHEEL TOPOGRAPHY USING IN-FEED GRINDING

### 7.6.1 Setup

The in-feed grinding technique was chosen to help facilitate the ability to measure and detect the individual grit force pulses during microgrinding. A diagram of the experimental setup used to measure the individual grit force pulses is shown in Figure 7.8. The WC workpiece is rigidly fixtured to a 22 kHz force transducer with a 25 kHz accelerometer attached for supplemental grit pulse measurement. The forces are measured in the cutting force direction. The fixture was designed to provide maximum stiffness with minimal moving mass in order to maximize the system natural frequency to that of the sensors themselves. The horizontally-configured spindle is mounted on a 3-axis high precision linear actuator stage by Aerotech.

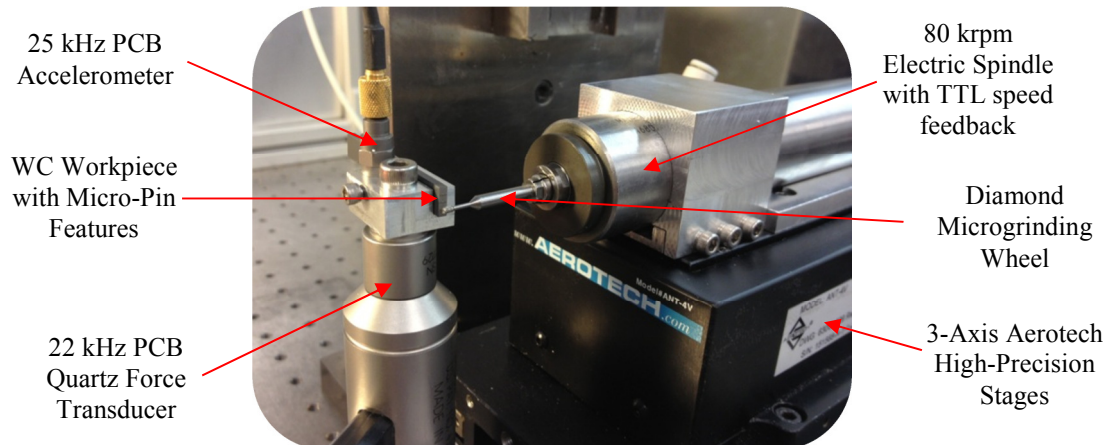


**Figure 7.8 – Experimental setup for measuring microgrinding forces using the in-feed technique**

The WC workpiece consists of a bulk substrate with micro-pins machined on an exposed surface. The micro-pins were machined using WEDM in order to achieve high

dimensional accuracy and minimal residual stress in the micro-pin surface. An example of one of the micro-pins is shown in Figure 7.9 along with the dimensional specifications. The workpiece width of 150  $\mu\text{m}$  provides a grind zone angle of  $17^\circ$  on a 1mm grind wheel. The thickness of the workpiece is 50  $\mu\text{m}$  which corresponds to the mean grit diameter for the wheels used for the experimentation. This allows for only a single line-of-action segment along the grind wheel width to participate in grinding at once. A 125  $\mu\text{m}$  radius fillet is machined into the rectangular pin base in order to minimize the likelihood of complete pin fracture.



**Figure 7.9 – Micrographs of WC workpiece micro-pin features with a 150 $\mu\text{m}$  engagement width in the circumferential direction (a) and a 50 $\mu\text{m}$  engagement width in the axial direction (b) of the grind wheel**

The natural response of the grinding setup was measured using impact testing with the resulting response shown in Figure 7.10. It is seen that the responses of the measured force and acceleration are similar. The system natural frequency is measured to be 18 kHz.

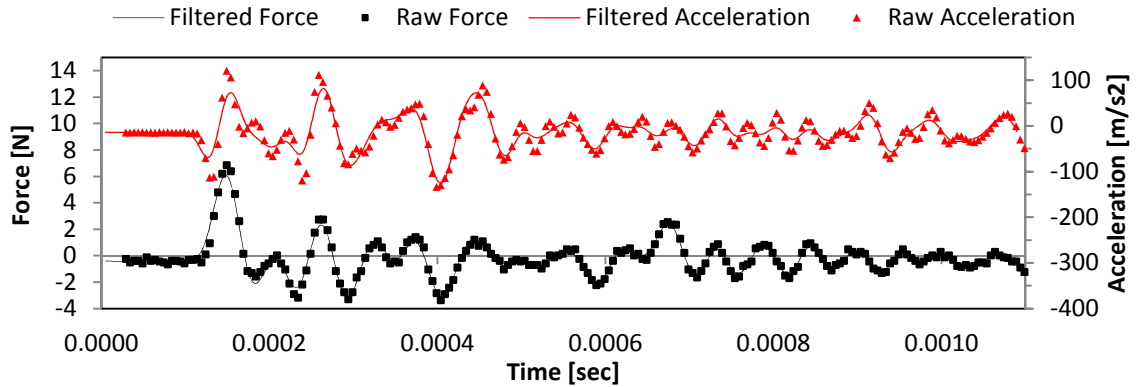


**Figure 7.10 – Impact response of in-feed experimental measurement system to force pinging on workpiece without grind wheel interaction with 30 kHz lowpass filtering**

## 7.6.2 Details of Experimentation

The experimentation needs to measure the distributions of dynamic grit density, dynamic grit spacing, and grit cutting force magnitudes across different grinding infeed angles. Many repetitious measurements of these attributes need to be conducted in order to capture these distributions. Therefore, wheel set A was created from a selection of 5 grind wheels from wheel set 3 presented in Table 4.4. The wheels chosen were the ones with the most similar measured concentration numbers. They are summarized in Table 7.2. The grinding infeed angles chosen were selected from the middle of the range investigated by the analytic model and numerical simulation presented earlier in this chapter. Four duplicate measurements were taken for each wheel at each infeed angle for a total of 80 grinding tests.

**Table 7.2 – Wheel set A chosen for measurement of dynamic topography distributions**

Wheel #	Manufacturer Specifications			Measured Specifications				Measured Characteristics		
	$\hat{G}\#$	$\hat{D}$ [ $\mu\text{m}$ ]	$\hat{w}$ [ $\mu\text{m}$ ]	$\hat{C}$	$D_{\text{shank}}$ [ $\mu\text{m}$ ]	$t_{\text{bond}}$ [ $\mu\text{m}$ ]	$w$ [ $\mu\text{m}$ ]	$C$	$N_a$	$C_s$ [ $\#/\text{mm}^2$ ]
3.1	#400	1016	1588	140	903.4	43.3	1317	136.28	798	194.78
3.4					921.8	40.1	1309	141.30	774	187.75
3.7					895.5	44.4	1581	133.42	953	195.04
3.12					912.2	43.9	1459	134.20	891	194.42
3.15					910.0	43.0	1454	136.09	878	193.06

A summary of the experimental plan and test naming convention is outlined in Table 7.3. The execution order of the tests was randomized to mitigate systematic errors. The micro-pin workpieces were machine from 2 different stocks of fine-grained WC. The source stock for each test sample was also randomized. The feedrate for each test was fixed to the values in the experimental plan. The spindle speeds required to achieve the desired infeed angle for each test was calculated using the measured bond diameter for each specific wheel.

**Table 7.3 – Outline of experimental test plan with measured dynamic grit density.  
Test execution order was randomized.**

Test #	Wheel #	Tan $\alpha$	Infeed-rate [mm/s]	Approximate Spindle Speed [krpm]	Duplicate #	Measured Dynamic Grit Density
1	3.1	0.003	1	6.4	1	38.08
2					2	35.70
3					3	47.60
4					4	40.80
5		0.008	2	4.8	1	61.73
6					2	68.59
7					3	56.12
8					4	51.44
9		0.020	4	3.9	1	85.74
10					2	73.49
11					3	92.60
12					4	92.46
13		0.050	4	1.5	1	120.04
14					2	108.03
15					3	132.28
16					4	84.18
Test blocks continue to wheels 3.4, 3.7, 3.12, and 3.15 sequentially						

A sample of the measured force and acceleration profiles is shown in Figure 7.11 for test 26 on wheel 3.4 with an infeed angle of 0.020, feedrate of 4 mm/sec, and a spindle speed of 3.864 krpm. The electric spindle is driven by a synchronous PM electrical machine allowing for feedback from the spindle drive voltage profile to provide TTL logical signal of the wheel position. The square wave logic signal discretized each spindle revolution into 24 segments allowing for accurate measurement of the spindle speed and interpolation of the spindle angular position over time.

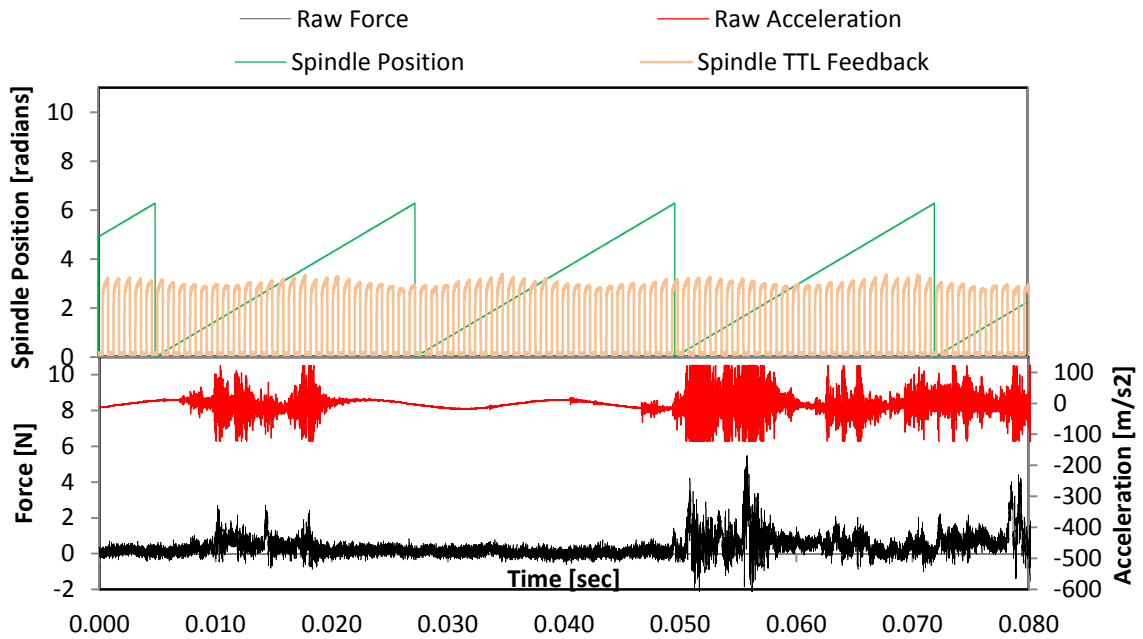


**Figure 7.11 – Characteristic experimental force data, from test 26, showing discernible force pulses and entry-zone of initial wheel contact**

The grind force signature for test 26 shows initial wheel contact followed by wheel clearance caused by initial micro-pin fracturing. The following force signatures began a period of repetitious force profiles created by stable cutting action. The accelerometer was able to capture force pulses of very small grit engagements that were lost in the noise of the force transducer as can be seen in Figure 7.11. However, the acceleration signal contained excessive dynamics that saturated the signal at times and provided little information for the significant force pulses. The low frequency modulation observed in the acceleration profile is attributed to electromagnetic noise.

The force profile for one revolution of the grind wheel in the stable cutting period in test 23 is shown in Figure 7.12. Lowpass filtering was implemented to remove

frequencies above 12 kHz. The measurement of the cutting forces induced by the cutting action of individual abrasives involves the identification of the force peaks that have a sudden increase of force at the cutting entry and a sharp decrease of force at the cutting exit on the workpiece. Appropriately identified cutting force peaks have a sharp force rise followed by corresponding fall at the appropriate time spacing required for the grit to move through the 150 $\mu$ m grind zone. The example calculation for test 23 is shown in Equation 7.23 where it is determined that a force pulse that results from a grit interacting across the full length of the workpiece should be 0.593 milliseconds long. Here,  $L$  is the length of the workpiece.

$$t_{\text{cut}} = \frac{L}{v_{\text{cut}}} = \frac{L}{\frac{2\pi N (D_{\text{bond}})}{60}} = \frac{0.150 \text{ mm}}{\frac{2\pi (3358 \text{ rpm}) (1.4377 \text{ mm})}{60}} = 0.593 \text{ msec} \quad \text{Equation 7.23}$$

The measured force profile for test 23 shows 5 grits identified using this criterion. The magnitude of the force pulse was measured at the entrance of the grits from the grind zone where the force change is most drastic. It is observed that grits 2 and 5 show more sloping of the force decrease at the grind zone exit. It is suspected that this is caused fracturing of the workpiece at the end of the cut where there is less resistive strength on the edge of the workpiece.

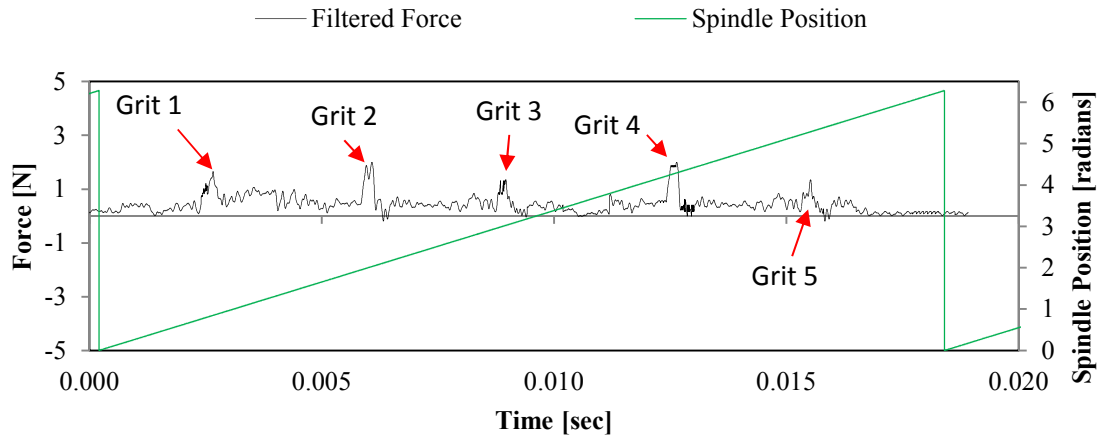


**Figure 7.12 - Detailed examination of the lowpass-filtered cutting force signal for test 23 after process stabilization**

The force profile for one revolution of the grind wheel in the stable cutting period in test 26 is shown in Figure 7.13 as a representation of some of the less clear force signatures experienced at larger infeed angles. It is observed that this cutting force profile has significantly more noise than that shown for test 23. The more aggressive cutting action occurring at the larger infeed angle causes larger forces and larger residual vibration in the workpiece and fixture. In addition, the penetration depth of the workpiece material into the grind wheel could be causing a number of grits that do not lie on the direct cutting action line along the wheel periphery to contact the workpiece. These other grits could be introducing a significant amount of rubbing and side-plowing force on the workpiece in addition to the direct cutting forces of the grits that do lie on the line of action. In addition, the larger penetration depth of the workpiece into the grind wheel could be causing rubbing between the workpiece and the bond layer itself further complicating the force signature.

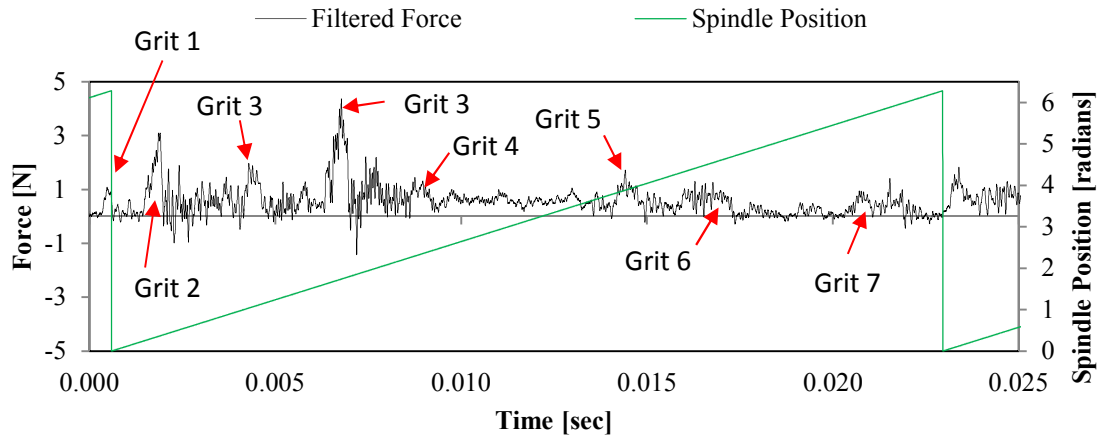


**Figure 7.13 – Detailed examination of the lowpass-filtered cutting force signal for test 26 after process stabilization**

### 7.6.3 Results

The measured grit pulse spacings and force magnitudes recorded during each test are detailed in APPENDIX B. The number of grits identified in each test was divided by the wheel bond surface area to calculate the dynamic grit density. The dynamic grit densities for wheel 3.1 are shown in Table 7.3 while the measured dynamic grit densities of the other tests are included in APPENDIX B. The experimental results for wheel 3.1, consisting of tests 1-16, were analyzed for mean and standard deviation of the dynamic grit density at each infeed angle. The results are shown in Table 7.4 along with the values predicted by the analytic model. It is observed that the measured dynamic grit density mean and standard deviation both increase for larger infeed angles as predicted by the model. However, the predicted values are significantly lower than that measured.

**Table 7.4 – Comparison between measured dynamic grit density distribution parameters for wheel 3.1 with predicted parameters from analytic model using 10% grit retainment depth**

$\tan \alpha$	Experimental Measurement		Analytic Model Prediction	
	$\mu[G_d]$	$\sigma[G_d]$	$\mu[G_d]$	$\sigma[G_d]$
0.003	40.54	5.14	21.03	7.16
0.008	59.47	7.39	35.99	9.46
0.020	87.07	10.08	57.40	11.56
0.050	111.13	20.52	90.28	14.82

It is hypothesized that the significantly smaller values predicted in the analytic model are caused by an erroneous assumption about the minimal retainment depth of each grit in the wheel bond. Larger retainment depths correspond to grits having to be embedded deeper in the wheel bond in order to maintain bonding force during grinding. In fact, other research has observed retainment depths near 35% for electroplated diamond wheels which differs drastically from the 10% adopted in the current model from Koshy [12]. In addition, the other initial assumptions about the grind wheel geometry, including the abrasive diameters and the uniform distribution in Cartesian space, have been measured and validated by multiple studies. In addition, the static wheel measurements in CHAPTER 4 validated the grit position distribution for this wheel set. The retainment depth, however, was not grounded in actual wheel measurement.

The retainment depth parameter was explored by optimizing the retainment assumption in the analytic model. The evaluation metric that was chosen is the correlation coefficient between the predicted dynamic grit density mean and standard deviation and the measured values across the 4 infeed angles. The correlation coefficient  $R^2$  was calculated for the mean and standard deviation separately utilizing only the results from wheel 3.1 out of wheel set A. The impact of the retainment depth on the predicted

parameters is shown in Figure 7.14 where the chosen optimal retainment depth of 48% is seen to maximize  $R^2$  for the both the dynamic grit density mean and standard deviation.

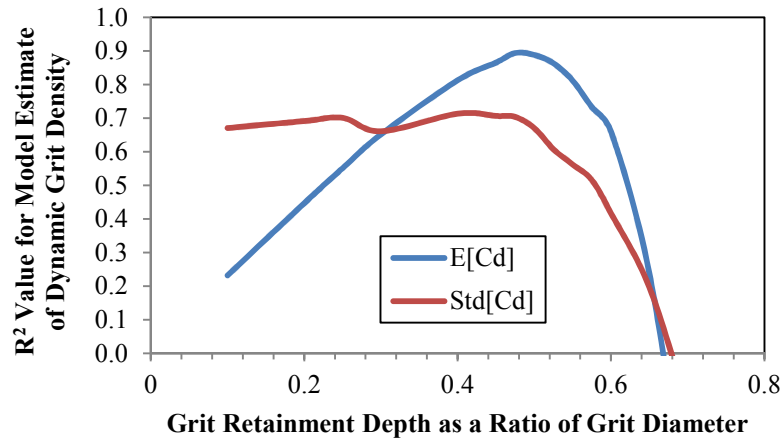


**Figure 7.14 – Actual grit retainment depth determined to be 48% at the maximum  $R^2$  value between the analytic model and measured dynamic grit density parameters**

The accuracy of the analytic model in predicting the distribution parameters for the dynamic grit density was analyzed using the measured data from the remaining wheels in wheel set A (wheels 3.4, 3.7, 3.12, 3.15). The model values were calculated using the optimized 48% retainment depth. A comparison between the measured values and the model is shown in Figure 7.15. It is observed that dynamic grit density mean is predicted accurately across all three wheels and at all of the infeed angles. The dynamic grit density standard deviation prediction is observed to capture the average effect of the measured values. However, there is significant variation between the values measured at the smallest three infeed angles.

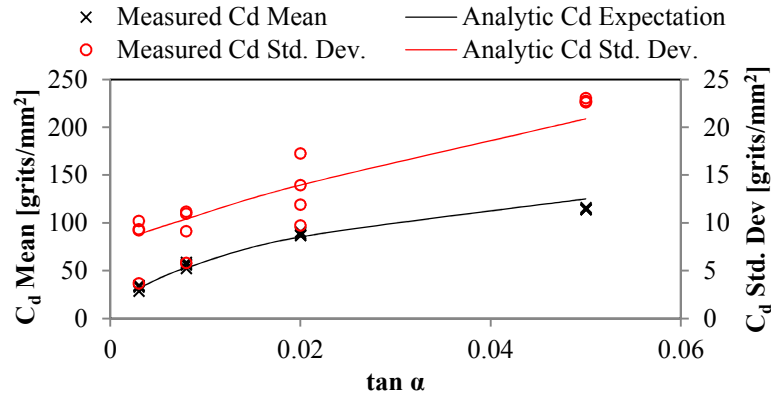


**Figure 7.15 – Comparison of the dynamic grit density distribution parameters between the measured values for grind wheels 3.4, 3.7, 3.12, and 3.15 and that predicted by the analytic model using 48% retainment**

The total set of measured grit spacings and force magnitudes across all wheels in wheel set A measured at an infeed angle of 0.02 are used to examine the distributions of these attributes. The occurrence histogram for the dynamic grit spacings is shown in Figure 7.16. In total, 255 grit pulses were identified. The histogram shows a near Gaussian distribution of the dynamic spacings with a range that spans from as small as the average grit diameter up to 18% of the wheel circumference. A fitting of a Gaussian distribution to the measured data yielded a mean of 310  $\mu\text{m}$  and a standard deviation of 114  $\mu\text{m}$ . The p-value for the fitting of the Gaussian distribution is 0.06, which is greater than the selected rejection rate of 0.05, meaning that the Gaussian fit cannot be rejected as the underlying probability distribution.

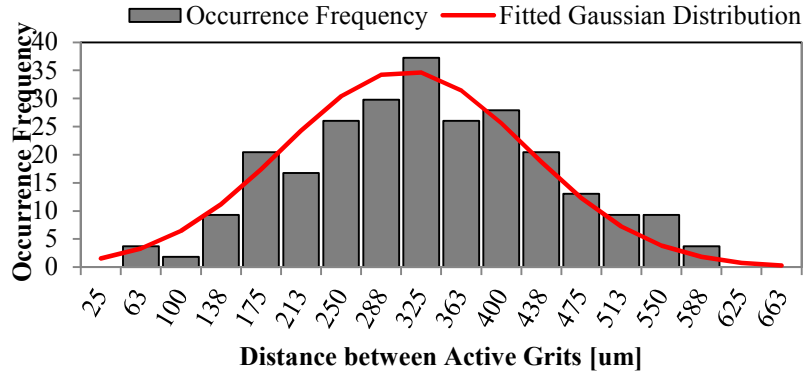


**Figure 7.16 – Distribution of dynamic distance between active grits along wheel periphery for grinding Wheel Set A,  $\tan \alpha = 0.02$**

The occurrence histogram and for the dynamic grit spacings is shown in Figure 7.17. The distribution is seen to closely resemble the Rayleigh distribution, which has been identified as the appropriate distribution in multiple studies at the conventional grind wheel scale. However, the minimal presence of very small grinding forces can be attributed to the inability to identify them using the instrumentation used. The signal-to-noise ratio for the force transducer inhibits the ability to identify such a small force peak. Therefore, it is hypothesized that there are a significant number of grits that interact with the workpiece with such a small force as they move through the grind zone with only rubbing contact and possibly some localized deflection of the workpiece and grit. A fitting of a Rayleigh Distribution yielded a distribution parameter of 0.6576. The p-value for the Rayleigh fitting is 0.02 meaning that the measured force magnitudes did not come from the fitted distribution. However, qualitative assessment shows that the Rayleigh distribution does capture the overarching trend in the occurrence frequency of the measured force peaks.

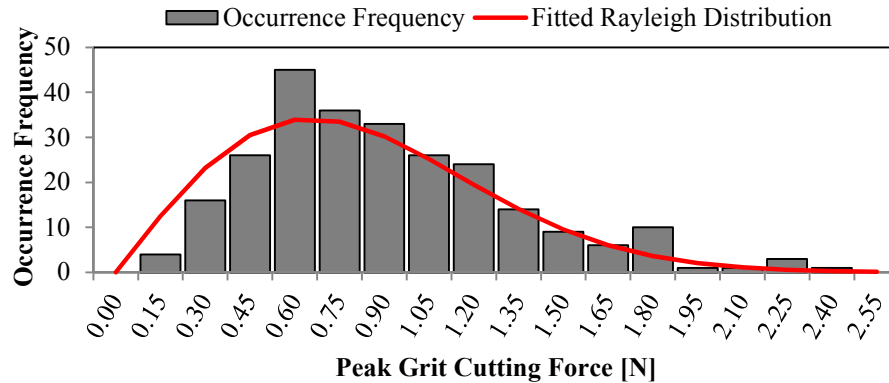


**Figure 7.17 – Distribution of measured peak individual grit cutting force for grinding Wheel Set A,  $\tan \alpha = 0.02$**

## 7.7 DISCUSSION

The probabilistic model was seen to accurately capture the results of the numerical simulation with overlapping grits. The analytic model could not yield a complete PDF of the dynamic grit density. However, numerical simulation shows that it can be approximated by a Gaussian distribution that can be created by the analytically predicted mean and standard deviation [73]. This corresponds to approximating the binomial distributed number of active grits by a Gaussian distribution which is known to be accurate for a large number of trials (greater than 20) as is the case here for the number of abrasives in a wheel [74]. The analytic method predicts the dynamic grit density for a given process in less than 29% of the time needed to execute 1,000 numerical simulations. The major advantage of the analytic model is the elimination of the need thousands of duplicate simulations to eliminate sampling effects.

The infeed grinding approach was shown to facilitate the identification and measurement of the cutting forces of individual microgrinding wheel grits. However, a large single-to-ratio in the force transducer caused a failure to identify possible grit-workpiece interactions that result in very small forces. In addition, the use of a thin

workpiece to identify single grits does not preclude the possibility of multiple grits cutting simultaneously due to the workpiece being located between them in the axial direction of the wheel. However, this geometric interference would incorporate both grits exerting side-plowing forces on the workpiece which would not produce the characteristic large sharp increase and delayed decrease in force that was used as criteria for the cutting force identification. Therefore, the identified force peaks only incorporate the *cutting* action of grits along the line of action of the workpiece.

The investigation into the accuracy of the analytic model in predicting the dynamic grit density mean and standard deviation yielded a method to calculate the minimal retainment depth of grits in wheel bond. The measured dynamic grit density parameters showed that there is large variability in the action of the microgrinding wheels with dynamic grit density standard deviations as high as 27% of the mean value. However, this variation could be partially explained by the inaccuracies in the determination of the measured dynamic grit density resulting from the inherent experimental uncertainty in the grit identification within the measurements. It is noted, however, that any errors associated with the identification of grits would average out in the measurement of the dynamic grit density mean. However, the errors would manifest into an overall increase in the measured standard deviations of the dynamic grit density which was not seen to be significant in the results. The lack of current literature on the dynamic grit density of these microgrinding wheels limits the ability to compare the results to that of other studies. However, it is noted that the ratio between the static grit density and dynamic grit density, 15-50% depending on the infeed angle, is similar to that seen in studies of conventional grind wheels [2].

The analysis of the distribution of the individual grit cutting forces showed that they resemble that of a Rayleigh distribution although the fitted distribution was statistically rejected. The average cutting force measured was 0.83 N while the peak force measured was 2.29 N which is over 2.8 times larger than the average.

The microgrinding wheels used in this study are electroplated with the diamond abrasives and then roughly dressed in order to dislodge any abrasives that are not strongly bonded to the surface. This directly results in the minimum retainment depth of the grits being slightly larger than that measured by other studies. In addition, this dressing creates initial wheel surfaces that provide a semi-stationary wheel topography for the initial grinding process. This was observed in the cutting force profile appearing repetitive during the grinding tests. Therefore, it is concluded that the tests were of sufficiently short length, approximately 10 wheel revolutions, and there was not significant time for abrasive wear or wheel heating despite the lack of process coolant. As the process progresses the stationary model will slowly become inaccurate due to wheel wear of different forms. Enhancements to the model can be made to consider these effects. In addition, the process can be observed in order to adapt the model over time such that accuracy can be maintained.

## **7.8 SUMMARY**

The infeed microgrinding approach provided a method to capture individual grit force data. The probabilistic model is seen to provide a method of quickly and accurately calculating the stochastic properties of the dynamic grinding wheel topography. This technique has the strength of being able to accept any probability function for the

protrusion heights of static grits or for the spacings between grits. The technique was seen to predict the outcome of the numerical simulations that model wheel simulations that do not have overlapping grits. The analytic model was used to show that superabrasive microgrinding wheels suffer from large variability due to the low number of grits in them and that the dynamic grit density standard deviation can be as high as 45% of the mean with a high dependence on the grinding infeed angle.

Results from the experimental measurement of microgrinding forces showed that the initial assumption of only 10% minimal retainment of the grits in the bond layer is inaccurate. The analytic model was used to calculate the more accurate minimal retainment depth of 48% by minimizing the error between the model and the experimental results of a single grind wheel. This model-fitting method is identified as a possible technique for calculating the minimal grit retainment depth in microgrinding wheels. The prediction of the dynamic grit density distribution parameters for the other tested wheels was seen to be accurate with the tuned wheel characteristic of minimal retainment depth. Results showed that the measured dynamic grit density standard deviation was as high as 27% of the mean dynamic grit density. This means that for a given process, different microgrinding wheels from the same manufacturer with almost identical specifications can have a variation in the number of grits removing material upwards of 27%.

The experimental measurement of the dynamic grit spacings showed that statistically they come from a Gaussian distribution. It was observed that a single process executed on 4 times on 4 identical wheels yielded grit spacings between 34  $\mu\text{m}$  and 560  $\mu\text{m}$  with varying probability. In addition, the probability distribution of the cutting force of

individual grits was observed to have a significant skew towards smaller forces. Results show that across 16 grinding tests of identical process parameters using 4 wheels of identical specifications, the maximum cutting force observed was 2.8 times larger than the average force observed. Although the Rayleigh distribution was statistically rejected, the occurrence frequency of the individual grit cutting forces is closely captured by the fitted distribution.

The large variations in the number of grits participating in a given process and the peak force exerted on the workpiece could be detrimental in the microgrinding of HAR ceramic micro-features if the process control does not use stochastic predictions of the grinding forces. The probabilistic model provides a method to accurately predict these forces but wheel topography measurement needs to be conducted to account for the effects of wheel manufacturing specification accuracy and unknown wheel attributes such as the minimal retainment depth of grits on the wheel surface.

## CHAPTER 8– CONCLUSIONS

### 8.1 SUMMARY AND CONCLUSIONS

This work has addressed the stochastic issues of microgrinding wheels that make it difficult to machine high aspect ratio, ceramic micro-features using straight traverse grinding. Statistical propagation was used to generate a comprehensive stochastic model for static grit density mean and variance based rudimentary assumptions about the distribution of grits in Cartesian space. The model statistics were validated using a new wheel simulation technique but was shown to be significantly faster than the simulation.

The accuracy of the model prediction of microgrinding wheel static grit density was verified using an *in situ* machine vision technique to measure the wheel surface. Characterization of microgrinding wheel specifications revealed that the wheel manufacturing errors can be modeled using Gaussian distributions. The analytic model prediction of static grit density distribution parameters was shown to have large error when the wheel specification errors are not measured. Statistical calculations showed that the *in situ* machine vision measurement system would only need a few sample images of the wheel surface to sufficient estimate the concentration number and static grit density for a given wheel.

Scaling effects associated with the few number of abrasives in microgrinding wheels were identified. Measurement of microgrinding wheel surface topography showed that the static grit density relative standard deviation increases significantly as the number of abrasives in the wheel is decreased at the micro scale. Investigation into this effect using the probabilistic model confirmed that the number of abrasives is the best scaling parameter for relative standard deviation of the static grit density. It was also shown that

the relative standard deviation of the wheel concentration number can dominate the total variability in the static grit density in both conventional and microgrinding wheels.

An analytic model for the prediction of the Gaussian distribution parameters of the dynamic grit density was generated for straight traverse grinding. Numerical simulation showed that the spindle frequency and its harmonics dominate the microgrinding force frequency profile. The straight traverse microgrinding of a razorblade using a micromachining tool confirmed this dominant frequency response of the process.

An infeed grinding approach was adopted to facilitate the measurement of the individual grit force pulses in microgrinding. A probabilistic model was generated to predict the dynamic grit density mean and standard deviation for this grinding method. Grinding tests confirmed the ability to identify and measure individual grit cutting forces at constant infeed angles through the grind zone. Comparison of the measured dynamic grit densities to the analytic model revealed that the 10% grit retainment depth assumption is invalid. Optimization of the analytic model revealed that a grit retainment depth of 48% resulted in the largest correlation coefficient between the model and the measured values. The optimized retainment depth model was shown to accurately predict the dynamic grit density expectation and variance in other grinding tests.

Analysis of the distributions of the measured dynamic grit spacings and individual grit cutting forces showed that there is a large range of values at the micro-scale. It was also observed that the dynamic grit spacings of microgrinding wheels can be described by a Gaussian distribution while the distribution of the grit cutting force closely resembles that of a Rayleigh distribution as has been measured by others at the conventional scale.

Pursuant to the work summarized above and presented in the preceding chapters, the following conclusions can be drawn:

1. The number of abrasives in a grind wheel has a Gaussian distribution that can be closed-form analytically predicted using statistical propagation.
2. Analytic statistical propagation can be used to develop probabilistic models that quickly predict the Gaussian distribution parameters that describe the distribution of static grit density in superabrasive grinding wheels.
3. Microgrinding wheel specification errors were shown to be significant and appropriately modeled using Gaussian distributions.
4. The probabilistic and numerical simulation models generated are able to capture static wheel topography and predict the static grit density in all 39 wheels measured within a 5% significance level.
5. Manufacturer wheel specification error limits the ability to predict static grit density to within 25.3% without wheel measurement.
6. The loglogistic distribution provides an improved model for the occurrence probability so static grit spacing along the periphery of microgrinding wheels.
7. The scale effect that best captures the increase in statistical variation of wheel topography characteristics in microgrinding is the number of abrasives in the wheel.
8. The force frequency content of straight traverse microgrinding is dominated by the spindle frequency. The spindle frequency harmonics do not consistently decay nor excite system natural frequencies.

9. The use of the probabilistic model for dynamic grit density and the measured results from infeed grinding allowed the calculation of the actual minimal grit retainment depth of 48%.
10. The probabilistic model for infeed microgrinding accurately predicted the dynamic grit density mean and standard deviation after calibration for the actual minimum grit retainment depth.

## 8.2 CONTRIBUTIONS

Pursuant the work summarized above and presented in the preceding chapters, the following contributions were made:

- A probabilistic model for the prediction of static wheel topography distribution parameters for superabrasive grind wheels was developed using statistical propagation.
- A new technique for numerical simulation of grind wheel static topography based on vectorized grit relocation to minimize the occurrence of grit overlap was developed.
- An *in-situ*, machine vision based technique for the measurement of microgrinding wheel surface topography was developed.
- An analytic formulation of the impact of grind wheel concentration number variation on the variation in static grit density was developed
- A probabilistic model for the prediction of dynamic grit density mean and standard deviation was developed for straight traverse grinding.

- A probabilistic model for the prediction of dynamic grit density mean and standard deviation was developed for infeed grinding.
- A method of measuring individual grit cutting forces in microgrinding without varying undeformed chip thickness was developed in infeed grinding.
- The following papers have been published or are currently under review:
  1. J. Kunz and J. Rhett Mayor, "Static Grit Density Measurement Methods for Medium-Grit Diamond Microgrinding Wheels," Proceedings of the 6<sup>th</sup> International Conference on Micro-Machining, Tokyo, Japan, March 7-10, 2011.
  2. J. Kunz and J. Rhett Mayor, "Stochastic Modeling of Microgrinding Wheel Topography," ASME Journal of Micro and Nano-manufacturing, 2012.
  3. J. Kunz and J. Rhett Mayor, "Stochastic Characteristics in Microgrinding Wheel Static Topography using Machine Vision," Proceedings of the 8th International Conference on Micro-Machining, Victoria, BC, Canada, March 25-28, 2013.
  4. J. Kunz and J. Rhett Mayor, "Analytic Stochastic Modeling of Dynamic Wheel Topography in Superabrasive Grinding," Proceedings of the 41<sup>st</sup> SME North American Manufacturing Research Conference, Madison, WI, USA, June 10-14, 2013.
  5. J. Kunz and J. Rhett Mayor, "Measurement and Modeling of Stochastic Characteristics in Microgrinding Wheel Static Topography," Submitted to the ASME Journal of Micro and Nano-Manufacturing, JMNM-13-1052, 2013.

6. J. Kunz and J. Rhett Mayor, “Measurement and Modeling of Stochastic Characteristics in Infeed Microgrinding,” In preparation for submission to the SME Journal of Manufacturing Processes, 2013.

### **8.3 RECOMMENDATIONS AND FUTURE WORK**

During the course of this study several additions and extensions to the work were considered. These additions and extensions are presented here as recommendations for future work.

- Advanced process control for the microgrinding of HAR ceramic micro-features

The probabilistic models presented in this study propagate statistical descriptions of the wheel topography and cutting parameters in order to capture the variability that exists in microgrinding forces. A process control technique should be generated to maximize the material removal rate of ceramic microgrinding without jeopardizing the integrity of the components. This should be done by using the analytic models to identify process controls that will limit the probability of a grit cutting force greater than the allowable magnitude for the HAR micro-feature. A schematic of such a control technique is shown in Figure 8.1 using pre-process optimization and adaptive model-based control.

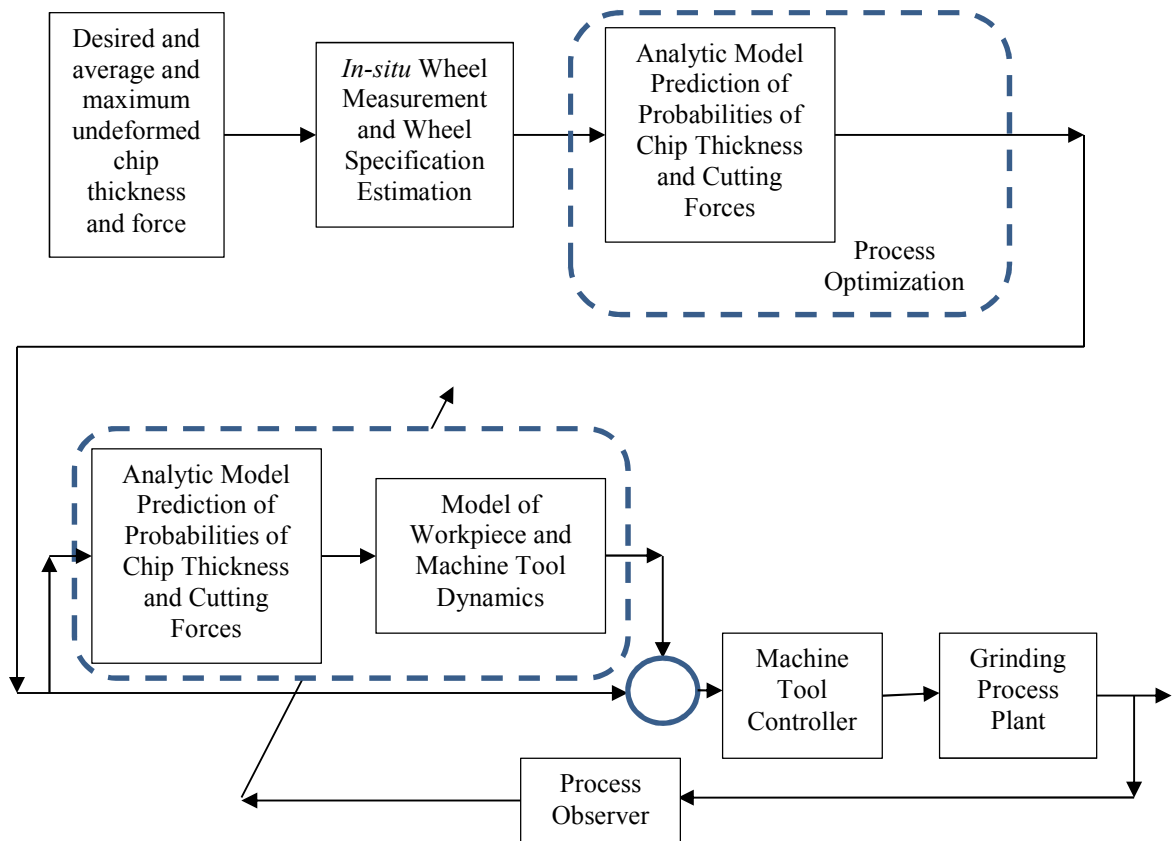


**Figure 8.1 – Potential algorithm for adaptive model-based control of microgrinding using the developed probabilistic models**

- Expansion of the probabilistic model to include grit cutting force

The probabilistic models presented in this work predict the distribution of dynamic grit density in microgrinding. The analytic prediction of the individual grit cutting force requires the convolution of the random variable distributions that govern the selected individual cutting force model. These often include the undeformed chip thickness of a particular grit, the grit diameter, the workpiece grain size and the orientation of the grain in the workpiece.

- Expanded investigation into the scale effects associated with individual grit cutting forces in the grinding of ceramics

The analysis of individual grit cutting force data requires extensive grinding tests in order to accumulate a measurement population large enough to make any statistical conclusions. More testing is needed to expand the measured grit cutting force distributions to wheels of varying sizes and concentrations. This will reveal any underlying scale effects associated the distributions of the force attributes.

- Investigation into the nature of the dominant force frequency signature of microgrinding in the micromachining tool

The investigation into the force frequency content of traverse microgrinding on a razorblade surface using the micromachining tool showed inconclusive results. The time-frequency analysis of the force measurements showed dominant contributions by extremely high spindle speed harmonics. No explanation could be generated to interpret this result and it inhibits the ability to measure microgrinding forces on the machine tool where parts are to be manufactured. More investigation into the source of the dominant spindle harmonics needs to be conducted.

## APPENDIX A – SOLUTION TO ANALYTIC STATIC MODEL

This appendix details the analytical solutions to the grind wheel static grit density model. The number of grits in a wheel follows a normal distribution as described by Equation A.1. The parameters of the distribution are described by the expectation calculated in Equation A.2 and the variance calculated in Equation A.3.

$$N_a \sim \text{Norm}\left(E[N_a], \sqrt{\text{Var}[N_a]}\right) \quad \text{Equation A.1}$$

$$E[N_a] = \frac{3Cw(d_w^2 - d_c^2)}{800\mu_D(\mu_D^2 + 3\sigma_D^2)} \quad \text{Equation A.2}$$

$$\text{Var}[N_a] = 36 \frac{\text{Var}[V_a] + \left(\frac{Cw\pi^2\sigma_D^2(d_w^2 - d_c^2)(3\mu_D^4 + 12\mu_D^2\sigma_D^2 + 5\sigma_D^4)}{3200\mu_D(\mu_{D_i}^2 + 3\sigma_D^2)}\right)}{\pi^2\mu_{D_i}^2(\mu_D^2 + 3\sigma_{D_i}^2)^2} \quad \text{Equation A.3}$$

The probability density functions for the location of any general grit centroid in cylindrical coordinates are shown in Equation A.4, Equation A.5, and Equation A.6.

$$f_R(r) \cong \frac{\left(1 - \frac{1}{2}\text{Erfc}\left[-\frac{\frac{5d_w}{4} - \frac{5r}{2} + \mu_D}{\sqrt{2}\sigma_D}\right]\right)\text{Erfc}\left[\frac{d_{wc} - 2r + \mu_D}{\sqrt{2}\sigma_D}\right]r}{\left(\frac{d_w}{2} + \frac{2\mu_D}{5}\right)^2 - \left(\frac{d_c}{2} + \frac{\mu_D}{2}\right)^2} \quad \text{Equation A.4}$$

$$f_\theta(\theta) = \frac{1}{2\pi} \quad \text{Equation A.5}$$

$$f_z(z) = \frac{1}{w} \quad \text{Equation A.6}$$

The analysis of the static grit density investigates the probability of grits intersecting a cylindrical surface of the wheel. The probability of any grit intersecting the surface involves the probability of a grit intersecting in the individual cylindrical coordinates. The probability of intersecting in the angular direction is shown in Equation A.7 while that for the axial direction is shown in Equation A.8.

$$\Pr(\mathcal{C}_\theta = \text{true}) = 1 \quad \text{Equation A.7}$$

$$\Pr(\mathcal{C}_Z = \text{true}) = \int_{-\infty}^{\infty} \frac{Z_b - Z_a - d_i}{w_w} f_{D_i}(d_i) dd_i = \frac{Z_b - Z_a - \mu_D}{w \sqrt{\frac{1}{\sigma_D^2} \sigma_D}} \quad \text{Equation A.8}$$

Single-layered grind wheels can be defined as wheels that only have enough room in the bond layer for one or two grits. It was shown that the condition that needs to be met for a wheel to be considered single-layered requires that most of the grit diameters be greater than the bond layer thickness. This condition is shown in Equation A.9.

$$\left( \frac{11(\mu_d + 3\sigma_d)}{10} > \frac{D_g - D_c}{2} \right) \quad \text{Equation A.9}$$

The probability of a grit intersecting the cylindrical surface in the radial domain is shown in Equation A.10 for a single layered wheel. Equation A.11 shows the solution for a multilayered wheel.



$$\begin{aligned}
\Pr(C_R = \text{true} | R_c) = & \int_{R_c - \frac{\mu_D}{2}}^{\frac{d_w + 2\mu_D}{2}} \frac{1}{4} (1 + \operatorname{Erfc}[\frac{-5d_w + 10R_c + \mu_D}{\sqrt{2}\sigma_D}]) (1 + \operatorname{Erfc}[\frac{5d_w - 10R_c + 9\mu_D}{9\sqrt{2}\sigma_D}]) \\
& \frac{(1 - \frac{1}{2} \operatorname{Erfc}[\frac{5d_w - 5r_i - \frac{5}{2} + \mu_D}{\sqrt{2}\sigma_D}]) \operatorname{Erfc}[\frac{d_c - 2r_i + \mu_D}{\sqrt{2}\sigma_D}] r_i}{(\frac{d_w}{2} + \frac{2\mu_D}{5})^2 - (\frac{d_c}{2} + \frac{\mu_D}{2})^2} dr_i \\
& \int_{R_c - \frac{\mu_D}{2}}^{R_c + \frac{\mu_D}{2}} \frac{1}{4} \operatorname{Erfc}[\frac{-5d_w + 10R_c + \mu_D}{\sqrt{2}\sigma_D}] \operatorname{Erfc}[\frac{d_c - 2R_c + 2\mu_D}{2\sqrt{2}\sigma_D}] \\
& \frac{(1 - \frac{1}{2} \operatorname{Erfc}[\frac{5d_w - 5r_i - \frac{5}{2} + \mu_D}{\sqrt{2}\sigma_D}]) \operatorname{Erfc}[\frac{d_c - 2r_i + \mu_D}{\sqrt{2}\sigma_D}] r_i}{(\frac{d_w}{2} + \frac{2\mu_D}{5})^2 - (\frac{d_c}{2} + \frac{\mu_D}{2})^2} dr_i \\
& \int_{R_c - \frac{\mu_D}{2}}^{R_c + \frac{\mu_D}{2}} \frac{1}{2} (1 + \operatorname{Erfc}[\frac{d_c - 2R_c + 2\mu_D}{2\sqrt{2}\sigma_D}]) (1 - \frac{1}{2} \operatorname{Erfc}[\frac{5d_w - 5r_i - \frac{5}{2} + \mu_D}{\sqrt{2}\sigma_D}]) \operatorname{Erfc}[\frac{d_c - 2r_i + \mu_D}{\sqrt{2}\sigma_D}] r_i \\
& \frac{(\frac{d_w}{2} + \frac{2\mu_D}{5})^2 - (\frac{d_c}{2} + \frac{\mu_D}{2})^2}{2} dr_i
\end{aligned}$$

The final probability of any grit intersecting a given cylindrical surface in a wheel can be described by a distribution with an expectation given by Equation A.12 and a variance given by Equation A.13.

$$E(\mathcal{C}) = \Pr(\mathcal{C}_R)\Pr(\mathcal{C}_\theta)\Pr(\mathcal{C}_Z) \quad \text{Equation A.12}$$

$$\text{Var}(\mathcal{C}) = (E(\mathcal{C}))(1 - E(\mathcal{C})) \quad \text{Equation A.13}$$

The probability of a wheel having a static grit density is a random variable. It is shown through Monte Carlo numerical simulation that the occurrence probability of this random variable can be described by a normal distribution which is summarized in Equation A.14.

$$C_s \sim \text{Norm}\left(E[C_s], \sqrt{\text{Var}[C_s]}\right) \quad \text{Equation A.14}$$

The expected value of the static grit density is calculated for a single-layered wheel in Equation A.15. The expected value of the static grit density is calculated for a multi-layered wheel in Equation A.16.



$$\begin{aligned}
E[C_s] &= \frac{3C(d_w^2 - d_{wc}^2)(-Z_a + Z_b - \mu_D)\sqrt{\sigma_D}}{800(-Z_a + Z_b)\mu_D\pi 2R_c(\mu_D^2 + 3\sigma_D^2)} \\
&\quad \frac{1}{4}(1 + \operatorname{Erf}[\frac{-5d_w + 10R_c + \mu_D}{\sqrt{2}\sigma_D}]) \left(1 \right. \\
&\quad \left. + \operatorname{Erf}[\frac{5d_w - 10R_c + 9\mu_D}{9\sqrt{2}\sigma_D}] \right) \int_{R_c - \frac{\mu_D}{2}}^{\frac{d_w + 2\mu_D}{2}} \frac{(1 - \frac{1}{2}\operatorname{Erfc}[\frac{5d_w - 5r_i + \mu_D}{\sqrt{2}\sigma_D}])\operatorname{Erfc}[\frac{d_{wc} - 2r_i + \mu_D}{\sqrt{2}\sigma_D}]r_i}{(\frac{d_w}{2} + \frac{2\mu_D}{5})^2 - (\frac{d_{wc}}{2} + \frac{\mu_D}{2})^2} dr_i \\
&\quad + \frac{1}{4}\operatorname{Erfc}[\frac{-5d_w + 10R_c + \mu_D}{\sqrt{2}\sigma_D}] \operatorname{Erfc}[\frac{d_{wc} - 2R_c + 2\mu_D}{2\sqrt{2}\sigma_D}] \int_{R_c - \frac{\mu_D}{2}}^{R_c + \frac{\mu_D}{2}} \frac{(1 - \frac{1}{2}\operatorname{Erfc}[\frac{5d_w - 5r_i + \mu_D}{\sqrt{2}\sigma_D}])\operatorname{Erfc}[\frac{d_{wc} - 2r_i + \mu_D}{\sqrt{2}\sigma_D}]r_i}{(\frac{d_w}{2} + \frac{2\mu_D}{5})^2 - (\frac{d_{wc}}{2} + \frac{\mu_D}{2})^2} dr_i + \frac{1}{2}(1 \\
&\quad + \operatorname{Erf}[\frac{d_{wc} - 2R_c + 2\mu_D}{2\sqrt{2}\sigma_D}]) \int_{\frac{d_{wc} + \mu_D}{2}}^{R_c + \frac{\mu_D}{2}} \frac{(1 - \frac{1}{2}\operatorname{Erfc}[\frac{5d_w - 5r_i + \mu_D}{\sqrt{2}\sigma_D}])\operatorname{Erfc}[\frac{d_{wc} - 2r_i + \mu_D}{\sqrt{2}\sigma_D}]r_i}{(\frac{d_w}{2} + \frac{2\mu_D}{5})^2 - (\frac{d_{wc}}{2} + \frac{\mu_D}{2})^2} dr_i
\end{aligned}$$

The variance in the static grit density can be calculated for either a single-layered or multi-layered wheel using Equation A.17 by substituting the corresponding variables for that wheel type.

$$\text{Var}[C_s] = \frac{E[N_a]\text{Var}[C_i] + (E[C_i])^2\text{Var}[N_a]}{(2\pi R_c(Z_b - Z_a))^2} \quad \text{Equation A.17}$$

## APPENDIX B – RESULTS FOR MEASURED INFEEED GRINDING FORCES

This appendix details the measured values of the experimental measurement of infeed microgrinding detailed in CHAPTER 7. Table B.1 shows the measured dynamic grit density for each grinding test. Table B.2 details the grit force pulse measurements.

**Table B.1 – Outline of experimental test plan with measured dynamic grit density. Test execution order was randomized.**

Test #	Wheel #	Tan $\alpha$	Infeed-rate [mm/s]	Approximate Spindle Speed [krpm]	Duplicate #	Measured Dynamic Grit Density
1	3.1	0.003	1	6.4	1	38.08
2					2	35.70
3					3	47.60
4					4	40.80
5		0.008	2	4.8	1	61.73
6					2	68.59
7					3	56.12
8					4	51.44
9		0.020	4	3.9	1	85.74
10					2	73.49
11					3	92.60
12					4	92.46
13		0.050	4	1.5	1	120.04
14					2	108.03
15					3	132.28
16					4	84.18
17	3.4	0.003	1	6.4	1	25.40
18					2	31.77
19					3	25.41
20					4	31.77
21		0.008	2	4.8	1	40.13
22					2	50.83
23					3	60.99
24					4	57.18
25		0.020	4	3.9	1	91.49
26					2	79.56
27					3	76.24
28					4	114.36
29		0.050	4	1.5	1	123.89
30					2	93.84
31					3	96.31
32					4	140.75

**Table B.1 –continued**

Test #	Wheel #	Tan $\alpha$	Infeed-rate [mm/s]	Approximate Spindle Speed [krpm]	Duplicate #	Measured Dynamic Grit Density
33	3.7	0.003	1	6.4	1	47.77
34					2	32.34
35					3	25.87
36					4	32.34
37		0.008	2	4.8	1	45.66
38					2	51.75
39					3	71.65
40					4	58.22
41		0.020	4	3.9	1	93.14
42					2	71.65
43					3	83.59
44					4	98.79
45		0.050	4	1.5	1	126.13
46					2	95.53
47					3	98.05
48					4	143.30
49	3.12	0.003	1	6.4	1	42.44
50					2	38.20
51					3	19.10
52					4	31.83
53		0.008	2	4.8	1	44.94
54					2	50.93
55					3	70.52
56					4	57.30
57		0.020	4	3.9	1	91.67
58					2	76.39
59					3	82.27
60					4	98.22
61		0.050	4	1.5	1	124.14
62					2	94.02
63					3	96.50
64					4	141.04
65	3.12	0.003	1	6.4	1	47.21
66					2	31.96
67					3	25.57
68					4	31.96
69		0.008	2	4.8	1	51.14
70					2	64.60
71					3	61.37
72					4	57.53
73		0.020	4	3.9	1	92.05
74					2	73.64
75					3	82.61
76					4	106.21
77		0.050	4	1.5	1	124.65
78					2	94.41
79					3	96.90
80					4	141.62











## REFERENCES

- [1] N. Otsu, "A threshold selection method from gray-level histograms," *Automatica*, vol. 11, pp. 23-27, 1975.
- [2] S. Malkin and C. Guo, *Grinding technology: theory and applications of machining with abrasives*: Industrial Pr, 2008.
- [3] Imec. (2009, Integration technology for wearable and implantable applications. *Imec Scientific Report 2009*.
- [4] GTRI. (2013, Powering an Energy Revolution: Fuel Cells Promise Improvements in Transportation, Electronics and Power Generation. *Industry Solutions*. Available: <http://www.gtri.gatech.edu/casestudy/powering-energy-revolution>
- [5] Maruwa. (2013). *Ceramic Valves*. Available: <http://www.maruwa-g.com/e/products/ceramic/000322.html>
- [6] P. M. Tool. (2010, August 17). *Home*. Available: <http://www.pmtnow.com/>
- [7] M. Goller, N. Lutz, and M. Geiger, "Micromachining of ceramics with excimer laser radiation," *Journal of the European Ceramic Society*, vol. 12, pp. 315-321, 1993.
- [8] J. Imasu, H. Fudouzi, and Y. Sakka, "Micro-scale patterning of ceramic colloidal suspension by micro molding in capillaries (MIMIC) with assistance of highly infiltrating liquid," *Nippon seramikusu kyokai gakujuutsu ronbunshi*, vol. 114, pp. 725-728, 2006.
- [9] M. Kumar, "Laser assisted micro milling of hard materials," 2011.
- [10] C. Zhang, E. Brinksmeier, and R. Rentsch, "Micro-USAL technique for the manufacture of high quality microstructures in brittle materials," *Precision engineering*, vol. 30, pp. 362-372, 2006.
- [11] H. Huang and T. Kuriyagawa, "Effect of microstructure on material removal mechanisms in nano/micro grinding of tungsten carbide mould inserts," 2010, pp. 877-882.
- [12] J. Aurich, J. Engmann, G. Schueler, and R. Haberland, "Micro grinding tool for manufacture of complex structures in brittle materials," *CIRP Annals-Manufacturing Technology*, vol. 58, pp. 311-314, 2009.
- [13] L. Yin, E. Vancoille, K. Ramesh, H. Huang, J. Pickering, and A. Spowage, "Ultraprecision grinding of tungsten carbide for spherical mirrors," *Proceedings of the Institution of Mechanical Engineers, Part B: Journal of Engineering Manufacture*, vol. 218, pp. 419-429, 2004.
- [14] L. Yin, A. Spowage, K. Ramesh, H. Huang, J. Pickering, and E. Vancoille, "Influence of microstructure on ultraprecision grinding of cemented carbides," *International Journal of Machine Tools and Manufacture*, vol. 44, pp. 533-543, 2004.

- [15] H. Ohmori, K. Katahira, T. Naruse, Y. Uehara, A. Nakao, and M. Mizutani, "Microscopic grinding effects on fabrication of ultra-fine micro tools," *CIRP Annals-Manufacturing Technology*, vol. 56, pp. 569-572, 2007.
- [16] K. Katahira, H. Ohmori, Y. Uehara, Y. Watanabe, W. Lin, J. Komotori, *et al.*, "Fabrication of high-quality surfaces on micro tools by the ELID grinding technique," *Key Engineering Materials*, vol. 257-258, pp. 441-6, 2004.
- [17] R. L. Hecker, I. M. Ramoneda, and S. Y. Liang, "Analysis of wheel topography and grit force for grinding process modeling," in *31st North American Manufacturing Research Conference, NAMRC 31, May 20, 2003 - May 23, 2003*, Hamilton, ON, Canada, 2003, pp. 281-288.
- [18] H. Park, "Development of micro-grinding mechanics and machine tools," PhD, Woodruff School of Mechanical Engineering, Georgia Institute of Technology, Atlanta, GA, USA, 2008.
- [19] Rollomatic. (2010, August 8). *Rollomatic Innovations*.
- [20] W. Rowe, L. Yan, I. Inasaki, and S. Malkin, "Applications of artificial intelligence in grinding," *CIRP Annals-Manufacturing Technology*, vol. 43, pp. 521-531, 1994.
- [21] E. Brinksmeier, J. Aurich, E. Govekar, C. Heinzl, H. Hoffmeister, F. Klocke, *et al.*, "Advances in modeling and simulation of grinding processes," *CIRP Annals-Manufacturing Technology*, vol. 55, pp. 667-696, 2006.
- [22] E. Brinksmeier, Y. Mutlugünes, F. Klocke, J. Aurich, P. Shore, and H. Ohmori, "Ultra-precision grinding," *CIRP Annals-Manufacturing Technology*, vol. 59, pp. 652-671, 2010.
- [23] I. Inasaki, "Grinding process simulation based on the wheel topography measurement," *CIRP Annals-Manufacturing Technology*, vol. 45, pp. 347-350, 1996.
- [24] R. Cai and W. Rowe, "Assessment of vitrified CBN wheels for precision grinding," *International Journal of Machine Tools and Manufacture*, vol. 44, pp. 1391-1402, 2004.
- [25] M. Miyashita, in *1st Annual Precision Engineering Conference*, North Carolina State University, Raleigh, USA, 1985.
- [26] D. Golini and S. D. Jacobs, "Transition between brittle and ductile mode in loose abrasive grinding," in *San Diego-DL Tentative*, 1990, pp. 80-91.
- [27] H. Hoffmeister and M. Hlavac, "Trueing of Micro-Grinding Wheels by Diamond Tools," 2005.
- [28] J. Feng, "Microgrinding of Ceramic Materials," The University of Michigan, 2010.

- [29] M. Hasegawa, "Statistical Analysis for the Generating Mechanism of Groudn Surface Roughness," *Wear*, vol. 29, pp. 31-39, 1974.
- [30] W. König and W. Lortz, "Properties of cutting edges related to chip formation in grinding," *Annals of the CIRP*, vol. 24, pp. 231-236, 1975.
- [31] P. Koshy, V. Jain, and G. Lal, "A model for the topography of diamond grinding wheels," *Wear*, vol. 169, pp. 237-242, 1993.
- [32] P. Koshy, V. Jain, and G. Lal, "Stochastic simulation approach to modelling diamond wheel topography," *International Journal of Machine Tools and Manufacture*, vol. 37, pp. 751-761, 1997.
- [33] Z. Hou and R. Komanduri, "On the mechanics of the grinding process-Part I. Stochastic nature of the grinding process," *International Journal of Machine Tools and Manufacture*, vol. 43, pp. 1579-1593, 2003.
- [34] S. M. Pandit and G. Sathyanarayanan, "Model for Surface Grinding Based on Abrasive Geometry and Elasticity," *Journal of engineering for industry*, vol. 104, pp. 349-357, 1982.
- [35] F. Huo, D. Guo, R. Kang, and Z. Jin, "Characteristics of the Wheel Surface Topography in Ultra-precision Grinding of Silicon Wafers," *Key Engineering Materials*, vol. 389, pp. 36-41, 2009.
- [36] T. Hwang and C. Evans, "High speed grinding of silicon nitride with electroplated diamond wheels, part 2: wheel topography and grinding mechanisms," *Journal of manufacturing science and engineering*, vol. 122, pp. 42-50, 2000.
- [37] S. Law and S. Wu, "Simulation study of the grinding process," *Journal of Engineering for Industry*, vol. 95, p. 972, 1973.
- [38] T. Orioka, "Probabilistic treatment on the grinding geometry," *Bulletin of the Japanese Society of Grinding Engineers*, vol. 1, pp. 27-29, 1961.
- [39] H. McAdams, "Markov chain models of grinding profiles," *Journal of Engineering for Industry*, vol. 86, p. 383, 1964.
- [40] M. Younis and H. Alawi, "Probabilistic analysis of the surface grinding process," *Transactions of the Canadian Society for Mechanical Engineers*, vol. 8, pp. 208-213, 1984.
- [41] P. Basuray, B. Sahay, and G. Lal, "Surface generated in fine grinding. Part 1 Probabilistic model," *The International Journal of Production Research*, vol. 19, pp. 677-688, 1981.
- [42] S. Agarwal and P. V. Rao, "A new surface roughness prediction model for ceramic grinding," *Proceedings of the Institution of Mechanical Engineers, Part B: Journal of Engineering Manufacture*, vol. 219, pp. 811-819, 2005.

- [43] Z. Shi and S. Malkin, "An investigation of grinding with electroplated CBN wheels," *CIRP Annals-Manufacturing Technology*, vol. 52, pp. 267-270, 2003.
- [44] Y. Gong, B. Wang, and W. S. Wang, "The simulation of grinding wheels and ground surface roughness based on virtual reality technology," *Journal of Materials Processing Technology*, vol. 129, pp. 123-126, 2002.
- [45] W. W. Hines, D. C. Montgomery, D. M. Goldsman, and C. M. Borror, *Probability and Statistics in Engineering (Forth Edition)*: Wiley, 2003.
- [46] S. M. Ross, *Introduction to Probability Models*, 2nd ed.: Academic press, 1980.
- [47] C. Davis, "The dependence of grinding wheel performance on dressing procedure," *International Journal of Machine Tool Design and Research*, vol. 14, pp. 33-52, 1974.
- [48] H. C. Chang and J. J. J. Wang, "A stochastic grinding force model considering random grit distribution," *International Journal of Machine Tools and Manufacture*, vol. 48, pp. 1335-1344, 2008.
- [49] N. Kramer and C. Wangenheim, "Model Based Characterization of the Grinding Wheel Effective Topography," *Key Engineering Materials*, vol. 389, pp. 258-263, 2009.
- [50] H. Tönshoff, J. Peters, I. Inasaki, and T. Paul, "Modelling and simulation of grinding processes," *CIRP Annals-Manufacturing Technology*, vol. 41, pp. 677-688, 1992.
- [51] S. S. Law, *Grinding process model-building and analysis*: University of Wisconsin--Madison, 1972.
- [52] X. Chen and W. Rowe, "Analysis and simulation of the grinding process. Part I: Generation of the grinding wheel surface," *International Journal of Machine Tools and Manufacture*, vol. 36, pp. 871-882, 1996.
- [53] J. Peklenik, "Kinematische Betrachtungen des Systems Werlaeugmaschine-Werkstueck-Werkzeug und die Systematik der Zerspanung," *Bericht des Werkzeugmaschinenlabors der TH Aachen*, pp. 1-35, 1957.
- [54] J. Verkerk, "Final report concerning CIRP cooperative work on the characterization of grinding wheel topography," *Annals of the CIRP*, vol. 26, pp. 385-395, 1977.
- [55] M. Shaw, "Fundamentals of grinding," 1972, pp. 221-258.
- [56] L. Yan, Z. Zhou, F. Jiang, and Y. Rong, "The Application of Three-Dimensional Surface Parameters to Characterizing Grinding Wheel Topography," *Advanced Materials Research*, vol. 126, pp. 603-608, 2010.
- [57] R. L. Hecker, S. Y. Liang, X. J. Wu, P. Xia, and D. G. W. Jin, "Grinding force and power modeling based on chip thickness analysis," *The International Journal of Advanced Manufacturing Technology*, vol. 33, pp. 449-459, 2007.

- [58] R. S. Hahn, "On the nature of the grinding process," 1962, pp. 129-154.
- [59] A. Perveen, W. Y. San, and M. Rahman, "Fabrication of different geometry cutting tools and their effect on the vertical micro-grinding of BK7 glass," *The International Journal of Advanced Manufacturing Technology*, pp. 1-15, 2011.
- [60] S. Lachance, R. Bauer, and A. Warkentin, "Application of region growing method to evaluate the surface condition of grinding wheels," *International Journal of Machine Tools and Manufacture*, vol. 44, pp. 823-829, 2004.
- [61] M. Malekian, S. Park, and M. Jun, "Tool wear monitoring of micro-milling operations," *Journal of Materials Processing Tech.*, vol. 209, pp. 4903-4914, 2009.
- [62] R. Gonzalez, R. Woods, and S. Eddins, *Digital image processing using MATLAB* vol. 624: Prentice Hall Upper Saddle River, NJ, 2004.
- [63] R. Lowry, *Concepts and applications of inferential statistics*: R. Lowry, 1998.
- [64] G. W. Corder and D. I. Foreman, *Nonparametric statistics for non-statisticians: a step-by-step approach*: John Wiley & Sons, 2009.
- [65] T. W. Anderson and D. A. Darling, "Asymptotic theory of certain "goodness of fit" criteria based on stochastic processes," *The annals of mathematical statistics*, vol. 23, pp. 193-212, 1952.
- [66] Z. Govindarajulu, "Elements of Sampling Theory and Methods," ed: Prentice Hall Upper Saddle River, NJ, 1999, pp. 29-33.
- [67] W. G. Cochran, *Sampling Techniques*, 3rd ed. New York: John Wiley & Sons, 1977.
- [68] L. Tigerstrom, "Dynamic Measuring of Number of Grinding Edges and Determination of Chip Parameters," 1980, pp. 1-7.
- [69] J. Kunz and J. R. Mayor, "Numerical Simulation of Microgrinding Wheel Topography," in *Journal of Micro and Nano-Manufacturing*, ed, 2012.
- [70] S. Law, S. Wu, and A. Joglekar, "On building models for the grinding process," *Journal of Engineering for Industry*, vol. 95, pp. 983-991, 1973.
- [71] L. Tigerstrom, "A model for determination of number of active grinding edges in various grinding processes," *Annals of the CIRP*, vol. 24, 1975.
- [72] J. Verkerk, *Final report concerning CIRP cooperative work on the characterization of grinding wheel topography*, 1977.
- [73] J. Kunz and J. R. Mayor, "Numerical Simulation for the Stochastic Dynamic Wheel Topography in Superabrasive In-Feed Grinding," in *NAMRC/SME*, 2013, pp. NAMRC41-1505.

- [74] G. Box, W. Hunter, and J. Hunter, "Statistics for experimenters An introduction to design, data analysis and model building John Wiley and Sons," *New York*, 1978.